SYNTHESIS OF HYBRID INORGANIC/ORGANIC NITRIC OXIDE-RELEASING SILICA NANOPARTICLES FOR BIOMEDICAL APPLICATIONS

Alexis Wells Carpenter

A dissertation submitted to the faculty of the University of North Carolina at Chapel Hill in partial fulfillment of the requirements for the degree of Doctor of Philosophy in the Department of Chemistry (Inorganic Chemistry).

Chapel Hill
2012

Approved by:

Dr. Mark Schoenfisch

Dr. Michel Gagné

Dr. Wenbin Lin

Dr. Royce Murray

Dr. Wei You

ABSTRACT

ALEXIS WELLS CARPENTER: Synthesis of Hybrid Inorganic/Organic Nitric Oxide-Releasing Silica Nanoparticles for Biomedical Applications (Under the direction of Professor Mark H. Schoenfisch)

Nitric oxide (NO) is an endogenously produced free radical involved in a number of physiological processes. Thus, much research has focused on developing scaffolds that store and deliver exogenous NO. Herein, the synthesis of *N*-diazeniumdiolate-modified silica nanoparticles of various physical and chemical properties for biomedical applications is presented.

To further develop NO-releasing silica particles for antimicrobial applications, a reverse microemulsion synthesis was designed to achieve nanoparticles of distinct sizes and similar NO release characteristics. Decreasing scaffold size resulted in improved bactericidal activity against *Pseudomonas aeruginosa*. Confocal microscopy revealed that the improved efficacy resulted from faster particle-bacterium association kinetics.

To broaden the therapeutic potential of NO-releasing silica particles, strategies to tune NO release characteristics were evaluated. Initially, surface hydrophobicity and NO release kinetics were tuned by grafting hydrocarbon- and fluorocarbon-based silanes onto the surface of *N*-diazeniumdiolate-modified particles. The addition of fluorocarbons resulted in a 10x increase in the NO release half-life. The addition of short-chained hydrocarbons to the particle surface increased their stability in hydrophobic electrospun polyurethanes. Although NO release kinetics were longer than that of unmodified particles, durations were still limited

to <7 days.

An alternative strategy for increasing NO release duration involved directly stabilizing the *N*-diazeniumdiolate using O^2-protecting groups. O^2-Methoxymethyl 1-(4-(3-(trimethoxysilyl)propyl))piperazin-1-yl)diazen-1-ium-1,2-diolate (MOM-Pip/NO) was grafted onto mesoporous silica nanoparticles to yield scaffolds with an NO payload of 2.5 μmol NO/mg and an NO release half-life of 23 d. Doping the MOM-Pip/NO-modified particles into resin composites yielded antibacterial NO-releasing dental restorative materials. A 3-log reduction in viable adhered *Streptococcus mutans* was observed with the MOM-Pip/NO-doped composites compared to undoped controls.

The greater chemical flexibility of macromolecular scaffolds is a major advantage over LMW NO donors as it allows for the incorporation of multiple functionalities onto a single scaffold. To demonstrate this advantage, dual functional particles were synthesized by covalently binding quaternary ammonium (QA) functionalities to the surface of NO-releasing silica particles. The QA functionality proved more effective against *Staphylococcus aureus* than *P. aeruginosa*, and increasing alkyl chain length correlated with increased efficacy. Nitric oxide-releasing QA-functionalized particles were found to be more effective against *S. aureus* compared to monofunctional particles.

To my parents, Mom and Pop,
whose love, support, and inspiration motivated me to pursue a PhD

and to my husband, Brandon,
whose love, support and inspiration helped me to get through it.

ACKNOWLEDGEMENTS

The contents of this dissertation would be much less successful without the help and support of many people. First, I would like to thank my advisor, Dr. Mark Schoenfisch, for providing invaluable lessons about research, learning, teaching and life. I have truly enjoyed being a part of the Schoenfisch lab, and I am grateful for all of the knowledge and experiences that I have gained under his guidance. The multidisciplinary research conducted in the Schoenfisch lab provided me with opportunities to think and learn about concepts outside the area of synthetic chemistry, and for that I am incredibly appreciative. I am also grateful for the opportunity to work alongside many great scientists from different disciplines that provided refreshing perspectives, challenging questions, and an enjoyable work environment. I thank Dr. Jae Ho Shin and Dr. Evan Hetrick for laying the ground work for NO-releasing silica nanoparticles that shaped my graduate career. I thank Brittany Worley for hitting the ground running and helping me round out the quaternary ammonium particle project. I thank Justin Johnson for helping with the electrospinning portion of the surface-modified particle project, and Ahyeon Koh for helping with imaging, experimental design, and keeping us from electrocuting ourselves. I thank Danielle Slomberg for doing confocal microscopy experiments that were such great contributions to the bacteria aspects of my dissertation. I thank Katey Reighard for enthusiastically helping kick start the NO- releasing dental resin composites work. I thank Wesley Storm, Dan Riccio, Peter Coneski,

and Laurel Miner for providing great discussions, guidance, motivation, and friendships. I am indebted to Dr. Masaomi Matsumoto for invaluable discussions and advice regarding organic chemistry. I am also thankful to our collaborator Dr. Joseph Saavedra for sharing his extensive knowledge of diazeniumdiolate chemistry with me.

I am grateful for the mentoring opportunities I experienced as a graduate student. I had the pleasure of working with exceptional undergraduates and high school students: Sarah Newton, Steven Nutz, Abriana Johnson and David Gu. I loved seeing their enthusiasm for learning and scientific research. I hope that they gained as much from our mentoring relationship as I did.

I also thank Dr. Carrie Donley for instruction on XPS analysis, Dr. Wallace Ambrose for assistance with TEM, and Dr. Amar Khumbar for help with SEM and EDS. I would like to thank Dr. Marc ter Horst for discussions and assistance with NMR investigations, as well as Dr. Habibi Sohrab for support and insight into ESI/MS analysis.

I thank my husband, Brandon Carpenter, for his unwavering support, endless patience and constant love, which helped me to persevere the hard times and celebrate the good times. I thank my parents, Jim and Nancy Wells, for being amazing role models and instilling in me the importance of hard work, dedication, and the desire to succeed. The love, support and encouragement you have always given me is undoubtedly the reason that I am where and who I am today.

TABLE OF CONTENTS

LIST OF TABLES

LIST OF FIGURES

LIST OF SCHEMES

LIST OF ABBREVIATIONS AND SYMBOLS

~	approximately
%	percentage(s)
$\%E_{conv}$	conversion efficiency
°C	degree(s) Celsius
×g	times the force of gravity
[…]	concentration
17FTMS	(heptadecafluoro-1,1,2,2-tetrahydodecyl)trimethoxysilane
µg	microgram(s)
µL	microliter(s)
µm	micrometer(s)
µM	micromolar
µmol	micromole
λ	wavelength
AEAP	*N*-(2-aminoethyl)-3-aminopropyltrimethoxysilane
AEAUD	*N*-(2-aminohexyl)-11-aminoundecyl-trimethoxysilane
AEMP	(aminoethylaminomethyl)phenethyltrimethoxysilane
AFM	atomic force microscope/microscopy
Ag^+	silver ion
$AgNO_3$	silver nitrate
AHAM	*N*-(6-aminohexyl)aminomethyltrimethoxysilane
AHAP	*N*-(6-aminohexyl)aminopropyltrimethoxysilane
AHAP/NO	*N*-diazeniumdiolate-modified *N*-(6-aminohexyl)aminopropyltrimethoxysilane
Ar	argon gas

ATCC	American Type Culture Collection
atm	atmosphere(s)
BAP	3-butylaminopropyltrimethoxysilane
BET	Brunauer-Emmett-Teller
BHI	brain heart infusion
BTMOS	isobutyltrimethoxysilane
butyl-AHAP	isobutyltrimethoxysilane-modified AHAP particles
butylQA	dimethylbutyl-quaternary ammonium
C. albicans	*Candida albicans*
ca.	approximately
Ca^{2+}	calcium ion
$CaCl_2$	calcium chloride
CDI	collagen density index
CFU	colony forming units
cGMP	cyclic guanosine monophosphate
$CHCl_3$	chloroform
cm	centimeter(s)
CO_2	carbon dioxide
CP	cross polarization
Cu	copper
d	day(s)
DAF-2	4,5-diaminofluorescein
DAF-2 DA	4,5-diaminofluorescein diacetate
DET	(3-trimethoxysilyl)diethylenetriamine
DI	deionized

DLS	dynamic light scattering
DMF	*N*,*N*-dimethylformamide
DMAc	*N*,*N*-dimethylacetamide
DNA	deoxyribonucleic acid
dodecylQA	dimethyldodecyl-quaternary ammonium
DP	direct polarization
E. coli	*Escherichia coli*
ECM	extracellular matrix
e.g.	for example
EDRF	endothelium-derived relaxation factor
eNOS	endothelial nitric oxide synthase
EPR	enhance permability retention effect
ESEM	environmental scanning electron microscopy/microscope
ESI/MS	electrospray ionization mass spectrometry
et al.	and others
etc.	and so forth
ethyl-AHAP	ethyltrimethoxysilane-modified AHAP particles
EtOH	ethanol
Fig.	figure
h	hour(s)
H_2O	water
HCl	hydrochloric acid
heptadecyl-AHAP	(heptadecafluoro-1,1,2,2-tetrahydrodecyl)-trimethoxysilane-modified AHAP particles
i.e.	that is

ICP-OES	inductively coupled plasma atomic emission spectroscopy
IgG	immunoglobulin G
iNOS	inducible nitric oxide synthase
IR	infrared
kg	kilogram
kHz	kilohertz
KOH	potassium hydroxide
kV	kilovolts
LMW	low molecular weight
m	meter(s)
M	molar
MΩ	megaohm(s)
MAP	3-methylaminopropyltrimethoxysilane
MAS	magic angle spinning
MBC	minimum bactericidal concentration
MeOH	methanol
methylQA	trimethyl-quaternary ammonium
mg	milligram(s)
MHz	megahertz
MIC	minimum inhibitory concentration
min	minute(s)
mL	milliliter(s)
mm	millimeter(s)
mM	millimolar
mmol	millimole(s)

mol	mole(s)
mol%	percent of total moles
MOM-Pip/NO	O^2-methoxymethyl 1-(piperazin-1-yl)diazen-1-ium-1,2-diolate
MOM-Pip/NO-TMS	O^2-methoxymethyl 1-(4-(3-(trimethoxysilyl)propyl))piperazin-1-yl)diazen-1-ium-1,2-diolate
MPTMS	3-mercaptopropyltrimethoxysilane
MRSA	methicillin-resistant *Staphylococcus aureus*
MSN	mesoporous silica nanoparticle
MTS	(3-(4,5-dimethylthiazol-2-yl)-5-(3-carboxymethoxyphenyl)-2-(4-sulfophenyl)-2H-tetrazolium
N.A.	numerical aperture
N_2	nitrogen gas
NaCl	sodium chloride
NaOMe	sodium methoxide
NaOH	sodium hydroxide
NH_4OH	ammonium hydroxide
nm	nanometer(s)
nmol	nanomole(s)
NMR	nuclear magnetic resonance spectroscopy
nNOS	neuronal nitric oxide synthase
NO	nitric oxide
NO_2	nitrogen dioxide
NO_2^-	nitrite
$[NO]_{max}$	maximum NO flux
$[NO]_T$	total amount of NO release at time T
NOA	chemiluminescent nitric oxide analyzer

NONOate	*N*-diazeniumdiolate
NOS	nitric oxide synthase
O_2	oxygen gas
octadecyl-AHAP	octadecyltrimethoxysilane-modified AHAP particles
octylQA	dimethyloctyl-quaternary ammonium
OH^-	hydroxide ion
$ONOO^-$	peroxynitrite
P. aeruginosa	*Pseudomonas aeruginosa*
PBS	phosphate buffered saline, pH 7.4
PDI	polydispersity index
PEG	poly(ethylene glycol)
pH	-log of proton concentration
PI	propidium iodide
pmol	picomole(s)
ppb	parts per billion
ppm	parts per million
PROLI/NO	*N*-diazeniumdiolate-modified L-proline
PU	polyurethane
PVC	poly(vinyl) chloride
QA	quaternary ammonium
R	water to surfactant ratio in a reverse microemulsion
RSNO	*S*-nitrosothiol
s	second(s)
S. auerus	*Staphylococcus aureus*
S. epidermidis	*Staphylococcus epidermidis*

S. mutans	*Streptococcus mutans*
SEM	scanning electron microscope/microscopy
SS	solid state
$t_{1/2}$	half-life
t	time
t_{max}	time to max NO flux
TEOS	tetraethoxysilane
TEM	transmission electron microscope/microscopy
THF	tetrahydrofuran
TMOS	tetramethoxysilane
TSA	tryptic soy agar
TSB	tryptic soy broth
U.S.	United States
UV	ultraviolet
UV-Vis	ultraviolet-visible spectroscopy
v/v	volume/volume
VEGF	vascular endothelial growth factor
wt%	percent by weight
wt/wt	weight/weight
XPS	x-ray photoelectron spectroscopy

Chapter 1:

Designing Silica Particles for the Delivery of Therapeutic Nitric Oxide

A wide range of nitric oxide (NO)-releasing materials have emerged as potential therapeutics that exploit NO's vast biological roles. Macromolecular scaffolds, such as silica nanoparticles, are particularly promising due to their ability to store and deliver larger NO payloads in a more controlled and effective manner compared to low molecular weight NO donors. In this introductory chapter, the synthesis and design of silica particles for drug delivery is presented, followed by a discussion on the development of NO-releasing silica nanoparticles for therapeutic applications.

1.1 Overview of silica nanoparticles for drug delivery

Over the past forty years, nanotechnology has revolutionized scientific research, impacting the world in ways that parallel the development of electricity, biotechnology and digital information.[1] Drawn by the fascinating properties exhibited by materials in the nanometer regime (≤100 nm), research in nearly all area of science have directed some focus into using nanotechnology. Drug delivery in particular has benefited from the use of nanomaterials as nanomedicine is poised to significantly change the future of healthcare and disease treatment.[2]

Silica-based nanoparticles represent a significant area in nanomedicine research.[3-5] Although silica does not adopt exceptionally different properties on the nanoscale, its wide-

spread use arises from well-defined and tunable structures that can be tailored towards a desired therapeutic application. Indeed, any number of functionalities may be incorporated into the silica network through facile sol–gel chemistry. Physical properties such as particle size, shape, and porosity can also be easily tuned, allowing researchers to investigate their influence on drug delivery (e.g., cellular uptake, clearance/fate, and aggregation). Furthermore, silica's inherent biocompatibility and water-solubility provide two distinct advantages when designing practical drug delivery scaffolds.

1.1.1 Sol–gel chemistry

The sol–gel process to form silica-based materials involves the hydrolysis and condensation of silane precursors to form a solid network.[6] In basic conditions, hydrolysis occurs with the displacement of a labile ligand on the silicon atom by a hydroxyl ion (Figure 1.1A). The hydrolyzed monomer then undergoes a condensation reaction with a second hydrolyzed molecule to form a siloxane bond (Figure 1.1B). Hydrolysis and condensation continue, forming a colloidal suspension (sol) that cross-links to form a solid network suspended in a continuous liquid phase (gel). Depending on the reaction conditions, the condensed products resulting from the sol–gel process can range from highly porous, nanocrystalline materials to dense amorphous networks. In addition to synthetic control, other advantages of sol–gel chemistry include mild reaction conditions, low-temperature preparation, and easy purification.[7]

The type of material that results from sol–gel processing is dependent on the type of precursor and the pH of the reaction. Precursors can be mono-, bi-, tri- or tetrafunctional based on the number of hydrolyzable ligands present (Figure 1.2). Silanes where one or

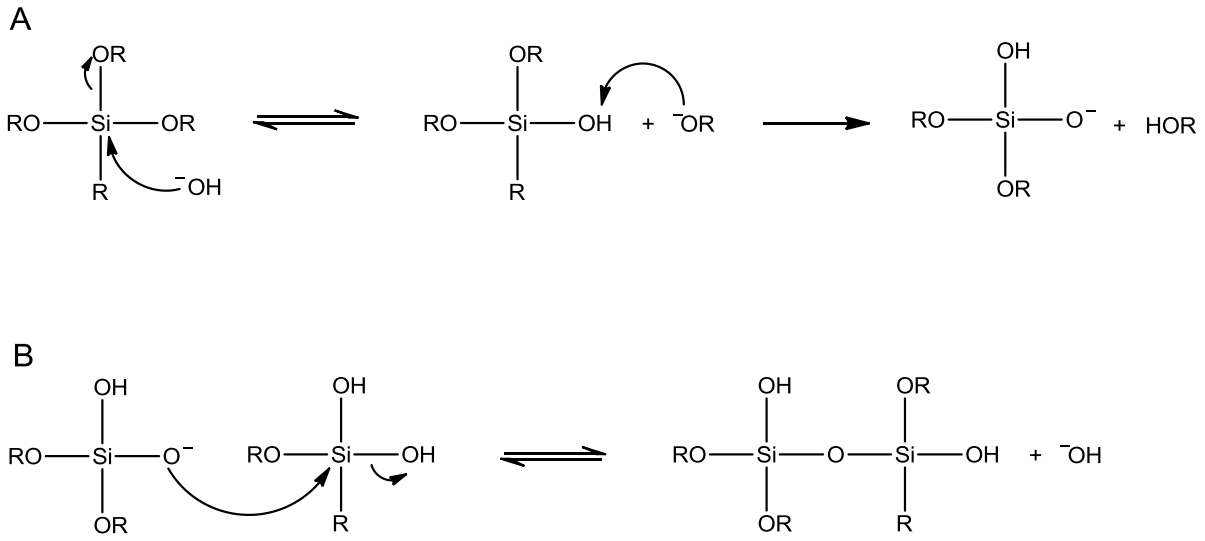

Figure 1.1 (A) Hydrolysis and (B) condensation reactions involved in the sol–gel process under basic conditions.

more of the hydrolyzable groups have been replaced with a non-hydrolyzable organic ligand are called organosilanes. The substituents on the central silicon atom govern the rate of hydrolysis and condensation through both steric and inductive effects. Larger or branched ligands hinder the access of nucleophiles to the silicon atom, thereby slowing the rate of hydrolysis. The incorporation of an electron-donating alkyl group also contributes to slower hydrolysis as the central silicon atom has a higher electron density and is therefore less electrophilic.

An acid or base catalyst is used to promote hydrolysis and condensation as well as govern the structure of the condensed product.[6] In acid-catalyzed reactions, the rates of hydrolysis are fast and the rates of condensation are slow. Acidic conditions with low water to silane ratios favor the formation of linear and branched polymers that interpenetrate with each other to form films. Alternatively, base-catalyzed sol–gel reactions with high water to silane ratios promote slow rates of hydrolysis and rapid condensation, leading to highly branched clusters that do not entangle. The preparation of silica particles is thus usually base catalyzed. Base-catalyzed hydrolysis and condensation of a single tetrafunctional silane, such as tetraethoxysilane (TEOS), represents the simplest synthesis of silica particles. To broaden their applicability, it is often desirable to vary the chemical and physical characteristics of silica particles. Thus, modified sol–gel techniques have been developed that allow for precise control over particle growth to result in materials with specific properties. The two general classes of silica particles are nonporous silica particles, synthesized by the Stöber method or the reverse microemulsion technique, and mesoporous silica particles, prepared via a surfactant-templated method.

As shown in Figure 1.3A, the Stöber method involves the hydrolysis and

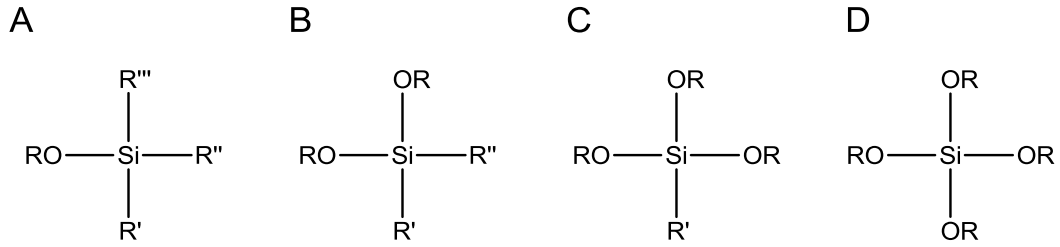

Figure 1.2 Silane precursors for sol–gel chemistry can be (A) monofunctional, (B) bifunctional, (C) trifunctional, or (D) tetrafunctional.

condensation of silane precursors in a solution of water, an alcohol solvent (typically ethanol) and a base catalyst.[8] A short-chain alcohol solvent is necessary to create a homogenous reaction solution as the tetraalkoxysilane is immiscible with water. The Stöber method yields monodisperse, spherical particles typically in the micron to submicron size range and is scalable to increase throughput. The Stöber method can be conducted in a "one-pot" reaction where all reactants are combined simultaneously. Alternatively, a seeded-growth method utilizes small particles that are initially grown and used as seeds upon which larger particles form following multi-step addition of more silane precursors. Lastly, a semi-batch approach can be used where one reactant (e.g., silane or catalyst) is added at a constant (typically slow) rate to a vessel containing the other reactants. As will be discussed in Section 1.3.1, each of these synthetic strategies allows for particle size to be tuned by changing the concentration of water or reactants, reaction temperature, and solvent type. Particles with specific organic functionalities can be created by using a corresponding silane precursor, the details of which are discussed in Section 1.4.1.

The growth of monodisperse particles via the Stöber method can be described using the LaMer theory.[9,10] These models relate the concentration of hydrolyzed silane ([monomer]) to reaction time and the number of particles formed. As hydrolysis reactions occur, the [monomer] increases with time until it reaches a critical concentration ($[monomer]_{nucleation}$) where initial sites of particle formation (i.e., nuclei) form. While $[monomer] \geq [monomer]_{nucleation}$, hydrolyzed silanes can either react with each other to form new nuclei or add to already formed nuclei. Eventually, [monomer] falls below that of the sequential addition of hydrolyzed monomers. To achieve monodisperse particle populations in Stöber reactions, the duration of the nucleation phase should be short such that

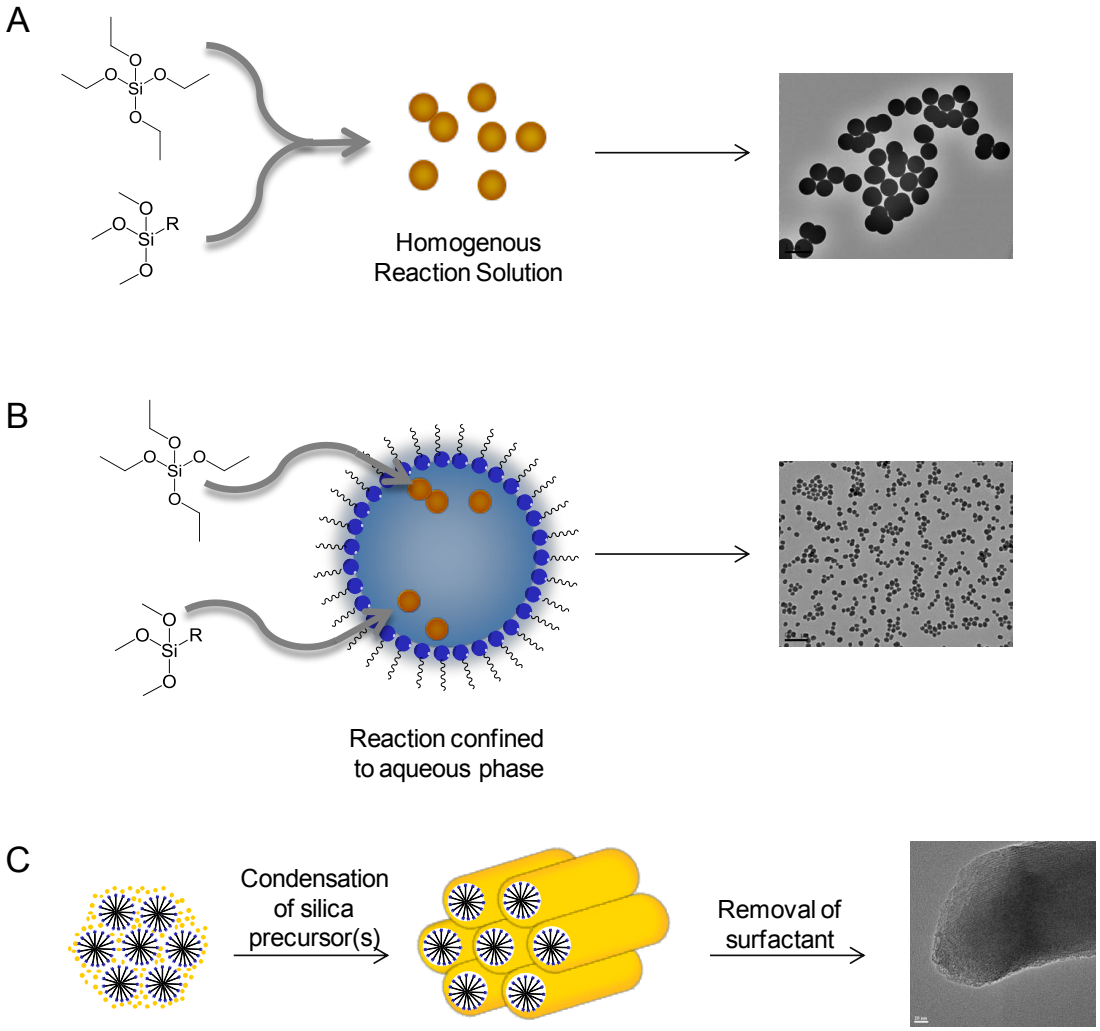

Figure 1.3 Synthetic techniques for synthesizing silica nanoparticles for drug delivery include (A) the Stöber method, (B) the reverse microemulsion technique, and (C) surfactant-templated synthesis.

most nuclei are created at the same time and experience the same growth histories. The Stöber method typically produces particles larger than 100 nm as the reaction conditions do not stabilize nuclei, causing them to aggregate and form larger particles.

The reverse microemulsion technique is a method to produce silica particles less than 100 nm with improved monodispersity.[11] In contrast to the Stöber method where the sol–gel process occurs throughout the bulk of the reaction solution, the reverse microemulsion confines particle formation to the aqueous interior of micelles stabilized in an organic solvent (Figure 1.3B). Surfactants used to form the micelles can be cationic (e.g., cetyltrimethylammonium bromide), anionic (e.g., sodium bis(2-ethylhexyl) sulfosuccinate), or nonionic (e.g., Triton X-100 or polyoxyethylene nonylphenyl ether). Typically a co-surfactant, such as 1-hexanol, is employed to stabilize the micelles. The interior of the micelles is composed of water and the base catalyst and act as nanoreactors for silica nanoparticle synthesis.

In a reverse microemulsion system, particle formation is also described according to the LaMer theory but is believed to occur at a much slower rate.[12] Upon addition to the reaction mixture, the unhydrolyzed silanes become dispersed throughout the organic phase. As they slowly come in contact with the micelles, the silanes are hydrolyzed and enter the micelle's aqueous interior.[13] Nucleation occurs when [monomer] reaches the critical concentration (e.g., $[\text{monomer}]_{\text{nucleation}}$) within the micelle. Similar to the Stöber method, the decrease in [monomer] after the onset of the nucleation phase occurs mainly through the diffusion-controlled growth of particles and nuclei. However, the diffusion-controlled growth occurs at a much slower rate in a microemulsion due to the micellar structure's effect on viscosity and diffusion coefficients. As such, the nucleation period is longer, resulting in

a greater number of particles and smaller particle sizes. Furthermore, the nuclei formed in a reverse microemulsion are believed to be stabilized by the surfactant molecules, thus the extent of nuclei aggregation is lower than in the Stöber method. Particle growth is confined to the micelle, thus particle size can be finely tuned by controlling micelle size. For example, the water to surfactant ratio, surfactant to solvent ratio, the type of organic solvent, and reaction time all affect the resulting particle size. Functionalized particles can be obtained by the addition of organosilanes to the emulsion. The major drawbacks to synthesizing silica particles via a reverse microemulsion are low yields and extensive purification steps. Particularly for biomedical applications, complete removal of the potentially cytotoxic surfactant is necessary and requires copious washing with a variety of alcohols. The ability to achieve small particles with narrow size distributions is the main advantage over the Stöber method.

The two previously discussed techniques for sol–gel chemistry result in nonporous silica particles. More recently, mesoporous silica particles (MSN) have been designed as a strategy to achieve greater functionalization potential and drug-loading capacity.[14] The surface area of MSNs is typically >900 m^2/g, while that of Stöber and reverse microemulsion-prepared silica particles is typically 5–200 m^2/g. The pores of MSNs typically have a large volume (>0.9 cm^3/g) with tunable sizes of narrow distributions (2–10 nm). Mesoporous silica particles are synthesized via a surfactant-templated approach, as illustrated in Figure 1.3C. Surfactants are used to form liquid-crystalline mesophases that act as templates for the condensation of silane precursors. Ammonium hydroxide (NH_4OH) and sodium hydroxide (NaOH) have both been employed as base catalysts, each also providing morphological control as NH_4OH and NaOH favor long and short micelles, respectively.[15]

Once the siloxane polymerization is complete, the surfactant molecules are removed either by solvent extraction with acidic ethanol or by calcination to reveal empty channels throughout the silica network.

1.1.2 Drug delivery

Silica-based nanomaterials are a popular scaffold for drug delivery due to their low cytotoxicity, chemical stability and high capacity for functionalization.[4] Compared to "soft" nanoparticles (e.g., dendrimers, polymers, and vesicles), silica exhibits increased stability at high temperatures and varied pHs and is more resistant to mechanical stresses and hydrolysis-induced degradation

Ideally, a successful drug delivery scaffold would be biocompatible and capable of high drug loading.[14] Delivery to a specific site (e.g., cell type, tissue, or organ) is a desirable trait for most therapeutic applications and can be achieved using targeting moieties, as will be discussed later. The major challenge in developing drug-releasing nanoparticles is the need for a scaffold that exhibits zero drug release prior to arrival at the site of interest and then provides complete delivery of drug payload. Furthermore, the rate of drug release from the nanoscaffold often governs its biological effect,[16] thus triggerable release of therapeutics is also desirable. In general, achieving these goals with soft nanomaterials is difficult due to uncontrollable leaching and limited functionalization ability.[14]

The two strategies that are used to load drugs onto/into silica particles include covalent incorporation and non-covalent encapsulation. Covalent incorporation provides a more secure drug storage method that decreases the chance of premature release; however, a release trigger is required to cleave the bond securing the drug to the scaffold. The most

notable release triggers for covalently loaded drugs include redox chemistry, enzymatic cleavage, pH, photolysis and thermolysis.[3] Redox chemistry is a common strategy for achieving intracellular drug delivery due to the reducing environment present inside cells. Drugs can be tethered to organically modified silica scaffolds via reduction-sensitive linkages such as disulfide[17] or organometallic[18] bonds. Hydrolysable or enzymatically cleavable bonds such as esters, carbonates, carbamates, hydrazones and amides are also common methods of covalent incorporation into silica.[19] Alternatively, pH-sensitive functionalities can be incorporated into the silica network that result in drug release once the scaffold enters an area of a certain pH. For example, the interior of endosomes is characterized by a lower pH than that of extracellular fluid (pH 5–6.5 vs 7.4, respectively). Thus, incorporating groups that are labile at lower pH values allows for selective drug release within cells. Light-responsive materials have been designed where the bond tethering the drug to the scaffold is photo-labile such that drug release can be triggered with light irradiation. Gold nanoparticles can be also be used for drug release as they will absorb light and convert the energy to heat to trigger thermolytic cleavage. While UV, visible, and near-IR active materials have been developed, near-IR irradiation (650–900 nm) is the most promising photo-trigger as it is only minimally absorbed by skin and tissue. When using covalent incorporation for drug delivery, one must ensure that the chemical modifications necessary to covalently incorporate the drug do not alter the drugs' efficacy or the scaffolds' cytotoxicity.

Alternatively, drugs may be loaded non-covalently via an encapsulation strategy. Mesoporous silica nanoparticles offer an excellent option for drug encapsulation due to the presence of large, uniform, and continuous pores. Drugs can be loaded through the use of

diffusion by placing the porous particles in highly concentrated drug solutions; however, the upper limit of loading is relatively low for this method. Alternatively, electrostatic interactions between the negatively charged silica scaffold and positively charged drug molecules can be used to achieve higher loading. Increased loading of neutral or negatively charged drugs proves more difficult. Liu et al. reported a strategy to coerce negatively charged drugs into MSNs through the formation of "protocells". [20] In this method, a positively charged liposome is fused around the negatively charged silica particle in a solution containing the drug. The electrostatic interactions between the negatively charged drug and the positively charged liposome cause the drug to be forced into the MSNs as the liposome encapsulates the silica.

When drugs are not covalently bound to the scaffold, premature release represents a major obstacle.[14] Stability of the drug within the scaffold can be promoted through non-covalent interactions such as electrostatic or hydrogen-bonding. For example, increased drug loading efficiency and extended release profiles of ibuprofen-loaded MSNs were achieved with aminosilane-modified MSNs.[21] The hydrogen-bonding interactions between the protonated primary amines (at pH 7) tethered to the scaffold and the carboxylate groups of ibuprofen aided in drug loading stabilization.

Another method for inhibiting the release of encapsulated drugs from mesoporous particles is through the use of "gatekeepers", whereby zero premature release of drug is achieved by "plugging" the entrances of pores with protecting groups after drug loading.[14, 22] The aforementioned strategies for releasing covalently bound drugs have been translated to the gatekeeping concept. For example, Lai et al. blocked the entrances to the channels of MSNs using cadmium sulfide (CdS) nanoparticles that were tethered to the silica scaffold

with disulfide linkages.[23] Reduction of the disulfide bond released the gatekeeping particle from the pore, allowing the encapsulated drug to diffuse out. Other metallic nanoparticles as well as dendrimers and bulky organic molecules have also been employed as gatekeepers with release stimuli ranging from light to oscillating magnetic fields.[3, 22]

In summary, silica-based nanoparticles offer a stable and chemically flexible scaffold that can be loaded with high concentrations of drug. The numerous opportunities for drug loading and release mechanisms are unique to these materials as such functionalities are not easily incorporated into soft materials.

1.1.3 Influence of nanoparticle properties on nanoparticle-cell interactions

Efficient drug delivery is governed by the extent of direct interaction between the nanoparticle carrier and the targeted cells. Although the release of drug into the environment surrounding the target may still result in some therapeutic effect, diffusion of the drug away from the cell would necessitate a higher dosage to elicit the same therapeutic response if the drug were delivered directly into the cell. Additionally, some drugs may be unable to permeate the cell membrane unassisted, thus nanoparticle carriers aid in intracellular delivery. Nanoparticle characteristics (i.e., size, shape, and surface chemistry) govern particle-cell interactions both in terms of association and uptake. As such, much effort has been focused on modifying particles accordingly to enhance these interactions and improve drug delivery efficiency.

The smart design of particles for drug delivery requires an understanding of the various mechanisms by which a particle may interact with a cell. Both eukaryotic and prokaryotic cells are characterized by a net negative charge, thus electrostatic forces may

lead to nanoparticle association. Indeed, positively charged particles generally exhibit greater association and subsequent internalization into mammalian cells than neutral or negatively charged particles.[24] Similarly, the extent of association between positively charged particles and bacteria cells is greater than that of negatively charged particles.[25] In addition to carrying a negative charge, the surface of both prokaryotes and eukaryotes also express hydrophobic character due to membrane lipids. As such, cells have exhibited an affinity for particles expressing lipophilic ligands, such as fatty acids and fatty amines.[26] Due to the lipid bilayer comprising the cellular envelope, hydrophobic effects will also regulate whether a nanoparticle simply adsorbs to the membrane or is capable of penetrating into the interior of the cell.[27] Lastly, nanoparticle-cell association can be greatly enhanced by tethering molecules onto the particle that bind to cell surface receptors. For example, the inclusion of carbohydrates onto nanoparticle surfaces was found to enhance association with *Escherichia coli* by binding to the FimH adhesion protein in the bacterium's pili.[28] To date, several targeting moieties have been designed to increase the association of nanoparticles with both prokaryotic and eukaryotic cells, the details of which are discussed in Section 1.1.4.

For eukaryotic cells, once an association event has occurred cellular uptake may ensue. The process by which matter is taken into mammalian cells is called endocytosis. Phagocytosis and pinocytosis are the two most prominent endocytic mechanisms for eukaryotic cells. Large particles are taken up by phagocytosis ("cell eating"), while small particles, fluids, and solutes are taken up by pinocytosis ("cell drinking"). Phagocytosis mostly occurs with macrophages and polymorphonuclear neutrophils, as these immune cells are key in cleaning up cellular debris and removing pathogens. Pinocytosis is a common

internalization strategy for all types of mammalian cells and is the generally accepted method by which particles are internalized by eukaryotic cells.[5, 14, 29] The four main mechanisms for pinocytosis include macrophinocytosis, clathrin-mediated endocytosis, caveolae-mediated endocytosis, and clathrin- and caveolae-independent endocytosis.[29] Macrophinocytosis is an actin driven process where protrusions form, collapse, and then fuse onto the cell membrane to form large endocytic vesicles with diameters of 0.5–10 μm. In clathrin-mediated endocytosis, a coated pit is created by an assembly of clathrin, forming a vesicle ~120 nm in size. In caveolae-mediated endocytosis, flask-shaped invaginations are formed by the protein caveolin, and internalized vesicles (~60 nm) are directed to the endoplasmic reticulum and the nucleus. Clathrin- and caveolin-independent endocytosis occur through cholesterol-rich microdomains on the plasma membrane called lipid rafts (40–50 nm). In general, uptake of silica particles into eukaryotic cells occurs through clathrin-coated endocytosis pathways although the inclusion of certain ligands may direct other mechanisms of endocytosis.

Although endocytosis is a necessary function for eukaryotes, an endocytosis-like mechanism has not been identified for prokayrotes.[30, 31] Yet, the presence of nanoparticles in the interior of bacteria cells has been observed.[32-35] It is believed that the route of ingress of nanoparticles into uncompromised bacterial cells may be through pores present in the outer membrane.[25] Since these pores are used to secrete large proteins, only particles of very small sizes could pass through the pores. For example, ring-shaped pores formed by secretin proteins (GspD) in *Psuedomonas aeruginosa* are estimated to have a diameter as large as 9.5 nm, thus only nanoparticles less than 9 nm could pass.[36] Even so, the probability of nanoparticle internalization through these large pores is low as the channels are likely gated. Most often, the presence of nanoparticles is observed in bacteria with compromised cell

membranes. Thus, it is hypothesized that the particles entered the cellular interior only after the membrane had been compromised.[25]

The mechanism and extent of cellular uptake is greatly affected by the physical and chemical characteristics of the nanoparticle scaffold. It is generally believed that efficient uptake by non-phagocytic cells requires that the particle must be on the submicron scale,[14] although some have reported the internalization of particles as large as 5 μm.[29] Overall, smaller particles are able to accumulate in the cellular interior to a greater extent than larger particles. For example, the uptake of 50 nm MSNs by HeLa cells was 4, 20, and 11 times greater than that of 110, 170, and 280 nm particles, respectively.[37] Similarly, the uptake of nonporous silica particles also exhibited a size-dependency with 23 nm particles being uptaken to a greater extent than larger 85 nm particles.[38] The kinetics of internalization was also observed to be size dependent, with larger sized particles experiencing a slower rate of uptake. After 60 min incubation, the 85 nm nonporous particles mostly remained physically adsorbed to the cell surface, while the majority of the smaller 23 nm particles were distributed throughout the cytosol. [38] Similarly, a greater concentration of smaller metallic particles has been observed in the interior of bacteria cells compared to that of larger particles.[39] Due to the lack of endocytic mechanisms in prokaryotic cells, this size dependence is likely the result of Brownian motion across a damaged membrane. A dependence of bactericidal efficacy on particle size is evident and is the focus of Chapter 2.

Particle shape has also been observed to impact drug delivery efficiency by affecting particle-cell adhesion strength, internalization rate, cytotoxicity, circulation time and biodistribution.[29, 40, 41] For example, higher aspect ratio MSNs were found to be internalized by human melanoma cells to a greater extent and at a faster rate than spherical particles.[40]

Furthermore, high aspect ratio particles resulted in a greater impact on cell proliferation, apoptosis, cytoskeleton formation, adhesion and migration. In vivo experiments revealed that particle shape also governs biodistribution as MSNs with an aspect ratio of 1.5 accumulated in the liver, while those with an aspect ratio of 5 distributed in the spleen.[41] Furthermore, the lower aspect ratio MSNs experienced a more rapid clearance rate. Lu et al. observed a similar trend with antimicrobial MSNs, where those of higher aspect ratio exhibited a greater therapeutic impact.[42] It was hypothesized that higher aspect ratios allows for greater surface contact between MSNs and the microbes, which in turn allowed for more efficient drug delivery directly to the bacterial membrane.

In addition to physical characteristics, different surface chemistries present on the particle scaffold may influence the mechanism of cellular uptake. For example, amine and guanidinium-functionalized MSNs are reportedly taken up by clatherin- and caveolae-independent mechanisms, compared to the usual clathrin-coated endocytosis of silica particles.[43] The uptake mechanism greatly impacts the effectiveness of the drug as it dictates the localization of the internalized nanoparticle. Drug delivery to the cytosol of the cell is most ideal, but typically internalized particles remain trapped in endosomes. Methods for triggering endosomal release have been achieved by modifying the surface of the particle.[43] For example, Verma et al. found that particles modified with alternating anionic and hydrophobic groups in an ordered manner achieved endosomal release whereas particles modified with the same functionalities but in a random, unordered fashion remained trapped in the endosomes.[44]

When cellular uptake is undesirable, poly(ethylene glycol) (PEG) and other similarly structured polymers can be incorporated onto the particle surface to prevent blood serum

proteins from adsorbing to the particle.[24] Minimal protein adsorption results in decreased phagocytic cellular uptake and increased circulation time. PEG-modified particles are typically used for antitumor therapies where the passive targeting of tumor cells is achieved through the enhanced permeation and retention (EPR) effect.

Uptake of nanoparticles is most commonly monitored by flow cytometry, transmission electron microscopy, and confocal fluorescence microscopy.[45, 46] Internalization versus external association can be differentiated via a number of analytical techniques. In flow cytometry, the particles must be fluorescent in order to visualize their location on/in the cell. Particle internalization can be identified by the presence of fluorescence after copiously washing the cells or by employing extracellular fluorescence quenchers. The use of transmission electron microscopy (TEM) is advantageous as there is no need to modify the particles to allow for visualization. The localization of particles can be elucidated with TEM by using a microtome to obtain 100 nm thin slices of the specimen that can be imaged individually. Stains are normally used for TEM imaging to increase the contrast between different cellular compartments. However, TEM imaging requires fixation of the specimen, which can lead to artificially increased uptake. Alternatively, the use of Z-stack imaging with confocal microscopy allows for photographic "slices" to be taken along the z-axis of live cells in solution. Thus, real-time uptake and localization information can be obtained. The presence of particles in the interior or exterior of the cells is determined by identifying the location along the z-axis where fluorescence is the greatest. For now, the resolution of the Z-stack method limits this technique to investigating internalization by mammalian cells only.

1.1.4 Targeting strategies

The efficiency of drug delivery can be enhanced by increasing the probability and rate of an interaction between the nanoparticle and the intended tissue or cell. Targeted delivery of nanoparticles can be achieved passively through processes such as the enhanced permeability and retention (EPR) effect or actively through the use of targeting or directing moieties.

The EPR effect has been used for targeting nanoparticles to tumor sites by taking advantage of the fact that solid tumors and inflamed tissue have a more leaky vasculature than healthy tissue.[2] As nanoparticles circulate throughout the vasculature, they are more likely to extravasate into cancerous tissue than normal tissue. This phenomenon represents a passive strategy for the selective delivery of nanoparticles to cancerous tissue over normal tissue. Nanoparticles that utilize the EPR for selectivity must be between 100–300 nm and experience long circulation life-times.[4, 47] Micron-sized particles are quickly cleared by active phagocytosis of the reticuloendothelial system, while particles with diameters below 100 nm are insufficient due to rapid renal clearance. Increased circulation times can be achieved by modifying particle surfaces with PEG, which prevents non-specific binding of proteins and macrophages. While the EPR effect allows for passive targeting of nanoparticles to tumor sites, active targeting strategies allow for increased internalization and allow for targeted treatment of other diseases.

Nanoparticles can be actively directed or targeted to specific cells by including specific functionalities into the silica scaffold. The incorporation of magnetic materials, such as iron oxide nanoparticles, provides the ability to direct and concentrate the drug at the diseased site by applying an external magnetic field.[48-50] For example, Gang et al. reported

that nanoparticles loaded with a chemotherapeutic agent and smaller magnetite (Fe_3O_4) nanoparticles could be magnetically directed to a tumor site and resulted in a 15-fold higher drug concentration at the tumor site compared to freely circulating drug.[51] Additionally, once the nanoparticle carrier has reached the targeted site, the application of an oscillating magnetic field can be used for heat generation to trigger drug release.[52, 53]

Other active targeting strategies involve incorporating ligands on the particle surface that may increase the affinity of the intended cell for the particle by seeking a particular aspect that is more present on the targeted cell than other cells. The most direct method of active targeting is to employ molecules that bind to receptors on the targeted cell surface.[47] For example, proteins, such as antibodies and glycoproteins, have been tethered to particle surfaces for active targeting. Transferrin and transferrin receptor antibodies have proven effective antitumor targeting moieties as the majority of cancer cells overexpress transferrin receptors.[54] Conjugating nanoparticles with the secondary human immunoglobulin (IgG) that targets protein A on the bacteria cell wall resulted in a significant increase in binding of the nanoparticles to bacteria compared to unmodified controls.[55, 56] Moreover, the addition of the glycoprotein D-mannose onto nanoparticles was also found to increase binding to the bacteria cell wall compared to unmodified controls.[28, 57] Avidity, the strength of multiple bonding interactions, can be enhanced through the use of larger multivalent targeting moieties; however, sterics limits the number of groups that can be tethered to the particle surface. Smaller biomolecules have been employed to increase the probability of binding to the target. One such type of small biomolecules are aptamers, which are a recently developed targeting strategy composed of single-stranded oligonucleotides such as DNA or RNA.[58] The advantage of aptamers is their ability to bind to a wide range of non-nucleic

acid targets including peptides, proteins, and even whole cells with high affinity and specificity. Other small molecules such as carbohydrates, vitamins, or peptides can also be tethered to the particle surface to actively target tumor cells.[5, 47] For example, the addition of folic acid ligands allows for high-affinity binding to the folate receptor that is overexpressed on numerous types of cancer cells compared to normal cells.[59] The fusion of nanoparticles to the cell membrane (and subsequent uptake into the cytoplasm) can be further enhanced by incorporating cell-penetrating peptides such as RGD, allatostatin 1, PLL, and arginine-rich peptides.[60] The active targeting of prokaryotic cells has also been investigated by tethering the clinically used antibiotic glycopeptide vancomycin to nanoparticles for targeting Gram-positive bacterium. Vancomycin binds to the terminal peptide (D-alanyl-D-alanine) on the cell wall of Gram-positive bacteria through five hydrogen-bonds, increasing the avidity of the bacterium for the vancomycin-modified nanoparticles.[61, 62]

In addition to increasing the efficiency of drug-delivering silica particles, the incorporation of targeting strategies also lowers the potential toxicity associated with exposure of non-diseased tissue, decreasing side-effects. For example, the addition of folic acid ligands to silica particles was shown to increase preferential uptake by cancer cells up to five times that of normal cells.[63]

1.2 Silica nanoparticles for the delivery of nitric oxide

Thus far, the use of silica nanoparticles for drug delivery was discussed broadly to introduce the advantages inherent to these materials. At this point, the focus is narrowed to describe the use of silica particles for delivering nitric oxide (NO), a small gaseous endogenously produced diatomic radical at the center of a wide variety of physiological

processes. First identified for its cardiovascular role,[64-66] NO is now known to play key roles in human physiology and pathophysiology, including cancer biology, the innate immune response, as well as the wound healing cascade.[67-72] Due to the fastidious nature of NO chemistry and biology, a thorough knowledge of NO's physiological effects is vital to designing successful therapies.

1.2.1 The biological and therapeutic roles of nitric oxide

In the vascular endothelium, NO is generated to maintain proper blood flow and pressure.[73] When NO is produced from vascular endothelial cells, it influences the cellular activities of smooth muscle cells, platelets, and immune cells (Figure 1.4). After generation, NO diffuses into vascular smooth muscle cells and reacts with the iron of soluble guanylate cyclase. This activation of guanylate cyclase results in the production of cyclic guanosine monophosphate (cGMP), leading to relaxation of the smooth muscle cells and an overall dilation of blood vessels. Deficiencies in NO occur when the endothelium is injured or not functioning properly as is the case for several cardiovascular conditions, including atherosclerosis, heart failure, hypertension, arterial thrombotic disorders, coronary heart disease, and stroke.[72] The administration of exogenous NO or the upregulation of endogenous NO production has vasoactive effects for treating ischemic heart disease, heart failure, and hypertension.[74]

In cancer biology, NO is often described as a "double-edged sword" serving as either a tumor progressor or suppressor based on concentration and duration of exposure (Figure 1.5).[75] High NO concentrations produce reactive nitrogen species, which along with reactive oxygen species can cause oxidative and nitrosative stress that lead to DNA base deamination,

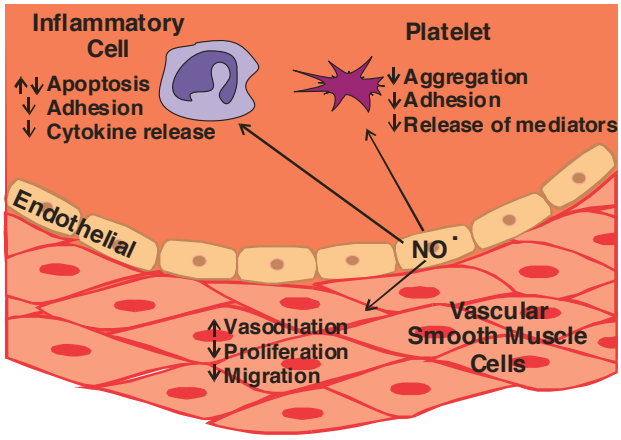

Figure 1.4 Schematic of nitric oxide's role in the vascular endothelium and its effects on cellular activities.

nitrosylation of enzymes, impaired cellular function, enhanced inflammatory reactions, inhibited mitochondrial respiration and tumor cell apoptosis.[76] Alternatively, low concentrations of NO present anti-apoptotic effects and promote angiogenesis thereby increasing nutrient delivery and facilitating tumor growth. All three isoforms of nitric oxide synthase (NOS) have been found in human solid tumors and are typically at higher levels than in normal tissue, indicating that NO may be a mediator of tumor progression.[77] Alternatively, the production of NO is part of the innate antitumor immune response mechanism of macrophages. This complex relationship between NO concentration and tumor development/regression has ignited much research into both pro- and anti-NO cancer therapies. Anti-NO therapies are essentially NOS inhibitors, which have shown to decrease endogenous NO levels and subsequently decrease tumor growth.[75] Use of NOS inhibitors requires long term, systemic administration that can cause hypertension and tumor regrowth if treatment is halted prior to complete eradication.[78] Pro-NO cancer therapies aim to increase NO concentrations at the tumor site to cause apoptosis and/or necrosis of cancer cells.[77]

Nitric oxide is also a potent antimicrobial agent, released from inducible nitric oxide synthase (iNOS) in macrophages to eliminate pathogens.[79] As depicted in Figure 1.6, NO exhibits antimicrobial effects both alone and upon reaction with oxygen or reactive oxygen intermediates (e.g., superoxide and hydrogen peroxide) to form other antimicrobial species including peroxynitrite, RSNOs, nitrogen dioxide, dinitrogen trioxide, and dinitrogen tetroxide.[79] These reactive species can then interact with microbial proteins, DNA and metabolic enzymes, ultimately disrupting vital cellular structures and functions and leading to potent antimicrobial efficacy. Evidence of NO's efficacy against Gram-positive, Gram-

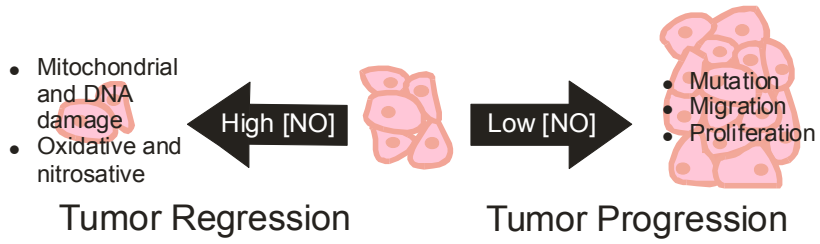

Figure 1.5 The dual role of nitric oxide in cancer biology.

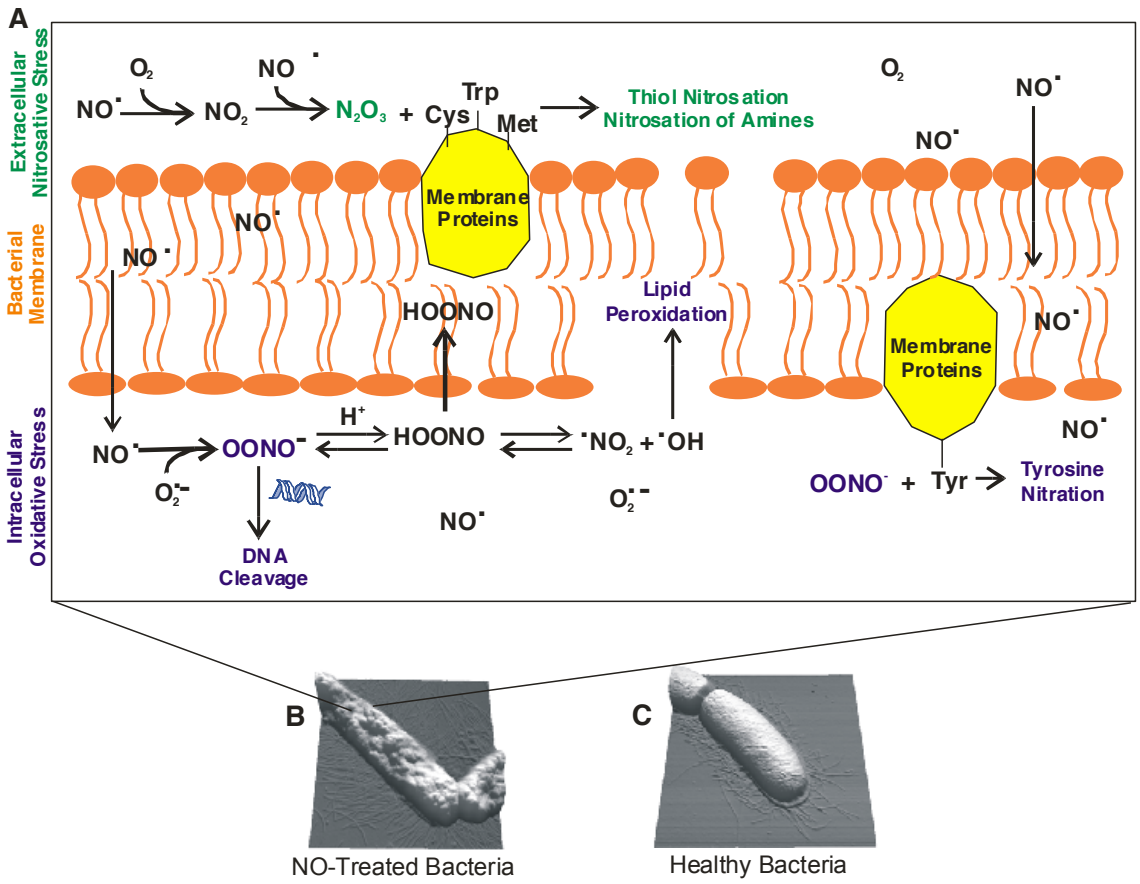

Figure 1.6 The numerous antibacterial mechanisms of nitric oxide and its byproducts (A) lead to decreased bacterial viability and decreased adhesion on NO-releasing surfaces (B) compared to control surfaces (C). Images of bacteria were obtained using atomic force microscopy

negative, and fungal microbes is well documented.[79-84] Furthermore, NO is capable of eliminating not only planktonic bacteria but also biofilms,[85] which contribute to the persistence of infections due to their protective exopolysaccharide matrix that resists penetration of immune cells and antibiotics.[86] The broad spectrum and multi-mechanistic nature of NO suggest it may be the basis for a new paradigm of antimicrobials that decrease the chance of resistance.

Nitric oxide is also active in each phase of the wound healing cascade, indicating that NO-based therapeutics would be advantageous for promoting proper wound healing.[87, 88] The wound healing cascade consists of blood coagulation, inflammation, cell proliferation, lesion contraction, and remodeling. This process begins immediately following tissue injury and continues up to months after the initial wounding. Coagulation occurs to limit further blood loss by platelet adhesion and clot formation. The secretion of growth factors activates fibroblasts, endothelial cells, and macrophages in an attempt to regain normal homeostatis.[87, 88] During the inflammation phase, neutrophils, macrophages, and lymphocytes collectively defend against invading microorganisms and help to remove damaged tissue. Proliferation involves fibroblast migration, angiogenesis and re-epithelialization, beginning three days following injury and lasting up to several weeks. During lesion contraction, the area of damage is reduced to prepare for remodeling, the last phase of wound healing. This final phase consists of changes in the extracellular matrix (ECM) composition, decreases in macrophage and fibroblast density, and reduction in growth factor migration. Finally, avascularization occurs upon decreased metabolism of neovascular tissues to form a flat surface. Rapid recovery with minimal scarring and maximal function are the ultimate goal of wound healing. However, in the case of severe injuries or because of preexisting

conditions (e.g., diabetes), the cascade leading to proper wound healing is not achievable without therapeutic intervention.[89] The therapeutic potential for NO in promoting normal wound healing is indicated by its pro-angiogenic and anti-inflammatory nature as well as its ability to promote cellular proliferation/differentiation and collagen deposition.

Although many details still remain to be elucidated regarding NO's role in physiology, the positive role of NO in a variety of human diseases is widely accepted.[90-92] As described above, the application of exogenous NO can be used for blood pressure regulation, tumor regression, elimination of microbial infection, and promotion of proper wound healing. However, the administration of NO for these applications is not a trivial task due to the highly reactive nature of NO. Gaseous NO can be used for some medical applications, but control over dosage and location is difficult. Thus, gaseous NO is mainly used topically or for inhaled pulmonary treatment. More controlled NO administration is achieved via compounds that can reversibly bind NO and release it upon some stimuli (i.e., NO donors).

A wide variety of NO donors exist including metal nitrosyls, *S*-nitrosothiols (RSNOs), organic nitrites and nitrates, and *N*-diazeniumdiolates (NONOates). *S*-nitrosothiols and *N*-diazeniumdiolates represent the most widely used classes of NO donors for biomedical applications due to their ability to release NO under physiological conditions. *S*-nitrosothiols are endogenous NO donors that may be formed exogenously by reacting thiols with nitrosating agents (e.g. alkyl nitrite, dinitrogen trioxide, or nitrous acid) (Figure 1.7).[93] The release of NO from RSNOs occurs via numerous mechanisms. The S–N bond may be cleaved photolytically or thermally to generate NO and a thiyl radical. Alternatively, the reaction of an RSNO with Cu(I) generates a thiolate, NO and Cu(II). Regeneration of

Cu(I) occurs when the thiolate reacts with Cu(II), leading to a catalytic decomposition of RSNOs. If free thiols are present, transnitrosation may occur where the nitroso functionality is transferred and may subsequently decompose via the aforementioned pathways.

As shown in Figure 1.8, *N*-diazeniumdiolates are formed on amine sites upon exposure to gaseous NO in the presence of a base via one of two proposed mechanisms.[94] In one mechanism, an NO dimer (N_2O_2) is first formed that subsequently reacts with the amine resulting in the formation of the NONOate (Figure 1.8A). Alternatively, the amine may serve as the nucleophile, attacking one molecule of NO to first form a nitrosoamine radical anion that undergoes electrophilic attack on a second molecule of NO (Figure 1.8B). The NO dimer mechanism is the more accepted version.[94] Typically, a strong base such as a metal alkoxide is added to the system to promote NONOate formation. In the presence of a strong base, the proposed mechanisms are altered as the amine is likely first deprotonated to facilitate nucleophilic attack. The decomposition of *N*-diazeniumdiolates occurs in the presence of a proton source (i.e., aqueous physiological conditions) to release two molecules of NO and regenerate the parent amine (Figure 1.8C). The ability to store two moles of NO per binding site is an advantage of NONOates over RSNOs; however, NONOates are plagued by the possibility of forming carcinogenic nitrosoamines. In aerobic conditions, N_2O_3 is an oxidative product of NO and can react with secondary amines to form nitrosamines.

1.2.2 Small molecule NO donors and their limitations

A number of low molecular weight (LMW) compounds have been designed that employ NO donor functionalities as NO delivery compounds. Some LMW NO donors have

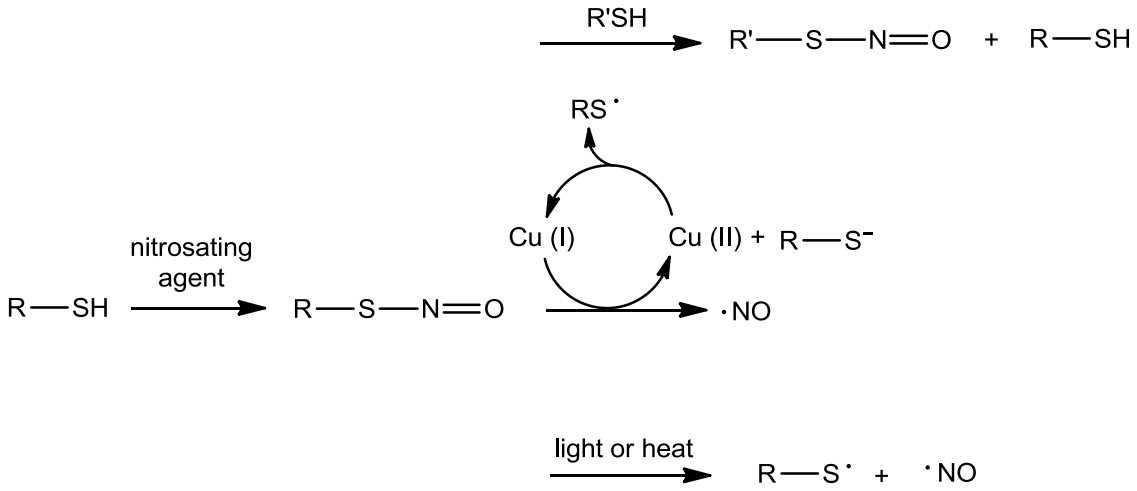

Figure 1.7 Reactions for *S*-nitrosothiol formation and degradation.

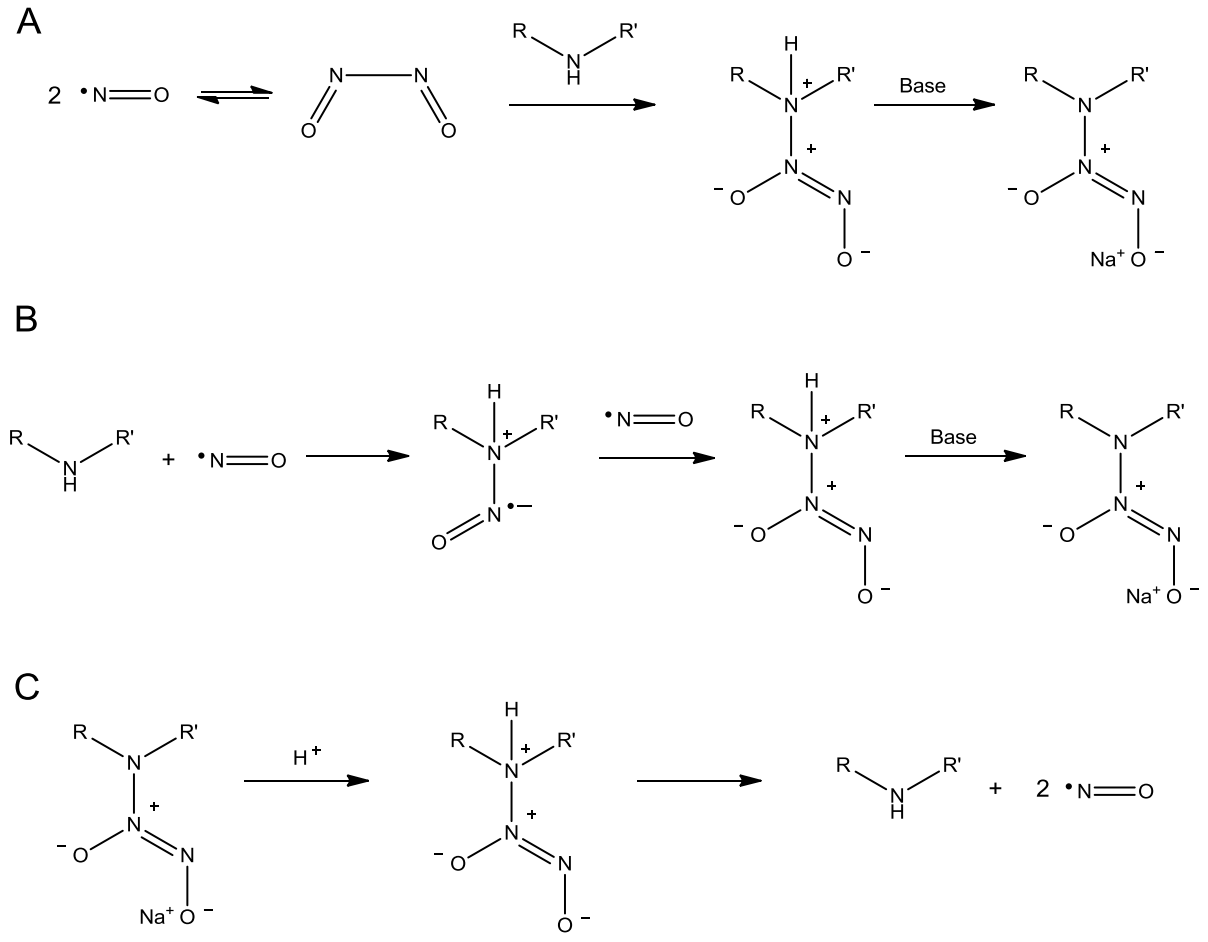

Figure 1.8 The two proposed mechanisms of *N*-diazeniumdiolate formation involve (A) the formation of the NO dimer or (B) the formation of nitrosamine anion. (C) The decomposition of NONOates via proton-initiated decomposition.

found clinical success, such as the use of sodium nitroprusside for blood pressure regulation and glyceryl trinitrate and isosorbide mononitrate for treating angina, anal fissures, heart failure and pulmonary hypertension.[67] Despite their clinical use, common LMW NO donors are plagued by significant drawbacks, including hypotension, headaches, and cyanide poisoning. Furthermore, continued use and reduced bioconversion of NO prodrugs can lead to tolerance. Most of these drawbacks could be alleviated with directed NO administration as LMW NO donors typically diffuse quickly requiring higher doses. However, small molecule scaffolds do not lend themselves to the inclusion of the targeting moieties.

Indeed, the major challenge in developing a clinically successful NO-based therapeutic is the need for effective and selective NO delivery. The therapeutic consequence of any NO-based drug depends strongly on the concentration and duration of NO delivered. As discussed above, micromolar NO concentrations can inhibit the growth of tumor cells, while picomolar NO concentrations have an angiogenic effect leading to cell proliferation.[75] As a result, NO-based therapies must store and deliver a precise NO dose and exhibit specific durations to be effective. In addition, NO delivery must be selective due to NO's short half-life (seconds) limiting its sphere of influence to ~100 μm from its origin.[95] Thus, it is necessary that these parameters (i.e., delivery site, NO concentration, and rate of NO release) be controllable and tunable.

1.2.3 The development of silica particles for NO delivery

One strategy for achieving effective and selective NO delivery is through the use of macromolecular scaffolds.[96] Examples of such scaffolds include biopolymers (i.e., nucleic acids, proteins, lipids, carbohydrates), dendrimers, zeolites, metal-organic frameworks,

synthetic polymers and films, and nano- or microparticles. Macromolecular NO-releasing therapies have many advantages, the most significant of which is greater chemical tunability to allow for targeting, tuning NO release characteristics, and improving biocompatibility. Furthermore, given NO's short half-life, delivery of high NO doses at a localized site is a clear advantage over LMW NO donors. As a result of targeted delivery, the effectiveness of the NO-releasing drug may be increased and the occurrence of side effects including tolerance and toxicity may be decreased. Macromolecular scaffolds can also be modified to delay or stimulate NO release in order to achieve tunable NO release characteristics, as different disease states require certain NO levels. With gaseous or LMW NO donors, control of these parameters is difficult to achieve. In Section 1.1, numerous examples were provided illustrating the potential of silica nanoparticles for drug delivery. As a result of promising preliminary research on silica-based nanomedicine, silica nanoparticles have also been developed for use as NO release vehicles.

The first report of NO-releasing silica particles was by Zhang et al., where aminosilanes were grafted onto the surface of fumed silica and subsequently *N*-diazeniumdiolated.[97] This work proved the ability to significantly increase the duration of NO release through the use of a macromolecular scaffold, as the half-lives ($t_{1/2}$) of the surface-grafted *N*-diazeniumdiolate-modified silica particles were much longer than the half-lives of the corresponding *N*-diazeniumdiolated aminosilane monomers. Inspired by this work, Frost et al. translated this chemistry to prepare *S*-nitrosothiol-modified particles by coupling *N*-acetyl-L-cysteine or *N*-acetyl-D,L-penicillamine to primary amines grafted onto fumed silica particles via amide chemistry.[98] While these works pioneered future A homogenous particle design where sites for NO donor formation are incorporated

throughout the entire particle would theoretically allow for significantly higher NO payloads. Motivated by this concept, Shin et al. synthesized hybrid particles by hydrolyzing and co-condensing TEOS or TMOS with one of three aminosilanes (i.e., *N*-(6-aminohexyl)-aminopropyltrimethoxysilane (AHAP), (*N*-(2-aminoethyl)-3-aminopropyl-trimethoxysilane (AEAP), or (aminoethylaminomethyl)phenethyltrimethoxysilane (AEMP)) (Figure 1.9).[99] *N*-diazeniumdiolates were subsequently formed on secondary amines site via a "post-formation strategy". The amount of aminosilane incorporated throughout the particle was varied from 10–77 mol%, allowing for a range of NO release totals and nanoparticle sizes to be achieved. As expected, the amount and type of aminosilane greatly influenced the observed NO release payloads and kinetics. In general, increasing the amount of aminosilane added to the sol resulted in an increase in nitrogen content in the resulting particles. Following particle formation, the chemical environment surrounding the amine sites was also observed to influence *N*-diazeniumdiolate formation and degradation. For example, the total NO payloads from TEOS-based particles with 10 mol% AEAP and AHAP were 0.145 and 0.380 μmol/mg, respectively. Surprisingly, the 10 mol% AEAP had higher nitrogen content (3.39 wt%) than 10 mol% AHAP (2.74 wt%), as determined by elemental analysis. The type of backbone silane was also found to influence the total NO payload. Particles composed of 10 mol% AHAP and 90 mol% TMOS or TEOS released 0.101 or 0.380 μmol/mg, respectively. For this system, elemental analysis showed that higher NO payloads were achieved due to higher nitrogen contents as the 10 mol% AHAP/TEOS particles contained 2.74 wt% N, while the 10 mol% AHAP/TMOS particles contained only 1.45 wt% N.

In addition to NO totals, the kinetics of NO release were also found to depend on the backbone silane. Particles composed of 10 mol% AHAP co-condensed with TEOS were

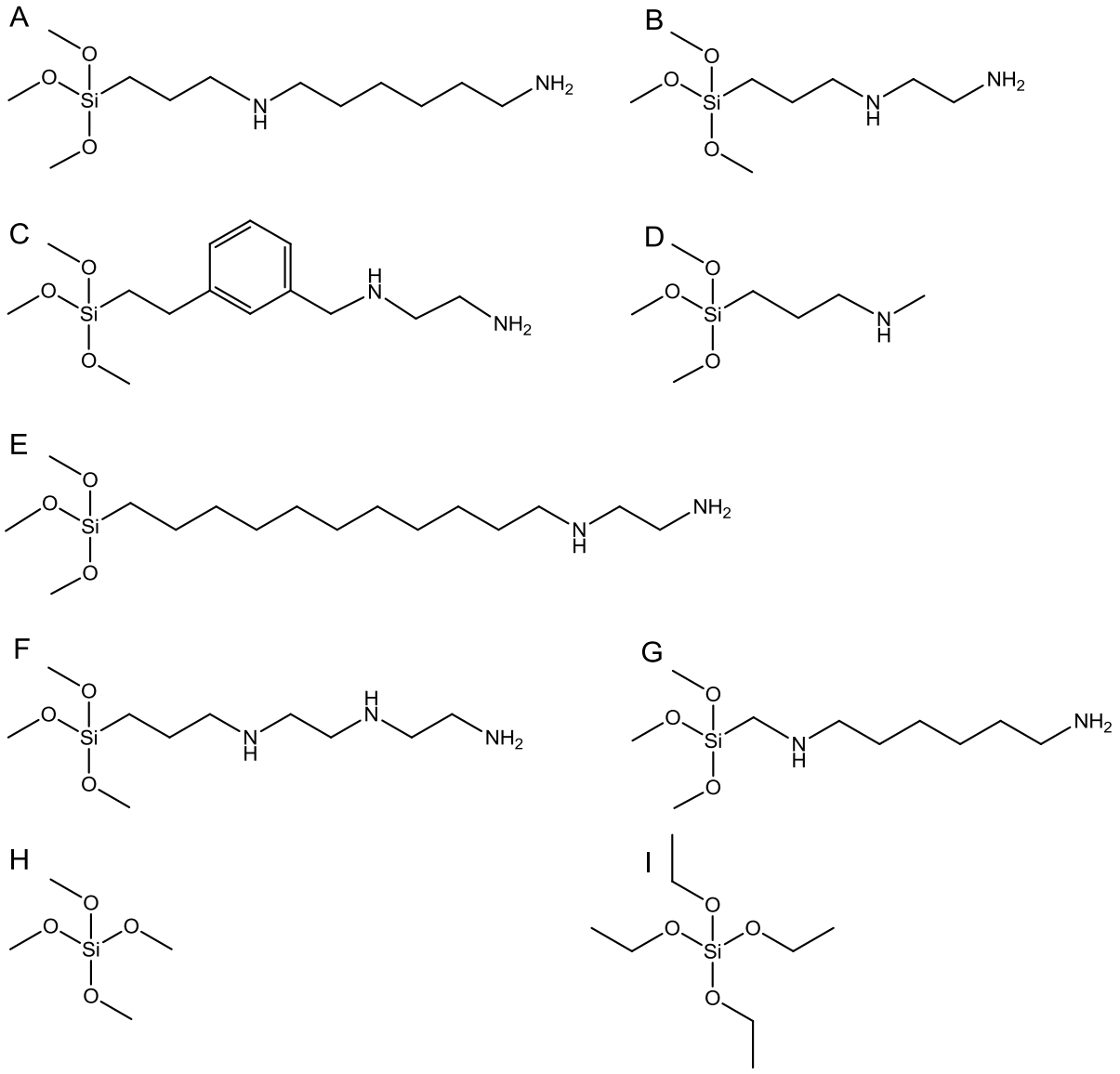

Figure 1.9 Aminosilanes (A-G) and tetraalkoxysilanes (H-I) used to synthesize hybrid silica particles. (A) *N*-(6-aminohexyl)aminopropyltrimethoxysilane (AHAP), (B) *N*-(2-aminoethyl)-3-aminopropyltrimethoxysilane (AEAP), (C) (aminoethylaminomethyl)-phenethyltrimethoxysilane (AEMP) (D) 3-methylaminopropyltrimethoxysilane (MAP), (E) *N*-(2-aminohexyl)-11-aminoundecyltrimethoxysilane (AEAUD), (F) (3-trimethoxysilane)-diethylenetriamine (DET), (G) *N*-(6-aminohexyl)aminomethyl-trimethoxysilane (AHAM), (H) tetramethoxysilane (TMOS), and (I) tetraethoxysilane (TEOS).

characterized by a $t_{1/2}$ of 0.9 h whereas 10 mol% AHAP co-condensed with TMOS had a shorter $t_{1/2}$ of 0.2 h. Again, this is likely because lower AHAP incorporation with TMOS leads to lower NO loading and thus shorter release duration. Varying the type of aminosilane also resulted in changes in NO release kinetics. Since NONOate decomposition is proton-initiated, the kinetics of NO release directly related to the rate that the NONOates react with water. As such, faster NO release kinetics were observed from smaller particle sizes as more of their functional groups are closer to the particle surface compared to larger diameter particles. It also follows that aminosilanes with more hydrophobic character would lead to longer NO release kinetics. This was evidenced with the AEMP-containing particles, which exhibited long half-lives of 5.4–6.0 h due to the hydrophobic conjugated ring present in the silane structure. Unexpectedly, the longest half-life was achieved with 10 mol% AEAP/TEOS, even though the AEAP precursor is not significantly more hydrophobic than AEMP or AHAP. Clearly, the environment within the silica matrix has as great an effect on *N*-diazeniumdiolate stability as the properties of the silane precursors.

While the homogenous particle design allowed for higher NO loading than the surface-grafted particle system, the maximum NO loading was still limited by the low porosity and limited mobility of amines within the silica network. Hydrogen-bonding between amines and silanol groups was believed to limit the availability of amines to be converted to *N*-diazeniumdiolates. Thus, subsequent work by Shin and Schoenfisch involved forming *N*-diazeniumdiolates on the aminosilane precursors prior to particle formation ("pre-formation method") to achieve higher NO payloads.[100] By forming the *N*-diazeniumdiolate moiety on the aminosilane precursors prior to incorporation within a silica particle, NO donor sites were present throughout the entire particle and total NO payloads per particle were

increased. In addition to the aminosilanes previously employed, the aminosilanes used to prepare particles via the pre-formation method were expanded to include *N*-(6-aminohexyl)aminomethyltrimethoxysilane (AHAM), *N*-(2-aminohexyl)-11-aminoundecyl-trimethoxysilane (AEAUD), and (3-trimethoxysilane) diethylenetriamine (DET).

The pre-formation method yielded NO totals that were orders of magnitude greater than what was achieved by the post-formation method. The largest conversion efficiency (i.e., number of *N*-diazeniumdiolates per secondary amines) via the post-formation strategy was 52%, while the pre-formation method resulted in particles where ~100% of amine sites were *N*-diazeniumdiolated. Exceptionally large NO totals of up to 11 μmol/mg were achieved, while the highest NO total achieved with the post-formation method was 1.7 μmol/mg. Based on elemental analysis, the pre-formation method also allowed for greater aminosilane incorporation, which contributed to improved NO loading. As a result of these higher NO loadings, the duration of NO release was also significantly increased. For example, NO release durations of up to 101 h were achieved with *N*-diazeniumdiolated DET/TMOS particles, which is nearly 6 times longer than durations measured from post-formation particles. Unfortunately, the pre-formation strategy was burdened by a decrease in control over particle formation. As a result of the instability of the *N*-diazeniumdiolate group, it is likely that both modified and unmodified aminosilanes were present in the sol. Just as the addition of one organosilane complicates particle formation compared to a sol containing only tetraalkoxysilane monomers, the addition of two types of organosilanes complicates the reaction further. Moreover, excess base, salt and other possible byproducts from the *N*-diazeniumdiolate reaction make controlled particle formation significantly more difficult with the pre-formation strategy compared to the post-formation method.

The therapeutic utility of surface-grafted and homogenous NO-releasing particles was preliminarily evaluated for use as thromboresistant and antimicrobial therapies, respectively.[97, 101, 102] Surface-grafted silica particles were doped into polyurethane coatings on the inner walls of excorporeal blood circulatory tubes to evaluate their ability to inhibit thrombosis on blood-contacting devices.[97] The NO release from these polymers mimicked the NO flux from stimulated endothelial cells (i.e., ~7 pmol cm^{-2} s^{-1}) and effectively decreased platelet adhesion and activation. The homogenous NO-releasing silica particles capable of higher NO payloads were evaluated for their antimicrobial efficacy. Hetrick et al. observed >99% killing of *Pseudomonas aeruginosa*, *Escherichia coli*, *Staphylococcus aureus*, *Staphylococcus epidermidis*, and *Candida albicans* biofilms.[101]

1.2.4 Limitations of NO-releasing silica particles

The work of Zhang and Meyerhoff[97] and Shin, Hetrick and Schoenfisch[99-102] exemplified the therapeutic potential of NO-releasing silica particles. Encouraged by these reports, much remains to be discovered in terms of what specific particle characteristics can be tuned to improve these materials. As has been discussed in previous sections, the chemical and physical characteristics of silica nanoparticles greatly affect their therapeutic potential. More precise control over the physical and chemical properties of NO-releasing silica particles would allow for investigations in nanoparticle-dependent therapeutic effects and broaden the impact of these materials.

To pinpoint the effect of a certain aspect, all other chemical and physical parameters must remain constant, a synthetic feat that is not trivial. For example, Shin et al. observed a change in particle size, amine content, NO storage capacity, and NO release kinetics merely

by changing the backbone of 10 mol% AHAP silica particles from TMOS to TEOS.[99] As discussed above, the use of alternative synthetic techniques for sol–gel chemistry, such as the reverse microemulsion, might allow for greater size control while keeping other particle characteristics constant. Additionally, the therapeutic impact of NO-releasing nanoparticles may be enhanced by modifying the particle surface chemistry (e.g., surface charge and hydrophobicity). Furthermore, expanding the chemical flexibility of NO-releasing silica particles may enable the design of multifunctional scaffolds as combination strategies that are characterized by increased therapeutic efficacy.[103, 104]

1.3 Modifying physical properties of NO-releasing silica nanoparticles

The development of NO-releasing silica particles for therapeutic applications requires that the physical properties be optimized as these characteristics will greatly influence nanoparticle-cell interactions and drug delivery efficiency. Efficient delivery is of the utmost importance given NO's reactive nature and concentration-dependent biological effects. Physical characteristics may govern NO release kinetics by influencing the rate of water diffusion into the network and subsequent NONOate degradation. For example, smaller particles are characterized by significantly higher surface area to volume ratios compared to larger particles. Thus, NO release may be faster for smaller particles as a greater percentage of the NONOates are closer to the particle surface where they will contact water more quickly. Furthermore, NONOates present at the interior of nonporous scaffolds will be more protected from decomposition than those present at the interior of porous particles due to decreased water diffusion. In this section, methods for tuning size, shape and porosity of silica nanoparticle systems are discussed.

1.3.1 Size

A wide range of particle sizes can be achieved with the Stöber method by changing specific reaction parameters including solvent type, reaction temperature, and concentration of water or ammonia. The use of larger molecular weight water-miscible alcohol solvents can result in an increase in particle size. Hydrolysis is slowed in solvents with larger molar volumes and results in a lower overall number of nuclei formed. As discussed in Section 1.1.1, when fewer nuclei are formed the resulting particles are fewer in number and larger in size.[10] Indeed, TEOS particles synthesized in methanol, ethanol, or propanol exhibited average sizes around 30, 200, and 300 nm, respectively.[105] Decreased hydrolysis rates and increased particle sizes can also be achieved by decreasing the reaction temperature.[10] Lastly, the concentration of water and ammonia may be varied to control particle size in a Stöber reaction. Increasing water concentration above 9 M results in a decrease in particle size by promoting hydrolysis.[8, 106, 107] Conversely, decreasing water concentration below 9 M increases particle size as a result of greater nuclei aggregation.[10, 106] Generally, an increase in ammonia concentrations results in improved particle morphology (i.e., spherical shape) as high ammonia concentrations are required to provide sufficient stability of the particles in solution. Thus, non-spherical and aggregated particles are often observed at low ammonia concentrations.[107, 108]

With the reverse microemulsion technique, particle size is governed by the size and stability of the micelle, which is impacted by the type of organic solvent, the water to surfactant ratio, the water to solvent ratio, and the ammonia concentration.[11, 38] The viscosity and polarity of the organic solvent, as well as the size and molecular structure, influence the intermolecular forces between the surfactant molecules and the organic phase. As a result,

the identity of the organic solvent greatly impacts the micelle diameter and the resulting particle size.[109] Smaller organic solvent molecules can penetrate deeper into the surfactant layer, decreasing the overall size of the water droplet. As the size of the water droplet decreases, the resulting particle size decreases.[38] The water to solvent ratio (R) in a reverse microemulsion also affects particle size.[13] At low R values, most water molecules are bound to the surfactant molecules comprising the micelle. The mobility of hydroxide (OH^-) is thus limited, and hydrolysis and nucleation are not favored. Additionally, less water results in fewer TEOS monomers present per micelle, decreasing the probability of intramicellar nucleation. At large R values, both hydrolysis and condensation are favored as most water molecules are unbound. There are also more TEOS monomers per micelle, favoring intramicellar nucleation and the formation of particles with smaller diameters. As ammonia catalyzes the hydrolysis of the silane precursors, its concentration in the micelles also has a great effect on particle size and morphology.[13] At low water concentrations, increasing ammonia concentration promotes hydrolysis and nucleation resulting in smaller particle sizes. At larger water concentrations, increasing ammonia concentration causes an increase in particle size as particle agglomeration occurs within the micelle. A loss in control over particle morphology can occur at too high of ammonia concentrations due to siloxane bond cleavage. The last parameter affecting particle size in reverse microemulsion syntheses is reaction time. Interdroplet percolation occurs when two micelles collide and transfer silica cores, which may fuse and form one larger particle.[38] Thus, increasing reaction time leads to a greater probability of interdroplet percolation, ultimately resulting in larger particles.

Analagous to non-porous silica particles, the size of MSNs is controlled by modifying the rate of nucleus formation and monomer condensation.[14] Methods for tuning particle

morphology include tuning reactant (silane or base) concentrations and varying reaction temperature. For example, increasing reaction temperature results in an increase in the length of mesporous silica nanorods.[110] Additionally, changing the type and concentration of surfactant will result in a change in particle size. For example, lower surfactant concentrations will lead to less particle aggregation and a narrower size distribution (300–600 nm).[111] Co-condensation of an organosilane along with a tetraalkoxysilane also affects the resulting MSN particle size. Huh et al. found that the incorporation of hydrophobic organosilanes resulted in a decrease in particle size compared to the unmodified MCM-41 counterpart.[112]

1.3.2 Shape

The ability to create silica particles of various shapes is generally only achievable with surfactant-templated MSNs because the Stöber and reverse microemulsion techniques inherently produce spherical particles. Since MSN grow along the micelles, their shape may be tuned by changing the geometry of the micelle.

As with solid silica particles, the addition of an organosilane during the silane polymerization greatly impacts particle morphology of MSNs. For example, the co-condensation of TEOS with 3-aminopropyltrimethoxysilane resulted in curved hexagonal tubular structures.[14] Alternatively, co-condensing TEOS with a polyaminosilane *N*-(2-aminoethyl)-3-aminopropyltrimethoxysilane or 3-[2-(2-aminoethylamino)ethyl]propyl-trimethoxysilane yielded MSNs of twisted columns or micron spheres, respectively.[112] The incorporation of ureidopropyltrimethoxysilane also yielded micron-sized spheres but with a raspberry-like surface. The influence of silane type on the resulting particle morphology is

attributed to the orientation that the organosilanes adopt with respect to the surfactant molecules during polymerization. Hydrophilic silanes will orient themselves with their nonhydrolyzable groups positioned away from the micelles, while hydrophobic silanes will align such that the nonhydrolyzable portions are associated towards the hydrophobic domains of the micelle.

The type of surfactant used to template the growth of MSN can also be modified to gain morphological control over MSNs. The structure and packing of the micelle is greatly affected by the characteristics of the surfactant. Again, since particle growth occurs around the micelles, it follows that micelle geometries will affect particle geometries. This was observed experimentally by Trewyn et al. who utilized a range of room-temperature ionic liquids including 1-tetradecyl-3-methylimidaxolum bromide, 1-hexadecyl-3-methylimidazolium bromide, 1-octadecyl-3-methylimidazolium bormide and 1-tetradecyloxymethyl-3-methylimidazolium chloride to achieve spheres, ellipsoids, rods and tubes, respectively.[113]

1.3.3 Porosity

By definition, porosity is the volume of the voids in a network per unit mass. Pores are classified according to size as nanopores (≤2 nm), mesopores (2–50 nm), and macropores (0.05–10 μm).[114] As drug type and release rates are dependent on the porosity of the delivery scaffold, much effort has focused on developing methods to control the porosity of silica particles to accommodate drug delivery needs.

Nanoporous silica particles can be achieved without the use of a surfactant through a modified Stöber synthesis where an *n*-alkyltrialkoxysilane is added to the reaction as a

porogen.[115] The hydrophobic ligands of the organosilanes orient towards each other with the hydrolyzable groups directed out towards the aqueous reaction conditions. As hydrolysis and condensation proceed, hydrophobic pockets are formed throughout the silica network. After particle formation, the organic groups can be removed by calcination to reveal silica particles with hollow nanopores. Similarly, primary alkyl amines have also been included in a modified Stöber reaction to form nanopores throughout the silica scaffold.[116] However, nanoporous silica particles are limited in the size and amount of drugs that may be loaded within the small diameter pores.

Silica particles with larger mesopores are created through the use of the surfactant-templated method (Section 1.1.1). The pore volume of MSNs can be increased with no change in pore diameter by decreasing the reaction temperature.[117] Post-synthesis hydrothermal treatment in acidic conditions was also found to increase pore diameter.[117] Control of pore structure and dimensions has been exemplified with additives such as 1,3,5-substituted benzenes, long chain alkyls, and alkylamines as well as co-surfactants.[118] Alternatively, control over pore structure can also be achieved through the use of polymer additives. For example, the triblock copolymer Pluronic P-123 was used in addition to CTAB to create larger pore diameters of 8 nm.

1.4 Modifying chemical properties of NO-releasing silica nanoparticles

As discussed in Section 1.1.3, particle surface charge and hydrophobicity will influence nanoparticle-cell interactions and in turn govern drug delivery efficiency. For NO-releasing silica particles specifically, chemical properties will have a considerable effect on drug delivery both in terms of NONOate formation and degradation rate as well as cellular

interactions. Below, methods for tuning the chemical properties of NO-releasing silicaparticles are discussed.

1.4.1 Particle architecture

To create *N*-diazeniumdiolate-modified particles, the silica network must be modified to include secondary amine sites. The location of the amines within the network impacts both *N*-diazeniumdiolate formation and degradation rates. Organically modified silica particles can be constructed via surface-grafted, core-shell or homogenous particle designs.

The surface-grafting method involves condensing organosilanes with silanols present on the surface of a preformed particle. This method allows for control over the scaffolds' physical properties because the preformed particles are generally made from TEOS alone. In the case of nonporous particles, the amount of organic functionalities that can be surface-grafted is constrained by the low number of silanol groups present on the particle surface. Theoretically, there is a maximum of ~8 μmol silanols per m^2 of silica, and at most only ~50% can be modified due to steric hinderance.[119] Surface-grafting aminosilanes onto nonporous particles, typically 5–200 m^2/g, does not allow for significant NO-loading. Conversely, surface-modifications of MSNs result in a greater degree of functionalization due to a significantly larger specific surface area (>900 m^2/g).[14] Large NO payloads thus can be achieved by surface-grafting aminosilanes onto MSNs.[42] The external surface is selectively modified by functionalizing prior to surfactant removal.[14] The internal surfaces may then be modified following external modification and surfactant removal to impart a second functionality.

A core-shell particle design allows for larger organic content while still employing a

template particle for fine control of particle morphology. In this design, a core particle is formed typically from a tetraalkoxysilane (i.e., TMOS or TEOS). A silica shell containing additional tetraalkoxysilane and an organosilane is then condensed around it.[5] Since particles synthesized from TEOS or TMOS alone are generally monodisperse, the core-shell design yields particles with well-defined sizes and morphologies while still allowing for greater organosilane incorporation compared to surface-grafting.

A homogeneous particle design allows for the greatest degree of functionalization because the organic groups are present throughout the entire scaffold. To achieve equal distribution, organically modified silanes are hydrolyzed and co-condensed with a tetraalkoxysilane. Although this method allows for greater concentrations of specific functionalities, the inclusion of a second type of silane during the sol–gel process typically disrupts uniform particle formation. As a result, the synthesis of hybrid particles often requires greater effort in optimizing reaction conditions to achieve control over particle monodispersity and size. In general, methods to ensure that the rate of hydrolysis and condensation of the two silanes are similar aid in obtaining well-defined hybrid particles. If a large disparity exists between the rates of hydrolysis of the two silanes, a pre-hydrolysis step can be used for the silane with a slower rate. Immiscibility between the two silanes may also disrupt homogeneous mixing and subsequently complicate uniform particle formation.

1.4.2 Particle composition

For NONOate-based materials, NO payloads are governed by both the total number of amines present and their accessibility to deprotonation and reaction with NO. Clearly, the ability to incorporate larger aminosilane concentrations into nanoparticles will increase the

potential for greater NO payloads. However, the immobility and steric hindrance of amines fixed within a solid silica network result in conversion efficiencies (%E_{conv}) around 30%.[97, 99] As previously discussed, Shin and Schoenfisch obtained greater NO payloads (%E_{conv}≈100) by synthesizing particles composed of *N*-diazeniumdiolate-modified aminosilane precursors and a backbone tetraalkoxysilane. The efficiency of *N*-diazeniumdiolate formation is significantly greater on aminosilane monomers dissolved in solution compared to those immobilized in a solid network.[100]

In addition to NO payload, the chemical composition of the particle will govern the NO release kinetics. For example, the structure of the aminosilane has been shown to affect NO release kinetics by altering intra/intermolecular bonding stabilization and hydrophobicity. The inclusion of primary amines that can participate in hydrogen-bonding to stabilize the NONOate structure will prolong NO release. As such, particles composed of the mono-aminosilane 3-methylaminopropyltrimethoxysilane (MAP; one secondary amine) exhibit fast NO release kinetics, whereas those of the di-aminosilane *N*-(2-aminoethyl)-3-aminopropyltrimethoxysilane (AEAP; one secondary, one primary amine) have longer NO release kinetics. Furthermore, the accessibility of the NONOate to protons (i.e., water) will influence NO release kinetics. Increasing the hydrophobicity of the particles to decrease the diffusion of water into the silica network will also extend NO release. For example, particles composed of (aminoethylaminomethyl)phenethyltrimethoxysilane (AEMP), which contains a conjugated ring, or *N*-(2-aminohexyl)-11-aminoundecyltrimethoxysilane (AEAUD), which contains a long alkyl chain, are characterized by longer NO release kinetics than particles composed of MAP.

Nitric oxide release can be tuned by both changing the structure of the amine to

which the NONOate is bound and/or by modifying the structure of the NONOate group directly. O^2-Protected NONOates are synthesized upon reaction of *N*-diazeniumdiolates with alkyl halides, epoxides, alkyl sulfates and aryl halides.[94] These modified NONOates were designed to undergo hydrolytic or enzymatic cleavage such that the protecting group is removed in physiological conditions. These functionalities are stable in basic conditions and withstand high temperatures, making them amenable to a wide variety of processing or post-synthesis modifications.

1.4.3 Surface chemistry

The chemistries present on the particle surface will influence drug delivery efficiency by affecting NO release and governing nanoparticle-cell interactions. As discussed in Section 1.1.3, the hydrophobicity and surface charge expressed by a particle will govern a cell's affinity for it. This is particularly important for NO-releasing particles due to the reactive nature of NO as well as its concentration/duration-dependent therapeutic effects.

The surfaces of NO-releasing particles may be modified by grafting functional silanes onto the particle or covalently binding ligands to reactive groups near the particle surface. Surface-grafting is limited by the number of surface silanols, especially with hybrid particles. Covalent modification via ring-opening reactions, Michael additions, or *N*-hydroxysuccinimide/ethyl(dimethylaminopropyl)carbodiimide (NHS/EDC) chemistry with primary amines present on the particle surface provide facile methods to modify particle surfaces. Hydrophobicity may be modified through the addition of long-chain alkanes or fluorinated groups as discussed in Chapter 3. Positively charged particles can be achieved through the inclusion of primary amines or quaternary ammoniums. Alternatively, the

addition of carboxylates and phosphates yield negatively charged particles. Lastly, particles may be modified with targeting moieties (Section 1.1.4) to direct NO delivery.

1.5 Summary of dissertation research

The goal of my dissertation research was to design and synthesize NO-releasing silica nanoparticles with physical and chemical properties that may influence their therapeutic consequence. Specifically, my research aimed to:

1. develop synthetic techniques to achieve control over particle size, monodispersity, amine-content and surface chemistry of silica nanoparticles;
2. evaluate the influence of particle size on the bactericidal efficacy of nitric oxide-releasing silica nanoparticles;
3. achieve *N*-diazeniumdiolate-based silica particles with prolonged NO release duration; and,
4. synthesize NO-releasing quaternary ammonium-modified silica nanoparticles as dually functional antimicrobials.

In this introductory chapter, I sought to explain and justify the development of silica nanoparticles as drug delivery scaffolds. The inherent physical and chemical flexibility of these materials represent advantages over other macromolecular scaffolds. For example, specific properties can be tuned to influence nanoparticle-cell interactions and drug delivery efficiency. This introduction also serves to demonstrate the therapeutic potential of NO-releasing silica nanoparticles and describe methods for improving their effectiveness by tuning both their physical and chemical properties. In Chapter 2, the reverse microemulsion technique is used to achieve silica particles of three distinct size and equal amine-content.

These scaffolds allowed for the study of the influence of scaffold size of NO-releasing silica nanoparticles on the bactericidal efficacy against *P. aeruginosa*. In Chapter 3, the surface hydrophobicity of silica particles was modified via surface grafting to yield tunable and prolonged NO release kinetics. Modifying particle surface chemistry was also found to enhance the stability of the particles in porous hydrophobic polymer films. In Chapter 4, O^2-protected *N*-diazeniumdiolates are employed to achieve NO-releasing silica particles with NO release kinetics longer than any other silica particle scaffold to date. The extended NO release scaffolds proved effective at inhibiting adhesion of plaque bacteria to dental composites compared to materials with shorter NO release durations. Lastly, the chemical flexibility of silica particles is demonstrated Chapter 5. Specifically, NO release is combined with quaternary ammonium groups to achieve multi-mechanistic antimicrobial nanomaterials. Finally, Chapter 6 provides an overall summary of my dissertation work and suggests future steps for designing more effective NO-release scaffolds.

References

1. Roco, M. C.; Mirkin, C. A.; Hersam, M. C. *Nanotechnology research directions for societal needs in 2020*. Springer: New York, 2011.

2. Farokhzad, O. C.; Langer, R. "Impact of nanotechnology on drug delivery." *ACS Nano* **2009**, *3*, 16-20.

3. Ambrogio, M. W.; Thomas, C. R.; Zhao, Y. L.; Zink, J. I.; Stoddartt, J. F. "Mechanized silica nanoparticles: A new frontier in theranostic nanomedicine." *Acc. Chem. Res.* **2011**, *44*, 903-913.

4. Lee, J. E.; Lee, N.; Kim, T.; Kim, J.; Hyeon, T. "Multifunctional mesoporous silica nanocomposite nanoparticles for theranostic applications." *Acc. Chem. Res.* **2011**, *44*, 893-902.

5. Vivero-Escoto, J. L.; Huxford-Phillips, R. C.; Lin, W. "Silica-based nanoprobes for biomedical imaging and theranostic applications." *Chem. Soc. Rev.* **2012**, *41*, 2673-2685.

6. Brinker, C. J.; Scherer, G. W. *Sol-gel science: The physics and chemistry of sol-gel processing*. Academic Press: San Diego, 1990.

7. Wright, J. D.; Sommerdijk, A. J. M. *Sol-gel materials: Chemistry and applications*. Gordon and Breach Science Publishers: Amsterdam, 2001.

8. Stober, W.; Fink, A.; Bohn, E. "Controlled growth of monodisperse silica spheres in micron size range " *J. Colloid Interf. Sci.* **1968**, *26*, 62-69.

9. LaMer, V. K.; Dinegar, R. H. "Theory, production and mechanism of formation of monodispersed hydrosols." *J. Am. Chem. Soc.* **1950**, *72*, 4847-4854.

10. Huang, Y.; Pemberton, J. E. "Synthesis of uniform, spherical sub-100 nm silica particles using a conceptual modification of the classical Lamer model." *Colloids Surf., A* **2010**, *360*, 175-183.

11. Osseo-Asare, K.; Arriagada, F. J. "Preparation of SiO_2 nanoparticles in a nonionic reverse micellar system." *Colloids Surf., A* **1990**, *50*, 321-339.

12. Schmidt, J.; Guesdon, C.; Schomäcker, R. "Engineering aspects of preparation of nanocrystalline particles in microemulsions." *J. Nanopart. Res.* **1999**, *1*, 267-276.

13. Arriagada, F. J.; Osseo-Asare, K. "Synthesis of nanosize silica in a nonionic water-in-oil microemulsion: Effects of the water/surfactant molar ratio and ammonia concentrations." *J. Colloid Interf. Sci.* **1999**, *211*, 210-220.

14. Slowing, I. I.; Vivero-Escoto, J. L.; Wu, C. W.; Lin, V. S. Y. "Mesoporous silica nanoparticles as controlled release drug delivery and gene transfection carriers." *Adv. Drug Deliv. Rev.* **2008**, *60*, 1278-1288.

15. Cai, Q.; Luo, Z.-S.; Pang, W.-Q.; Fan, Y.-W.; Chen, X.-H.; Cui, F.-Z. "Dilute solution routes to various controllable morphologies of MCM-41 silica with a basic medium." *Chem. Mater.* **2001**, *13*, 258-263.

16. Barzegar-Jalali, M.; Adibkia, K.; Valizadeh, H.; Shadbad, M. R. S.; Nokhodchi, A.; Omidi, Y.; Mohammadi, G.; Nezhadi, S. H.; Hasan, M. "Kinetic analysis of drug release from nanoparticles." *J. Pharm. Pharmac. Sci.* **2008**, *11*, 167-177.

17. Vivero-Escoto, J. L.; Taylor-Pashow, K. M. L.; Huxford, R. C.; Della Rocca, J.; Okoruwa, C.; An, H. Y.; Lin, W. L.; Lin, W. B. "Multifunctional mesoporous silica nanospheres with cleavable Gd(III) chelates as MRI contrast agents: Synthesis, characterization, target-specificity, and renal clearance." *Small* **2011**, *7*, 3519-3528.

18. Della Rocca, J.; Huxford, R. C.; Comstock-Duggan, E.; Lin, W. B. "Polysilsesquioxane nanoparticles for targeted platin-based cancer chemotherapy by triggered release." *Angew. Chem. Int. Edit.* **2011**, *50*, 10330-10334.

19. Greenwald, R. B.; Choe, Y. H.; McGuire, J.; Conover, C. D. "Effective drug delivery by PEGylated drug conjugates." *Adv. Drug Deliv. Rev.* **2003**, *55*, 217-250.

20. Liu, J.; Stace-Naughton, A.; Jiang, X.; Brinker, C. J. "Porous nanoparticle supported lipid bilayers (protocells) as delivery vehicles." *J. Am. Chem. Soc.* **2009**, *131*, 1354-1355.

21. Manzano, M.; Aina, V.; Arean, C. O.; Balas, F.; Cauda, V.; Colilla, M.; Delgado, M. R.; Vallet-Regi, M. "Studies on MCM-41 mesoporous silica for drug delivery: Effect of particle morphology and amine functionalization." *Chem. Eng. J.* **2008**, *137*, 30-37.

22. Saha, S.; Leung, K. C. F.; Nguyen, T. D.; Stoddart, J. F.; Zink, J. I. "Nanovalves." *Adv. Funct. Mater.* **2007**, *17*, 685-693.

23. Lai, C.-Y.; Trewyn, B. G.; Jeftinija, D. M.; Jeftinija, K.; Xu, S.; Jeftinija, S.; Lin, V. S.-Y. "A mesoporous silica nanosphere-based carrier system with chemically removable CdS nanoparticle caps for stimuli-responsive controlled release of neurotransmitters and drug molecules." *J. Am. Chem. Soc.* **2003**, *125*, 4451-4459.

24. Mout, R.; Moyano, D. F.; Rana, S.; Rotello, V. M. "Surface functionalization of nanoparticles for nanomedicine." *Chem. Soc. Rev.* **2012**, *41*, 2539-2544.

25. Neal, A. L. "What can be inferred from bacterium-nanoparticle interactions about the potential consequences of environmental exposure to nanoparticles?" *Ecotoxicol.* **2008**, *17*, 362-371.

26. Tan, S. J.; Jana, N. R.; Gao, S. J.; Patra, P. K.; Ying, J. Y. "Surface-ligand-dependent cellular interaction, subcellular localization, and cytotoxicity of polymer-coated quantum dots." *Chem. Mater.* **2010**, *22*, 2239-2247.

27. Li, Y.; Chen, X.; Gu, N. "Computational investigation of interaction between nanoparticles and membranes: Hydrophobic/hydrophilic effect." *J. Phys. Chem. B* **2008**, *112*, 16647-16653.

28. Lin, C.-C.; Yeh, Y.-C.; Yang, C.-Y.; Chen, C.-L.; Chen, G.-F.; Chen, C.-C.; Wu, Y.-C. "Selective binding of mannose-encapsulated gold nanoparticles to type 1 pili in *Escherichia coli*." *J. Am. Chem. Soc.* **2002**, *124*, 3508-3509.

29. Gratton, S. E. A.; Ropp, P. A.; Pohlhaus, P. D.; Luft, J. C.; Madden, V. J.; Napier, M. E.; DeSimone, J. M. "The effect of particle design on cellular internalization pathways." *Proc. Natl. Acad. Sci. U.S.A.* **2008**, *105*, 11613-11618.

30. Lonhienne, T. G. A.; Sagulenko, E.; Webb, R. I.; Lee, K.-C.; Franke, J.; Devos, D. P.; Nouwens, A.; Carroll, B. J.; Fuerst, J. A. "Endocytosis-like protein uptake in the bacterium Gemmata obscuriglobus." *Proc. Natl. Acad. Sci. U.S.A.* **2010**, *107*, 12883-12888.

31. One recent report has indicated that *Gemmata obscurilgobus* does exhibit an endocytosis-like mechansim. However, this bacterium is exceptional among Bacteria possessing other characteristics that are not found in any other bacterium but are similar to eukaryotic cells.

32. Sondi, I.; Salopek-Sondi, B. "Silver nanoparticles as antimicrobial agent: A case study on *E. coli* as a model for gram-negative bacteria." *J. Colloid Interf. Sci.* **2004**, *275*, 177-182.

33. Stoimenov, P. K.; Klinger, R. L.; Marchin, G. L.; Klabunde, K. J. "Metal oxide nanoparticles as bacterial agents." *Langmuir* **2002**, *18*, 6679-6686.

34. Morones, J. R.; Elechiguerra, J. L.; Camacho, A.; Holt, K.; Kouri, J. B.; Ramirez, J. T.; Yacaman, M. J. "The bactericidal effect of silver nanoparticles." *Nanotechnology* **2005**, *16*, 2346-2353.

35. Brayner, R.; Ferrari-Iliou, R.; Brivois, N.; Djediat, S.; Benedetti, M. F.; Fievet, F. "Toxicological impact studies based on *Escherichia coli* bacteria in ultrafine ZnO nanoparticles colloidal medium." *Nano Lett.* **2006**, *6*, 866-870.

36. Bitter, W.; Koster, M.; Latijnhouwers, M.; de Cock, H.; Tommassen, J. "Formation of oligomeric rings by XcpQ and PilQ, which are involved in protein transport across the outer membrane of *Pseudomonas aeruginosa*." *Molecul. Microbiol.* **1998**, *27*, 209-219.

37. Lu, F.; Wu, S.-H.; Hung, Y.; Mou, C.-Y. "Size effect on cell uptake in well-suspended, uniform mesoporous silica nanoparticles." *Small* **2009**, *5*, 1408-1413.

38. Jin, Y.; Lohstreter, S.; Pierce, D. T.; Parisien, J.; Wu, M.; Hall, C.; Zhao, J. X. "Silica nanoparticles with continuously tunable sizes: Synthesis and size effects on cellular contrast imaging." *Chem. Mater.* **2008**, *20*, 4411-4419.

39. Naizi, J. H.; Gu, M. B. *Toxicity of metallic nanoparticles in microorganisms- a review*. Springer: New York, 2009.

40. Huang, X. L.; Teng, X.; Chen, D.; Tang, F. Q.; He, J. Q. "The effect of the shape of mesoporous silica nanoparticles on cellular uptake and cell function." *Biomaterials* **2010**, *31*, 438-448.

41. Huang, X. L.; Li, L. L.; Liu, T. L.; Hao, N. J.; Liu, H. Y.; Chen, D.; Tang, F. Q. "The shape effect of mesoporous silica nanoparticles on biodistribution, clearance, and biocompatibility in vivo." *ACS Nano* **2011**, *5*, 5390-5399.

42. Lu, Y.; Slomberg, D.; Sun, B.; Schoenfisch, M. H. "Shape-dependent bactericidal efficacy of nitric oxide-releasing mesoporous silica nanorods." *Small*, *submitted*.

43. Slowing, I.; Trewyn, B. G.; Lin, V. S. "Effect of surface functionalization of MCM-41-type mesoporous silica nanoparticles on the endocytosis by human cancer cells." *J. Am. Chem. Soc.* **2006**, *128*, 14792-14793.

44. Verma, A.; Uzun, O.; Hu, Y. H.; Hu, Y.; Han, H. S.; Watson, N.; Chen, S. L.; Irvine, D. J.; Stellacci, F. "Surface-structure-regulated cell-membrane penetration by monolayer-protected nanoparticles." *Nature Mater.* **2008**, *7*, 588-595.

45. Weir, E.; Lawlor, A.; Whean, A.; Regan, F. "The use of nanoparticles in anti-microbial materials and their characterization." *Analyst* **2008**, *133*, 835-845.

46. Marquis, B. J.; Love, S. A.; Braun, K. L.; Haynes, C. L. "Analytical methods to assess nanoparticle toxicity." *Analyst* **2009**, *134*, 425-439.

47. Wang, J.; Byrne, J. D.; Napier, M. E.; DeSimone, J. M. "More effective nanomedicines through particle design." *Small* **2011**, *7*, 1919-1931.

48. Gupta, P. K.; Hung, C. T. "Magnetically controlled targeted micro-carrier systems." *Life Sci.* **1989**, *44*, 175-186.

49. Hafeli, U.; Schutt, W.; Teller, J.; Zborowski, M. *Scientific and clinical applications of magnetic carriers*. 1 Ed.; Plenum Press: New York, 1997.

50. Widder, K. J.; Senyei, A. E.; Ranney, D. F. "Magnetically responsive microspheres and other carriers for the biophysical targeting of antitumor agents." *Adv. Pharmacol. Chemother.* **1979**, *16*, 213-271.

51. Gang, J.; Park, S.-B.; Hyung, W.; Choi, E. H.; Wen, J.; Kim, H.-S.; Shul, Y.-G.; Haam, S.; Song, S.-Y. "Magnetic poly ε−caprolactone nanoparticles containing Fe_3O_4 and gemcitabine enhance anti-tumor effect in pancreatic cancer xenograft mouse model." *J. Drug Target.* **2007**, *15*, 445-453.

52. Baeza, A.; Guisasola, E.; Ruiz-Hernandez, E.; Vallet-Regi, M. "Magnetically triggered multidrug release by hybrid mesoporous silica nanoparticles." *Chem. Mater.* **2012**, *24*, 517-524.

53. Chen, X.; Klingeler, R.; Kath, M.; El Gendy, A. A.; Cendrowski, K.; Kalenczuk, R. J.; Borowiak-Palen, E. "Magnetic silica nanotubes: Synthesis, drug release, and feasibility for magnetic hyperthermia." *ACS Appl. Mater. Interfaces* **2012**, *4*, 2303-2309.

54. Choi, C. H. J.; Alabi, C. A.; Webster, P.; Davis, M. E. "Mechanism of active targeting in solid tumors with transferrin-containing gold nanoparticles." *Proc. Natl. Acad. Sci. U.S.A.* **2009**, *107*, 1235-1240.

55. Zharov, V. P. M., K. E.; Galitovskaya, E. N.; Smeltzer, M. S. "Photothermal nanotherapeutics and nanodiagnostics for selective killing of bacteria targeted with gold nanoparticles." *Biophys. J.* **2006**, *90*, 619-627.

56. Ho, K.-C.; Tsai, P.-J.; Lin, Y.-S.; Chen, Y.-C. "Using biofunctionalized nanoparticles to probe pathogenic bacteria." *Anal. Chem.* **2004**, *76*, 7162-7168.

57. El-Boubbou, K.; Gruden, C.; Huang, X. "Magnetic glyco-nanoparticles: A unique tool for rapid pathogen detection, decontamination, and strain differentiation." *J. Am. Chem. Soc.* **2007**, *129*, 13392-13393.

58. Yang, L.; Zhang, X. B.; Ye, M.; Jiang, J. H.; Yang, R. H.; Fu, T.; Chen, Y.; Wang, K. M.; Liu, C.; Tan, W. H. "Aptamer-conjugated nanomaterials and their applications." *Adv. Drug Deliv. Rev.* **2011**, *63*, 1361-1370.

59. Lu, J.; Li, Z. X.; Zink, J. I.; Tamanoi, F. "In vivo tumor suppression efficacy of mesoporous silica nanoparticles-based drug-delivery system: Enhanced efficacy by folate modification." *Nanomed. Nanotech. Biol. Med.* **2012**, *8*, 212-220.

60. Saha, K.; Bajaj, A.; Duncan, B.; Rotello, V. M. "Beauty is skin deep: A surface monolayer perspective on nanoparticle interactions with cells and biomacromolecules." *Small* **2011**, *7*, 1903-1918.

61. Gu, H. W.; Xu, K. M.; Xu, C. J.; Xu, B. "Biofunctional magnetic nanoparticles for protein separation and pathogen detection." *Chem. Comm.* **2006**, 941-949.

62. Gu, H.; Ho, P. L.; Tong, E.; Wang, L.; Xu, B. "Presenting vancomycin on nanoparticles to enhance antimicrobial activities." *Nano Lett.* **2003**, *3*, 1261-1263.

63. Rosenholm, J. M.; Meinander, A.; Peuhu, E.; Niemi, R.; Eriksson, J. E.; Sahlgren, C.; Linden, M. "Targeting of porous hybrid silica nanoparticles to cancer cells." *ACS Nano* **2008**, *3*, 197-206.

64. Furchgott, R. F.; Khan, M. T.; Jothianandan, D. "Comparison of endothelium-dependent relaxation and nitric oxide-induced relaxation in rabbit aorta." *Fed. Proc.* **1987**, *46*, 385-385.

65. Ignarro, L. J.; Buga, G. M.; Wood, K. S.; Byrns, R. E.; Chaudhuri, G. "Endothelium-derived relaxing factor produced and released from artery and vein is nitric oxide." *Proc. Natl. Acad. Sci. U.S.A.* **1987**, *84*, 9265-9269.

66. Arnold, W. P.; Mittal, C. K.; Katsuki, S.; Murad, F. "Nitric oxide activates guanylate cyclase and increases guanosine 3'-5'-cyclic monophosphate levels in various tissue preparations." *Proc. Natl. Acad. Sci. U.S.A.* **1977**, *74*, 3203-3207.

67. Bauer, V.; Sotnikova, R. "Nitric oxide - the endothelium-derived relaxing factor and its role in endothelial functions." *Gen. Physiol. Biophysics* **2010**, *29*, 319-340.

68. Bhagat, K. "Nitric oxide 9 years on." *J. R. Soc. Med.* **1996**, *89*, 667-673.

69. Steinert, J. R.; Chernova, T.; Forsythe, I. D. "Nitric oxide signaling in brain function, dysfunction, and dementia." *Neuroscientist* **2010**, *16*, 435-452.

70. Paradise, W. A.; Vesper, B. J.; Goel, A.; Waltonen, J. D.; Altman, K. W.; Haines, G. K.; Radosevich, J. A. "Nitric oxide: Perspectives and emerging studies of a well known cytotoxin." *Int. J. Mol. Sci.* **2010**, *11*, 2715-2745.

71. Hill, B. G.; Dranka, B. P.; Bailey, S. M.; Lancaster, J. R., Jr.; Darley-Usmar, V. M. "What part of NO don't you understand? Some answers to the cardinal questions in nitric oxide biology." *J. Biol. Chem.* **2010**, *285*, 19699-19704.

72. Ferrari, C. K. B.; Franca, E. L.; Honorio-Franca, A. C. "Nitric oxide, health and disease." *J. Appl. Biomed.* **2009**, *7*, 163-173.

73. Loscalzo, J.; Vita, J. A., *Nitric oxide and the cardiovascular system*. Humana Press, Inc.: Totowa, New Jersey, 2000.

74. Ignarro, L. J.; Napoli, C.; Loscalzo, J. "Nitric oxide donors and cardiovascular agents modulating the bioactivity of nitric oxide." *Circ. Res.* **2002**, *90*, 21-28.

75. Mocellein, S.; Bronte, V.; Nitti, D. "Nitric oxide, a double edged sword in cancer biology: Searching for therapeutic opportunities." *Med. Res. Rev.* **2007**, *27*, 317-352.

76. Wink, D. A.; Vodovotz, Y.; Laval, J.; Laval, F.; Dewhirst, M. W.; Mitchell, J. B. "The multifaceted roles of nitric oxide in cancer." *Carcinogenesis* **1998**, *19*, 711-721.

77. Hirst, D.; Robson, T. "Nitric oxide in cancer therapeutics: Interaction with cytotoxic chemotherapy." *Curr. Pharm. Des.* **2010**, *16*, 411-420.

78. Kennovin, G. D.; Hirst, D. G.; Stratford, M. R. L.; Flitney, F. W., Inducible nitric oxide synthase is expressed in tumour-associated vasculature inhibtion retards tumour growth. In *The biology of nitric oxide*, Moncada, S.; Feelisch, M.; Busse, R.; Higgs, E. A., Eds. Portland Press: London, 1994; pp 259-263.

79. Jones, M. L.; Ganopolsky, J. G.; Labbe, A.; Wahl, C.; Prakash, S. "Antimicrobial properties of nitric oxide and its application in antimicrobial formulations and medical devices." *Appl. Microbiol. Biotechn.* **2010**, *88*, 401-407.

80. DeGroote, M. A.; Fang, F. C. Antimicrobial properties of nitric oxide: nitric oxide and infection. Springer US: 2002; pp 231-261.

81. Deupree, S. M.; Schoenfisch, M. H. "Morphological analysis of the antimicrobial action of nitric oxide on gram-negative pathogens using atomic force microscopy." *Acta Biomater*. **2009**, *5*, 1405-1415.

82. Ghaffari, A.; Miller, C. C.; McMullin, B.; Ghahary, A. "Potential application of gaseous nitric oxide as a topical antimicrobial agent." *Nitric Oxide* **2006**, *14*, 21-29.

83. Privett, B. J.; Deupree, S. M.; Backlund, C. J.; Rao, K. S.; Johnson, C. B.; Coneski, P. N.; Schoenfisch, M. H. "Synergy of nitric oxide and silver sulfadiazine against gram-negative, gram-positive, and antibiotic-resistant pathogens." *Mol*. *Pharmaceut*. **2010**, *7*, 2289-2296.

84. Raulli, R.; McElhaney-Feser, G.; Hrabie, J. A.; Cihlar, R. L. "Antimicrobial properties of nitric oxide using diazeniumdiolates as the nitric oxide donor." *Rec*. *Res*. *Devel*. *Microbiol*. **1992**, *6*, 177-183.

85. Barraud, N.; Hassett, D. J.; Hwang, S.-H.; Rice, S. A.; Kjelleberg, S.; Webb, J. S. "Involvement of nitric oxide in biofilm dispersal of *Pseudomonas aeruginosa*." *J*. *Bacteriol*. **2006**, *188*, 7344-7353.

86. Stephens, C. "Microbiology: Breaking down biofilms." *Current Biology* **2002**, *12*, R132-R134.

87. de Fatima, A.; Modolo, L. V.; Sanches, A. C. C.; Porto, R. R. "Wound healing agents: The role of natural and non-natural products in drug development." *Mini-Rev*. *Med*. *Chem*. **2008**, *8*, 879-888.

88. Rizk, M.; Witte, M. B.; Barbul, A. "Nitric oxide and wound healing." *World J*. *Surg*. **2004**, *28*, 301-306.

89. Cortivo, R.; Vindigini, V.; Iacobellis, L.; Abatangelo, G.; Pinton, P.; Zavan, B. "Nanoscale particle therapies for wound and ulcers." *Nanomedicine* **2010**, *5*, 641-656.

90. Eroy-Reveles, A. A.; Mascharak, P. K. "Nitric oxide-donating materials and their potential in pharmacological applications for site-specific nitric oxide delivery." *Future Med*. *Chem*. **2009**, *1*, 1497-1507.

91. Miller, M. R.; Megson, I. L. "Recent developments in nitric oxide donor drugs." *Brit*. *J*. *Pharmacol*. **2007**, *151*, 305-321.

92. Carpenter, A. W.; Schoenfisch, M. H. "Nitric oxide release: Part II. Therapeutic applications." *Chem*. *Soc*. *Rev*. **2012**, *41*, 3742-3752.

93. Wang, P. G.; Xian, M.; Tang, X.; Wu, X.; Wen, Z.; Cai, T.; Janczuk, A. J. "Nitric oxide donors: Chemical activities and biological applications." *Chem*. *Rev*. **2002**, *102*, 1091-1134.

94. Hrabie, J. A.; Keefer, L. K. "Chemistry of the nitric oxide-releasing diazeniumdiolate ("Nitrosohydroxylamine") functional group and its oxygen-substituted derivatives." *Chem*. *Rev*. **2002**, *102*, 1135-1154.

95. Ignarro, L. J. *Nitric oxide: Biology and pathobiology*. Academic Press: San Diego, CA, 2000.

96. Riccio, D. A.; Schoenfisch, M. H. "Nitric oxide release: Part I. Macromolecular scaffolds." *Chem. Soc. Rev.* **2012**, *41*, 3731-3741.

97. Zhang, H.; Annich, G. M.; Miskulin, J.; Stankiewicz, K.; Osterholzer, K.; Merz, S. I.; Bartlett, R. H.; Meyerhoff, M. E. "Nitric oxide-releasing fumed silica particles: Synthesis, characterization, and biomedical application." *J. Am. Chem. Soc.* **2003**, *125*, 5015-5024.

98. Frost, M. C.; Meyerhoff, M., E. "Synthesis, characterization, and controlled nitric oxide release from *S*-nitrosothiol-derivatized fumed silica polymer filler particles." *J. Biomed. Mater. Res.* **2005**, *72*, 409-419.

99. Shin, J. H.; Metzger, S. K.; Schoenfisch, M. H. "Synthesis of nitric oxide-releasing silica nanoparticles." *J. Am. Chem. Soc.* **2007**, *129*, 4612-4619.

100. Shin, J. H.; Schoenfisch, M. H. "Inorganic/organic hybrid silica nanoparticles as a nitric oxide delivery scaffold." *Chem. Mater.* **2008**, *20*, 239-249.

101. Hetrick, E. M.; Shin, J. H.; Paul, H. S.; Schoenfisch, M. H. "Anti-biofilm efficacy of nitric oxide-releasing silica nanoparticles." *Biomaterials* **2009**, *30*, 2782-2789.

102. Hetrick, E. M.; Shin, J. H.; Stasko, N. A.; Johnson, C. B.; Wespe, D. A.; Holmuhamedov, E.; Schoenfisch, M. H. "Bactericidal efficacy of nitric oxide-releasing silica nanoparticles." *ACS Nano* **2008**, *2*, 235-246.

103. Allahverdiyev, A. M.; Kon, K. V.; Abamor, E. S.; Bagirova, M.; Rafailovich, M. "Coping with antibiotic resistance: Combining nanoparticles with antibiotics and other antimicrobial agents." *Exp. Rev. Anti. Infect. Ther.* **2011**, *9*, 1035-1052.

104. Deshpande, D.; Devalapally, H.; Amiji, M. "Enhancement in anti-proliferative effects of paclitaxel in aortic smooth muscle cells upon co-administration with ceramide using biodegradable polymeric nanoparticles." *Pharm. Res.* **2008**, *25*, 1936-1947.

105. Yoo, J. W.; Yun, D. S.; Kim, H. J. "Influence of reaction parameters on size and shape of silica nanoparticles." *J Nanosci. Nanotechnol.* **2006**, *6*, 3343-3346.

106. Bogush, G. H.; Tracy, M. A.; Zukoski, C. F. "Preparation of monodisperse silica particles: Control of size and mass fraction." *J. Non-Cryst. Solids* **1988**, *104*, 95-106.

107. Riccio, D. A.; Nugent, J. L.; Schoenfisch, M. H. "Stober synthesis of nitric oxide-releasing *S*-nitrosothiol-modified silica particles." *Chem. Mater.* **2010**, *23*, 1727-1735.

108. van Blaaderen, A.; Vrij, A. "Synthesis and characterization of colloidal dispersion of fluorescent, monodisperse silica spheres." *Langmuir* **1992**, *8*, 2921-2931.

109. Langevin, D. "Micelles and microemulsions." *Annu*. *Rev*. *Phys*. *Chem*. **1992**, *43*, 341-369.

110. Naik, S. P.; Elangovan, S. P.; Okubo, T.; Sokolov, I. "Morphology control of mesoporous silica particles." *J*. *Phys*. *Chem*. *C* **2007**, *111*, 11168-11173.

111. Kim, T.-W.; Chung, P.-W.; Lin, V. S. Y. "Facile synthesis of monodisperse spherical MCM-48 mesoporous silica nanoparticles with controlled particle size." *Chem*. *Mater*. **2010**, *22*, 5093-5104.

112. Huh, S.; Wiench, J. W.; Yoo, J.-C.; Pruski, M.; Lin, V. S. Y. "Organic functionalization and morphology control of mesoporous silicas via a co-condensation synthesis method." *Chem*. *Mater*. **2003**, *15*, 4247-4256.

113. Trewyn, B. G.; Whitman, C. M.; Lin, V. S. Y. "Morphological control of room-temperature ionic liquid templated mesoporous silica nanoparticles for controlled release of antibacterial agents." *Nano Lett*. **2004**, *4*, 2139-2143.

114. Calvino-Casilda, V.; Lopez-Peinado, A. J.; Vaganova, E.; Yitzchaik, S.; Pacios, I. E.; Pierola, I. F. "Porosity inherent to chemically crosslinked polymers. Poly(n-vinylimidazole) hydrogels." *J*. *Phys*. *Chem*. *B* **2008**, *112*, 2809-2817.

115. Buchel, G.; Grun, M.; Unger, K. K.; Matsumoto, A.; Tsutsumi, K. "Tailored syntheses of nanostructured silicas: Control of particle morphology, particle size and pore size." *Supramol*. *Sci*. **1998**, *5*, 253-259.

116. Gref, R.; Minamitake, Y.; Paracchia, M. T.; Trubetskoy, V.; Torchilin, V. P.; Langer, R. "Biodegradable long-circulating polymeric nano-spheres." *Science* **1994**, *263*, 1600-1603.

117. Yu, M.; Zhou, L.; Zhang, J.; Yuan, P.; Thorn, P.; Gu, W.; Yu, C. "A simple approach to prepare monodisperse mesoporous silica nanospheres with adjustable sizes." *J*. *Colloid Interf*. *Sci* **2012**, *376*, 67-75.

118. Widenmeyer, M.; Anwander, R. "Pore size control of highly ordered mesoporous silica MCM-48." *Chem*. *Mater*. **2002**, *14*, 1827-1831.

119. Neue, U. D. *HPLC columns: Theory, technology, and practice*. John-VCH: 1997.

Chapter 2:

Influence of Scaffold Size on Bactericidal Activity of Nitric Oxide-Releasing Silica Nanoparticles

2.1 Introduction

The endogenous free radical nitric oxide (NO) is involved in numerous physiological processes, including neurotransmission, wound healing, blood pressure regulation, platelet adhesion, and the immune response.[1-5] While the delivery of exogenous gaseous NO has been shown to elicit promising antimicrobial effects against Gram-positive and Gram-negative bacteria, and even antibiotic-resistant strains,[6] the utility of NO as an effective therapeutic has been limited due to its reactive and concentration-dependent behavior. As a result, much research has focused on the development of NO donors that store and generate NO in a controlled manner.[7-11] Examples of NO donors that reversibly bind NO include metal nitrosyls, *S*-nitrosothiols, *N*-diazeniumdiolates, and organic nitrates. *N*-Diazeniumdiolate NO donors, formed upon the reaction of secondary amines with NO under basic conditions, are of particular interest as they undergo proton-initiated decomposition in physiological solution (pH 7.4, 37 °C) to release two equivalents of NO per functional group.[7]

Although useful as tools for studying the role of NO in biology, most low molecular weight (LMW) NO donors release NO indiscriminately with undesirable cytotoxicity to healthy cells.[3, 12, 13] In Section 1.2.3, macromolecular NO-releasing silica particles

synthesized via the Stöber method were introduced as a new class of NO release materials that store/release substantial levels of NO with great potential for future targeting strategies due to versatile surface chemistries for attaching cell targeting and/or tracking (*i.e.*, fluorescent) ligands.[14, 15] Employing a hybrid silica design allows for a wide range of NO doses and release kinetics by changing the type and concentration of the aminosilane precursor. Silica particles have also proven effective at delivering NO to bacteria (*i.e.*, *Pseudomonas aeruginosa*) with greater bactericidal action than comparable small molecule NO donors.[13] Other recent reports corroborate the utility of nanomaterials for delivering antimicrobial agents.[16] Indeed, nanoparticles composed of silver,[17-20] copper,[21-23] zinc oxide,[24-28] titanium dioxide,[24, 29, 30] and magnesium oxide exhibit a broad range of bactericidal activity. As discussed in Section 1.1.3, the bactericidal efficacy of such materials is dependent on both the chemical composition and the particle diameter, with smaller diameters generally enhancing killing. For example, Morones et al. reported more effective *Escherichia coli* (*E. coli*) killing using smaller diameter (~1–10 nm) silver nanoparticles due to greater particle interaction with the bacteria.[17] Likewise, Nair et al. observed tunable killing as a function of particle size for zinc oxide nanoparticles, with the greatest killing efficacy observed for the smallest particle system prepared.[28] Since particle association with bacteria appears to be critical to antimicrobial activity,[17, 31-33] we sought to study the influence of nanoparticle size on nanoparticle-bacteria interactions and the resulting bactericidal efficacy of NO-releasing nanoparticles. In this chapter, a reverse microemulsion approach was used to synthesize monodisperse NO-releasing silica particles of three distinct sizes (50, 100, and 200 nm) with equal NO release. The size-dependent antibacterial action of these particles against *Pseudomonas aeruginosa* was then evaluated.

2.2 Materials and methods

Tetraethoxysilane (TEOS) and *N*-(6-aminohexyl)aminopropyltrimethoxysilane (AHAP) were purchased from Gelest (Morrisville, PA). Triton X-100, 1-hexanol, heptane, pentane, sodium methoxide (NaOMe, 5.4 M solution in methanol), dimethylformamide, methanol, and rhodamine isothiocyanate were purchased from Acros Organics (Morris Plains, NJ). Ethanol, butanol, and 1-propanol were purchased from Fisher Scientific (Fair Lawn, NJ). Tryptic soy broth, tryptic soy agar, and minimum essential media (MEM) were purchased from Becton, Dickinson and Company (Sparks, MD). *Pseudomonas aeruginosa* (ATCC #19143) was purchased from American Type Culture Collection (Manasses, VA). L929 mouse fibroblasts were obtained from the UNC Tissue Culture Facility (Chapel Hill, NC). Nitric oxide (99.5%), nitrogen (N_2), and argon (Ar) gases were purchased from National Welders (Raleigh, NC). Distilled water was purified using a Millipore Milli-Q UV Gradient A-10 system (Bedford, MA) resulting in a total organic content of ≤6 ppb and a final resistivity of 18.2 mΩ·cm.

2.2.1 Reverse microemulsion synthesis of amine-functionalized silica nanoparticles

Amine-functionalized silica nanoparticles of select sizes were synthesized by adjusting the type and volume of organic solvent used in the reverse microemulsion.[34-36] Initially, reverse micelles were formed by mixing 3.54 g Triton X-100, 3.6 mL 1-hexanol, and the appropriate amount and type of organic solvent for 30 min. Then, 240 μL water, 120 μL ammonium hydroxide solution (28 wt% in water), and 40 μL TEOS were added sequentially in 30 min intervals. Hydrolysis and condensation were allowed to proceed for 3 or 18 h, depending on the desired particle size, to form a TEOS seed particle. The organic

solvent type and volume as well as the reaction time for initial TEOS seed growth for each particle size are listed in Table 2.1. Following the formation of the TEOS core particle, an additional 40 μL (0.179 mmol) TEOS was added to the microemulsion, after which 84 μL (0.335 mmol) AHAP was added 30 min later. Hydrolysis and co-condensation of TEOS and AHAP were allowed to proceed for an additional 18 h to form the amine-functionalized shell. The emulsion was broken upon the addition of ethanol. Silica precipitates were collected via centrifugation at 3645×*g* for 5 min. The supernatant was removed, and the particles were washed by resuspension in 1-butanol, 2-propanol, and ethanol, sequentially. To ensure removal of Triton X-100, particles were resuspended in 45 mL of a 50/50 ethanol/water (v/v) solution, sonicated for 5 min in chilled water, and collected via centrifugation (3645×*g*, 5 min). This process was repeated three times before a final wash with ethanol to aid in drying of the particles. The resulting surfactant-free particles (confirmed by UV-Vis) were dried in vacuo overnight. Product yields were typically between 10–20 mg per reaction.

2.2.2 N-Diazeniumdiolation of amine-functionalized silica nanoparticles

The procedure for loading NO onto the core-shell particles was modified from a previously reported method.[14, 37] Briefly, particles were suspended in a 1:9 mixture of DMF and methanol (5 mg mL^{-1}) by sonication. Sodium methoxide, the base catalyst (5.4 M in MeOH), was added in either a 2.5:1 for 50 nm particles or 5:1 for 100 and 200 nm particles molar ratio relative to the concentration of secondary amines as determined by elemental analysis. Following thorough mixing of this solution (vortexed for 1 min), 3.5 mL aliquots were placed in vials equipped with a stir bar. The open vials were then placed in a 160 mL Parr general purpose stainless steel pressure vessel with magnetic stirring and connected to

Table 2.1 Variable synthetic parameters for each amine-functionalized nanoparticle size.

Particle Size (nm)	Organic Solvent		TEOS Core Particle Reaction Time (h)
	Type	Volume (mL)	
50	pentane	45.6	3
100	heptane	15.2	3
200	heptane	15.2	18

an in-house NO reactor. Oxygen was removed from the solutions by purging with Ar three times rapidly, followed by three 10 min Ar purges at 8 bar. The vessel was then filled to a pressure of 10 bar with NO that had been scrubbed with KOH. The pressure in the reactor was maintained at 10 bar for 72 by repressuring with fresh NO to accommodate loss due to reaction and/or gas leak. After 72 h, the NO was released from the vessel, and the solutions were again purged with Ar to remove unreacted NO. The resulting *N*-diazeniumdiolate-modified silica nanoparticles were collected by centrifugation (3645*g*, 5 min), washed three times with ethanol, and dried in vacuo. The NO donor-modified nanoparticles were then stored in a vacuum sealed package at -20 °C until further use (up to one week). No loss in NO loading was observed for particles stored in this manner up to 8 d (the longest period investigated) as determined by chemiluminescence upon comparing NO release immediately following diazeniumdiolate formation to that measured on day 8.

2.2.3 Nitric oxide release measurements

Total amounts of NO released from each particle size were evaluated using the Griess assay.[38] The NO-loaded particles were placed in oxygenated phosphate buffered saline (PBS) upon which the liberated NO is oxidized to nitrite (NO_2^-). After removing the particles via centrifugation, the supernatant containing NO_2^- was reacted with 1 wt% solutions of sulfanilamide and *N*-1-naphthylethylenediamine to form an azo-compound. By detecting the absorbance at 540 nm and comparing the results to a calibration curve, the concentration of NO released from the particles is deduced. While the Griess assay allows for the measurement of total NO concentrations, real-time diazeniumdiolate degradation and NO release kinetics were determined using a Sievers NOA 280i chemiluminescence NO analyzer

(Boulder, CO) in PBS (pH 7.4) at 37 °C, as described previously.[39] The absence of nitrite byproducts was confirmed by equal total NO concentrations measured from the Griess assay and the NOA. Prior to analysis, the NO analyzer was calibrated with air passed through a NO zero filter (0 ppm NO) and a 26.39 ppm NO standard gas (balance N_2).

2.2.4 Nanoparticle characterization

The hydrodynamic particle diameter and zeta potential (*i.e.*, surface charge) were measured using a Malvern Zetasizer Nano-ZS (Malvern Instruments, Ltd.; Worcestershire, UK) equipped with a 10 mW HeNe laser (633 nm) and a NIBS® detector at an angle of 173°. All samples were prepared at 1 mg/mL concentrations in PBS (size) or phosphate buffer (zeta potential) and analyzed at 37 °C to mimic the media used for NO-release and bacteria assays. Phosphate buffer (non-saline, pH 7.4) was employed for zeta potential measurements because the high ionic content of PBS was found to corrode the folded capillary electrodes.[40] Particle size and morphology were also characterized using a JEOL 100 CX II Transmission Electron Microscope (TEM) at 100 kV.

Covalent incorporation of AHAP and TEOS within the silica network was confirmed using solid-state cross-polarization/magic angle spinning (CP/MAS) ^{29}Si NMR with a Bruker 360 MHz DMX spectrometer (Billerica, MA) equipped with wide-bore magnets (triple-axis pulsed field gradient double-resonance probes). Samples were packed into a 4 mm rotor (double-resonance frequency of 71.548 Hz) and spun at a speed of 10 kHz. Chemical shifts were determined in parts per million relative to a tetramethylsilane external standard. Elemental analysis was performed using a PerkinElmer CHN/S O Elemental Analyzer Series 2400 (Waltham, MA) instrument.

2.2.5 Bactericidal assays

Pseudomonas aeruginosa was cultured to a concentration of 10^8 colony forming units (CFUs) per mL, collected via centrifugation, resuspended in sterile PBS and adjusted to a concentration of 10^6 CFU mL^{-1}. This starting concentration was chosen to accurately show at least 3 logs reduction as the limit of detection for the plate counting method is $2.5x10^3$ CFU mL^{-1}.[41] Aliquots of the 10^6 CFU mL^{-1} bacteria suspension were added to pre-massed amounts of nanoparticles to obtain the following concentrations 0, 0.025, 0.05, 0.1, 0.2, 0.3, 0.4, 0.5, 0.6, 0.7, 0.8, 0.9, 1.0 mg/mL. The nanoparticle/bacteria suspensions were vortexed for 30 s to adequately suspend the nanoparticles, then incubated at 37 °C with gentle agitation. Aliquots were then taken from each suspension after 2 and 24 h and diluted 10- and 100-fold in PBS before plating on tryptic soy agar. Bacterial viability was measured after incubating plates at 37 °C overnight by counting observed colonies.

2.2.6 Confocal microscopy studies

Nanoparticles were fluorescently labeled by covalent modification with rhodamine isothiocyanate (RITC).[42] Briefly, 50 mg of particles were suspended in 100 mL ethanol and mixed with 5 mg RITC, protected from light, for 48 h. The particles were then washed copiously with ethanol using the suspension/centrifugation method described above until a colorless supernatant was achieved. All confocal images were obtained with a Zeiss 510 Meta Laser Scanning Confocal Microscope. Brightfield and fluorescent images (543 nm HeNe excitation laser) were collected at room temperature with a N.A. 1.2 C-apochromat water immersion lens with either a 40 or 63× objective as indicated for each image. *Pseudomonas aeruginosa* cultures (10^6 CFU mL^{-1}) were placed in a glass bottom petri dish

and allowed to adhere for 45 min at 37 °C prior to imaging. The slide was then rinsed with fresh PBS to remove loosely or unadhered bacteria. Brightfield images of untreated bacteria were obtained as controls. For all experiments, suspensions of rhodamine isothiocyanate (RITC)-modified AHAP/TEOS nanoparticles (500 μL of 10 μg mL^{-1} in PBS) were added to the bacteria on the glass slide. To observe association of NO-releasing particles with bacteria over time, fluorescence images were taken immediately following the addition of particles at 20 s intervals for 40 min. To compare the influence of particle size on the extent of particle-bacteria association, fluorescence images were obtained of bacteria treated with 10 μg mL^{-1} of 50, 100, and 200 nm particles for 10 min. After the 10 min incubation period, the suspension was removed, and the bacteria were copiously washed with fresh PBS to remove unassociated particles. Fresh PBS was then added, and the bacteria were imaged.

2.2.7 Cytotoxicity assays

In vitro cellular toxicity of both control (i.e., control AHAP/TEOS particles) and NO-releasing particles of all three sizes was evaluated using L929 fibroblast cells. Briefly, the fibroblasts were cultivated in MEM supplemented with 10% fetal bovine serum (v/v, FBS) and 1% penicillin/streptomycin, then incubated in 5% CO_2/95% air under humidified conditions at 37 °C. After attaining confluency, the cells were trypsinized and then seeded onto tissue-culture treated polystyrene 96-well plates at a density of $3x10^5$ cells mL^{-1}. Three days later, cells were incubated with control and NO-releasing nanoparticles at a concentration range of 0–3.2 mg mL^{-1} for 2 h and 0–0.8 mg mL^{-1} for 24 h. Subsequently, the particles were aspirated, cells were washed with sterile PBS three times, and 100 μL fresh media was added to the cells. Cellular viability was assessed using the MTS assay (CellTiter

96 Aqueous Non-Radioactive Cell Proliferation Assay; Promega, Madison, WI). Briefly, the MTS reagent (20 μL) was added to each well until a purple formazan color was formed in the control (untreated) wells. The supernatant (90 μL) from each well was then transferred to a new 96-well plate prior to reading the absorbance at 490 nm using a microplate reader (Thermoscientific Multiskan® EX; Waltham, MA). Untreated cells were used as controls and results were expressed as percent viability relative to the untreated controls.

2.3 Results and discussion

While metallic and metal oxide nanoparticles with diameters of 1 to 500 nm have been reported to exhibit toxicity towards both Gram-positive and Gram-negative microorganisms, nanoparticles of diameters ≤100 nm are generally more effective biocides.[16] As such, we set out to investigate the influence of particle size on the bacteria killing efficacy of NO-releasing silica particles with diameters above, below, and equal to 100 nm. To achieve these specific sizes, the reverse microemulsion technique was used as it provides a method for synthesizing silica-based particles in the nanometer range with excellent control over size and particle composition by changing any number of synthetic parameters including the amount of water and ammonium hydroxide,[43-45] reaction time, the type of organic solvent, and the ratios of water to surfactant, surfactant to co-surfactant, and surfactant to organic solvent.[34, 45, 46] A clear benefit of this method is the ability to tune particle size while keeping the aminoalkoxysilane:alkoxysilane ratio constant.[35, 43, 47, 48] In general, particles synthesized by the reverse microemulsion method have a smaller size and narrower distribution than those produced via the Stöber method.[34, 49] Narrow size distributions are essential when investigating the influence of nanoparticle size on bacterial interactions.

Furthermore, the use of the reverse microemulsion technique provides a facile method for core-shell particle designs such that a variety of functionalities are easily incorporated as part of the silica scaffold.[34-36, 43, 47, 48]

2.3.1 Size-controlled synthesis of amine-functionalized silica nanoparticles

Scheme 2.1 illustrates the reverse microemulsion approach used to obtain amine-functionalized silica nanoparticles. For the three sizes (50, 100, and 200 nm), the micelles were prepared using Triton X-100 (surfactant) and 1-hexanol (co-surfactant) suspended in pentane or heptane. Following micelle formation, an aqueous phase was introduced by adding water and ammonium hydroxide, sequentially. Following the formation of a stable microemulsion as indicated by a clear and colorless solution (step 1 of Scheme 2.1), the amine-modified silica nanoparticles were synthesized. *N*-(6-aminohexyl)aminopropyl-trimethoxysilane (AHAP) and tetraethoxysilane (TEOS) were chosen for study based on prior work that demonstrated NO-releasing AHAP/TEOS particles to be effective against *P. aeruginosa* and not toxic to fibroblast cells.[13] The addition of pure aminosilane to the microemulsion resulted in amorphous silica particulates at low yields (1–2 mg) (Figure 2.1.E). Thus, it was necessary to include a tetraalkoxysilane backbone to promote condensation as was seen for our previously reported particle systems.[14, 15] However, the simultaneous addition of both AHAP and TEOS resulted in particles of a wide size distribution, especially at high AHAP concentrations (Figure 2.1). By adopting a sequential silane addition method, the monodispersity of the particles was greatly improved. Thus, TEOS was added initially to the microemulsion to form monodisperse TEOS seed particles (step 2 of Scheme 2.1) prior to shell modification with 65 mol % AHAP

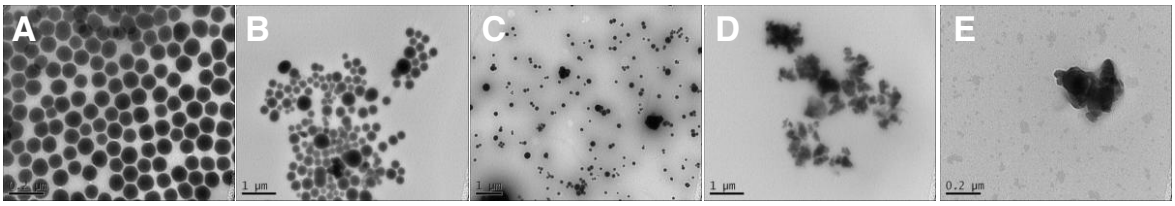

Figure 2.1 Transmission electron micrographs of silica particles resulting from the addition of (A) 0, (B) 27, (C) 53, (D) 77, or (E) 100 mol% aminosilane (balance TEOS).

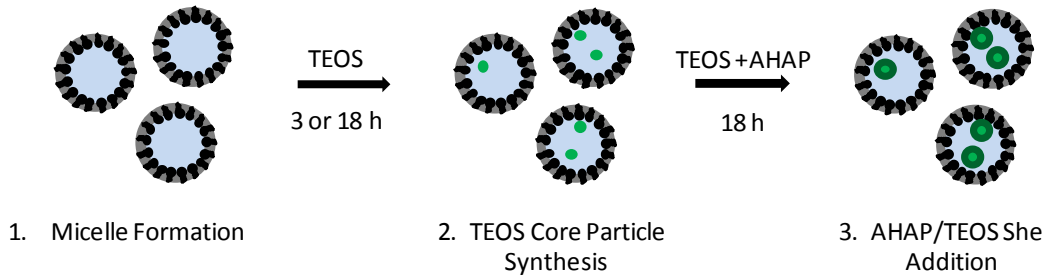

Scheme 2.1 Synthesis of amine-functionalized silica nanoparticles via a reverse microemulsion. Step 1 involves micelle formation. Step 2 is the addition of tetraethoxysilane (TEOS) to the emulsion to form monodisperse "seed" particles. Lastly, step 3 is the subsequent addition of TEOS and AHAP that co-condense to form the AHAP/TEOS silica nanoparticles.

(balance TEOS), as shown in step 3 of Scheme 2.1. The reverse microemulsion process allowed for higher aminosilane incorporation than was previously achievable via the Stöber process (10 mol %, balance TEOS)[14] due to diffusion controlled particle growth. Of note, adding AHAP alone to the microemulsion resulted in poor shell formation and low yield. Due to the mismatched hydrolysis and condensation rates of the two silane precursors,[50] TEOS was added 30 min prior to the addition of AHAP during shell modification to achieve monodisperse particle populations.

To tune particle size, a variety of synthetic parameters were adjusted (Table 2.1). The viscosity, polarity and molecular structure of the organic solvent are known to influence the intermolecular forces between the surfactant molecules and the organic phase, and thus greatly impact the micelle diameter and the resulting particle size.[51] Smaller organic solvent molecules can penetrate deeper into the surfactant layer, decreasing the overall size of the water droplet and ensuing particles.[34] For this reason, pentane was used to prepare the smallest AHAP/TEOS particles (50 nm), while heptane was used to form the larger diameter particles (*i.e.*, 100 and 200 nm). Thus, increasing reaction time can ultimately lead to larger particles.[34] For example, a 3 h TEOS seed reaction resulted in 5 nm particles whereas 12 nm seed particles were achieved after 18 h under the same solvent conditions. Additionally, increasing the volume of organic solvent decreases the occurrence of interdroplet percolation, resulting in smaller particles. The resulting particle sizes and surface charges of the three synthesized systems are provided in Tables 2.2 and 2.3. While electron microscopy provided a means to examine particle morphology, dynamic light scattering (DLS) allowed for the measurement of the hydrodynamic diameter and solution behavior of the particles.[52] When interpreting

Table 2.2 Particle size as determined by transmission electron microscopy (TEM) and dynamic light scattering (DLS).

Particle Size (nm)	TEM	DLS			
	Diameter (nm)	Z-Ave (nm)	PDI	Number PSD (nm)	Volume PSD (nm)
50	56 ± 7	80.0 ± 3.1	0.150 ± 0.041	52.7 ± 3.3	66.8 ± 3.4
100	93 ± 14	129.5 ± 13.7	0.087 ± 0.042	98.4 ± 6.7	127.3 ± 11.9
200	199 ± 27	209.0 ± 3.9	0.041 ± 0.029	191.0 ± 1.8	221.7 ± 8.8

Table 2.3 Zeta potential values of AHAP/TEOS and *N*-diazeniumdiolate AHAP/TEOS silica nanoparticles as determined by Laser Doppler Velocimetry.

Particle Size (nm)	Zeta Potential[b]	
	R_2NH (mV)	$R_2N[N(O)NO]^-$ (mV)
50	+11.8 ± 1.2	-5.2 ± 3.9
100	+12.5 ± 1.1	+5.9 ± 2.3
200	+11.4 ± 1.1	+8.4 ± 0.3

nanoparticle size, both DLS and electron microscopy data must be considered together for proper size characterization as particle size measurements from DLS better represent the entire particle population and the actual size in solution. The Z-average diameter, polydispersity index (PDI), and particle size distributions (PSD), and diameters as measured from transmission electron microscopy (TEM) are provided in Table 2.2. Taken together, the parameters reported in Table 2.2 provide a comprehensive evaluation of the actual particle sizes present during bacteria assays. Z-average diameters result from the cumulants analysis of the intensity of light scattered from the sample, thus it may only be compared between samples that were prepared in the same dispersant and measured by the same technique. The number PSD is a measure of the particle size distribution based on the number of particles that are a particular size within the sample. Alternatively, the volume PSD is a measure of the particle size distribution based on the volume of the sample that is occupied by certain sizes. Both the Z-average and the volume PSD are skewed to larger sizes as larger particles will scatter more light and account for significantly more signal/volume than smaller particles. The polydispersity index (PDI) is a width parameter of the mean size calculated from the cumulants analysis, and ranges from 0 to 1, with a 0 indicating a stable suspension and a perfectly monodisperse population. Although no official standard exists, a PDI of <0.2 is considered to be monodisperse, while a PDI ≤ 0.1 is considered to be highly monodisperse.[53] With respect to the synthesized silica particles, we observed increasing PDI values as the particle diameter decreased, indicating that while all sizes were monodisperse and formed stable suspensions in PBS, decreasing particle size resulted in a slight increase in size distribution. This monodispersity was further corroborated by TEM (Figure 2.2 and Table 2.2). Collectively, the DLS and TEM data indicate that these particle systems are suitable for

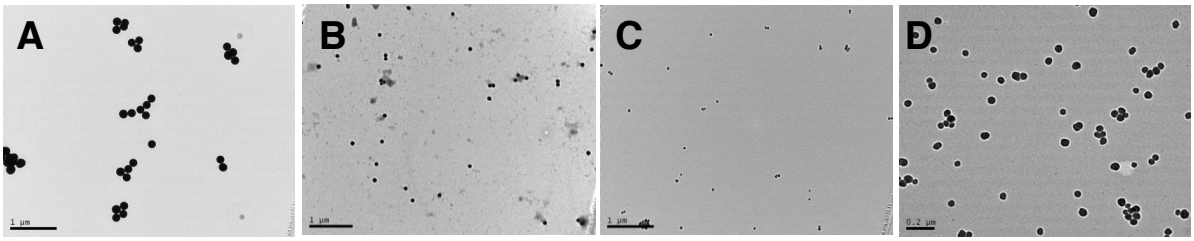

Figure 2.2 TEM micrographs of (A) 200, (B) 100, and (C, D) 50 nm AHAP/TEOS silica nanoparticles. Scale bar is 1 μm for A–C and 0.2 μm for D.

investigating the influence of particle size on particle-bacteria interactions based on their narrow size distribution and solution stability.

Solid state ^{29}Si nuclear magnetic resonance (NMR) confirmed the covalent incorporation of the aminosilane into the silica network. Cross-polarization (CP) and magic angle spinning (MAS) techniques were used to enhance the sensitivity toward silicon atoms near CH_x or OH groups and improve peak resolution.[54, 55] As shown in Figure 2.3, the spectrum of each particle system contained both T- and Q-bands, representing silicon atoms that are bound to three (AHAP) and four (TEOS) oxygen atoms, respectively. Changes in the neighboring oxygen environments surrounding the observed silicon atom were indicated by peak splitting within the T- and Q-bands denoted by superscripted numbers corresponding to the number of siloxane bonds.[54] The ^{29}Si NMR spectra therefore confirmed successful co-condensation and incorporation of AHAP and TEOS into the scaffold for each particle size. Of note, the ratios of the T-band to Q-band intensities are not reflective of the actual ratios of AHAP to TEOS within the particle because the core particles are likely pure SiO_2 and free of hydrogens.

Elemental analysis allowed for a more quantitative investigation of AHAP concentration within each particle system. We hypothesized that the amine content would remain constant regardless of particle diameter because the molar amounts of silane precursors (both TEOS and AHAP) were held constant for all three systems. Furthermore, the wt% N measured from CHN analysis may be translated to AHAP concentration as it is the only nitrogen-contributing component within the silica network. For the smallest particle system (50 nm), we measured a wt% N of 5.39, corresponding to 1.93 μmol AHAP per mg of particles. While the nitrogen amount increased slightly for the 100 nm particles

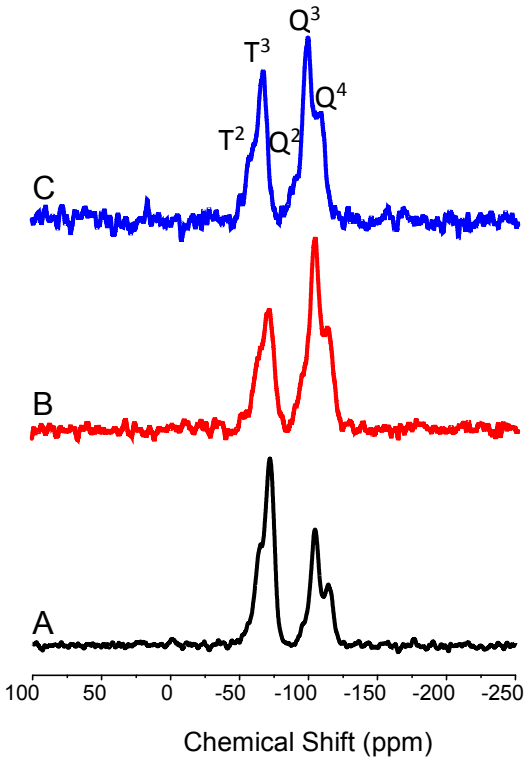

Figure 2.3 Solid state CP/MAS ^{29}Si NMR of (A) 50 nm, (B) 100 nm, and (C) 200 nm AHAP/TEOS nanoparticles. The T-band (ca. -70 ppm) represents silicon atoms that are bound to three oxygen atoms (*i.e.*, AHAP). The Q-band (ca. -100 ppm) indicates silicon atoms with four siloxane bonds (*i.e.*, TEOS).

(6.64 wt% N or 2.37 μmol AHAP per mg of particles), the larger 200 nm particle system was characterized by a slightly lower nitrogen content (5.29 wt% N corresponding to 1.89 μmol N per mg of particles), indicating a similar amine content regardless of a change in particle size for the three systems synthesized here.

2.3.2 N-Diazeniumdiolate NO donor functionalization

Nitric oxide was loaded onto the silica scaffolds via *N*-diazeniumdiolate formation on the secondary amine sites of AHAP by exposing the particles to high pressure of NO in the presence of a base catalyst (NaOMe) (Scheme 2.2).[14, 37] *N*-diazeniumdiolate formation was confirmed via NO release and zeta potential (*i.e.*, surface charge) changes observed after NO loading (Table 2.3). Initially, each particle system was characterized by a slightly positive charge of ca. +12 mV, an expected result due to the protonated primary amines at pH 7.4. Following NO loading, the zeta potential for each size became neutral (zeta potential between -10 and +10 mV)[40] from the contribution of the zwitterionic *N*-diazeniumdiolate functionality (Scheme 2.2). The particles regained their positive charge within 10 min as the result of *N*-diazeniumdiolate decomposition and regeneration of parent amines.

As shown in Table 2.4, the total amount of NO released from the particles was 1.49±0.29, 1.26±0.17, and 1.01±0.08 μmol mg^{-1} for the 50, 100, and 200 nm AHAP/TEOS particles, respectively. Based on the AHAP content per mg particle (Table 2.4), NO donor loading efficiencies were determined to be 38.6, 26.6, and 26.7% for 50, 100, and 200 nm particles, respectively. Such NO loading efficiency is consistent with previously reported *N*-diazeniumdiolate-modified silica particles.[14, 37] The greater conversion efficiency for the smallest particle size may be attributed to the increased surface area to volume ratio,

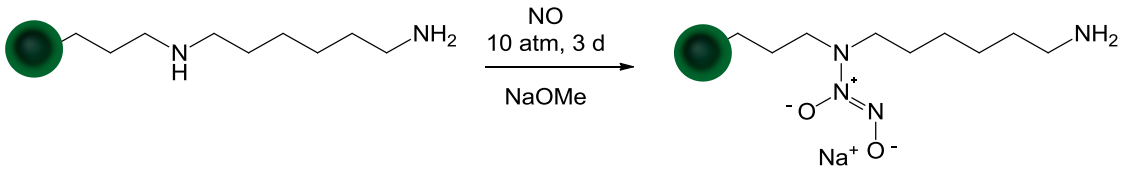

Scheme 2.2 *N*-Diazeniumdiolate formation on aminosilane-modified silica nanoparticle.

resulting in a larger concentration of amines nearer to the particle surface and therefore more accessible to reaction. These hybrid silica particles have low porosity with surface areas (S_{BET}) of 4–20 m^2/g and pore volumes of 0.008–0.989 cm^3/g (at $p/p_o = 0.99$) as determined from nitrogen adsorption-desorption isotherms. Indeed, the high density and low porosity resulting from the co-condensation method used to synthesize amine-modified hybrid silica materials have been previously observed.[14, 15] As a result of low porosity, amine sites farther from the particle surface are less accessible to diazeniumdiolation. To ascertain the dose of NO delivered from the particles over the course of the bactericidal assays, the total amounts of NO released over 2 and 24 h were measured and are provided in Table 2.4. As expected, each particle system was depleted of NO by 24 h. The NO release data indicates that over the course of 24 h, bacteria were exposed to similar amounts of NO regardless of nanoparticle size as there is no statistical difference in the total amount of NO released from each particle system. Since NO release occurs upon protonation of the secondary amine of the *N*-diazeniumdiolate, it is inevitable that the kinetics of NO release differ slightly for each particle size based on the *N*-diazeniumdiolate groups' proximity to the particle surface and therefore differing rate of contact with the aqueous solvent. As shown in Figure 2.4, the instantaneous release of NO from the particles was characterized by an initial burst of NO due to immediate decomposition of surface *N*-diazeniumdiolate NO donors upon solution immersion. This instantaneous maximum concentration of NO release is defined as $[NO]_m$. The particles exhibited a $[NO]_m$ of 49.7, 43.5, and 44.7 ppm mg^{-1} from the 50, 100, and 200 nm particles, respectively.

Table 2.4 Nitrogen content, NO release properties, and extent of amine to *N*-diazeniumdiolate conversion for the amine-functionalized silica nanoparticles.

Particle Size (nm)	μmol AHAP[a] per mg particle	$[NO]_t$[b] (μmol mg^{-1})		% C[c]	$[NO]_m$[d] (ppm mg^{-1})	t_m[e] (min)	t_d[f] (h)
		2 h	total				
50	1.93	0.47 ± 0.02	1.49 ± 0.29	39	49.7 ± 16.8	0.8 ± 0.1	15.2 ± 2.1
100	2.37	0.38 ± 0.01	1.26 ± 0.17	27	43.5 ± 5.2	0.6 ± 0.1	13.0 ± 3.8
200	1.89	0.42 ± 0.01	1.01 ± 0.08	27	44.7 ± 8.0	0.7 ± 0.1	9.9 ± 1.6

[a]Determined by CHN elemental analysis of control particles, [b]$[NO]_t$, total number of moles of NO released per mg of particle as measured by the Griess assay, [c] Percent conversion of secondary amines to *N*-diazeniumdiolate based on assumption that 100% diazeniumdiolate conversion would result in 2 mol NO per 1 mol of AHAP in particle scaffold, [d]$[NO]_m$, maximum concentration of NO released as measured with NOA. [e]t_m, time required to reach $[NO]_m$, [f]t_d, duration of NO release.

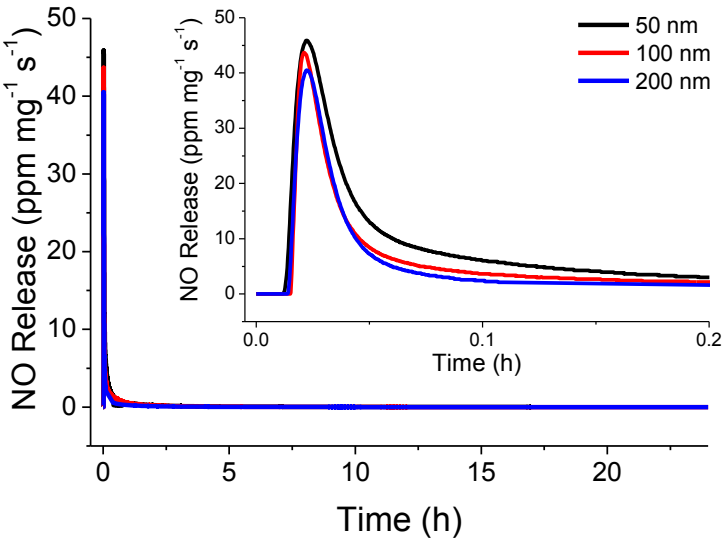

Figure 2.4 Real time NO release profile for 50 (black), 100 (red), and 200 (blue) nm NO-releasing AHAP/TEOS particles from t=0 to t=24 h. Inset: NO release from t=0 to t=0.2 h, corresponding to the shortest time period at which particle-bacteria association was investigated with confocal microscopy.

2.3.3 *Effect of nanoparticle size on bactericidal activity against* Pseudomonas aeruginosa

Based on prior work suggesting particles less than 100 nm are more effective antimicrobial materials,[16] we hypothesized that the 50 nm NO-releasing silica nanoparticles would be more effective at bacteria killing than the larger 100 and 200 nm particles. Minimum bactericidal concentration (MBC) assays were performed under nutrient-free conditions in phosphate buffered saline (PBS) to eliminate bacteria replication as our goal was to more accurately emphasize the role of size on the particle's bactericidal activity. The MBCs listed in Table 2.5 were determined as a function of NO-releasing nanoparticle size against 10^6 colony forming units (CFU) mL^{-1} *P. aeruginosa* cultures. The minimum particle concentrations required to achieve complete killing (3 log reduction) after short (2 h) and long (24 h) exposures were thus determined using bacteria in the healthiest state (*i.e.*, mid-log growth stage).[41] As shown in Table 2.5, the smaller particles were notably more effective at killing *P. aeruginosa* after 2 h compared to larger particles (MBC_{2h} of 0.8 mg mL^{-1} for 50 nm versus 1.5 mg mL^{-1} for 100 and 200 nm NO-releasing AHAP/TEOS particles, respectively). This two-fold difference in MBC_{2h} is significant given that there is only a slight difference in total NO released after 2 h from each particle size (Table 2.4). The total NO released from each particle size after 24 h was not statistically different, yet a two-fold difference in MBC_{24h} was still observed. Furthermore, the increased NO release exposure resulted in nearly a 4-fold decrease in the particle concentrations required to kill *P. aeruginosa* with MBC_{24h} of 0.2 mg mL^{-1} for 50 and 100 nm and 0.4 mg mL^{-1} for 200 nm NO-releasing particles (Table 2.5). Of note, the 100 nm particles exhibited similar bactericidal properties as the 200 nm particles at short incubation times, while at longer periods the bactericidal efficacy of the 100 nm particles resembled that of the 50 nm

Table 2.5 Minimum bactericidal concentration of NO-releasing AHAP/TEOS of each size after 2 and 24 h incubation with *P*. *aeruginosa*.

Particle Size nm	MBC_{2h} mg/mL	MBC_{24h} mg/mL
50	0.8	0.2
100	1.5	0.2
200	1.5	0.4

Table 2.6 Viability of *P*. *aeruginosa* following treatement with blank (i.e., in PBS only) or control (i.e., non-NO-releasing control AHAP/TEOS particles). Initial bacteria concentration is 10^6 CFU/mL.

	Dose mg/mL	Exposure Time h	Bacterial Viability CFU/mL
Blank (PBS)	0	2	$6.3(\pm0.5)\text{x}10^6$
	0	24	$8.6(\pm0.2)\text{x}10^6$
50 nm	0.8	2	$1.2(\pm0.2)\text{x}10^6$
	0.2	24	$9.6(\pm2.3)\text{x}10^6$
100 nm	1.5	2	$3.5(\pm0.4)\text{x}10^6$
	0.2	24	$2.7(\pm0.2)\text{x}10^6$
200 nm	1.5	2	$1.27(\pm0.03)\text{x}10^6$
	0.4	24	$5.2(\pm1.5)\text{x}10^6$

nanoparticles. This data corroborates the well-known relationship between biocidal activity and materials in the nanoscale (i.e., materials with size measuring 100 nm or less in one dimension). The considerable decrease in MBC over time indicates that the efficacy of the NO-releasing nanoparticles improves as more NO is released. Neither blanks (i.e., in PBS only) nor control (non-NO-releasing) AHAP/TEOS particles at MBC concentrations affected *P. aeruginosa* viability (Table 2.6).

Although the observed relationship between particle size and MBC may be expected, the mechanism for this phenomenon remained uncertain. Confocal microscopy was thus used to qualitatively observe particle fate. To allow for visualization using fluorescence imaging, the surface-accessible primary amines of the AHAP particles were chemically modified with rhodamine isothiocyanate (RITC).[42] Although NO release was decreased slightly (by 9%), no change in particle size or particle surface charge was observed following RITC modification. Similar to the non-fluorescent particles, a slight decrease in zeta potential was noted following diazeniumdiolation of the RITC-modified particles (ca. +13 mV to ca. +7 mV for control and NO-releasing, respectively). Initially, a time-based experiment was conducted where the bacteria were treated with RITC-modified NO-releasing AHAP/TEOS particles, and images were collected at 20 sec intervals over the course of 40 min. The particles rapidly associated with the bacteria within 2 min (Figure 2.5), a favorable attribute given the bolus release of NO. Immediately following this interaction, membrane degradation, cellular collapse, blebbing and decreased adhesion to the substrate were observed and attributed to the antimicrobial action of NO (*e.g.*, lipid peroxidation) (Figure 2.6).[56] Such severe morphological changes hindered our ability to distinguish between individual bacteria cells. Thus, the remaining confocal experiments were carried out using

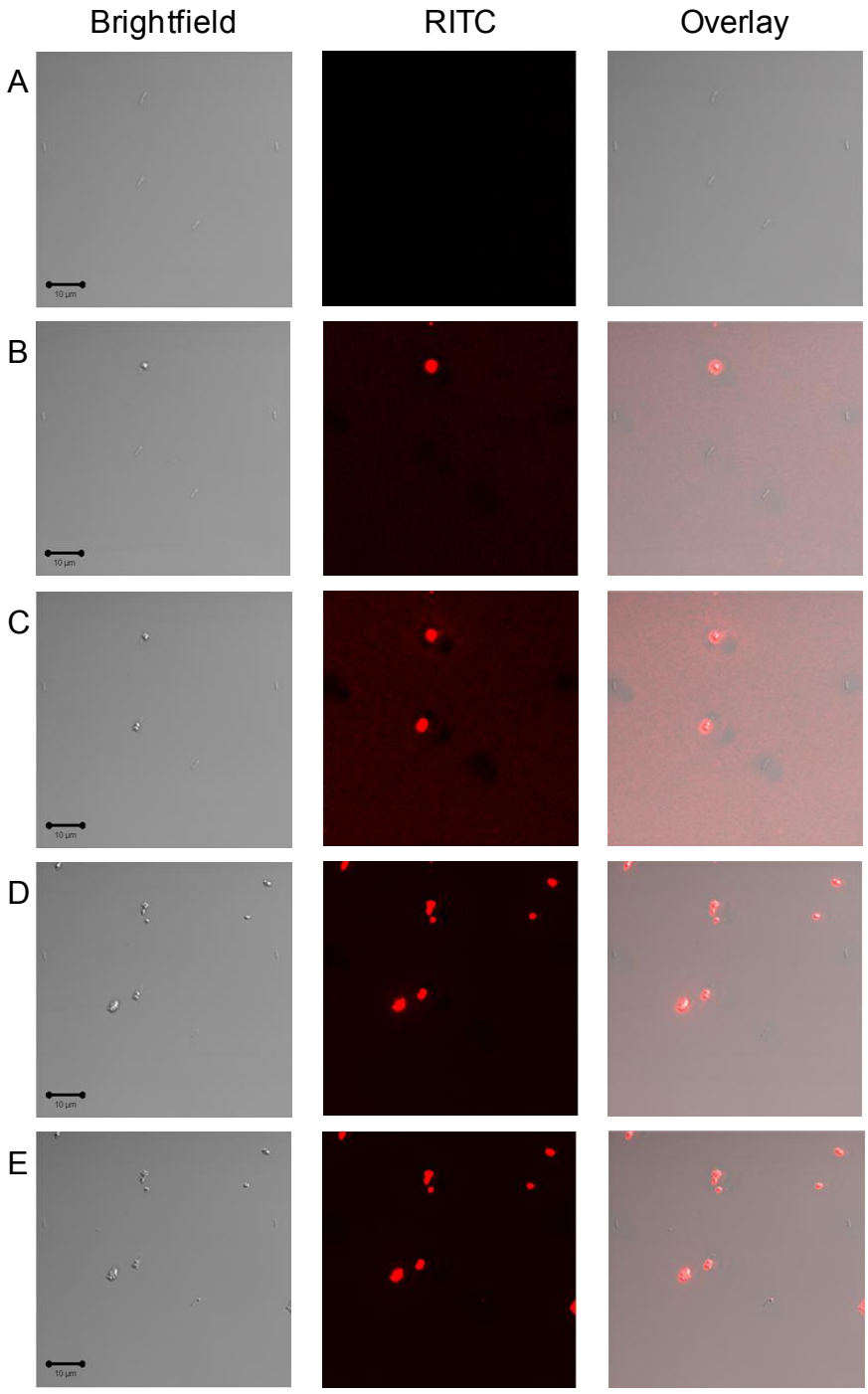

Figure 2.5 Scanning confocal images of *P. aeruginosa* treated with 50 nm RITC-modified NO-releasing AHAP/TEOS nanoparticles. Brightfield, fluorescence (RITC), and overlay images were acquired (A) 0 (addition of particles), (B) 2.4, (C) 6.4, (D) 19.5, and (E) 39 min after addition of 10 μg mL^{-1} nanoparticles. Scale bars are 10 μm.

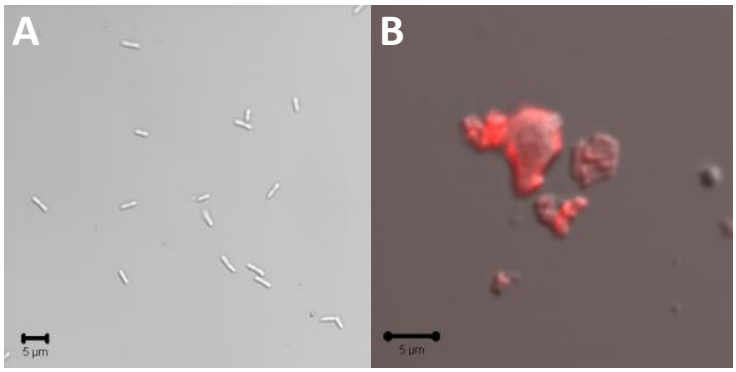

Figure 2.6 Scanning confocal images of *P. aeruginosa* treated with 50 nm RITC-modified NO-releasing AHAP/TEOS nanoparticles. Brightfield image (A) was acquired before addition of 10 µg mL^{-1} nanoparticles and fluorescence overlay image (B) was acquired after 10 min incubation with nanoparticles. Scale bars are 5 µm.

RITC-modified control AHAP/TEOS particles to maintain bacteria viability and potentially glean information on particle-bacteria association. Given that the size and surface charge are similar between the NO-releasing and control RITC-modified particles, particle-bacteria interactions that occur with control particles are an accurate representation of those that occur with NO-releasing RITC particles. When *P. aeruginosa* were exposed to particles at 50 μg mL^{-1} for longer than 30 min, fluorescence was present in all bacteria regardless of the particle size. By exposing the bacteria to decreased doses of 50, 100, and 200 nm RITC-modified nanoparticles (i.e., 10 μg mL^{-1}) for shorter time (i.e., 10 min), a difference in the rate and extent of association was observed fluorescently (Figure 2.7). The greatest RITC fluorescence was observed upon treatment of bacteria with the 50 nm nanoparticles (Figure 2.7A). Bacteria exposed to 100 nm nanoparticles exhibited some fluorescence but at a lower magnitude than the 50 nm treated cells (Figure 2.7B). Finally, little fluorescence was observed from the cells treated with the 200 nm particles (Figure 2.7C). Collectively, these results indicate that although all particle systems tested interact with the bacteria, the smaller diameter particles do so more rapidly. As shown in the inset of Figure 2.4 and provided in Table 2.4, a large amount of NO is released within the initial 10 min. Therefore, the rate of association governs the amount of NO delivered to the bacteria. Greater association with decreasing particle diameter corroborates our finding that smaller particles were more bactericidal at lower concentrations than larger particles. Indeed, the faster diffusion rate of smaller particles allows for a more rapid association with bacteria. As such, a larger portion of the stored NO is likely delivered to the bacteria from the 50 nm particles compared to the 100 and 200 nm particles, thereby lowering the necessary particle and overall NO concentrations required for effective killing.

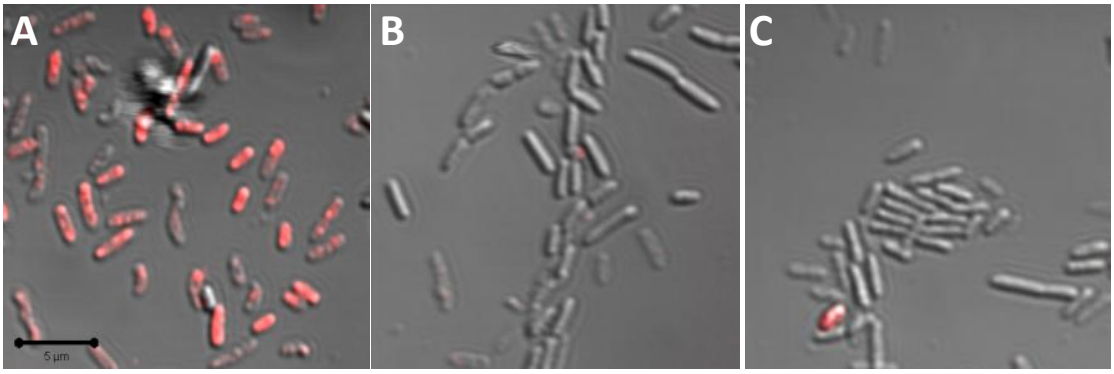

Figure 2.7 Overlay of fluorescence and brightfield scanning confocal microscopy images of *P. aeruginosa* treated with 10 µg mL^{-1} of (A) 50, (B) 100, and (C) 200 nm RITC-modified AHAP/TEOS silica nanoparticles for 10 min. Magnification is 63×, and scale bar is 5 µm.

2.3.4 Cytotoxicity against L929 mouse fibroblasts

The use of NO-donor functionalized silica scaffolds is motivated by both the synthetic versatility and biologically inert qualities of silica.[57] To be useful as a potential therapeutic, such materials must possess favorable toxicity to normal cells. The cytotoxicity of both NO-releasing and control AHAP/TEOS particles was thus evaluated against L929 mouse fibroblasts. Fibroblast viability screening represents a first test for evaluating cytotoxicity of both systemic and topical antibacterial agents as these cells play a critical role in wound healing.[58, 59] Although our lab has previously observed that AHAP/TEOS particles synthesized via the Stöber method exhibited no toxicity toward fibroblast cells,[13] the cytotoxicity of the particles reported herein was not obvious due to the modified synthesis (i.e., reverse microemulsion). In addition, our prior report did not investigate the role of size on toxicity. The MTS assay was used to measure cell viability after exposure to both control and NO-releasing particles for 2 and 24 h to mimic the two exposure times of the bactericidal assays. Particle concentrations up to double the MBC values for each time point were tested to evaluate cytotoxicity above the concentration required for bacteria killing. Theoretical total NO doses delivered from each particle concentration after 2 and 24 h were calculated from the NO release data and are provided in Table 2.7. As shown in Figure 2.8A, no toxicity was observed after 2 h from the NO-releasing particles up to their respective MBC_{2h} doses regardless of particle size. Control particles of 50 and 100 nm were also not toxic at their respective bactericidal concentrations. However, the MBC_{2h} dose of control 200 nm particles (1.6 mg mL^{-1}) decreased fibroblast viability by 36%. Although toxicity was observed at the highest concentration tested (3.2 mg mL^{-1}) for control 50 nm and both NO-releasing and control 200 nm particles, we note that these concentrations were well above the

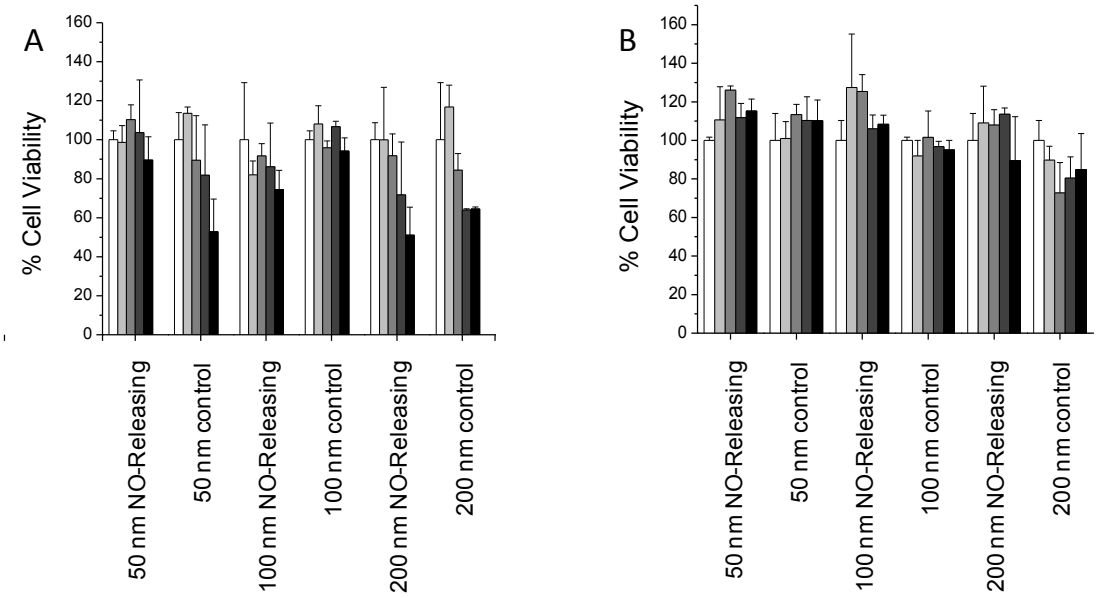

Figure 2.8 Cytotoxicity of control and NO-releasing particles against L929 mouse fibroblast cells as measured using the MTS assay after (A) 2 h exposure at 0 (white), 0.4 (light grey), 0.8 (grey), 1.6 (dark grey), and 3.2 (black) mg mL^{-1} and after (B) 24 h exposure at 0 (white), 0.1 (light grey), 0.2 (grey), 0.4 (dark grey), and 0.8 (black) mg mL^{-1}.

Table 2.7 Concentration of NO corresponding to the particle concentrations tested in cytotoxicity assays.

Particle Size (nm)	Particle Dose (mg mL^{-1})	Total NO Dose (μmol) 2 h	24 h
50	0.1	0.05	0.15
	0.2	0.09	0.30
	0.4	0.19	0.60
	0.8	0.37	1.19
	1.6	0.75	2.38
	3.2	1.49	4.77
100	0.1	0.04	0.13
	0.2	0.08	0.25
	0.4	0.15	0.50
	0.8	0.30	1.01
	1.6	0.61	2.02
	3.2	1.22	4.03
200	0.1	0.04	0.10
	0.2	0.08	0.20
	0.4	0.17	0.40
	0.8	0.34	0.81
	1.6	0.68	1.62
	3.2	1.35	3.23

therapeutic doses required for complete bacteria killing (0.8 and 1.5 mg mL^{-1}, respectively). As shown in Figure 2.8B for 24 h treatment, no significant toxicity was observed for either NO-releasing or control particles at concentrations up to 2x MBC_{24h} for all three sizes. Taken together, these results indicate that increased treatment time with NO-releasing AHAP/TEOS particles has the combined advantage of lower therapeutic dose required for sufficient bacteria killing with negligible effect on fibroblast cell viability.

2.4 Conclusions

A reverse microemulsion synthesis was developed to prepare three sizes of highly monodisperse aminosilane-modified silica nanoparticles. The particles were characterized by high amine-loading with surface accessible primary amines that allowed for straightforward coupling of fluorescent markers. Conjugation of other biorecognition agents should be compatible in the same way, further expanding the potential therapeutic utility of these scaffolds. By maintaining constant NO loading/release for each particle size, the relationship between nanoparticle size and bactericidal efficacy was probed. At shorter exposure time, the smaller NO-releasing silica nanoparticles (50 nm) were found to exhibit the greatest bactericidal activity. Such behavior may be attributed to their increased rate of association and subsequent greater NO payload delivered directly to the bacteria. We hypothesize that increasing the rate at which NO-releasing particles associate with bacteria may further improve their antibacterial properties. Future research should focus on how the amount and kinetics of NO delivered into bacterial cells influences the observed bactericidal efficacy. Although particles with both neutral and positive surface charges were shown to interact with the bacteria, the rate of particle association is likely influenced by particle surface charge as

bacteria are characterized by a net negative charge. More effective antibacterial nanoparticle therapeutics may be realized by understanding the role of particle-bacteria interactions on bactericidal activity.

References

1. Ignarro, L. J. *Nitric oxide: Biology and pathobiology*. Academic Press: San Diego, CA, 2000.

2. Bredt, D. S. "Endogenous nitric oxide synthesis: Biological functions and pathophysiology." *Free Rad. Res.* **1999**, *31*, 577-597.

3. Hill, B. G.; Dranka, B. P.; Bailey, S. M.; Lancaster, J. R., Jr.; Darley-Usmar, V. M. "What part of NO don't you understand? Some answers to the cardinal questions in nitric oxide biology." *J. Biol. Chem.* **2010**, *285*, 19699-19704.

4. Zhang, J.; Snyder, S. H. "Nitric oxide in the nervous system." *Ann. Rev. Pharmacol. Toxicol.* **1995**, *35*, 213-233.

5. Fang, F. C. "Antimicrobial reactive oxygen and nitrogen species: Concepts and controversies." *Nat. Rev. Microbiol.* **2004**, *2*, 820-832.

6. Ghaffari, A.; Miller, C. C.; McMullin, B.; Ghahary, A. "Potential application of gaseous nitric oxide as a topical antimicrobial agent." *Nitric Oxide* **2006**, *14*, 21-29.

7. Hrabie, J. A.; Keefer, L. K. "Chemistry of the nitric oxide-releasing diazeniumdiolate ("nitrosohydroxylamine") functional group and its oxygen-substituted derivatives." *Chem. Rev.* **2002**, *102*, 1135-1154.

8. Miller, M. R.; Megson, I. L. "Recent developments in nitric oxide donor drugs." *Brit. J. Pharmacol.* **2007**, *151*, 305-321.

9. Seabra, A. B.; Duran, N. "Nitric oxide-releasing vehicles for biomedical applications." *J. Mater. Chem.* **2010**, *20*, 1624-1637.

10. Wang, P. G.; Cai, T. B.; Taniguchi, N. *Nitric oxide donors: For pharmaceutical and biological applications*. Wiley-VCH: Weinheim, Germany, 2005.

11. Wang, P. G.; Xian, M.; Tang, X.; Wu, X.; Wen, Z.; Cai, T.; Janczuk, A. J. "Nitric oxide donors: Chemical activities and biological applications." *Chem. Rev.* **2002**, *102*, 1091-1134.

12. Scatena, R.; Bottoni, P.; Pontoglio, A.; Giardina, B. "Pharmacological modulation of nitric oxide release: New pharmacological perspectives, potential benefits and risks." *Curr. Med. Chem.* **2010**, *17*, 61-73.

13. Hetrick, E. M.; Shin, J. H.; Stasko, N. A.; Johnson, C. B.; Wespe, D. A.; Holmuhamedov, E.; Schoenfisch, M. H. "Bactericidal efficacy of nitric oxide-releasing silica nanoparticles." *ACS Nano* **2008**, *2*, 235-246.

14. Shin, J. H.; Metzger, S. K.; Schoenfisch, M. H. "Synthesis of nitric oxide-releasing silica nanoparticles." *J. Am. Chem. Soc.* **2007**, *129*, 4612-4619.

15. Shin, J. H.; Schoenfisch, M. H. "Inorganic/organic hybrid silica nanoparticles as a nitric oxide delivery scaffold." *Chem*. *Mater*. **2008**, *20*, 239-249.

16. Naizi, J. H.; Gu, M. B. *Toxicity of metallic nanoparticles in microorganisms- a review*. Springer: New York, 2009.

17. Morones, J. R.; Elechiguerra, J. L.; Camacho, A.; Holt, K.; Kouri, J. B.; Ramirez, J. T.; Yacaman, M. J. "The bactericidal effect of silver nanoparticles." *Nanotechnology* **2005**, *16*, 2346-2353.

18. Kim, J. S.; Kuk, E.; Yu, K. N.; Kim, J. H.; Park, S. J.; Lee, H. J.; Kim, S. H.; Park, Y. K.; Park, Y. H.; Hwang, C. Y.; Kim, Y. K.; Lee, Y. S.; Jeong, D. H.; Cho, M. H. "Antimicrobial effects of silver nanoparticles." *Nanomedicine* **2007**, *3*, 95-101.

19. Chen, X.; Schluesener, H. J. "Nanosilver: A nanoproduct in medical application." *Toxicol*. *Lett*. **2008**, *176*, 1-12.

20. Feng, Q. L.; Wu, J.; Chen, G. Q.; Cui, F. Z.; Kim, T. N.; Kim, J. O. "A mechanistic study of the antibacterial effect of silver ions on *Escherichia coli* and S*taphylococcus aureus*." *J*. *Biomed*. *Mater*. *Res*. **2000**, *52*, 662-668.

21. Anyaogu, K. C.; Fedorov, A. V.; Neckers, D. C. "Synthesis, characterization, and antifouling potential of functionalized copper nanoparticles." *Langmuir* **2008**, *24*, 4340-4346.

22. Esteban-Cubillo, A.; Pecharroman, C.; Aguilar, E.; Santaren, J.; Moya, J. S. "Antibacterial activity of copper monodispersed nanoparticles into sepiolite." *J*. *Mater*. *Sci*. **2006**, *41*, 5208-5212.

23. Mary, G.; Bajpai, S. K.; Chand, N. "Copper (II) ions and copper nanoparticles-loaded chemically modified cotton cellulose fibers with fair antibacterial properties." *J*. *Appl*. *Polym*. *Sci*. **2009**, *113*, 757-766.

24. Adams, L. K.; Lyon, D. Y.; Alvarez, P. J. J. "Comparative eco-toxicity of nanoscale TiO_2, SiO_2, and ZnO water suspensions." *Water Res*. **2006**, *40*, 3527-3532.

25. Liu, Y.; He, L.; Mustapha, A.; Li, H.; Hu, Z. Q.; Lin, M. "Antibacterial activities of zinc oxide nanoparticles against *Escherichia coli* O157:H7." *J*. *Appl*. *Microbiol*. **2009**, *107*, 1193-1201.

26. Rekha, K.; Nirmala, M.; Nair, M. G.; Anukaliani, A. "Structural, optical, photocatalytic and antibacterial activity of zinc oxide and manganese doped zinc oxide nanoparticles." *Physica B* **2010**, *405*, 3180-3185.

27. Zhang, L. L.; Jiang, Y. H.; Ding, Y. L.; Povey, M.; York, D. "Investigation into the antibacterial behaviour of suspensions of ZnO nanoparticles (ZnO nanofluids)." *J*. *Nanopart*. *Res*. **2007**, *9*, 479-489.

28. Nair, S.; Sasidharan, A.; Rani, V. V. D.; Menon, D.; Nair, S.; Manzoor, K.; Raina, S. "Role of size scale of ZnO nanoparticles and microparticles on toxicity toward bacteria and osteoblast cancer cells." *J. Mater. Sci.: Mater. Med.* **2008**, *20*, 235-241.

29. Armelao, L.; Barreca, D.; Bottaro, G.; Gasparotto, A.; Maccato, C.; Maragno, C.; Tondello, E.; Stangar, U. L.; Bergant, M.; Mahne, D. "Photocatalytic and antibacterial activity of TiO_2 and Au/TiO_2 nanosystems." *Nanotechnology* **2007**, *18*, 375709-375716.

30. Brunet, L.; Lyon, D. Y.; Hotze, E. M.; Alvarez, P. J. J.; Wiesner, M. R. "Comparative photoactivity and antibacterial properties of C-60 fullerenes and titanium dioxide nanoparticles." *Environ. Sci. Technol.* **2009**, *43*, 4355-4360.

31. Choi, O.; Hu, Z. Q. "Size dependent and reactive oxygen species related nanosilver toxicity to nitrifying bacteria." *Environ. Sci. Technol.* **2008**, *42*, 4583-4588.

32. Martinez-Castanon, G. A.; Nino-Martinez, N.; Martinez-Gutierrez, F.; Martinez-Mendoza, J. R.; Ruiz, F. "Synthesis and antibacterial activity of silver nanoparticles with different sizes." *J. Nanopart. Res.* **2008**, *10*, 1343-1348.

33. Lok, C. N.; Ho, C. M.; Chen, R.; He, Q. Y.; Yu, W. Y.; Sun, H.; Tam, P. K. H.; Chiu, J. F.; Che, C. M. "Silver nanoparticles: Partial oxidation and antibacterial activities." *J. Biol. Inorg. Chem.* **2007**, *12*, 527-534.

34. Jin, Y.; Lohstreter, S.; Pierce, D. T.; Parisien, J.; Wu, M.; Hall, C.; Zhao, J. X. "Silica nanoparticles with continuously tunable sizes: Synthesis and size effects on cellular contrast imaging." *Chem. Mater.* **2008**, *20*, 4411-4419.

35. Yang, Y.; Jing, L.; Yu, X.; Yan, D.; Gao, M. "Coating aqueous quantum dots with silica via reverse microemulsion method: Toward size-controllable and robust fluorescent nanoparticles." *Chem. Mater.* **2007**, *19*, 4123-4128.

36. Bagwe, R. P.; Hilliard, L. R.; Tan, W. "Surface modification of silica nanoparticles to reduce aggregation and nonspecific binding." *Langmuir* **2006**, *22*, 4357-4362.

37. Zhang, H.; Annich, G. M.; Miskulin, J.; Stankiewicz, K.; Osterholzer, K.; Merz, S. I.; Bartlett, R. H.; Meyerhoff, M. E. "Nitric oxide-releasing fumed silica particles: Synthesis, characterization, and biomedical application." *J. Am. Chem. Soc.* **2003**, *125*, 5015-5024.

38. Hetrick, E. M.; Schoenfisch, M. H. "Analytical chemistry of nitric oxide." *Annu. Rev. Anal. Chem.* **2009**, *2*, 409-433.

39. Riccio, D. A.; Nugent, J. L.; Schoenfisch, M. H. "Stöber synthesis of nitric oxide-releasing *S*-nitrosothiol-modified silica particles." *Chem. Mater.* **2010**, *23*, 1727-1735.

40. Clogston, J. D., NCI method PCC-2: Measuring zeta potential of nanoparticles. Nanotechnology Characterization Laboratory, N. C. I., Ed. Frederick, MD, 2009.

41. Breed, R. S.; Dotterrer, W. D. "The number of colonies allowable on satisfactory agar plates." *J*. *Bacteriol*. **1916**, *1*, 321-331.

42. Santra, S.; Yang, H.; Dutta, D.; Stanley, J. T.; Holloway, P. H.; Tan, W.; Moudgil, B. M.; Mericle, R. A. "TAT conjugated, FITC doped silica nanoparticles for bioimaging applications." *Chem*. *Comm*. **2004**, *24*, 2810-2811.

43. Bagwe, R. P.; Yang, C.; Hilliard, L. R.; Tan, W. "Optimization of dye-doped silica nanoparticles prepared using a reverse microemulsion method." *Langmuir* **2004**, *20*, 8336-8342.

44. Arriagada, F. J.; Osseo-Asare, K. "Synthesis of nanosize silica in a nonionic water-in-oil microemulsion: Effects of the water/surfactant molar ratio and ammonia concentrations." *J*. *Colloid Interface Sci*. **1999**, *211*, 210-220.

45. Chang, C.; Fogler, H. "Controlled formation of silica particles from tetraethyl orthosilicate in nonionic water-in-oil microemulsions." *Langmuir* **1997**, *13*, 3295-3307.

46. Stjerndahl, M.; Andersson, M.; Hall, H. E.; Pajerowski, D. M.; Meisel, M. W.; Duran, R. S. "Superparamagnetic Fe_3O_4/SiO_2 nanocomposites: Enabling the tuning of both the iron oxide load and the size of the nanoparticles." *Langmuir* **2008**, *24*, 3532-3536.

47. Han, Y.; Jiang, J.; Lee, S. S.; Ying, J. Y. "Reverse microemulsion-mediated synthesis of silica-coated gold and silver nanoparticles." *Langmuir* **2008**, *24*, 5842-5848.

48. Yi, D. K.; Selvan, S. T.; Lee, S. S.; Papaefthymiou, G. C.; Kundaliya, D.; Ying, J. Y. "Silica-coated nanocomposites of magnetic nanoparticles and quantum dots." *J*. *Am*. *Chem*. *Soc*. **2005**, *127*, 4990-4991.

49. Naka, Y.; Komori, Y.; Yoshitake, H. "One-pot synthesis of organo-functionalized monodisperse silica particles in w/o microemulsion and the effect of functional groups on addition in polystyrene." *Colloids Surf., A* **2010**, *361*, 162-168.

50. Brinker, C. J.; Scherer, G. W. *Sol-gel science: The physics and chemistry of sol-gel processing*. Academic Press: San Diego, 1990.

51. Langevin, D. "Micelles and microemulsions." *Annu*. *Rev*. *Phys*. *Chem*. **1992**, *43*, 341-369.

52. Murdock, R. C.; Braydich-Stolle, L.; Schrand, A. M.; Schlager, J. J.; Hussain, S. M. "Characterization of nanomaterial dispersion in solution prior to in vitro exposure using dynamic light scattering technique." *Toxicol*. *Sci*. **2008**, *101*, 239-253.

53. Blosi, M.; Albonetti, S.; Dondi, M.; Martelli, C.; Baldi, G. "Microwave-assisted polyol synthesis of Cu nanoparticles." *J*. *Nanopart*. *Res*. **2010**, *13*, 127-138.

54. Albert, K.; Bayer, E. "Characterization of bonded phases by solid-state NMR spectroscopy." *J*. *Chromatogr*. **1991**, *544*, 345-370.

55. Hennel, J. W.; Klinowski, J. "Magic-angle spinning: A historical perspective." *Top*. *Curr*. *Chem*. **2004**, *246*, 1-14.

56. Deupree, S. M.; Schoenfisch, M. H. "Morphological analysis of the antimicrobial action of nitric oxide on gram-negative pathogens using atomic force microscopy." *Acta Biomater*. **2009**, *5*, 1405-1415.

57. Barbe, C.; Bartlett, J.; Linggen, K.; Finnie, K.; Qiang, L. H.; Larkin, M.; Calleja, S.; Bush, A.; Calleja, G. "Silica particles: A novel drug-delivery system." *Adv*. *Mat*. **2004**, *16*, 1959-1966.

58. Thelestam, M.; Mollby, R. "Cultured human-fibroblasts as a model for evaluation of potential in vivo toxicity of membrane damaging antibiotics." *Chem*. *Biol*. *Interact*. **1980**, *29*, 315-325.

59. Lineaweaver, W.; McMorris, S.; Soucy, D.; Howard, R. "Cellular and bacterial toxicities of topical antimicrobials." *Plastic Reconstruct*. *Surg*. **1985**, *75*, 394-396.

Chapter 3:

Surface Modification of Nitric Oxide-Releasing Silica Nanoparticles

3.1 Introduction

Nitric oxide (NO) is produced endogenously as a regulator of numerous physiological processes including angiogenesis, wound healing, vasodilation, and the immune response.[1] As such, much research has been devoted to designing methods for delivering exogenous NO in a manner that mimics its biological generation in order to treat medical conditions such as hypertension, ischemia/reperfusion injury, thrombosis, restenosis, and cancer.[2] The major factor inhibiting the clinical success of NO-based therapeutics stems from the gaseous and reactive nature of NO that make it difficult to control its delivery both in terms of release kinetics and location.

Improved control over NO delivery can be achieved by incorporating NO donors, such as *N*-diazeniumdiolates and *S*-nitrosothiols, into macromolecular scaffolds to achieve biologically relevant NO release activity.[3] For example, Zhou et al. designed polymers doped with *S*-nitrosothiol-modified silica particles to achieve NO fluxes that mimicked NO generation by endothelial cells (i.e., $1–4x10^{-10}$ mol cm^{-2} s^{-1}).[4] The advantage of *N*-diazeniumdiolate (NONOate)-based materials over other NO donor moieties (e.g., *S*-nitrosothiols) is their ability to store two molecules of NO per amine site with subsequent controlled release under physiological conditions without the need for an external trigger. Unfortunately, the labile nature of the NONOate functionality in aqueous media often results in materials with relatively short NO release durations (i.e., less than 24 h). While fast

release of large NO payloads (i.e., micromolar) are sufficient for some applications, such as eradicating tumor or bacteria cells, the release of lower levels of NO (i.e., picomolar) for extended periods are required for other therapies (e.g., wound healing and treatment of cardiovascular dysfunctions).[1] Methods for extending the NO release duration of *N*-diazeniumdiolate-based macromolecules are thus needed to broaden their therapeutic impact.

Due to the proton-initiated decomposition of *N*-diazeniumdiolate NO donors, the chemical environment surrounding the NONOate governs NO release kinetics.[5] The zwitterionic NONOate can be stabilized directly through hydrogen bonding. For example, silica nanoparticles composed of the diamine *N*-(6-aminohexyl)aminopropyl-trimethoxysilane (AHAP) exhibit slower release kinetics compared to particles composed of the monoamine *N*-methylaminopropyltrimethoxysilane (MAP) as the primary amine of AHAP can stabilize through hydrogen bonding.[6] Another strategy for prolonging NONOate lifetimes is to increase the hydrophobicity of the environment surrounding the NO donor, thus slowing water diffusion and protonation of the *N*-diazeniumdiolate-bearing amine. Koh et al. doped *N*-diazeniumdiolate-based silica particles into polyurethanes of increasing hydrophobicity to achieve materials with prolonged NO release.[7] Electrospun polyurethane fibers capable of NO release are particularly attractive for applications such as wound healing and implant coatings due to their porous nature.[8] Unfortunately, silica particles can leach from the fibers in physiological conditions (i.e., pH 7.4, 37 °C), preventing their development as implant coatings.

Based on the proton-initiated decomposition of *N*-diazeniumdiolates to release NO, we hypothesize that NO release durations from silica nanoparticles will be extended by modifying the particle surface with hydrophobic groups. Increasing the surface

hydrophobicity of the NO-releasing particles may further improve their stability in hydrophobic polymers. In this Chapter, the surface hydrophobicity of NO-releasing silica particles was varied by grafting ethyl-, isobutyl-, octadecyl-, or heptadecafluorotrimethoxysilane onto the surface of particles synthesized by co-condensing AHAP with tetramethoxysilane (TMOS). The influence of modifying the surface hydrophobicity on NO payloads and release kinetics was then evaluated, along with studies doping the hydrophobic particles into electrospun polymer fibers. Specifically, NO release and dopant stability were evaluated as a function of surface modification and polymer type.

3.2 Materials and Methods

N-(6-aminohexyl)aminopropyltrimethoxysilane (AHAP), ethyltrimethoxysilane, isobutyl-trimethoxysilane, octadecyltrimethoxysilane, (heptadecafluoro-1,1,2,2-tetrahydrodecyl)-trimethoxysilane, and tetramethoxysilane (TMOS) were purchased from Gelest, Inc. (Morrisville, PA). Ethanol, aqueous ammonium hydroxide solution (28 wt%), anhydrous toluene, anhydrous *N*,*N*-dimethylformamide, anhydrous tetrahydrofuran, anhydrous methanol, sodium methoxide (5.4 M solution in methanol), and potassium *tert*-butoxide (20 wt% in tetrahydrofuran) were purchased from Fisher Scientific (Fair Lawn, NJ). Sodium trimethylsilanolate was purchased from Sigma Aldrich (St. Louis, MO). Nitrogen (N_2), argon (Ar), and nitric oxide calibration (26.81 PPM, balance N_2) gases were purchased from National Welders (Raleigh, NC). Pure nitric oxide gas (99.5%) used for *N*-diazeniumdiolate formation was purchased from Praxair (Sanford, NC). Distilled water was purified using a Millipore Milli-Q UV Gradient A-10 system (Bedford, MA), resulting in a total organic content of ≤6 ppb and a final resistivity of 18.2 mΩ·cm.

3.2.1 Stöber synthesis of amine-containing silica nanoparticles

Hybrid inorganic/organic silica nanoparticles were synthesized via a modified Stöber method. Briefly, AHAP (1.173 mL) and TMOS (0.708 mL) were premixed and added to a mixture of ethanol (59.16 mL), water (27.84 mL), and 28 wt% ammonium hydroxide (9.8 mL). The reaction was stirred at room temperature for 2 h. The resulting white particle precipitates were collected by centrifugation (3645*g*, 10 min, 4 °C) and washed thrice with ethanol to remove unreacted reagents. The particles were then dried in vacuo and stored in a sealed container until further use.

3.2.2 Grafting of organosilanes onto the surface of silica nanoparticles

A suspension of AHAP silica particles (50 mg) in 10 mL toluene was prepared via sonication. Pyridine (100 μL) and an organosilane (200 μL) were added, and the reaction was refluxed overnight. An excess of organosilanes was used as the silanes were found to condense with silanols on the glassware. The surface-modified silica particles were collected by centrifugation (3645×*g*, 10 min, 4 °C), washed twice with toluene, then twice with ethanol. The particles were then dried in vacuo and stored in a sealed container until further use.

3.2.3 N-diazeniumdiolate-modification of AHAP and surface-modified AHAP silica nanoparticles

Each particle composition was suspended in *N*,*N*-dimethylformamide or methanol via sonication at a concentration of 5 mg/mL. Sodium methoxide, potassium tertbutoxide (5 wt% in THF), or sodium trimethylsilanolate was then added in a 1:3 mol ratio of secondary amine to base. The mixtures were vortexed, aliquoted into 4 mL glass vials, placed in a 160 mL

Parr general purpose pressure vessel, and connected to an in-house NO reactor. The solutions were stirred magnetically with removal of oxygen by purging with Ar. The vessel was then filled to a pressure of 10 bar with NO that had previously been scrubbed with KOH. After 72 h, the NO was released from the vessel, and the solutions were again purged with Ar to remove unreacted NO. The resulting *N*-diazeniumdiolate-modified silica nanoparticles were collected by centrifugation (3645*g*, 10 min, 4 °C), washed thrice with ethanol, and dried in vacuo overnight. Particles were stored at -20 °C in a vacuum sealed container until use.

3.2.4 Particle-doped electrospun polymer fibers

Electrospun fibers were prepared using a custom electrospinning apparatus previously described.[9] Briefly, a Series 205B High Voltage Power Supply (Bertan Associates, Inc.) was used to apply a voltage of 6 kV to a stainless steel blunt-tip needle (22 gauge) on a syringe containing the particle/polymer suspensions. A grounded steel plate covered in aluminum foil was positioned perpendicular to the direction of flow, 15 cm from the needle tip. A syringe pump (Kent Scientific, Torrington, CT) was used to eject the particle-doped polymer solutions at a rate of 0.015 mL/min. The particle/polymer solutions were prepared by first dissolving 40 mg of polymer into 1.6 mL of a 3:1 (v/v) mixture of tetrahydrofuran and *N*,*N*-dimethylformamide, then adding 0.4 mL of a 40 mg/mL particle suspension in methanol.

3.2.5 Materials characterization

Particle morphology and size were evaluated using a Hitachi S-4700 Scanning Electron Microscope (Pleasanton, CA). Solid-state nuclear magnetic resonance (SS NMR) experiments were performed on an 11.7 T (500 MHz) spectrometer. A 3.2 mm HCN Balun

probe was used for ^{13}C detection with samples spun at the magic angle with a rate of 12 kHz. For ^{19}F detection, a 1.6 mm HFXY FastMAS probe was utilized with samples spun at the magic angle with a rate of 25 kHz. The direct polarization (DP) technique was applied for both ^{13}C and ^{19}F detection, and a solid state echo was incorporated to reduce background signal. X-ray photoelectron spectroscopy (XPS) was performed on a Kratos Axis Ultra DLD X-ray Photoelectron Spectrometer with a monochromatic Al Kα X-ray source (150 W). Electrons were collected at an angle of 90 degrees from the sample surface from a 300 x 700 μm area on the sample with pass energy set to 20 eV for high resolution spectra. All spectra were obtained with a step size of 0.1 eV and calibrated to the C 1s peak at 284.6 eV.

Particle-doped polymer fibers were visualized with an FEI Quanta 200 field emission gun environmental scanning electron microscope (ESEM) without additional coating. Stability of the particles within the polymer fibers was investigated by submerging the particle-doped fibers (10–40 mg) in 15 mL of phosphate buffered saline (PBS, pH 7.4) for 7 d and performing silicon elemental analysis on the soak solutions using a Teledyne Leeman Inductively Coupled Plasma-Optical Emission Spectrometer (ICP-OES). Metal wire was used to ensure the hydrophobic fiber mats remained submerged in the soak solution. Analysis was performed in the axial configuration at 251.611 nm calibrated with 0.01–50 ppm silica particle standard solutions of the corresponding particle system in PBS.

Real-time nitric oxide release was measured using a Sievers NOA 280i Chemiluminescence NO Analyzer (Boulder, CO) connected to a customized reaction vessel. Briefly, NO-releasing materials (i.e., particles or particle-doped fibers) were submerged in deoxygenated PBS (pH 7.4) at 37 °C with NO carried to the analyzer by passing N_2 through the solution at a constant rate of 70 mL/min. The analyzer was calibrated with air passed

through a NO zero filter (0 ppm NO) and a 26.39 ppm NO standard gas (balance N_2).

3.3 Results and Discussion

3.3.1 Surface modification of amine-containing silica nanoparticles

The hydrolysis and co-condensation of an organosilane and a tetraalkoxysilane under dilute, basic conditions produces spherical inorganic/organic hybrid silica particles.[10] On the surface of the resulting particles are both nonhydrolyzable organic groups and hydrolyzable silanol groups. Thus, additional silanes can be added through condensation with the surface silanols, in essence adding a third organic component for preparing hybrid silica nanoparticles (Scheme 3.1). Using such surface grafting methods, organosilanes of varying hydrophobicity were coupled to the surface of amine-containing silica particles (Figure 3.1). As shown in Figure 3.2, the surface grafting method did not result in a change in particle size or morphology.

The number of silanes grafted to the particle surface depends on both the particle and the ligand. For example, increasing the surface area of the particle allows for a greater number of surface silanols to facilitate ligand attachement. Neue described a relationship between surface area and silanol coverage (χ) in terms of $\mu mol/m^2$ according to Eq 3.1[11]

$$\chi = \frac{\%C}{100 \cdot n\mathrm{C} \cdot SA \cdot \left(1 - \frac{\%C}{100} \cdot \frac{MW - 1}{nC \cdot 12}\right)} \qquad \text{(Equation 3.1)}$$

where *%C* is carbon weight percent of modified particles as determined from elemental analysis, *nC* is the number of carbon atoms on the ligand, and *MW* is the molecular weight of the attached ligand. As the molecular weight of the ligand increases, the number of ligands that can be added to the particle should decrease due to steric hinderance. Theoretically, the

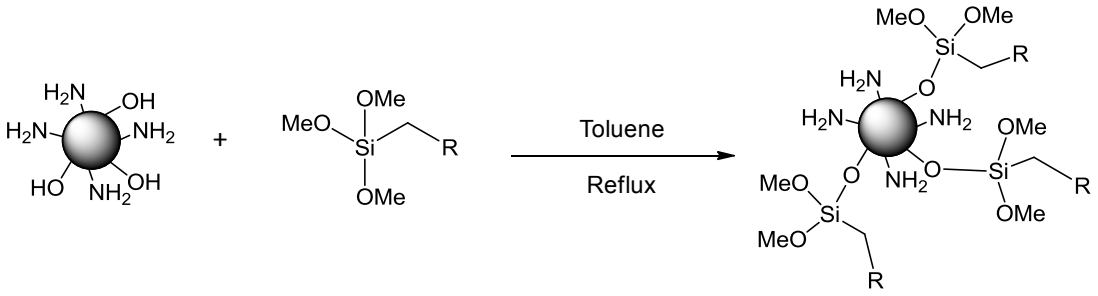

Scheme 3.1 Organosilanes are grafted onto the surface of hybrid silica nanoparticles through a condensation reaction between surface silanols on the particle and methoxides on the organosilane.

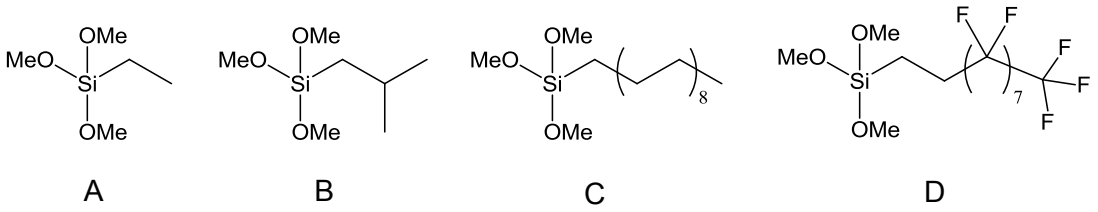

Figure 3.1 Structures of silanes of increasing hydrophobic character: (A) ethyltrimethoxysilane, (B) isobutyltrimethoxysilane, (C) octadecyltrimethoxysilane, and (D) (heptadecafluoro-1,1,2,2-tetrahydrodecyl)trimethoxysilane.

greatest χ achievable is ~4 μmol/m^2 when grafting a monofunctional amine onto TEOS particles in ideal conditions (i.e., anhydrous and singly hydrolyzable silane).[11] This number is decreased for hybrid silica particles as the number of surface silanols is reduced compared to particles synthesized from a tetraalkoxysilane alone. The %C as determined by CHN elemental analysis of unmodified AHAP, ethyl-AHAP, isobutyl-AHAP, octadecyl-AHAP, and heptadecafluoro-AHAP was 15.69, 15.14, 15.42, 15.66, and 15.35%, respectively. The lack of significant changes in the %C following surface grafting appears to be the result of the larger carbon content of AHAP prior to surface modification. Since the addition of organic groups to the particle surface did not significantly change their carbon content per mass, Eq 3.1 could not be used to calculate surface coverage for our particles.

Solid-state nuclear magnetic resonance (SS NMR) spectroscopy with direct polarization and magic angle spinning (DP/MAS) was used to confirm the presence of surface-bound ligands. Previous reports have shown that organosilanes bound to the surface of silica nanoparticles can be observed using SS NMR.[12] As shown in Figure 3.3A, the peaks obtained from SS ^{13}C NMR of unmodified AHAP were broad and difficult to evaluate quantitatively. In general, the peaks obtained from SS NMR are broader than those obtained from liquid samples due to the decreased mobility of ligands attached to a solid compared to those freely moving in solution.[13] The rigid structure of the nonporous particles that result from the Stöber synthesis further limits the mobility of the ligands, resulting in the broad peaks shown in Figure 3.3. The chemical shifts of carbon-bound carbons in AHAP were between 20–35 ppm, and silicon-bound carbons appeared at 12 ppm. Carbons bound to the secondary amine appeared at 51 ppm, and carbons bound to the primary amine at 42 ppm. Unfortunately, the chemical shifts of the alkyl surface groups overlapped with those of

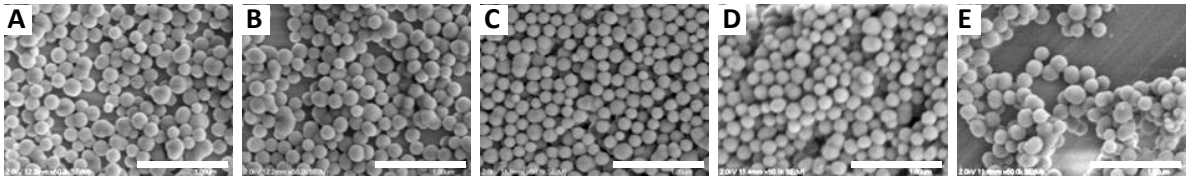

Figure 3.2 Scanning electron micrographs of (A) unmodified AHAP (d=148±23 nm), (B) ethyl-AHAP (d=146±22 nm), (C) butyl-AHAP (d=144±18 nm), (D) octadecyl-AHAP (d=152±17 nm), and (E) heptadecafluoro-AHAP (d=152±22 nm). Scale bar = 1 μm.

AHAP carbons, which were broader and of a larger intensity (Figure 3.3B–F). Thus, no quantitative information could be gleaned from the DP/MAS experiments. Of note, the presence of the surface groups was indicated by a decrease in the intensity of the AHAP peak at 21 ppm and broadening of the shoulder peak at 24 ppm. Furthermore, the fluorine-bound carbons were apparent in the SS ^{13}C NMR spectrum of heptadecafluoro-AHAP at 110 ppm. Solid-state ^{19}F NMR of the heptadecafluoro-AHAP confirmed the addition of the fluorinated ligand (Figure 3.4). The peaks in the ^{19}F NMR were more narrow than those in the ^{13}C spectra because the fluorinated ligands are only on the particle surface and therefore have greater mobility. Fluorines attached at the terminal carbons were confirmed by the presence of peaks at -85 and -86.9 ppm, with fluorines at the C2 position appearing at -130 ppm and fluorines at the C3-C8 positions appearing at -125 ppm.

X-ray photoelectron spectroscopy (XPS) was employed to more conclusively confirm the presence of the alkylsilanes (i.e., ethyl, butyl, and octadecyl) on the particle surface. Although XPS is traditionally used to observe chemical environments on flat surfaces, this technique has more recently been used investigate the surface modifications of silica particles.[14] In addition to identifying the types of elements present in a sample, XPS analysis can also provide semi-quantitative data regarding the relative amounts of chemical species present on or near the surface.[15] Table 3.1 lists the atomic concentrations obtained from XPS analysis of unmodified and surface-modified AHAP. To more directly evaluate the addition of surface-bound ligands, the number of carbons was normalized to nitrogens, as the nitrogen concentration should not change with surface modification. As expected, the C/N ratio was greater for all surface-modified particles compared to that of the unmodified AHAP. The addition of ethyl- or isobutyltrimethoxysilane resulted in an increase in C/N from 5.91

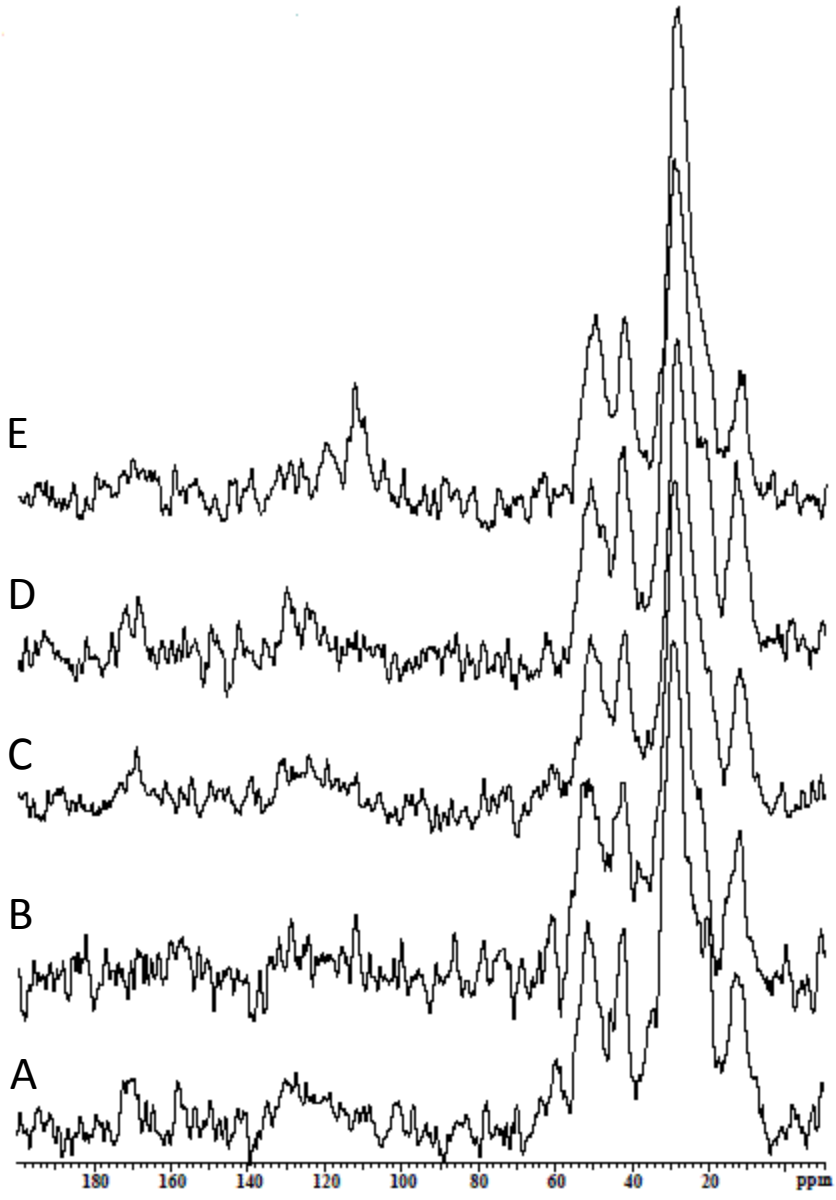

Figure 3.3 Solid state direct polarization-magic angle spinning (DP-MAS) ^{13}C NMR spectrum of (A) unmodified AHAP and (B) ethyl-, (C) butyl-, (D) octadecyl-, and (E) heptadecafluoro-AHAP silica nanoparticles.

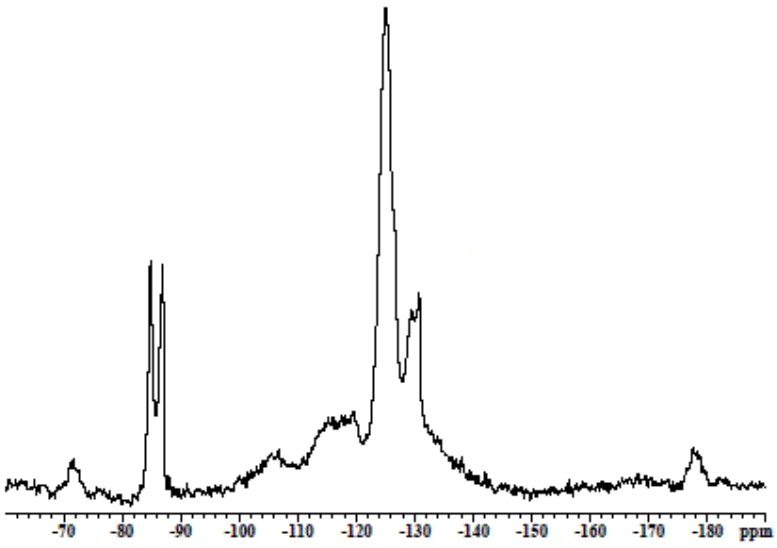

Figure 3.4 Solid state direct polarization-magic angle spinning (DP/MAS) ^{19}F NMR spectrum of heptadecafluoro-AHAP silica nanoparticles.

(AHAP) to 7.29 and 9.30, respectively. The C/N ratio of the octadecyl-AHAP was slightly less than that of the isobutyl-AHAP, indicating that a fewer number of octadecyltrimethoxysilanes were condensed onto the particle surface, as predicted by Eq. 3.1 for ligands of larger *MW*. The heptadecafluoro-AHAP were characterized by the greatest C/N ratio (12.02), even though this ligand is also characterized by a large *MW*. Thus, sterics alone are not the only ligand-dependent factor governing surface coverage. The increased C/N of heptadecafluoro-AHAP suggests that solubility may also influence the extent of condensation onto the particle surface. As fluorocarbons have a lower solubility in toluene compared to hydrocarbons,[16] it may be more favorable for the fluorocarbon-based silane to condense on the particle surface than remain in solution.

Dynamic light scattering (DLS) was used to evaluate the extent to which the hydrophobicity of the particles was affected by surface modification. Traditionally, DLS is used to determine the hydrodynamic radius of particles by focusing a laser on a sample of particles in solution and detecting the scattered light;[17] however, information regarding how particles behave in solution can also be elucidated from DLS analysis.[18] For example, the extent to which particles aggregate or sediment in solution may be characterized using the sample count rate, a parameter extracted from the number of photons detected per second.[17] A decrease in count rate would result from particle sedimentation as fewer particles would be suspended in solution and scatter light. Suspensions of unmodified and surface-modified AHAP were prepared at equal concentrations (0.5 mg/mL) in PBS to assess the impact of hydrophobicity on particle behavior. The count rate of unmodified AHAP remained constant throughout the experiment, indicating the particles formed a stable suspension in PBS. The addition of hydrophobic ligands to the surface of AHAP decreased the derived count rate,

Table 3.1 Atomic concentrations (%) and C/N ratios of unmodified AHAP and surface-modified AHAP silica nanoparticles as determined with X-ray photoelectron spectroscopy (XPS).

	Atomic Concentrations					C/N
	C 1s	N 1s	O 1s	Si 2p	F 1s	
AHAP	41.74	7.06	34.10	16.50	-	5.91
Ethyl-AHAP	42.64	5.85	32.6	16.26	-	7.29
Isobutyl-AHAP	43.23	4.65	24.14	11.35	-	9.30
Octadecyl-AHAP	46.62	5.85	29.39	16.32	-	8.12
Heptadecafluoro-AHAP	34.39	2.86	16.82	10.28	34.65	12.02

indicating such particles were less stable in aqueous media (i.e., PBS) compared to control (unmodified) AHAP particles (Figure 3.5). As expected, the relative hydrophobicity of the particles increased in relation to the hydrophobicity of the surface-grafted ligand as determined by decreasing count rates.

3.3.2 N-diazeniumdiolate modification

A number of solvents and bases were evaluated to determine the solution conditions that would allow for the greatest amine to NONOate conversion efficiency for the surface-modified AHAP particles. A stability test was initially conducted to select an appropriate solvent for *N*-diazeniumdiolate formation. Each particle system was suspended via sonication in hexane, tetrahydrofuran, *N*,*N*-dimethylformamide, or methanol (5 mg/mL) and allowed to sit undisturbed for 30 min. All particle systems were found to be most stable (i.e., remain suspended) in methanol (MeOH) or *N*,*N*-dimethylformamide (DMF), thus these two solvents were selected for *N*-diazeniumdiolate formation testing. To facilitate NONOate formation, a strong organic base is added to deprotonate the secondary amine and improve its nucleophilic character.[19] The three bases tested were sodium methoxide, potassium *tert*-butoxide, and sodium trimethylsilanolate. Each particle system was suspended in either MeOH or DMF at a concentration of 5 mg/mL with a 3.5:1 equivalent of base to secondary amine. Overall, the NO loading was lower when MeOH was used as the solvent compared to DMF (Table 3.2). The Hildebrand solubility parameter of DMF is closer to those of alkanes and fluorocarbons than MeOH,[20] suggesting increased swelling may occur in DMF and allow greater diffusion of base and NO into the silica network. Sodium methoxide facilitated the greatest conversion efficiency in DMF.

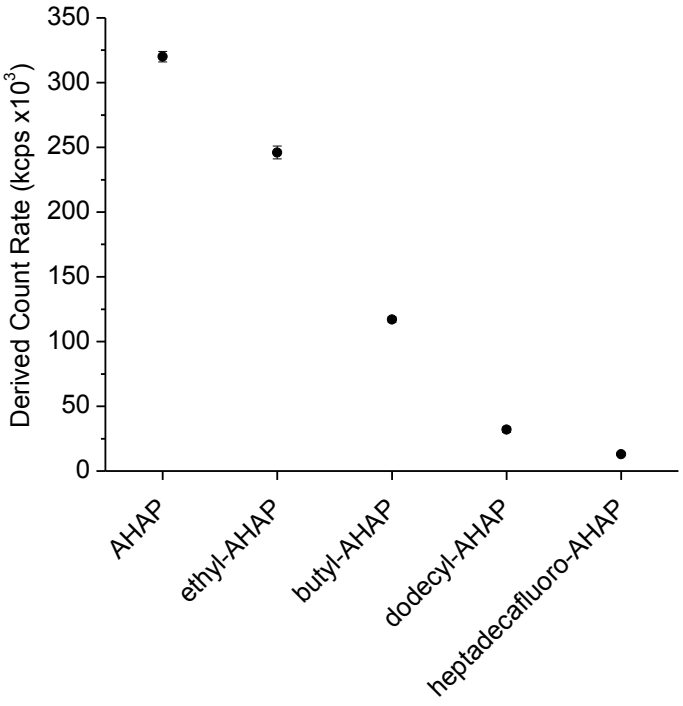

Figure 3.5 Derived count rate from dynamic light scattering analysis of unmodified and surface-modified AHAP particles (0.5 mg/mL) in phosphate buffered saline.

Table 3.2 Amine to *N*-diazeniumdiolate conversion efficiency of surface-modified AHAP particles using sodium methoxide in either a 1:9 mixture of MeOH in DMF or pure MeOH.

	$\%E_{conv}$	
	1:9 MeOH/DMF	MeOH
Ethyl-AHAP/NO	5.6%	1.3%
Butyl-AHAP/NO	5.4%	1.5%
Octadecyl-AHAP/NO	3.0%	0.6%
Heptadecafluoro-AHAP/NO	2.9%	0.1%

The NO release properties of unmodified AHAP/NO and surface-modified AHAP/NO are provided in Table 3.3. Each system reached a maximum instantaneous NO concentration ($[NO]_{max}$) within the first few minutes upon solution immersion, as is characteristic of *N*-diazeniumdiolate NO donors. This maximum NO level results from the initial, fast diffusion of water into the scaffold. As would be expected, the addition of hydrophobic surface ligands decreases the observed $[NO]_{max}$. Effects of surface ligand on the NO release kinetics were also evident in the NO release half-life ($t_{1/2}$) data. As expected, the addition of the hydrophobic surface groups increased $t_{1/2}$ as the diffusion of water into the silica scaffold slowed, and the average lifetime of the NONOate functionalities was prolonged. For example, increasing the alkyl chain length of the surface ligand from ethyl to butyl and octadecyl caused an increase in $t_{1/2}$ from 0.3 to 0.5 and 1.1 h, respectively. Heptadecafluoro-AHAP exhibited the longest $t_{1/2}$ of 2.7 h due to the extremely hydrophobic properties of fluorocarbons.

While the addition of hydrophobic groups to the particle surface allowed for tunable NO release kinetics, the NO payloads exhibited by the surface-modified AHAP/NO were lower than that of unmodified AHAP. Decreased diffusion of the base into the silica network due to the increased surface hydrophobicity would result in decreased NO donor conversion efficiency. These results corroborate those previously observed by Shin et al., in which silica particles composed of more hydrophobic aminosilanes exhibited lower amine to *N*-diazeniumdiolate conversion efficiencies.[21] Moreover, the total NO payload delivered from heptadecafluoro-AHAP was nearly half that of the hydrocarbon-modified systems. The low conversion efficiency suggests the access of the solvated base to amines is even more limited for fluorocarbon-modified particles compared to hydrocarbon-modified particles. Increased

Table 3.3 Nitric oxide release characterization of unmodified AHAP/NO and surface-modified AHAP/NO silica nanoparticles, including maximum instantaneous NO concentration ($[NO]_{max}$), time required to reach $[NO]_{max}$ (t_{max}), total amount of NO released ($[NO]_T$), and the time required for the systems to release half of $[NO]_T$ ($t_{1/2}$).

	$[NO]_{max}$ ppb/mg	t_{max} min	$[NO]_T$ μmol/mg	$t_{1/2}$ h
AHAP/NO	1528±86	2.2±0.4	0.279±0.03	0.6±0.04
Ethyl-AHAP/NO	2861±800	1.2±0.1	0.110±0.004	0.3±0.1
Isobutyl-AHAP/NO	1624±318	1.4±0.1	0.106±0.02	0.5±0.1
Octadecyl-AHAP/NO	474±174	2.6±0.3	0.120±0.036	1.1±0.1
Heptadecafluoro-AHAP/NO	85±2	1.3±0.2	0.051±0.005	2.7±0.2

NO loading with tunable NO release kinetics might be achieved by first forming the NONOate moieties throughout the network, then modifying the particle surface.

3.3.3 Particle-doped electrospun fibers

Electrospun polymer fibers have been previously used as tissue engineering scaffolds, wound dressings, and implant coatings.[8] Imparting NO release to such porous materials may further enhance their utility due to the positive role of NO in mitigating the foreign body response and improving tissue integration.[22-24] Our laboratory has previously reported NO-releasing electrospun polymer fibers by incorporating small molecule and macromolecular NO donors into the fibers.[9, 25] While the use of silica particles allowed for a greater range of NO release payloads and kinetics compared to the small molecule NO donor, particle leaching was observed at levels up to 85% that incorporated within the fibers.[25] We hypothesized that increasing the surface hydrophobicity of the particle dopants may enhance their stability in the hydrophobic Tecoplast fibers.

The solvent and concentration of the polymer solution, as well as the particle concentration, needle diameter, feed rate, applied voltage, and collection distance used in these experiments were based on previously optimized experimental parameters.[9, 25] Scanning electron micrographs of the resulting particle-doped fibers are shown in Figure 3.6. Ethyl-AHAP/NO and butyl-AHAP/NO are more uniformly incorporated within the fibers compared to octadecyl-AHAP/NO and heptadecafluoro-AHAP/NO, which formed large aggregates within the fiber mats. The diameters of octadecyl-AHAP/NO- and heptadecafluoro-AHAP/NO-doped fibers were similar to that of the fibers doped with unmodified AHAP/NO, which were also not uniformly dispersed throughout the fibers. Conversely, the diameters of the ethyl-AHAP/NO- and butyl-AHAP/NO-doped fibers were

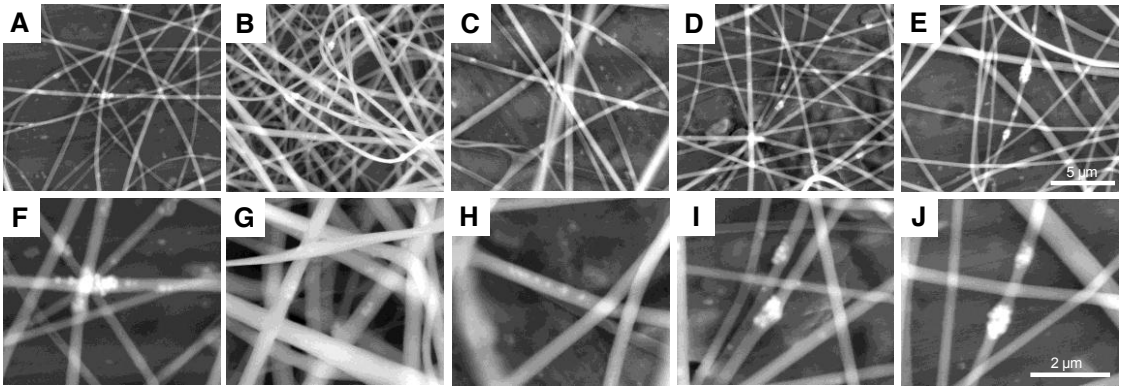

Figure 3.6 Scanning electron microscopy images of Tecoplast electrospun polymer fibers doped with 5 wt% (A,F) AHAP/NO (d=318±90 nm), (B,G) ethyl-AHAP/NO (d=353±185 nm), (C,H) butyl-AHAP/NO (d=427±141 nm), (D,I) octadecyl-AHAP/NO (d=299±101 nm), and (E,J) heptadecafluoro-AHAP/NO (d=309±176 nm) silica nanoparticles. Scale bars = 5 µm for A–E and 2 µm for F–J.

slightly larger, suggesting more uniform particle incorporation increases fiber diameter.

The stability of the NO-releasing particles within the Tecoplast electrospun fibers was evaluated by soaking the fibers in PBS at 37 °C and measuring silicon content in the soak solution with ICP-OES after 7 d. As shown in Table 3.4, unmodified AHAP/NO-doped fibers were characterized by 40% particle leaching, which was slightly less than the 59% leaching previously reported with 100 nm AHAP silica particles.[25] The decrease in particle leaching is likely the result of the larger particle diameters (d=150 nm), as increasing particle size is known to enhance the stability of particles within electrospun fibers.[25] Fibers doped with ethyl-AHAP/NO and butyl-AHAP/NO exhibited increased stability, as particle leaching decreased to 15% and 11%, respectively. The addition of the more hydrophobic octadecyl- and heptadecafluoro-trimethoxysilane ligands to the particle surface did not alter particle leaching from the fibers. In fact, heptadecafluoro-AHAP/NO were less stable than unmodified AHAP/NO as indicated by 55% particle leaching. These results corroborate the morphological data obtained by ESEM that indicated ethyl-AHAP/NO and butyl-AHAP/NO were better incorporated within the fibers compared to AHAP/NO, octadecyl-AHAP/NO, and heptafluoro-AHAP/NO.

Nitric oxide release from the particle-doped Tecoplast electrospun fibers was evaluated with chemiluminescent detection (Table 3.3). In general, increasing the hydrophobicity of the particle dopant resulted in lower NO fluxes and prolonged NO release durations. For example, Tecoplast fibers doped with heptadecafluoro-AHAP/NO exhibited the lowest $[NO]_{max}$ and longest t_d. The total NO released ($[NO]_T$) from the AHAP/NO-doped electrospun fibers was nearly double that of the surface-modified particle systems, as expected based on the higher NO payload of the unmodified AHAP/NO scaffolds. The

Table 3.4 Characterization of Tecoplast electrospun polymer fibers doped with unmodified and modified NO-releasing silica particles including nitric oxide release, and particle leaching.

Particle Dopant	$[NO]_T$ [b] (nmol/mg)	$[NO]_{max}$ [c] (pmol $mg^{-1}s^{-1}$)	t_d [d] (h)	Particle Leaching[e] (%)
AHAP/NO	13.8±3.1	4.2±1.1	12.9±1.1	40.4±0.3
Ethyl-AHAP/NO	2.6±0.5	2.7±0.2	10.1±4.1	15.5±0.3
Butyl-AHAP/NO	2.1±0.2	1.3±0.3	9.0±5.1	11.5±0.9
Octadecyl-AHAP/NO	8.7±0.2	4.1±0.8	15.3±8.8	42.2±1.5
Heptadecafluoro-AHAP/NO	2.0±0.9	0.4±0.2	20.9±5.7	55.1±2.3

[a] As measured by scanning electron microscopy; [b] Total nmol NO released per mg of particle as determined by chemiluminescent nitric oxide analyzer (NOA); [c] Maximum instantaneous concentration of NO release as measured by NOA; [d] Duration of NO release; [e]As determined by ICP-OES.

heptadecafluoro-AHAP/NO-doped fibers had the lowest NO payload, an expected result based on the low NO loading of these particles. Overall, the duration of NO release was not significantly influenced by changing particle hydrophobicity; however, heptadecafluoro-AHAP/NO-doped fibers did exhibit prolonged NO release durations. Of note, the NO release durations of the ethyl-AHAP/NO- and butyl-AHAP/NO-doped fibers were nearly as long as that of AHAP/NO-doped fibers even though the modified systems were characterized by less than one-fifth of the total NO storage. The addition of ethyl and butyl groups to the particle surface may result in NO-releasing particle-doped electrospun fibers with enhanced stability and increased NO release durations.

3.4 Conclusions

Due to the concentration dependence of NO's therapeutic activity, methods for tuning the NO release kinetics from macromolecular scaffolds are desirable as materials could thus be tailored to fit specific applications. As described herein, the addition of hydrophobic ligands to the surface of silica nanoparticles allows for a wide range of NO release kinetics ($t_{1/2}$ = 0.3–2.7 h) without affecting particle size or morphology. Unfortunately, surface modifications with hydrocarbon- and fluorocarbon-based silanes decreased the amine to diazeniumdiolate conversion efficiencies. Future studies should focus on investigating whether first forming the *N*-diazeniumdiolate prior to surface modification will improve NO payloads. The ability to modify particle surface properties broadens the utility of these NO-releasing systems, as demonstrated by their increased stability as dopants in electrospun polymer fibers. The addition of ethyl and butyl groups to the particle surface improves their stability in the fibers with little influence on fiber diameter and NO release kinetics. Further

tuning of surface hydrophobicity using octadecyl and heptadecafluoro ligands did not enhance dopant stability, suggesting that an optimal hydrophobicity may exist for achieving stable polymer composites.

References

1. Ignarro, L. J. *Nitric oxide: Biology and pathobiology*. Academic Press: San Diego, CA, 2000.

2. Carpenter, A. W.; Schoenfisch, M. H. "Nitric oxide release: Part II. Therapeutic applications." *Chem. Soc. Rev.* **2012**, *41*, 3742-3752.

3. Riccio, D. A.; Schoenfisch, M. H. "Nitric oxide release: Part I. Macromolecular scaffolds." *Chem. Soc. Rev.* **2012**, *41*, 3731-3741.

4. Zhou, Z.; Meyerhoff, M. E. "Preparation and characterization of polymeric coatings with combined nitric oxide release and immobilized active heparin." *Biomaterials* **2005**, *26*, 6506-6517.

5. Davies, K. M.; Wink, D. A.; Saavedra, J. E.; Keefer, L. K. "Chemistry of the diazeniumdiolates 2. Kinetics and mechanism of dissociation to nitric oxide in aqueous solution." *J. Am. Chem. Soc.* **2001**, *123*, 5473-5481.

6. Stevens, E. V.; Carpenter, A. W.; Shin, J. H.; Liu, J.; Der, C. J.; Schoenfisch, M. H. "Nitric oxide-releasing silica nanoparticle inhibition of ovarian cancer cell growth." *Mol. Pharmaceut.* **2010**, *7*, 775-785.

7. Koh, A.; Riccio, D. A.; Sun, B.; Carpenter, A. W.; Nichols, S. P.; Schoenfisch, M. H. "Fabrication of nitric oxide-releasing polyurethane glucose sensor membranes." *Biosens. Bioelectron.* **2011**, *28*, 17-24.

8. Leung, V.; Ko, F. "Biomedical applications of nanofibers." *Polym. Adv. Technol.* **2011**, *22*, 350-365.

9. Coneski, P. N.; Nash, J. A.; Schoenfisch, M. H. "Nitric oxide-releasing electrospun polymer microfibers." *ACS Appl. Mater. Interfaces* **2011**, *3*, 426-432.

10. Stober, W.; Fink, A.; Bohn, E. "Controlled growth of monodisperse silica spheres in micron size range " *J. Colloid Interf. Sci* **1968**, *26*, 62-69.

11. Neue, U. D. *HPLC columns: Theory, technology, and practice*. John-VCH: 1997.

12. Huh, S.; Wiench, J. W.; Yoo, J.-C.; Pruski, M.; Lin, V. S. Y. "Organic functionalization and morphology control of mesoporous silicas via a co-condensation synthesis method." *Chem. Mater.* **2003**, *15*, 4247-4256.

13. Albert, K.; Bayer, E. "Characterization of bonded phases by solid-state NMR spectroscopy." *J. Chromatogr.* **1991**, *544*, 345-370.

14. Corrie, S. R.; Lawrie, G. A.; Trau, M. "Quantitative analysis and characterization of biofunctionalized fluorescent silica particles." *Langmuir* **2006**, *22*, 2731-2737.

15. Moulder, J. F.; Stickle, W. F.; Sobol, P. E.; Bomben, K. D. *Handbook of X-ray photoelectron spectroscopy*. Perkin-Elmer Corp.: Eden Prairie, MN, USA, 1992.

16. Krafft, M. P.; Riess, J. G. "Highly fluorinated amphiphiles and colloidal systems, and their applications in the biomedical field. A contribution." *Biochimie* **1998**, *80*, 489-514.

17. Malvern *Zetasizer nano series user manual*. Malvern Instruments, Ltd.: Worcestershire, 2007.

18. Murdock, R. C.; Braydich-Stolle, L.; Schrand, A. M.; Schlager, J. J.; Hussain, S. M. "Characterization of nanomaterial dispersion in solution prior to in vitro exposure using dynamic light scattering technique." *Toxicol*. *Sci*. **2008**, *101*, 239-253.

19. Hrabie, J. A.; Keefer, L. K. "Chemistry of the nitric oxide-releasing diazeniumdiolate ("Nitrosohydroxylamine") functional group and its oxygen-substituted derivatives." *Chem*. *Rev*. **2002**, *102*, 1135-1154.

20. Barton, A. F. M. *CRC handbook of solubility parameters and other cohesion parameters, second edition*. CRC Press: Boca Raton, FL, 1991.

21. Shin, J. H.; Metzger, S. K.; Schoenfisch, M. H. "Synthesis of nitric oxide-releasing silica nanoparticles." *J*. *Am*. *Chem*. *Soc*. **2007**, *129*, 4612-4619.

22. Nichols, S. P.; Le, N. N.; Klitzman, B.; Schoenfisch, M. H. "Increased in vivo glucose recovery via nitric oxide release." *Anal*. *Chem*. **2011**, *83*, 1180-1184.

23. Hetrick, E. M.; Prichard, H. L.; Klitzman, B.; Schoenfisch, M. H. "Reduced foreign body response at nitric oxide-releasing subcutaneous implants." *Biomaterials* **2007**, *28*, 4571-4580.

24. Frost, M. C.; Rudich, S. M.; Zhang, H.; Maraschio, M. A.; Meyerhoff, M. E. "In vivo biocompatibility and analytical performance of intravascular amperometric oxygen sensor prepared with improved nitric oxide-releasing silicone rubber coating." *Anal*. *Chem*. **2002**, *74*, 5942-5947.

25. Koh, A.; Carpenter, A. W.; Sun, B.; Slomberg, D.; Riccio, D. A.; Coneski, P. N.; Schoenfisch, M. H. "Nitric oxide-releasing silica nanoparticle-doped polyurethane electrospun fibers." ***in preparation***.

Chapter 4:

O^2-Protected Diazeniumdiolate-Modified Silica Nanoparticles for Extended Nitric Oxide Release

4.1 Introduction

Given the proven antimicrobial nature of nitric oxide (NO) and the use of silica particles in commercial oral-care products, NO-releasing silica nanoparticles may prove useful for combating the plaque bacteria infections that plague dental restorative treatments. Indeed, 50–60% of restorative treatments result in secondary caries that necessitate replacement of the restoration.[1] While dental composites modified with antimicrobial agents have been proposed to prolong the life-time of restorative materials, sustained release over the course of days–weeks has yet to be achieved.[2-4]

The gaseous and reactive nature of NO requires the use of NO donors (e.g., *N*-diazeniumdiolates, *S*-nitrosothiols, and metal nitrosyls) to achieve controlled therapeutic NO delivery.[5, 6] *N*-diazeniumdiolate (NONOate) are among the most widely used NO donors as they are comprised of two molecules of NO covalently bound to an amine site, thus allowing for greater NO payloads compared to donors that store only one molecule of NO per donor site (e.g., *S*-nitrosothiols). Moreover, the NONOate functionality results in the spontaneous generation of NO in physiological solutions via a highly efficient proton-initiated decomposition. While advantageous, the labile nature of *N*-diazeniumdiolates often hinder the preparation of materials with prolonged release durations necessary for promoting implant integration. Modifying macromolecular scaffolds, such as silica nanoparticles, with

NO donors allows for more localized NO-release payloads and greater tunability of NO-release kinetics by controlling water diffusion into the scaffold.[6] Unfortunately, NO release from NONOate-based silica particles remains limited to only days at best.[7, 8] The stability of the NONOate can be increased by adding a protecting group at the O^2-position. Release of NO then requires hydrolytic or metabolic cleavage of the protecting group prior to *N*-diazeniumdiolate decomposition.[9, 10] Indeed, O^2-protected NONOates bound to LMW structures exhibit half-lives on the order of days compared to seconds or minutes for unprotected analogs. O^2-substituted diazeniumdiolate NO donors have previously been used to covalently modify proteins and polymers to yield materials with extended NO release.[9, 11, 12] To date, these structures have not been used to modify silica nanoparticle scaffolds, which hold great promise in a wide range of biomedical applications as discussed in Chapter 1.

The lifetime of dental composites is often shortened due to the formation of plaque biofilms that degrade the material, increasing surface roughness and promoting further bacterial adhesion.[13] Given that silica particles are a major component of commercial dental resin composites for strength and abrasion resistance,[14] functionalized silica particles are excellent candidates to impart antimicrobial properties to the composite. We hypothesize that replacing the non-functionalized silica filler particles with silica particles capable of sustained NO release may result in improved antimicrobial dental composites with longer lifetimes.

Herein, mesoporous silica nanoparticles were functionalized with an O^2-substituted *N*-diazeniumdiolate-modified organosilane synthesized by coupling an alkyl halide organosilane with O^2-methoxymethyl 1-(piperazin-1-yl)diazen-1-ium-1,2-diolate. After evaluating the release from the resulting scaffolds, the particles were doped into a dental

composite resin to yield a new class of antimicrobial restorative materials. The ability of these materials to decrease adhesion and viability of *Streptococcus mutans* over a 24 h period was evaluated in vitro.

4.2 Materials and Methods

Tetraethoxysilane, chloropropyltrimethoxysilane, bromopropyltrimethoxysilane, iodopropyltrimethoxysilane, *N*-(6-aminohexyl)aminopropyltrimethoxysilane, and tetramethoxysilane were purchased from Gelest, Inc. (Morrisville, PA). *N*,*N*-dimethylformamide (anhydrous), methanol (anhydrous), acetonitrile (anhydrous), tetrahydrofuran (anhydrous), ethanol, and ammonia solution (30%) were purchased from Fisher Scientific (Fair Lawn, NJ). 1-Ethoxycarbonylpiperazine, 5.4 M sodium methoxide in methanol, anhydrous sodium carbonate, chloromethyl methyl ether, sodium sulfate, magnesium sulfate and cetyltrimethylammonium bromide were purchased from Sigma Aldrich (St. Louis, MO). Nitrogen (N_2), argon (Ar), and nitric oxide calibration (26.81 PPM, balance N_2) gases were purchased from National Welders (Raleigh, NC). Pure nitric oxide gas (99.5%) used for *N*-diazeniumdiolate formation was purchased from Praxair (Sanford, NC). Reagents for the Griess assay (sulfanilamide, *N*-1-naphthylethylenediamine, and nitrite standard) were purchased from Sigma Aldrich (St. Louis, MO). Distilled water was purified using a Millipore Milli-Q UV Gradient A-10 system (Bedford, MA), resulting in a total organic content of ≤6 ppb and a final resistivity of 18.2 mΩ·cm. *Streptococcus mutans* (ATCC # 25175) was received from American Type Culture Collection (Manasses, VA). Estelite Σ Quick (Tokuyama Dental) resin-based dental composite was a gift from UNC Dental School.

4.2.1 Synthesis of mesoporous silica nanoparticles

Cetyltrimethylammonium bromide (290 mg) was added to 50 mL of a 5 mM solution of ammonium hydroxide in Milli-Q-purified water. The mixture was stirred for 1 h and heated to 40 °C to allow micelle formation. An initial 110 μL aliquot of tetraethoxysilane (TEOS) was added to the solution, with subsequent stirring for 5 h. A second 600 μL aliquot of TEOS was then added, and the solution was stirred for an additional 2 h. The particles were then allowed to age without stirring at 40 °C for 24 h. The resulting mesoporous silica nanoparticles were collected by centrifugation at 16,770×*g* for 20 mins, washed thrice with ethanol and dried in vacuo. The surfactant was removed by stirring the particles in 50 mL acidic ethanol (1:9 HCl:EtOH) at 60 °C overnight.

4.2.2 Synthesis of O^2-methoxymethyl 1-(4-(3-(trimethoxysilyl)propyl)piperazin-1-yl)diazen-1-ium-1,2-diolate

O^2-Methoxymethyl 1-(piperazin-1-yl)diazen-1-ium-1,2-diolate (MOM-Pip/NO) was prepared as previously described.[9] Briefly, 10 g of 1-ethoxycarbonylpiperazine was dissolved in 30 mL of methanol with 1.167 mL 5.4 M sodium methoxide in methanol. The solution was placed in a Parr stainless steel pressure vessel connected to an in-house NO reactor, purged thoroughly with Ar, then pressurized to 10 bar with NO that had been scrubbed with KOH. The pressure was maintained at 10 bar for 2 d, after which it was released and the solutions were again purged with Ar to remove unreacted NO. Cold ether was added, and the resulting white precipitate (**1**) was collected by filtration, washed with cold methanol followed by ether and dried in vacuo. To a slurry of **1** (2.2 g) and anhydrous sodium carbonate in tetrahydrofuran (100 mL) was added 0.75 mL chloromethyl methyl ether and 1 mL methanol simultaneously and dropwise under nitrogen at 0 °C. The mixture

was then brought to room temperature and stirred overnight. The reaction was then filtered, evaporated to dryness, and taken up in dichloromethane. The product (**2**) was dried over sodium sulfate, filtered through magnesium sulfate, and evaporated to dryness. The ethoxycarbonyl protecting group was then removed by heating **2** to reflux in 10% ethanolic sodium hydroxide for 1 h. After cooling to room temperature, the ethanol was removed and the residue was extracted in dichloromethane, filtered, extracted with aqueous hydrochloric acid, washed with dichloromethane, and then made basic with aqueous sodium hydroxide. Lastly, the product was extracted with dichloromethane, dried over sodium sulfate and filtered through magnesium sulfate. Removal of dichloromethane yielded MOM-Pip/NO, which was further purified by Flash 40 chromatography using a 4x15 cm KP-Sil column and an eluent of 10:1 dichloromethane/methanol.

Hünig's base (0.79 mmol) was added to a solution of MOM-Pip/NO (0.53 mmol) in 1 mL anhydrous *N*,*N*-dimethylformamide. Chloro-, bromo-, or iodopropyltrimethoxysilane (0.58 mmol) was then added, and the reaction was allowed to proceed for 24 h at 60 °C to yield O^2-methoxymethyl 1-(4-(3-(trimethoxysilyl)propyl)piperazin-1-yl)diazen-1-ium-1,2-diolate (MOM-Pip/NO-TMS). *N*,*N*-dimethylformamide was removed by vacuum and the residue was taken up in THF. The insoluble HI salt of Hünig's base was removed by filtration, and the solvent was removed. The percent yields from chloro-, bromo- and iodotrimethoxysilane were 58, 81 and 94% as determined by ^{1}H NMR. ^{1}H NMR (CD_3CN) δ 0.61 (t, $SiCH_2$), 1.64 (m, $SiCH_2CH_2CH_2$), 2.57 (t, $Si(CH_2)_2CH_2N$), 2.83 (t, NCH_2CH_2N), 3.41 (s, OCH_2OCH_3), 3.51 (s, $Si(OCH_3)_3$), 3.55 (t, NCH_2CH_2N), 5.16 (s, OCH_2OCH_3) ppm. ^{13}C NMR (CD_3Cl) δ 6.46 ($SiCH_2CH_2$), 12.08 ($SiCH_2CH_2$), 50.56 ($SiOCH_3$), 50.97 (CH_2NCH-CHN), 54.48 (OCH_2OCH_3), 57.07 ($CH_2NCH_2CH_2N$), 59.94 ($SiCH_2CH_2CH_2N$), 97.88

(OCH_2OCH_3) ppm. ESI/MS (in CH_3CN): 353.08 m/z.

4.2.3 Synthesis of O^2-protected diazeniumdiolate-modified silica nanoparticles

MOM-Pip/NO-TMS was dissolved in 1 mL tetrahydrofuran and added to a suspension of 10 mg of MSNs in 9 mL tetrahydrofuran. The mixture was refluxed overnight, and the resulting MOM-Pip/NO-modified MSNs were collected by centrifugation (3645×*g*, 10 min), washed twice with tetrahydrofuran, then twice with ethanol. The particles were then dried in vacuo overnight, and stored in a vacuum-sealed container protected from light at -20 °C until further use.

4.2.4 Synthesis of unprotected diazeniumdiolate-modified silica nanoparticles

Silica nanoparticles composed of *N*-(6-aminohexyl)-aminopropyltrimethoxysilane (AHAP) and tetramethoxysilane (TMOS) were synthesized via a modified Stöber method as previously described.[15] Briefly, AHAP (1.173 mL) and TMOS (0.708 mL) were mixed and added to a solution of ethanol (59.16 mL), water (27.84 mL), and ammonium hydroxide (9.8 mL). After 2 h reaction at room temperature, the resulting particles were collected by centrifugation (3645×*g*, 10 min, 4 °C) and washed three times with ethanol. After drying in vacuo, 20 mg of AHAP particles were suspended by sonication in 4 mL of a 1:9 mixture of methanol and *N*,*N*-dimethylformamide with 50 μL 5.4 M sodium methoxide in methanol. The particles suspensions were then purged with Ar and exposed to NO in the same manner as described above. After 3 d, the resulting *N*-diazeniumdiolate-modified silica nanoparticles (AHAP/NO) were collected by centrifugation (3645×*g*, 10 min, 4 °C), washed three times with ethanol, and dried in vacuo.

4.2.5 Characterization

Total amounts of NO released from the particles were evaluated using the Griess assay. MOM-Pip/NO-modified particles were suspended in oxygenated phosphate buffered saline (PBS, pH 7.4) and liberated NO was converted to nitrite (NO_2^-). Aliquots of the particle suspension were taken at the time points indicated in Figure 4.5. The particles were removed by centrifugation, and 50 μL aliquots of the supernatant were reacted with equal volumes of 1 wt% solutions of sulfanilamide and *N*-1-naphthylethylenediamine. The formation of an azo compound was detected by measuring the absorbance at 540 nm and comparing the results to a calibration curve constructed using nitrite standards to determine the total NO released from the particles. Real-time nitric oxide release was monitored using a Sievers NOA 280i Chemiluminescence NO Analyzer (Boulder, CO) connected to a customized reaction vessel. Nitric oxide-releasing materials were placed in deoxygenated media at 37 °C with NO carried to the analyzer by passing N_2 through the solution at a constant rate of 70 mL/min. The analyzer was calibrated with air passed through a NO zero filter (0 ppm NO) and a 26.39 ppm NO standard gas (balance N_2).

Particle size and morphology were characterized using a Hitachi S-4700 Scanning Electron Microscope (Pleasanton, CA). Covalent incorporation of MOM-Pip/NO-TMS onto the MSNs was confirmed using solid-state cross-polarization/magic angle spinning (CP/MAS) ^{29}Si NMR with a Bruker 360 MHz DMX spectrometer (Billerica, MA) equipped with wide-bore magnets (triple-axis pulsed field gradient double-resonance probes). Samples were packed into a 4 mm rotor (double-resonance frequency of 71.548 Hz) and spun at 10 kHz. Chemical shifts were determined in parts per million relative to a tetramethylsilane external standard. Nitrogen adsorption/desorption isotherms were obtained using a

Micromeritics Tristar II Porosimeter (Norcross, GA) after outgassing the particles at 110 °C for 18 h. The specific surface area was calculated using Brunauer-Emmet-Teller theory. Carbon, hydrogen and nitrogen content were determined on a Perkin Elmer CHN/S elemental analyzer operated in CHN mode.

4.2.6 MOM-Pip/NO-MSN-doped dental composites

Particle-doped resins were prepared by mixing 1.4 mg particles into 138.6 mg resin with a spatula. Particle-doped resins were pressed between glass slides into uniform disks with a diameter of 1 cm and a thickness of 0.1 cm. The composites were cured using a Translux Power Blue dental curing light (440–480 nm) from Heraeus Kulzer (South Bend, IN).

4.2.7 Bacterial adhesion assay

Streptococcus mutans was grown to 10^8 CFU/mL in BHI broth, centrifuged (3645×*g*, 10 min), resuspended in PBS, and diluted to 10^6 CFU/mL in 10% (v/v) BHI in PBS. Particle-doped composite resins were placed in 1.0 mL of 10^6 CFU/mL and incubated at 37 °C with gentle shaking. After 24 h, the composites were removed and rinsed with distilled water to remove loosely adhered bacteria. The composites were then placed in 1.0 mL of fresh PBS. Adhered bacteria were removed by sonication (60 kHz, 10 min). Complete removal of adhered bacteria was confirmed by imaging the composites with atomic force microscopy (AFM). Aliquots (100 μL) were taken from the resulting bacteria suspensions, plated on BHI agar nutrient plates, and enumerated after incubating for 48 h at 37 °C.

4.2.8 Atomic force microscopy imaging of composites

Prior to imaging, substrates were gently rinsed in sterile water and allowed to dry under ambient conditions. AFM images were collected in contact mode using an Asylum MFP-3D AFM (Santa Barbara California) and Olympus TR400PSA silicon nitride probes. At least three 10 μm^2 images of each substrate were taken at a resolution of 1024x1024 pixels and scan speed of 1 Hz. Root-mean-squared (rms) roughness of substrates was determined using MFP-3D software over four 2 μm^2 scan regions.

4.3 Results and Discussion

4.3.1 Synthesis of MOM-Pip/NO-modified mesoporous silica nanoparticles

While the therapeutic utility of NO-releasing macromolecular scaffolds has been proven both in vitro and in vivo,[5] the need for prolonged NO release scaffolds (i.e., weeks to months) remains a major hurdle. O^2-protected diazeniumdiolates are a promising class of NO donors as the functionality is still labile in physiological conditions but with significantly increased NO release lifetimes. Previously, Saavedra et al. described the preparation of piperazine-based methoxymethyl (MOM)-protected diazeniumdiolates that could be coupled to macromolecular structures through reaction with the free secondary amine on the piperazine ring.[9] Since this seminal report, piperazine-based MOM-protected scaffolds with half-lives up to 3 weeks have been developed.[9, 11, 12] Based on the advantages of silica nanoparticles for drug delivery, we sought to design a new class of extended NO release scaffolds by modifying silica particles with methoxymethyl-protected diazeniumdiolate-based silanes.

The incorporation of O^2-protected NONOates into silica nanoparticles first required

the synthesis of an O^2-protected NONOate-modified organosilanes. As shown in Scheme 4.1, ethoxycarbonyl piperazine was first *N*-diazeniumdiolated and subsequently alkylated with chloromethyl methyl ether. Removal of the ethoxycarbonyl group revealed MOM-Pip/NO with a free secondary amine. Full details of this synthesis have been previously described.[9] A methoxymethyl protecting group was selected as it hydrolyzes slowly under physiological conditions (pH 7.4). Other protecting groups have been designed that require enzymatic cleavage; however, such methodologies are not suitable for polymer dopants where access to enzymes would be low.

As shown in Scheme 4.2, the MOM-protected NONOate silane was synthesized by coupling MOM-Pip/NO with an alkylhalide trimethoxysilane. Initially, chloropropyltrimethoxysilane was chosen as the alkylhalide trimethoxysilane based on a previous report describing the coupling of MOM-Pip/NO to poly(vinyl chloride).[9] Acetonitrile, *N*,*N*-dimethylacetamide and *N*,*N*-dimethylformamide (DMF) were tested as the reaction solvent, as each is aprotic and has a dielectric constant sufficient for promoting S_N2 reactions. After 24 h reaction time at 60 °C, DMF proved to be the best solvent as indicated by ^{1}H NMR analysis. The successful formation of MOM-Pip/NO-TMS was indicated by a shift in the piperazine protons alpha to the secondary amine from 3.04 to 2.83 ppm. The protons alpha to the halide also shifted from 3.57 to 2.57 ppm upon formation of MOM-Pip/NO-TMS. However, the reaction of chloropropyltrimethoxysilane and MOM-Pip/NO under these conditions only proceeded to 58% completion. Thus, the more reactive bromo- and iodopropyltrimethoxysilanes were tested under the same reaction conditions (DMF, 24 h, and 60 °C). The reaction of MOM-Pip/NO with bromopropyltrimethoxysilane went to 81% completion, while reaction with iodopropyltrimethoxysilane resulted in a near complete

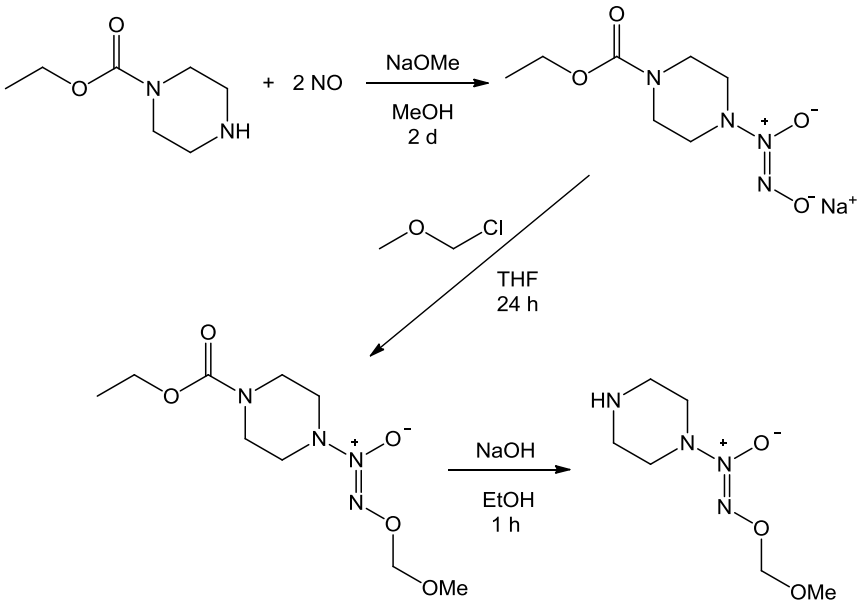

Scheme 4.1 Synthesis of O^2-methoxymethyl 1-(piperazin-1-yl)diazen-1-ium-1,2-diolate (MOM-Pip/NO).[9]

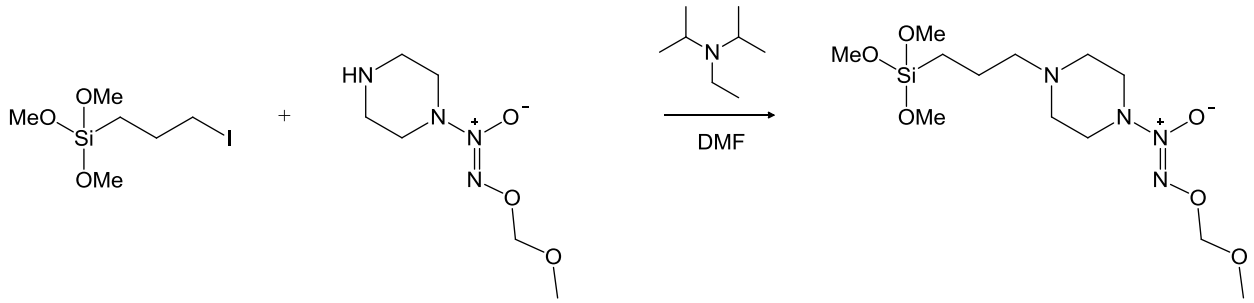

Scheme 4.2 Synthesis of O^2-methoxymethyl 1-(4-(3-(trimethoxysilyl)propyl)piperazin-1-yl)diazen-1-ium-1,2-diolate (MOM-Pip/NO-TMS).

reaction (94%) due to the superior leaving group ability of the iodo group. The successful formation of MOM-Pip/NO-TMS was also confirmed with ESI mass spectrometry. Excess Hunig's base was used to stabilize the MOM protecting group, which is unstable in acidic solutions. The stability of the MOM protecting group was confirmed by monitoring the singlet at 5.16 ppm that corresponds to the protons of the terminal methyl group.

As discussed in Section 1.1.1, the incorporation of organic functionalities onto silica nanoparticles can be achieved via a modified Stöber or a surface grafting method. Although the Stöber method results in particles with the organosilanes incorporated throughout the entire particle, large organosilane concentrations often result in less control over particle size distribution and morphology. Moreover, large sterically hindered organosilanes restrict the polycondensation reactions required for uniform particle formation.[7] Alternatively, the surface-grafting method involves condensing organosilanes with surface silanols on preformed particles.[16] Typically, the preformed particles are synthesized from tetraalkoxysilane precursors, allowing for more uniform particles to be easily achieved. Particles with large organosilane concentrations can be prepared using mesoporous silica nanoparticles (MSN) due to their large specific surface area. Mesoporous silica nanoparticles are synthesized using micellular structures as templates for silica polymerization (Figure 4.1).[17] Upon hydrolysis, the silicate species bind to the surfactant molecules at the micelle interface through electrostatic interactions. Condensation of silicate species ensues, ultimately resulting in particle formation. The surfactant molecules are then removed using an acid wash to yield mesoporous silica particles. Numerous reports have demonstrated the ability to modify particle morphology by altering reaction conditions such as pH, temperature, and silane concentration.[18, 19] For example, increasing reaction

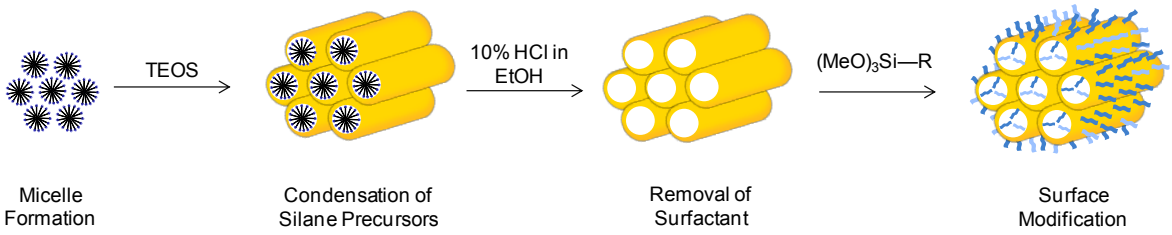

Figure 4.1 Synthesis of mesoporous silica nanoparticles (MSNs) involves the condensation of silane precursors around micelle structures to yield porous silica nanoparticles. Following surfactant removal, organosilanes can be condensed onto the MSNs through reaction with surface silanols.

temperature has been found to increase the aspect ratio of the resulting silica particles, while increasing alkalinity results in increased aspect ratio and improved monodispersity.[20] The reaction conditions used here (i.e., pH 11 and 40 °C) resulted in monodisperse rod-shaped silica nanoparticles with an aspect ratio of 3 (Figure 4.2). Using Brauner-Emmett-Teller analysis of nitrogen adsorption-desorption isotherms, the MSNs were found to have a specific surface area of 1145 m^2/g.

O^2-protected diazeniumdiolate-modified silica particles were subsequently prepared by condensing MOM-Pip/NO-TMS onto the MSNs (Figure 4.1). The successful addition of the MOM-Pip/NO-TMS into the silica network was confirmed using solid state ^{29}Si nuclear magnetic resonance spectroscopy (SS ^{29}Si NMR) with cross polarization and magic angle spinning (CP/MAS). As shown in Figure 4.3, the resulting SS ^{29}Si NMR spectra consisted of two peaks at -110 and -60 ppm corresponding to the Q-band and the T-band, respectively. The Q-band results from ^{29}Si bound to four functionalizable groups, representing silicon atoms originating from the TEOS precursor.[21] The T-band results from ^{29}Si bound to three hydrolyzable groups, corresponding to the MOM-Pip/NO-TMS precursor.[21] Elemental analysis further confirmed MOM-Pip/NO-TMS modification as indicated by an increase in the carbon wt% from 8.97 to 17.26% and nitrogen wt% from 0.31 to 6.77%. Of note, the small carbon content present within the particle prior to modification is likely due to unreacted ethoxy ligands. The elemental analysis results indicate that 1.2 μmol MOM-Pip/NO-TMS were incorporated per mg of MSNs, which is comparable to the organosilane concentrations of previously reported amine-modified silica nanoparticles prepared via the Stöber method.[7] The stability of the MOM-Pip/NO moiety during the functionalization step was confirmed by the presence of an absorbance maximum in the UV-Vis spectrum at ca.

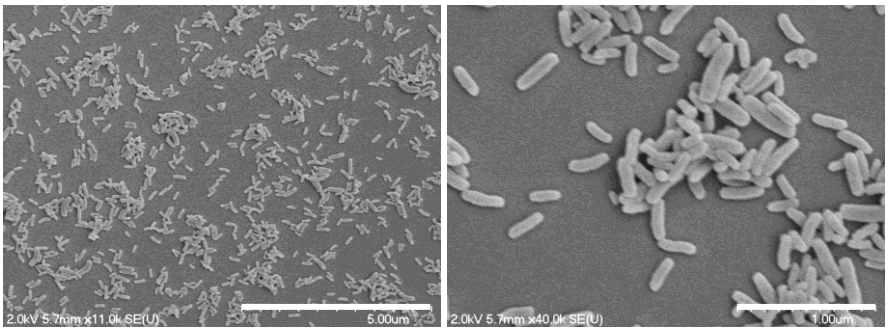

Figure 4.2 Scanning electron micrographs of mesoporous silica nanoparticles synthesized via a surfactant templated approach.

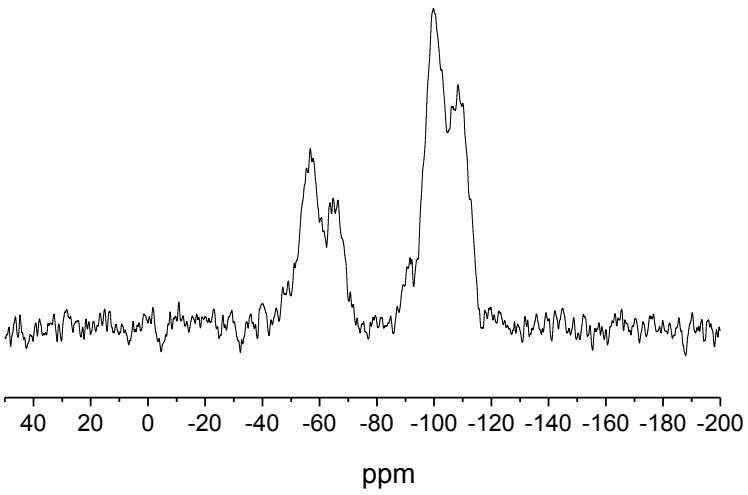

Figure 4.3 Solid state CP/MAS ^{29}Si NMR spectrum of MOM-Pip/NO-modified MSNs. The T-band (ca. -60 ppm) indicates silicon atoms bound to three oxygens (i.e., MOM-Pip/NO-TMS), and the Q-band (ca -100 ppm) represents silicon atoms bound to four oxygens (i.e., TEOS).

220 nm (Figure 4.4), which is within the range of that reported for O^2-protected diazeniumdiolates.[9] The addition of MOM-Pip/NO-TMS did not affect particle size or morphology as determined by SEM.

Nitric oxide storage and release from the MOM-Pip/NO-modified particles were evaluated by elemental analysis and the Griess assay, respectively. The MOM-Pip/NO-modified particles were characterized by a total NO payload of 2.4 μmol NO/mg. As shown in Figure 4.5, the rate of NO generation from the MOM-Pip/NO-modified particles was slow and continued for several weeks at 0.5–1.0 pmol mg^{-1} s^{-1}. The half-life of NO release was ultimately determined to be 23 d, which is significantly longer than any other NO-releasing silica particle to date.[6] The longest previously reported NO release half-life from silica nanoparticles was 4.2 h from Stöber silica particles containing *N*-diazeniumdiolate-modified (3-trimethoxysilyl)diethylenetriamine.[8] Thus, NO-releasing silica particles with sustained NO release was achieved by covalently incorporating an O^2-protected *N*-diazeniumdiolate NO donor within the silica network.

4.3.2 Inhibition of bacterial adhesion

Nablo et al. previously showed that the release of NO from xerogel-coated silicon rubber implants significantly decreases subcutaneous *Staphylococcus aureus* infections in vivo.[22] A number of subsequent studies have demonstrated the ability of NO-releasing surfaces to decrease the adhesion of both Gram positive and Gram negative bacteria.[23-26] To date, most evaluations have employed short exposure periods (0.5–2 h) in non-nutrient conditions, which are less representative of the complex environment present in vivo. To assess the utility of MOM-Pip/NO-modified particles as dopants for antimicrobial dental

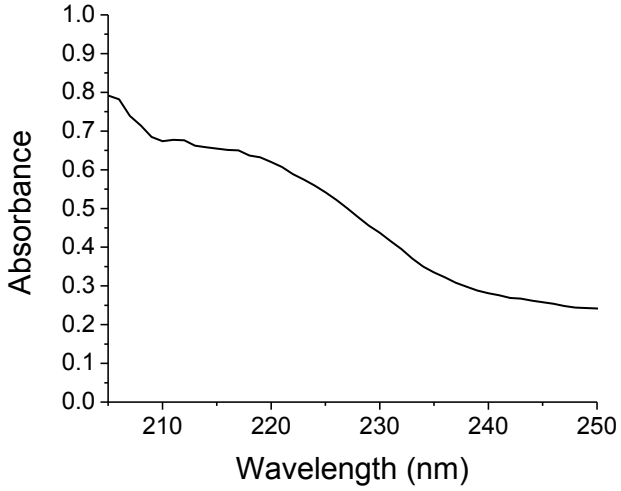

Figure 4.4 UV-Vis absorbance spectrum of MOM-Pip/NO-modified particles with an maximum absorbance at 220 nm indicating the presence of the MOM-protected diazeniumdiolates.

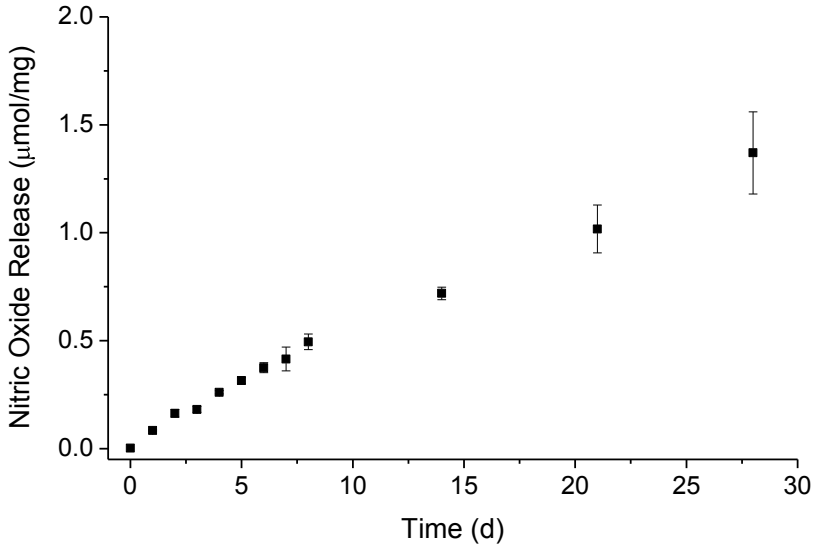

Figure 4.5 Nitric oxide release from MOM-Pip/NO-MSNs. Total NO storage is 2.5 μmol/mg as determined by elemental analysis.

restorative materials, we sought to evaluate the ability of these materials to resist bacterial adhesion over 24 h exposure times under nutrient conditions (10 vol% BHI in PBS). *Streptococcus mutans* was chosen as the test microbe as it has been implicated as a causative cariogenic bacterium.[27]

To evaluate the advantage of the sustained NO release scaffolds, composites doped with faster NO-releasing unprotected *N*-diazeniumdiolate-modified AHAP/NO particles were also prepared. Nitric oxide release from the particle-doped composites was evaluated in 10 vol% BHI in PBS over 24 h to mimic the bacterial adhesion assays. The total NO released from MOM-Pip/NO- and AHAP/NO-doped composites in this media was 6.7±0.1 and 19.2±0.04 nmol, respectively. As shown in Figure 4.6, the NO release flux from the composites was low (0.1–0.4 pmol cm^{-2} s^{-1}). This result was attributed to NO scavenging by proteins present in the nutrient broth and was not unexpected.[28] The NO release from MOM-Pip/NO-doped composites continually increased during the 24 h exposure period due to the slow decomposition rate of the protected *N*-diazeniumdiolate. Conversely, the AHAP/NO-doped composites reached a maximum NO flux within the first few minutes, and the NO levels gradually decreased over the 24 h exposure time. Both NO-releasing composites exhibited NO fluxes below that previously reported to be the minimum required in inhibit adhesion of Gram negative *Psuedomonas aeruginosa*.[23, 24] Despite the low NO release, composites doped with 1 wt% MOM-Pip/NO particles were characterized by a 3-log decrease in viable adhered bacteria compared to control and AHAP/NO-doped composites (Figure 4.7). No significant decrease in bacterial adhesion was observed between the undoped control and AHAP/NO-doped composite resins. Hetrick et al. reported a minimum flux of 20 pmol cm^{-2} s^{-1} required to inhibit adhesion of *P. aeruginos*a to xerogels films.[24]

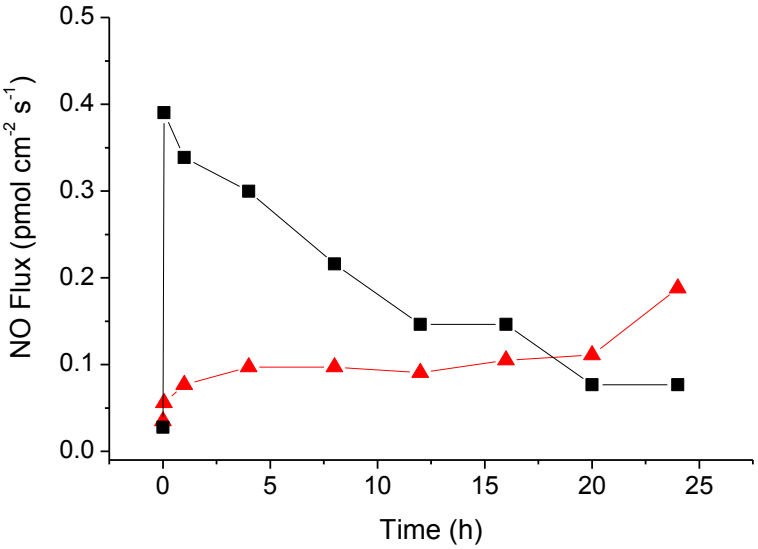

Figure 4.6 Nitric oxide release in 10 vol% BHI in PBS from dental composites doped with 1 wt% AHAP/NO (squares) and MOM-Pip/NO (triangle) particles.

However, Dobmeier and Schoenfisch previously noted a 50% reduction in adhesion of *P. aeruginosa* to xerogel microarrays with lower NO fluxes (1.0 pmol cm^{-2} s^{-1}).[23] Both prior studies were conducted in nutrient-free media at <2 h exposure times. The results presented here indicate that the NO flux required to decrease the number of viable bacteria adhered to a surface is dependent on the substrate, bacterial strain, and exposure conditions (e.g., time and media).

Atomic force microscopy images were obtained for each composite to ensure that differences in adhesion were not a result of changes in surface roughness due to the particle dopant (Figures 4.8A–C). The filler silica particles present in the composite were visible in each trace and clearly the major contributor to the surface roughness. Figure 4.8D provides a single 10 μm height trace, illustrating that the surface of each composite is similar regardless of the presence or absence of a functionalized particle dopant. Surface roughness measurements also confirmed that the addition of MOM-Pip/NO and AHAP/NO particles did not significantly alter the surface topography (Figure 4.8E). These results suggest that the reduction in viable *S. mutans* adhered to MOM-Pip/NO-doped composites was a result of their unique NO release.

4.4 Conclusions

While silica nanoparticles have distinct advantages for the therapeutic delivery of NO, limited NO release durations remains a major hindrance for their use in many biomedical applications. Herein, we demonstrated that NO-releasing silica particles with sustained NO release could be achieved by employing O^2-protected *N*-diazeniumdiolate chemistry. Indeed, O^2-protected N-diazeniumdiolate silane-modified silica particles

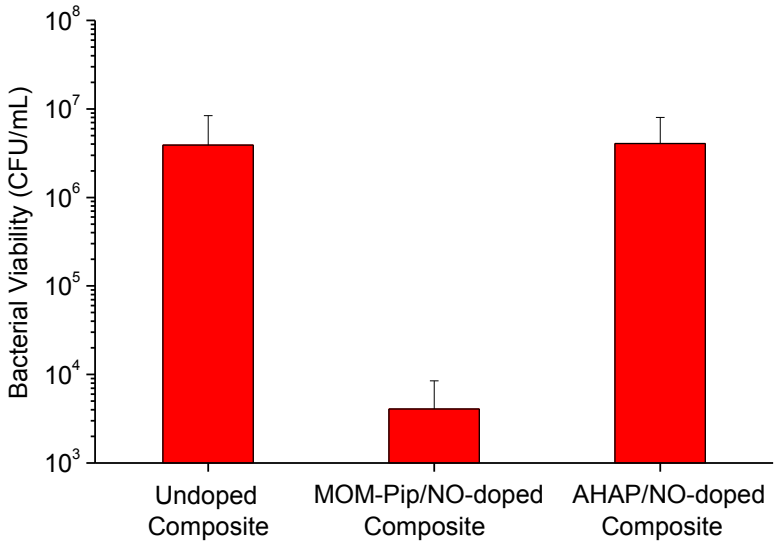

Figure 4.7 Viability of adhered *S*. *mutans* to control and particle-doped composites following 24 h incubation in 10 vol% BHI in PBS.

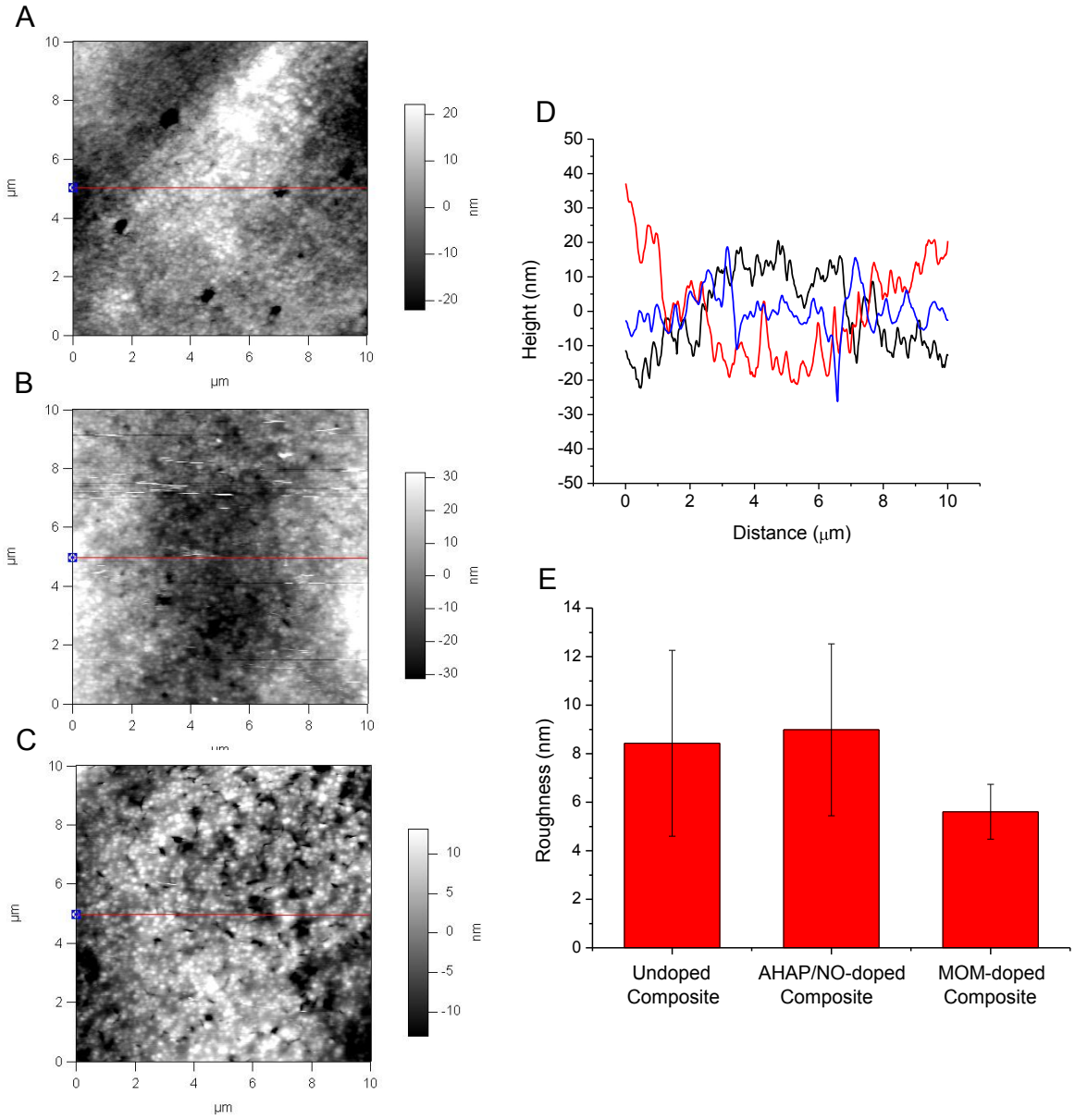

Figure 4.8 Atomic force micrographs of (A) control, (B), AHAP/NO-doped, and (C) MOM-Pip/NO-doped composites, (D) representative height trace from center section of each image (indicated by horizontal red line), and (E) rms surface roughness determined from four 2 μm^2 areas.

exhibited an NO release half-life of 3 weeks, the longest duration achieved from a silica particle scaffold to date. As a result, the potential applications of NO-releasing silica nanoparticles can be expanded to those requiring long durations of low NO fluxes.

The therapeutic utility of MOM-Pip/NO-modified silica nanoparticles was preliminarily demonstrated by preparing novel antimicrobial dental composites. The release of NO from the MOM-Pip/NO-doped composites effectively decreased the number of adhered viable *S. mutans* compared to control (undoped) composites. To evaluate the full potential of NO-releasing dental composites, future studies should evaluate longer bacterial exposure times and whether NO inhibits plaque biofilm formation. The effectiveness of composites doped with MOM-Pip/NO-modified particles in environments mimicking the oral cavity should also be evaluated as the lower pH will result in faster NO release, thus potentially influencing bacterial adhesion/viability. Greater NO payloads may be achieved by forming composites with larger NO-releasing silica nanoparticle concentrations. Indeed, unmodified silica particles comprise 70–90 wt% of commercial dental composites to provide increased modulus, strength, and abrasion resistance.[29] Designing new composites composed completely of NO-releasing silica particles may yield improved composites with respect to resistance to biofilm formation. The effect of the NO-releasing particle dopants on the properties of the polymer composites must be evaluated. Ultimately, a mixture of unmodified and modified particles may prove necessary to maintain composite integrity.

References

1. Deligeorgi, V.; Mjor, I. A.; Wilson, N. H. F. "An overview of reasons for the placement and replacement of restorations." *Prim. Dent. Care* **2001**, *8*, 5-11.

2. Beyth, N.; Yudovin-Farber, I.; Perez-Davidi, M.; Domb, A. J.; Weiss, E. I. "Polyethyleneimine nanoparticles incorporated into resin composite cause cell death and trigger biofilm stress in vivo." *Proc. Natl. Acad. Sci. U.S.A.* **2010**, *107*, 22038-22043.

3. Cheng, L.; Weir, M. D.; Xu, S. M.; Antonucci, J. M.; Kraigsley, A. M.; Lin, N. J.; Lin-Gibson, S.; Zhou, X. "Antibacterial amorphous calcium phosphate nanocomposites with a quaternary ammonium dimethacrylate and silver nanoparticles." *J. Dent. Res.* **2012**, *28*, 561-572.

4. Fan, C.; Chu, L.; Rawls, H. R.; Norling, B. K.; Cardenas, H. L.; Whang, K. "Development of an antimicrobial resin-a pilot study." *Dent. Mater.* **2011**, *27*, 322-328.

5. Carpenter, A. W.; Schoenfisch, M. H. "Nitric oxide release: Part II. Therapeutic applications." *Chem. Soc. Rev.* **2012**, *41*, 3742-3752.

6. Riccio, D. A.; Schoenfisch, M. H. "Nitric oxide release: Part I. Macromolecular scaffolds." *Chem. Soc. Rev.* **2012**, *41*, 3731-3741.

7. Shin, J. H.; Metzger, S. K.; Schoenfisch, M. H. "Synthesis of nitric oxide-releasing silica nanoparticles." *J. Am. Chem. Soc.* **2007**, *129*, 4612-4619.

8. Shin, J. H.; Schoenfisch, M. H. "Inorganic/organic hybrid silica nanoparticles as a nitric oxide delivery scaffold." *Chem. Mater.* **2008**, *20*, 239-249.

9. Saavedra, J. E.; Booth, M. N.; Hrabie, J. A.; Davies, K. M.; Keefer, L. K. "Piperazine as a linker for incorporating the nitric oxide-releasing diazeniumdiolate group into other biomedically relevant functional molecules." *J. Org. Chem.* **1999**, *64*, 5124-5131.

10. Saavedra, J. E.; Dunams, T. M.; Flippen-Anderson, J. L.; Keefer, L. K. "Secondary amine/nitric oxide complex ions, $R_2N[N(O)NO]^-$ O-functionalization chemistry." *J. Org. Chem.* **1992**, *57*, 6134-6138.

11. Reynolds, M. M.; Saavedra, J. E.; Showalter, B. M.; Valdez, C. A.; Shanklin, A. P.; Oh, B. K.; Keefer, L. K.; Meyerhoff, M. E. "Tailored synthesis of nitric oxide-releasing polyurethanes using O^2-protected diazeniumdiolate chain extenders." *J. Mater. Chem.* **2010**, *20*, 3107-3114.

12. Hrabie, J. A.; Saavedra, J. E.; Roller, P. P.; Southan, G. J.; Keefer, L. K. "Conversion of proteins to diazeniumdiolate-based nitric oxide donors." *Bioconjugate Chem.* **1999**, *10*, 838-842.

13. Busscher, H. J.; Rinastiti, M.; Siswomihardjo, W.; van der Mei, H. C. "Biofilm formation on dental restorative and implant materials." *J*. *Dent*. *Res*. **2010**, *89*, 657-665.

14. Chen, M. H. "Update on dental nanocomposites." *J*. *Dent*. *Res*. **2010**, *89*, 549-560.

15. Carpenter, A. W.; Worley, B. V.; Slomberg, D.; Schoenfisch, M. H. "Dual action antimicrobials: Nitric oxide release from quaternary ammonium-functionalized silica nanoparticles." *Biomacromolecules* **2012**, *accepted*.

16. Vivero-Escoto, J. L.; Huxford-Phillips, R. C.; Lin, W. "Silica-based nanoprobes for biomedical imaging and theranostic applications." *Chem*. *Soc*. *Rev*. **2012**, *41*, 2673-2685.

17. Slowing, I. I.; Vivero-Escoto, J. L.; Wu, C. W.; Lin, V. S. Y. "Mesoporous silica nanoparticles as controlled release drug delivery and gene transfection carriers." *Adv*. *Drug Deliv*. *Rev*. **2008**, *60*, 1278-1288.

18. Kim, T.-W.; Chung, P.-W.; Lin, V. S. Y. "Facile synthesis of monodisperse spherical MCM-48 mesoporous silica nanoparticles with controlled particle size." *Chem*. *Mater*. **2010**, *22*, 5093-5104.

19. Naik, S. P.; Elangovan, S. P.; Okubo, T.; Sokolov, I. "Morphology control of mesoporous silica particles." *J*. *Phys*. *Chem*. *C* **2007**, *111*, 11168-11173.

20. Lu, Y.; Slomberg, D.; Sun, B.; Schoenfisch, M. H. "Shape-and nitric oxide flux-dependent bactericidal efficacy of nitric oxide-releasing silica nanorods." *Small* **2012**, *submitted*.

21. Albert, K.; Bayer, E. "Characterization of bonded phases by solid-state NMR spectroscopy." *J*. *Chromatogr*. **1991**, *544*, 345-370.

22. Nablo, B. J.; Prichard, H. L.; Butler, R. D.; Klitzman, B.; Schoenfisch, M. H. "Inhibition of implant-associated infections via nitric oxide release." *Biomaterials* **2005**, *26*, 6984-6990.

23. Dobmeier, K. P.; Schoenfisch, M. H. "Antibacterial properties of nitric oxide-releasing sol-gel microarrays." *Biomacromolecules* **2004**, *5*, 2493-2495.

24. Hetrick, E. M.; Schoenfisch, M. H. "Antibacterial nitric oxide-releasing xerogels: Cell viability and parallel plate flow cell adhesion studies." *Biomaterials* **2007**, *28*, 1948-1956.

25. Coneski, P. N.; Rao, K. S.; Schoenfisch, M. H. "Degradable nitric oxide-releasing biomaterials via post-polymerization functionalization of cross-linked polyesters." *Biomacromolecules* **2010**, *11*, 3208-3215.

26. Riccio, D. A.; Coneski, P. N.; Nichols, S. P.; Broadnax, A. D.; Schoenfisch, M. H.

"Photoinitiated nitric oxide-releasing tertiary *s*-nitrosothiol-modified xerogels." *ACS Appl*. *Mater*. *Interfaces* **2012**, *4*, 796-804.

27. Poggio, C.; Arciola, C. R.; Rosti, F.; Scribante, A.; Saino, E.; Visai, L. "Adhesion of S*treptococcus mutans* to different restorative materials." *Int*. *J*. *Artif*. *Organs* **2009**, *32*, 671-677.

28. Hetrick, E. M.; Shin, J. H.; Stasko, N. A.; Johnson, C. B.; Wespe, D. A.; Holmuhamedov, E.; Schoenfisch, M. H. "Bactericidal efficacy of nitric oxide-releasing silica nanoparticles." *ACS Nano* **2008**, *2*, 235-246.

29. Stansbury, J.; Bowman, C. "The progress in development of dental restorative materials." *Mater*. *Matters* **2010**, *5*, 73-81.

Chapter 5:

Dual-action Antimicrobials: Nitric Oxide Release from Quaternary Ammonium-Functionalized Nanoparticles

5.1 Introduction

With increasing occurrences of microbial antibiotic resistance,[1] alternative approaches for fighting infections have become necessary. Co-administering two antimicrobials that act via different mechanisms has been shown to significantly reduce microbial resistance and often results in synergy where the two agents are more effective in combination than when administered alone.[2, 3] As such, researchers are developing strategies to modify macromolecular scaffolds (e.g., dendrimers, particles, polymers) with multiple antimicrobial agents.[4-6] For example, macromolecular scaffolds have been designed to consist of a permanent antimicrobial characteristic that remains after the depletion of the releasable agent.[7]

Long chain quaternary ammoniums (QA) are a popular non-depleting antimicrobial component due to their broad-spectrum efficacy, simple structure, and ability to kill bacteria with no affect on the QA structure.[8] The positively charged ammonium group promotes direct interaction with the negatively charged bacterial membrane, causing chemical imbalances by replacing essential metal cations. Simultaneously, the long alkyl chain of QAs inserts into the membrane and cause physical damage. The simple structure of the QA functionalities allows for straight forward integration into polymers,[9, 10] films,[11-13] dendrimers,[14] and particles,[8, 15, 16] while still retaining their antimicrobial properties.

Unfortunately, tethering QAs to polymers or particles limits their action to only those bacteria that come in direct contact with the macromolecule. Thus, coupling QA functionalities with a second releasable agent may increase the materials' sphere of influence and benefits from the advantages of the combination therapies discussed above. Indeed, QA-functionalized polymers impregnated with releasable silver ions (Ag^+) exhibited a wider zone of inhibition than QA polymers alone.[7, 17] Similarly, Wong et al. reported improved efficacy of QA-functionalized layer-by-layer coatings that leached gentamicin against biofilm formation.[18]

To date, most combination strategies have only been applied to polymeric coatings or films. Silica nanoparticles are well-poised as scaffolds for combination therapies due to their high surface area to volume ratio, chemical flexibility, and limited toxicity to mammalian cells.[19] Our laboratory has demonstrated the broad spectrum bactericidal efficacy of silica nanoparticles that actively release nitric oxide (NO),[20-22] a gaseous molecule produced endogenously as part of the innate immune response.[23] Nitric oxide and its reactive byproducts decrease bacterial viability via both lipid peroxidation and reaction with membrane proteins, DNA, and metabolic enzymes.[23] The key advantage of employing NO over other releasable agents (e.g., silver and antibiotics) involves NO's multimodal antimicrobial activity and low toxicity to mammalian cells at concentrations necessary for antimicrobial action.[24] Furthermore, initial studies suggest the inability of bacteria to develop resistance to nanoparticle-derived NO.[25] To date, the potential of NO-based therapeutics is evident in the immense research efforts focused on designing NO-releasing macromolecular scaffolds for biomedical applications.[26,27]

The storage of exogenous NO within silica nanoparticles is achieved by forming *N*-

diazeniumdiolate NO donors on secondary amine sites incorporated within the silica network (Scheme 5.1).[22, 28] Upon exposure to physiological solution (pH 7.4, 37 °C), the *N*-diazeniumdiolates undergo proton-initiated decomposition to release two molecules of NO per secondary amine site. Moreover, the rate of NO release is dependent on the NO donor structure and chemical environment. We hypothesize that the incorporation of long chain quaternary ammoniums onto the surface of NO-releasing silica nanoparticles may result in increased efficacy compared to singly functionalized particles (i.e., QA or NO release alone). Herein, we investigated the role of QA alkyl chain length and NO release capability on the bactericidal efficacy against Gram-positive *Staphylococcus aureus* and Gram-negative *Pseudomonas aeruginosa*.

5. 2 Materials and methods

Tetramethoxysilane and *N*-(6-aminohexyl)aminopropyltrimethoxysilane were purchased from Gelest (Morrisville, PA). Glycidyltrimethylammonium chloride, epichlorohydrin, dimethylbutylamine, dimethyloctylamine, dimethyldodecylamine, trimethylsilanolate, and propidium iodide (PI) were purchased from Sigma Aldrich (St. Louis, MO). *N*,*N*-dimethylacetamide, methanol (anhydrous), ethanol, ammonia solution (30%) and tetrahydrofuran (anhydrous) were purchased from Fisher Scientific (Fair Lawn, NJ). Media and reagents for bacteria and mammalian cell assays were purchased from Becton, Dickinson and Company (Sparks, MD). *Pseudomonas aeruginosa* (*P. aeruginosa*) (ATCC #19143) and Staphylococcus aureus (*S. aureus*) (ATCC #29213) were obtained from American Type Tissue Culture Collection (Manassas, VA), and L929 mouse fibroblasts were obtained from the UNC Tissue Culture Facility (Chapel Hill, NC). 4,5-Diaminofluorescein

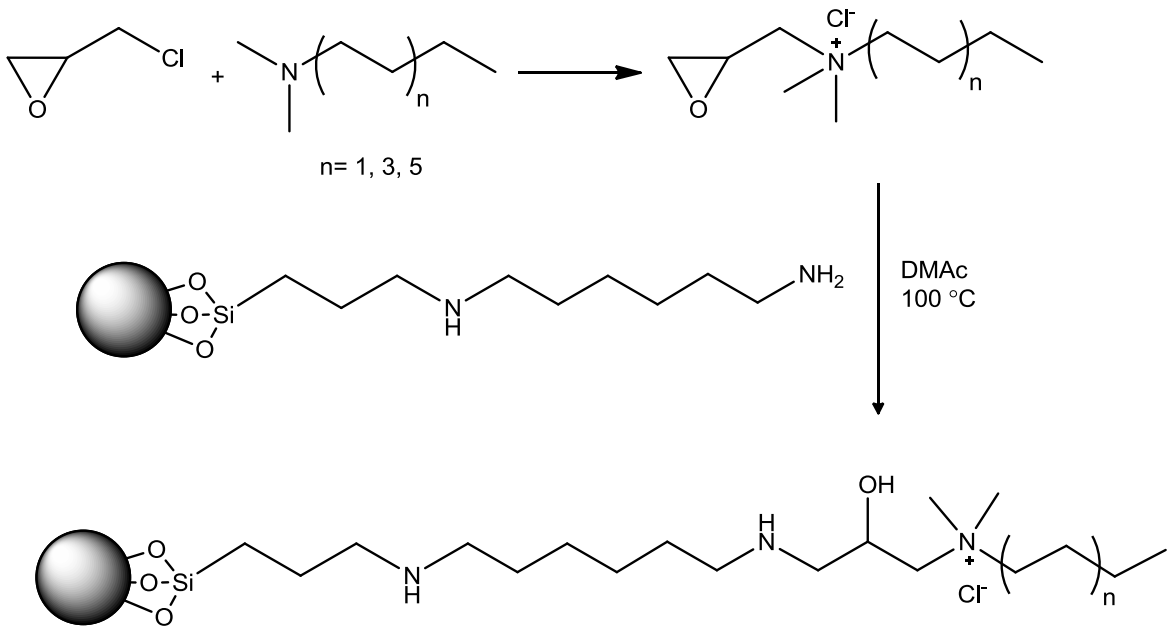

Scheme 5.1 Quaternary ammonium (QA) epoxides were synthesized via reaction of epichlorohydrin with a dimethylalkylamine and subsequently reacted with the primary amines on the surface of AHAP/TMOS particles to yield QA-functionalized silica nanoparticles.

diacetate (DAF-2 DA) was purchased from Calbiochem (San Diego, CA). Nitrogen (N2), argon (Ar), and nitric oxide calibration (26.81 PPM, balance N2) gases were purchased from National Welders (Raleigh, NC). Pure nitric oxide gas (99.5%) used for N-diazeniumdiolate formation was purchased from Praxair (Sanford, NC). Distilled water was purified using a Millipore Milli-Q UV Gradient A-10 system (Bedford, MA), resulting in a total organic content of ≤6 ppb and a final resistivity of 18.2 mΩ·cm.

5.2.1 Synthesis of amine-functionalized silica nanoparticles

The Stöber method was used to form monodisperse, spherical silica nanoparticles with amine functionalities throughout the particle scaffold as previously described.[29] Briefly, a premixed solution of *N*-(6-aminohexyl)aminopropyltrimethoxysilane (AHAP) (1.173 mL) and tetramethoxysilane (TMOS) (0.708 mL) was added to a solution of ethanol (59.16 mL), water (27.84 mL), and ammonium hydroxide (9.8 mL). The reaction was stirred at room temperature for 2 h. The resulting white particle precipitates were collected by centrifugation (3645*g*, 10 min, 4 °C) and washed thrice with ethanol to remove unreacted reagents. The particles were then dried in vacuo and stored in a sealed container at room temperature until further use.

5.2.2 Synthesis of quaternary ammonium-functionalized silica nanoparticles

The addition of QA functionalities to the particle surface involved the synthesis of quaternary ammonium epoxides (QA-epoxides) that were then subsequently reacted with primary amines on the particle scaffold via a ring opening reaction (Scheme 5.1). To form the QA-epoxides, 0.04 mmol epichlorohydrin was reacted with 0.01 mmol *N*,*N*-

dimethylbutylamine, *N*,*N*-dimethyloctylamine, or *N*,*N*-dimethyldodecylamine at room temperature overnight. The mixture was added dropwise to cold ether while sonicating, and the solid/viscous liquid QA-epoxides were collected via centrifugation (810*g*, 5 min). The supernatant containing excess epichlorohydrin and unreacted trialkylamines was decanted, 50 mL fresh cold ether was added, and the QA-epoxides were sonicated extensively. This washing procedure was repeated three times, followed by drying of the QA-epoxides in vacuo. The removal of unreacted epichlorohydrin and trialkylamines was confirmed with ^{1}H NMR. Glycidyldimethylbutylammonium chloride (butylQA) was a viscous liquid: ^{1}H NMR δ 0.98 (t, 3 H), 1.41 (m, 2H), 1.70 (m, 2H), 2.79 (dd, 1H), 2.98 (t, 1H), 3.24 (dd, 1H), 3.44 (s, 6H), 3.52 ppm (m, 1H), 3.63 ppm (dt, 2H), and 4.62 ppm (dd, 1H); ^{13}C NMR δ 13.8, 19.9, 25.5, 45.5, 45.3, 53.1, 65.4, and 66.9 ppm; ESI/MS m/z 158.09. Glycidyldimethyloctylammonium chloride (octylQA) was a tacky solid; ^{1}H NMR δ 0.87 (t, 3 H), 1.29 (m, 10 H) 1.71 (m, 2H), 2.74 (dd, 1H), 2.98 (t, 1H), 3.10 (dd, 1H), 3.49 (s, 6H), 3.54 (m, 1H), 3.67 (dt, 2H), and 4.96 ppm (dd, 1H); ^{13}C NMR δ 14.2, 22.9, 23.71, 26.6, 29.4, 32.02, 45.3, 45.5, 53.1, 65.8 and 66.9 ppm; ESI/MS m/z 214.16. Glycidyldimethyldodecylammonium chloride (dodecylQA) was a waxy solid; ^{1}H NMR δ 0.87 (t, 3 H), 1.27 ppm (m, 18H), 1.70 ppm (m, 2H), 2.74 ppm (dd, 1H), 2.98 ppm (t, 1H), 3.08 ppm (dd, 1H), 3.54 ppm (s, 6H), 3.58 ppm (m, 1H), 3.65 (dt, 2H), and 4.97 ppm (dd, 1H); ^{13}C NMR δ 14.2, 23.1, 23.7, 26.5, 29.5, 29.7, 29.8, 29.9, 32.38, 45.3, 45.5, 53.1, 65.4, and 66.9 ppm; ESI/MS m/z 270.25. The IR spectra were similar for all QA-epoxides with the exception of the intensity of the saturated C-H absorbance at 2919 and 2850 cm^{-1}, which increased with increasing alkyl chain length. IR (neat): 3019 cm^{-1} (methyl C-H), 2920 cm^{-1} (saturated C-H), 2850 cm^{-1} (saturated C-H), 1468 cm^{-1} (methyl C-H), 1267 cm^{-1} (epoxy ring),

972 (quaternary ammonium), 909 cm^{-1} (epoxy ring).

A ring opening reaction was subsequently performed between the QA-epoxides and the primary amines on the surface of the particle scaffolds (Scheme 5.1). The amine-containing silica particles (AHAP, 100 mg) were suspended in 2.5 mL *N*,*N*-dimethylacetamide via sonication, and 20 μL triethylamine was added. The QA-epoxides were dissolved in 5 mL *N*,*N*-dimethylacetamide and added in excess to the particle suspension. Dissolution of glycidyltrimethylammonium chloride required heating while all other QA-epoxides dissolved readily. The reaction was heated to 110 °C and allowed to proceed overnight. The resulting QA-modified particles were collected via centrifugation (3645*g*, 10 min, 4 °C), washed thrice with ethanol and dried in vacuo.

5.2.3 N-Diazeniumdiolation of silica nanoparticles

Silica particles were loaded with NO by forming *N*-diazeniumdiolate NO donors on secondary amine sites (Scheme 5.2). Briefly, 20 mg of AHAP/TMOS or QA-modified AHAP/TMOS particles were suspended by sonication in 4 mL of tetrahydrofuran, and trimethylsilanolate was added in a 3.5-fold excess relative to secondary amines, as determined with elemental analysis.[30, 31] The particle suspensions were then placed in a 160 mL Parr general purpose stainless steel pressure vessel with magnetic stirring and connected to an in-house NO reactor. The solutions were flushed 6 times with Ar to remove oxygen from the system, then pressurized to 10 bar with NO that had been scrubbed with KOH. The pressure was maintained at 10 bar for 3 d, after which it was released and the solutions were again purged with Ar to remove unreacted NO. The resulting *N*-diazeniumdiolate-modified silica nanoparticles were collected by centrifugation (3645*g*, 10 min, 4 °C), washed twice

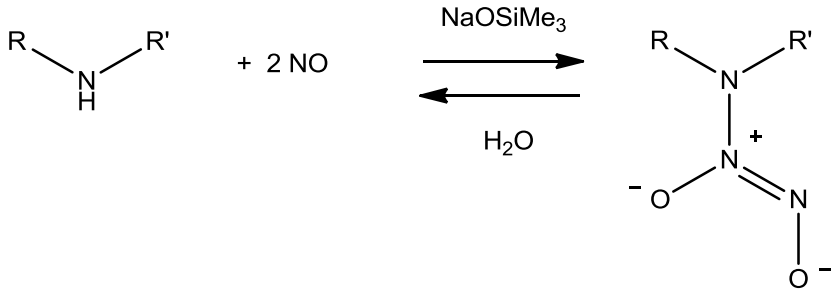

Scheme 5.2 *N*-Diazeniumdiolate NO donors were formed on secondary amines within the particle scaffold upon exposure to high pressures of NO in the presence of a base (e.g., $NaOSiMe_3$). In the presence of a proton source (e.g., H_2O), these NO donors breakdown to regenerate the parent amine and two molecules of NO.

with a 50:50 (v/v) mixture of 5 mM NaOH and methanol to remove unreacted base and byproducts from the particle suspension. The NO-loaded particles were then washed twice with ethanol and dried in vacuo.

5.2.4 Nitric oxide release measurements

Real-time NO release in deoxygenated PBS (pH 7.4) at 37 °C was monitored using Sievers NOA 280i chemiluminescence NO analyzer (NOA, Boulder, CO) connected to a customized reaction cell as described previously.[32] The absence of nitrite byproducts was confirmed by ensuring that total NO concentrations measured from both the Griess assay and the NOA were equal.[33] Prior to analysis, the NO analyzer was calibrated with air passed through a NO zero filter (0 ppm NO) and a 26.39 ppm NO standard gas (balance N_2).

5.2.5 Nanoparticle characterization

The particles' zeta potentials (i.e., surface charge) were measured using a Malvern Zetasizer Nano-ZS equipped with a 10 mW HeNe laser (633 nm) and a NIBS® detector at an angle of 173°. All samples were prepared at 0.5 mg/mL concentrations in either 10 mM NaOH or 10 mM phosphate buffer, sonicated briefly and analyzed at 37 °C. Phosphate buffer (non-saline, pH 7.4) was employed for zeta potential measurements to mimic the media used for bactericidal assays because the high ionic contents of phosphate buffered saline were found to corrode the folded capillary electrodes.[34] Particle size and morphology were characterized using a Hitachi S-4700 Scanning Electron Microscope (Pleasanton, CA). Carbon, hydrogen and nitrogen content were determined on a Perkin Elmer CHN/S elemental analyzer operating in CHN mode. X-ray photoelectron spectroscopy (XPS) analysis was

performed on a Kratos Axis Ultra DLD X-ray Photoelectron Spectrometer with a monochromatic Al Kα X-ray source (150W). Electrons were collected at an angle of 90 degrees from the sample surface from a 300 x 700 μm area on the sample. The pass energy was set to 20 eV to allow for high resolution spectra to be obtained. All spectra were obtained with a step size of 0.1 eV and calibrated to the C1s peak at 284.6 eV.

5.2.6 Bactericidal assays

P. aeruginosa and *S. aureus* were cultured in tryptic soy broth to a concentration of 10^8 colony forming units per mL (CFU/mL), collected by centrifugation, and resuspended in PBS or 1% glucose, 0.5% TSB in PBS, respectively. Of note, *S. aureus* was not viable in PBS alone after 24 h. Each bacteria was diluted to 10^6 CFU/mL and treated with the appropriate concentration of QA-modified, NO-releasing, or NO-releasing QA-functionalized silica nanoparticles. The samples were briefly sonicated and vortexed in order to suspend the particles. After 24 h of incubating at 37 °C, the particle-treated bacteria were spiral plated at 10- and 100-fold dilutions on tryptic soy agar plates. Bacterial viability was assessed by counting the number of colonies formed on the agar plate using a Flash & Go colony counter (IUL, Farmingdale, NY).

5.2.7 Confocal microscopy for detection of intracellular NO and cell death

S. aureus was cultured in TSB to a concentration of 1×10^8 cfu/mL, collected via centrifugation (3645g, 10 min), resuspended in sterile PBS, and adjusted to 1×10^6 cfu/mL in PBS supplemented with 10 μM DAF-2 DA and 30 μM PI. Aliquots of the *S. aureus* solution were incubated in a glass bottom confocal dish for 45 min at 37 °C. A Zeiss 510 Meta

inverted laser scanning confocal microscope with a 488 nm Ar excitation laser (2.0%) and a BP 505–530 nm filter was used to obtain DAF-2 (green) fluorescence images. A 543 nm HeNe excitation laser (25.3%) with a BP 560–615 nm filter was used to obtain PI (red) fluorescence images. The bright field and fluorescence images were collected by a N.A. 1.2 C-apochromat water immersion lens with a 40× objective. Suspensions (1.5 mL) of AHAP/NO (1 mg/mL) or dodecylQA-AHAP/NO (1 mg/mL) particles in PBS (supplemented with 10 μM DAF-2 DA, 30 μM PI) were sonicated and immediately added to the *S. aureus* solution (1.5 mL) in the glass confocal dish. Images were collected every 5 min to observe intracellular NO concentrations and bacteria cell death.

5.2.8 In vitro cytotoxicity

L929 mouse fibroblasts were grown in DMEM supplemented with 10% (v/v) fetal bovine serum (FBS) and 1 wt% penicillin/streptomycin, and incubated in 5% (v/v) CO_2 under humidified conditions at 37 ^{o}C. After reaching 80% confluency, the cells were trypsinized, seeded onto tissue-culture treated polystyrene 96-well plates at a density of 3×10^4 cells/mL and incubated at 37 ^{o}C for 48 h. The supernatant was then aspirated and replaced with 200 μL fresh DMEM and 50 μL of either control (AHAP, methylQA, butylQA, octylQA, dodecylQA) or NO-releasing (AHAP/NO, methylQA/NO, butylQA/NO, octylQA /NO, dodecylQA/NO) nanoparticle suspensions in PBS at the determined MBCs against *P. aeruginosa* or *S. aureus*. After incubation at 37 ^{o}C for 24 h, the supernatant was aspirated and 120 μL mixture of DMEM/MTS/PMS (105/20/1, v/v/v) was added to each well. After 1.5 h incubation at 37 ^{o}C, the solution in each well was transferred to a microcentrifuge tube and centrifuged for 2 minutes to remove the silica particles. Ninety microliters of the supernatant

was then added to a clean microtiter plate, and the absorbance of the colored solutions was quantified at 490 nm using a Thermoscientific Multiskan EX plate reader. The mixture of DMEM/MTS/PMS and untreated cells were used as blank and control, respectively. The cell viability was calculated by taking the ratio of the absorbance of treated cells to the absorbance of untreated cells after subtracting the absorbance of the blank from both.

5.3 Results and discussion

5.3.1 Nanoparticle synthesis and characterization

We have previously reported the synthesis of amine-functionalized silica particles capable of variable NO storage and release characteristics.[22, 28, 35] For this study, particles were synthesized by hydrolyzing and co-condensing *N*-(6-aminohexyl)aminopropyltrimethoxysilane (AHAP) and tetramethoxysilane (TMOS) via a modified Stöber process. *N*-(6-aminohexyl)aminopropyltrimethoxysilane was selected as the NO-donor precursor due to its suitability for tethering QA functionalities via primary amines. The AHAP particles employed in this study were characterized by a spherical morphology and diameters of 180±26 nm as determined by scanning electron microscopy (Figure 1A). Dynamic light scattering (DLS) analysis indicated that the particles were monodisperse with a polydispersity index (PDI) of 0.07±0.02 and a measured Z-average (190±7 nm), consistent with diameters observed with SEM. Employing a monodisperse particle system is important for studying antimicrobial efficacy as particle size has been shown to impact bactericidal activity.[22]

The AHAP silica particles were modified with QA functionalities via a ring-opening reaction between surface primary amines and QA-epoxides (Scheme 5.1). While

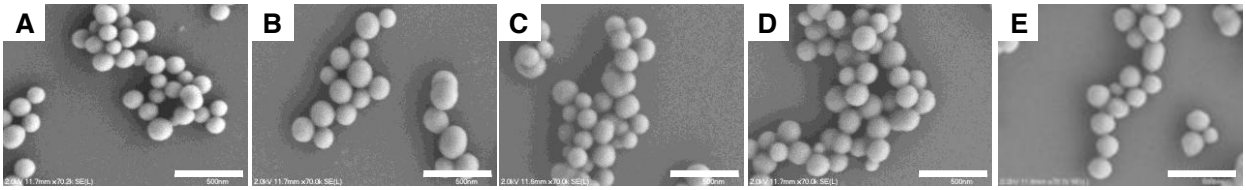

Figure 5.1 Scanning electron micrographs of (A) AHAP (d=180±26 nm), (B) methylQA (d=181±27 nm), (C) butylQA (d=187±23 nm), (D) octylQA (d=185±26 nm), and (E) dodecylQA (d=187±24 nm) nanoparticles. Scale bar = 500 nm.

glycidyltrimethylammonium chloride is commercially available, earlier work demonstrated optimal bactericidal efficacy with long chain QAs.[9, 36, 37] Quaternary ammonium-epoxides containing longer alkyl chains were thus synthesized by reacting epichlorohydrin with dimethylbutylamine, dimethyloctylamine, or dimethyldodecylamine (Scheme 5.1). The formation of the QA epoxides was confirmed with ^{1}H and ^{13}C NMR, IR spectroscopy, and ESI mass spectrometry (Appendix B). A shift in the ^{1}H NMR resonances corresponding to the protons alpha to Cl/N and those of the nitrogen-bound methyl groups confirmed the formation of the QA epoxide. Infrared absorbance bands indicating the QA-epoxide structure were also observed at 970 cm^{-1} (QA),[38] 1267 cm^{-1} (epoxide ring), and at 2920 and 2850 cm^{-1} (saturated CH). The intensity of the saturated CH absorbance increased with the increase in the length of the alkyl chain.

The addition of QA groups to the particle surface was confirmed by monitoring changes in the nitrogen environments (N 1s) using X-ray photoelectron spectroscopy (XPS). As shown in Figure 5.2A, the N 1s peak for unmodified AHAP particles was fit with two component peaks at binding energies of 399 and 400 eV, corresponding to primary and secondary amines, respectively. The N 1s peak of QA-functionalized particles consisted of a third component at 402 eV, representing the quaternary ammonium (Figure 5.2B–E).[39] The R_4N^+ peak was most intense for the methylQA-modified particles. The presence of a peak at 399 eV for all QA-functionalized particles indicates that not all primary amines at the particle surface were functionalized. As expected, the synthetic strategy for QA surface modification did not influence particle size or morphology (Figure 5.1B–E).

Quaternary ammonium functionalization was also verified by observing changes in the zeta potentials between AHAP and QA-modified AHAP particles using laser doppler

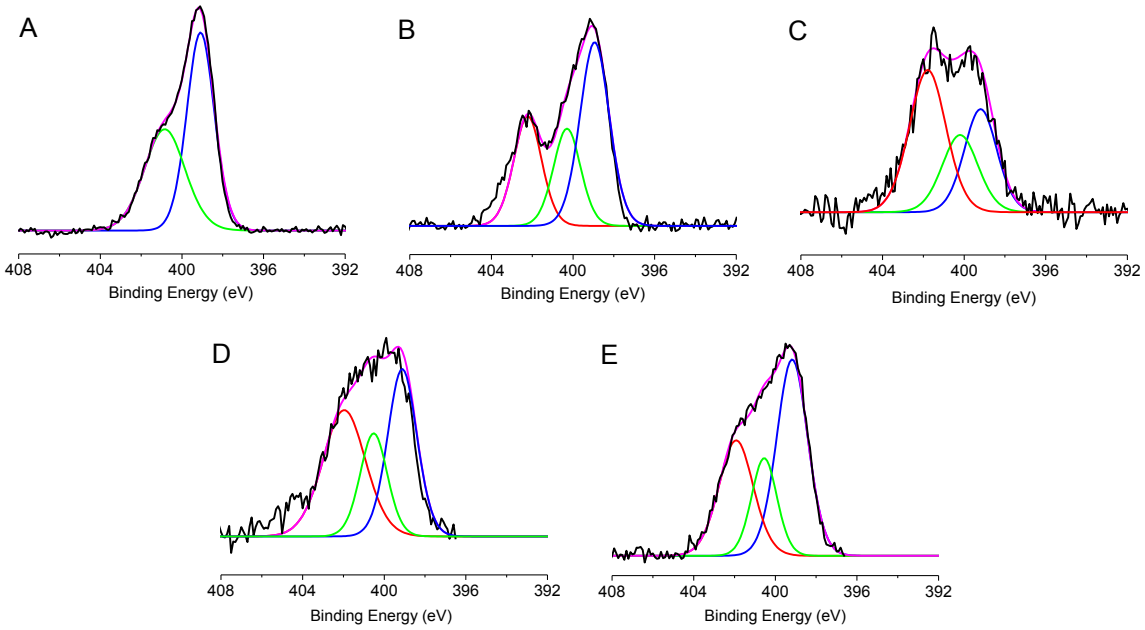

Figure 5.2 X-ray photoelectron (XPS) spectra of the N 1s peak of (A) AHAP, (B) methylQA, (C) butylQA, (D) octylQA, and (E) dodecylQA nanoparticles. The presence of primary (blue), secondary (green) and quaternary (red) amines are indicated by fitted curves at binding energies of 399, 401, and 402 eV, respectively.

velocimetry (LDV). In 10 mM phosphate buffer PB, both unmodified AHAP and QA-modified particles exhibited a positive zeta potential due to the presence of protonated primary amines or positively charged QAs, respectively. In contrast, the zeta potential for the unmodified AHAP particles became negative in basic media (10 mM NaOH), whereas the QA-functionalized particles remained positively charged (Table 5.1), indicating the presence of a permanent, pH-independent positive charge. A slight decrease in the zeta potential for longer chained QA-modified particles was observed with increasing pH, which was also accompanied by a decrease in the derived count rates. Since all samples were prepared at the same concentration using similarly sized particles, the decrease in the derived count rate indicates sedimenting particles,[40] an expected phenomenon for more hydrophobic particles. Of note, the derived count rate and zeta potential of methylQA particles did not change regardless of pH. Overall, the larger count rates for the QA-modified particles in 10 mM NaOH suggest the positively charged particles are more stabilized in basic solution due to an abundance of negatively charged ions supporting the Stern layer.[40]

5.3.2 Nitric oxide release analysis

The silica particles were exposed to high pressures of NO in the presence of a base to form *N*-diazeniumdiolates NO donors (i.e., NONOates) on the secondary amines. As shown in Figure 5.2, NONOate formation was confirmed by an absorbance maximum at 253 nm.[20] Figure 5.2 also depicts the absorbance from non-NO-releasing dodecyl-QA-modified AHAP, indicating the absence of the peak at 253 nm prior to exposure to NO. Of note, no absorbance maximum is present at 450 nm following exposure to NO, indicating the scaffolds are free of cytotoxic nitrosamines.[41]

Table 5.1 Zeta potential measured from AHAP and QA-modified AHAP particle solutions.

	Zeta Potential (mV)	
	10 mM NaOH	10 mM PB
AHAP	-9.4±0.6	20.5±1.0
MethylQA	24.6±1.9	23.7±1.7
ButylQA	20.9±0.9	16.8±1.1
OctylQA	23.0±1.4	11.6±1.4
DodecylQA	22.8±0.6	19.8±0.6

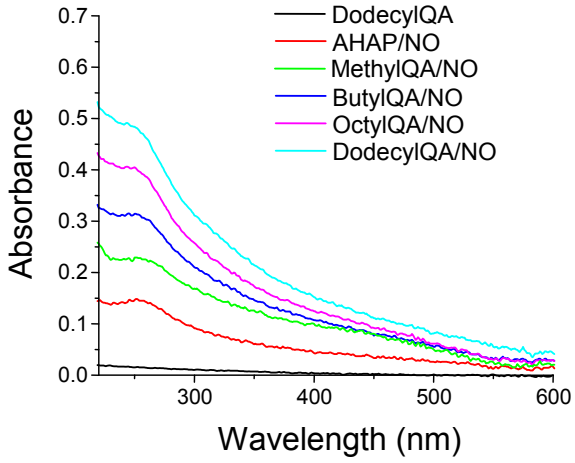

Figure 5.3 UV-Vis absorbance spectra of *N*-diazeniumdiolate-modified AHAP and QA silica nanoparticles. Unmodified dodecylQA is shown for comparison.

Nitric oxide storage and delivery was evaluated by monitoring NO production in real time via chemiluminescence. The addition of QA-functionalities did not influence the amine to NONOate conversion as each scaffold released similar NO payloads of ca. 0.3 μmol/mg (Table 5.2). As such, the role of QA alkyl chain length on bactericidal efficacy could be elucidated since NO release remained constant. The Griess assay was used to confirm that no nitrite was formed during the NONOate reaction and NO liberation.[33] As is typical for NONOate-based silica particles,[28, 35] the real-time NO release profiles exhibited a maximum instantaneous NO concentration ($[NO]_{max}$) that was achieved shortly after the particles were introduced into the solution. The unmodified AHAP/NO and methylQA/NO were characterized as having similar $[NO]_{max}$ values (1388±161 and 1034±32 ppb/mg, respectively), whereas butylQA/NO, octylQA/NO, and dodecyl/NO had lower $[NO]_{max}$ (882±36, 791±52, 617±68 ppb/mg, respectively). The decrease in $[NO]_{max}$ with increasing alkyl chain may be attributed to the increased surface hydrophobicity that slows the rate of water diffusion into the particle scaffold. Such behavior was further demonstrated by an increase in the time to reach $[NO]_{max}$ (i.e., t_{max}) with increasing QA alkyl chain length. The NO payloads for each particle system were completely depleted by 24 h.

5.3.3 Bactericidal efficacy

S. aureus and *P. aeruginosa* are two of the most commonly isolated species in chronic wounds and were therefore selected as the test microbes to evaluate the efficacy of the QA-functionalized nanoparticles presented herein.[42] We sought to test our nanoparticles against both Gram-positive (*S. aureus*) and Gram-negative (*P. aeruginosa*) bacteria strains as previous work has shown that the potency of both NO- and QA-based

Table 5.2 Nitric oxide release properties of unmodified and QA-modified silica nanoparticles, including total NO release ($[NO]_T$), maximum instantaneous concentration of NO ($[NO]_{max}$), and time to reach $[NO]_{max}$ (t_{max}).

	$[NO]_T$ (μmol/mg)	$[NO]_{max}$ (ppb/mg)	t_{max} (min)
AHAP/NO	0.27±0.04	1388±161	1.5±0.2
MethylQA/NO	0.30±0.03	1034±32	1.8±0.3
ButylQA/NO	0.27±0.03	882±36	2.3±0.2
OctylQA/NO	0.28±0.04	791±52	2.9±0.6
DodecylQA/NO	0.27±0.04	617±68	4.3±0.8

antimicrobials depend greatly on the bacterial membrane composition.[14, 43] Prior to evaluating the bactericidal activity of the dually functional nanoparticles, the efficacy of the monofunctional formulations alone (i.e., NO-releasing or QA-functionalized) were evaluated to fully understand the benefit of designing a combination approach.

The AHAP/NO particles proved to be significantly more effective against *P. aeruginosa* compared to *S. aureus* with MBC_{24h} of 1.5 and 3.5 mg/mL, respectively (Figure 5.4). These results are consistent with previously reported *N*-diazeniumdiolate-based NO-releasing nanoparticles.[21] Conversely, the antimicrobial activity of the QA-functionalized particles was greater against *S. aureus* than *P. aeruginosa* (Figure 5.4). Chen et al. also reported greater sensitivity of Gram-positive bacteria to QA-based antimicrobials compared to Gram-negative bacteria.[14] As shown in Figure 5.4, the methylQA particles did not present appreciable toxicity to either of the microbes tested. As expected, the bactericidal efficacy of QA-modified particles exhibited a strong dependence on alkyl chain length. Increasing the alkyl chain length from methyl to butyl, octyl and dodecyl resulted in a decrease in MBC_{24h} from 4.0, 3.0 and 1.5 mg/mL against *S. aureus*, respectively. OctylQA and dodecylQA particles were equally effective against *P. aeruginosa* and more effective than the butylQA scaffolds. Antimicrobial activity of short chained QAs results from the positively charged ammonium group complexing with the negatively charged bacterial cell membrane to disrupt membrane functions, alter the balance of essential ions (i.e., K^+, Na^+, Ca^{2+}, and Mg^{2+}), interrupt protein activity, and damage bacterial DNA.[44] Long alkyl chain QAs can exert additional antimicrobial activity by inserting into the bacterial membrane, resulting in physical disruption.[44] Indeed, longer alkyl chains have been shown to be more effective due to deeper penetration into the membrane and concomitant disruption.[9, 36, 37]

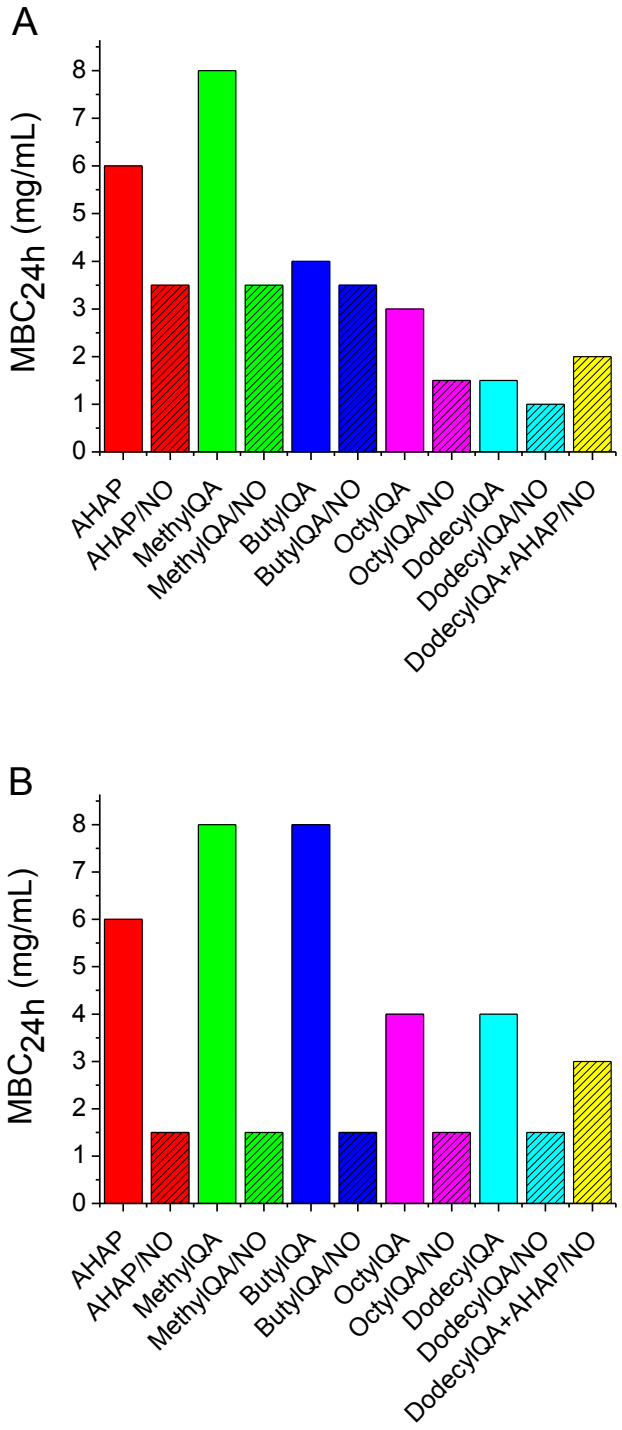

Figure 5.4 Minimum bactericidal concentrations (MBC_{24h}) against (A) *S. aureus* and (B) *P. aeruginosa* for non-NO-releasing (solid) and NO-releasing (hashed) AHAP (red), methylQA (green), butylQA (blue), octylQA (magenta), dodecylQA (cyan). Treatment with a 50:50 (w/w) mixture of dodecylQA and AHAP/NO particles is shown in yellow (hashed).

The advantages of combining antimicrobial strategies on the same scaffold have previously been demonstrated with QA-functionalized surfaces that release an antimicrobial agent, such as silver ion[7, 17] or gentamicin.[18] Although these releasable therapies are potent antimicrobials, resistance concerns plaque their wide-spread use.[45, 46] The QA-functionalized particles described herein were designed to allow for the release of NO, a broad-spectrum antimicrobial with low risk of resistance.[25] As shown in Figure 5.4, NO-releasing long chain (i.e., octyl and dodecyl) QA-functionalized particles exhibited increased toxicity against *S. aureus* compared to particles functionalized with short chain (i.e., methyl or butyl) QAs or NO release alone. Nitric oxide-releasing AHAP/NO, methylQA/NO, and butylQA/NO were equally effective against *S. aureus* with an MBC_{24h} of 3.5 mg/mL. Increasing the alkyl chain length of NO-releasing QA particles to octyl and dodecyl improved the antimicrobial activity with a substantial decrease in MBC_{24h} to 1.5 and 1.0 mg/mL, respectively. Disruption of the bacterial membrane by the long chain QAs may allow for greater oxidative stress due to increased intracellular NO levels compared to treatment with AHAP/NO.[43] The combination of NO release and QA modification (i.e., NO-releasing QA-functionalized particles) did not alter the antimicrobial efficacy against *P. aeruginosa* compared to unfunctionalized NO-releasing particles (i.e., AHAP/NO). These results reflect those of the monofunctional particles, where the MBC_{24h} of dodecylQA was much greater than that of AHAP/NO against *P. aeruginosa*.

To prove the advantage of co-treatment with QA-functionalized NO-releasing particles, we treated *S. aureus* and *P. aeruginosa* to 25% of the MBC_{24h} values of dodecylQA and AHAP/NO either simultaneous or at 30 min intervals. Sublethal doses were used to avoid complete killing and allow for viable enumeration, and short exposure intervals were

used to inhibit the production of new or repaired cells.[43] As shown in Figure 5.5, the simultaneous addition of the two separate antimicrobial particles resulted in greater antimicrobial action against *S. aureus* than when the microbes were exposed to one agent (e.g., AHAP/NO or dodecylQA) followed by the second 30 min later. In comparison, the decrease in *P. aeruginosa* viability was the same for all combination treatments regardless of the addition order. These latter results were not surprising as the antimicrobial activity of NO-releasing dodecylQA was equal to that of NO-releasing AHAP/NO against *P. aeruginosa*.

Confocal microscopy was used to study the antimicrobial mechanisms of NO-releasing dodecylQA/NO particles against *S. aureus*. DAF-2, a green fluorescent marker for intracellular NO, and PI, a red fluorescent marker for a compromised membrane, were used to visualize the effects of the NO-release scaffolds on the bacteria. As shown in Figure 5.7, treatment with dodecylQA/NO resulted in red fluorescence and weak green fluorescence after 60 min. Conversely, treatment with AHAP/NO for the same time period resulted in strong green fluorescence due to DAF without the presence of red fluorescence. Thus, the QA-functionalities were observed to cause membrane disruption, even before significant intracellular NO concentrations were achieved. As expected, the intensity of the green fluorescence increased with incubation time, indicating elevation of the intracellular NO concentrations. Moreover, the faster release kinetics of AHAP/NO compared to dodecylQA/NO resulted in greater intracellular NO concentrations at shorter exposure times.

Small differences in the physical and chemical properties of nanomaterials have been shown to greatly influence nanoparticle-cell interactions,[47] suggesting that the use of dual function nanoparticles may be more favorable than co-administering two different

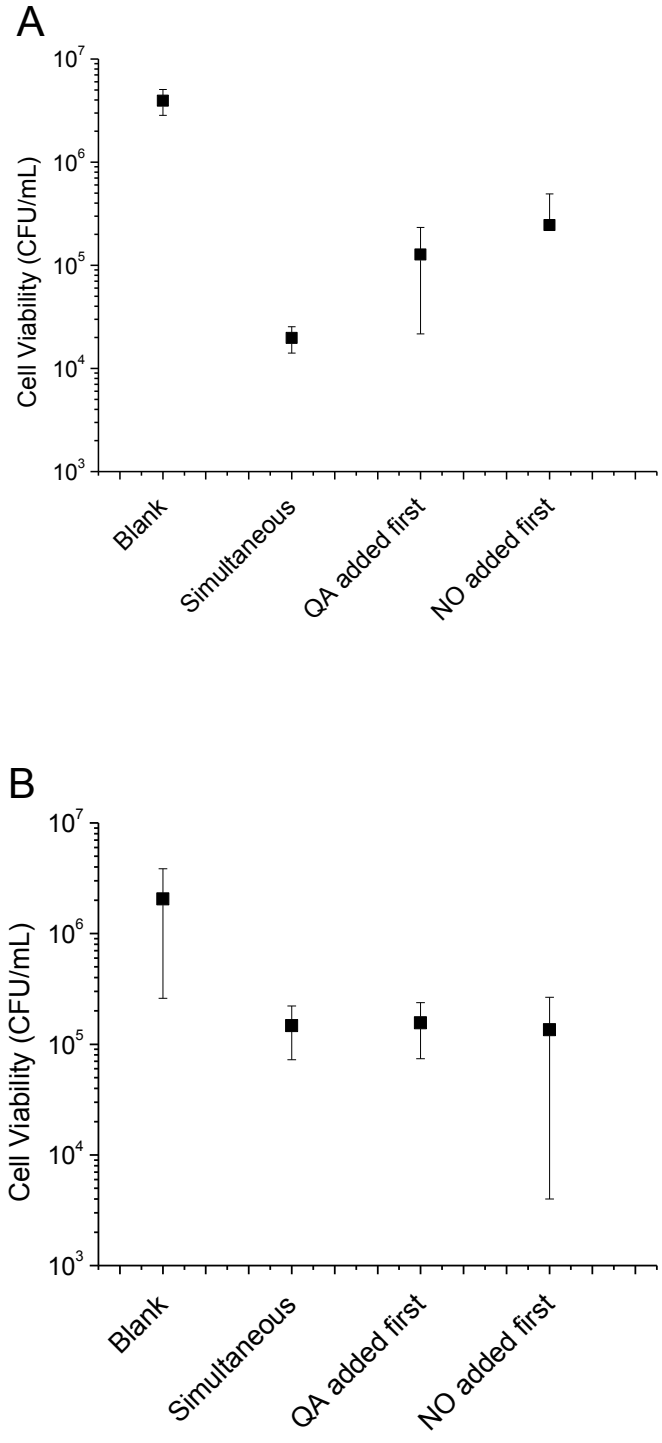

Figure 5.5 Change in bacterial viability of (A) *S*. *aureus* and (B) *P*. *aeruginosa* following exposure to sublethal doses of dodecylQA and/or AHAP/NO nanoparticles either simultaneously or at 30 min intervals.

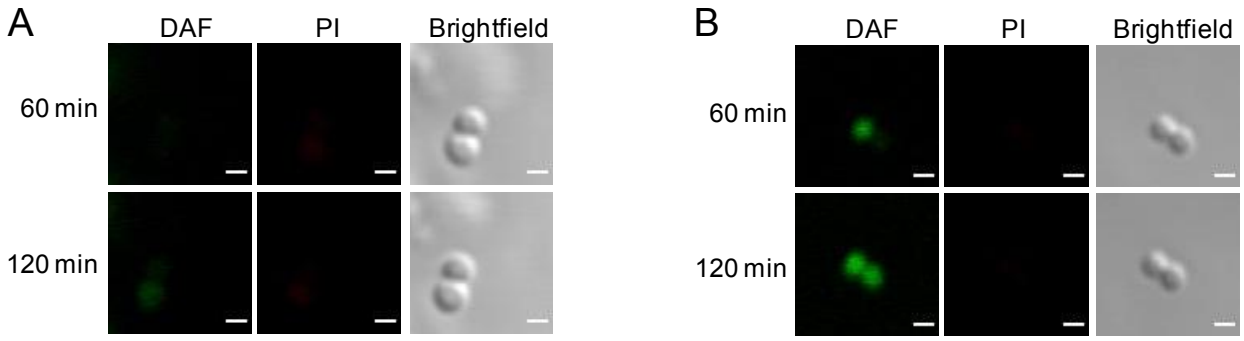

Figure 5.6 Confocal microscopy images of *S. aureus* exposed to (A) dodecylQA/NO and (B) AHAP/NO particles exhibit green fluorescence due to intracellular NO (DAF) and red fluorescence due to compromised membrane (PI). Scale bar = 1 μm.

monofunctional nanoparticles. To investigate the validity of this hypothesis, the MBC_{24h} of a mixture of dodecylQA and AHAP/NO (50:50 w/w) particles was also determined. The MBC_{24h} of the dodecylQA+AHAP/NO particle mixture was 2.0 and 3.0 mg/mL against *S. aureus* and *P. aeruginosa*, respectively. The NO and QA concentrations of the 50:50 dodecylQA+AHAP/NO mixture correspond to the same NO and QA concentrations delivered from the MBC_{24h} doses of dodecylQA/NO (i.e., 1.0 and 1.5 mg/mL, respectively). Thus, combining NO release and QA-functionalities on the same scaffold proved advantageous as a lower total dose of particles was required to induce bactericidal efficacy compared to treatment with a mixture of two monofunctional particles.

5.3.4 In vitro cytotoxicity

The ultimate utility of next generation antimicrobials is often governed by their toxicity to mammalian cells, assuming adequate microbial killing. Although long chain quaternary ammonium salts have long been used clinically, they are mostly restricted to topical applications due to their toxicity against mammalian cells.[37, 48] However, tethering QAs to a macromolecular scaffold has been shown to decrease their toxicity toward eukaryotic cells.[48] We thus evaluated the toxicity of QA- and NO-releasing QA-functionalized particles against L929 fibroblasts cells (Figure 5.7). Fibroblast cells represent the standard for cytotoxicity screening of new antimicrobials due to their involvement in wound healing and the immune response.[49, 50] The viability of fibroblasts cells was monitored via the MTS assay following 24 h exposure to the MBC_{24h} against both *S. aureus* and *P. aeruginosa*. Control AHAP particles exhibited significant toxicity at the high particle dose of 6.0 mg/mL due to the presence of primary amines.[21, 51] Conversion of the primary

amines to trimethylQA groups caused a significant decrease in the observed cytotoxicity, as 8 mg/mL of methylQA particles only decreased viability by 40%. The cytotoxicity of QA-functionalized particles against fibroblasts at their MBC increased with increasing alkyl chain length. For example, 4.0 mg/mL butylQA, octylQA or dodecylQA-modified particles resulted in a 45, 60, and 94% decrease in viability, respectively.

Due to the lower concentrations of particles required for microbial killing with NO release, the cytotoxicity of NO-releasing QA-particles against fibroblast was notably less. For example, the 94% decrease in fibroblast viability for 4.0 mg/mL dodecylQA (MBC_{24h} against *P. aeruginosa*) was reduced to only 31% for dodecylQA/NO (MBC_{24h} of 1.5 mg/mL). Unexpectedly, the addition of NO release resulted in an increase in cytotoxicity for the short-chained QAs, suggesting that lower fluxes of NO may be more biocompatible to mammalian cells. In combination, the decreased cytotoxicity and increased bactericidal efficacy of NO-releasing long chain QA-functionalized particles indicate their advantage over QA-functionalized particles alone.

5.4 Conclusions

Quaternary ammonium (QA)-functionalized particles exhibited antimicrobial action against both *S. aureus* and *P. aeruginosa*, with long alkyl-chain QAs (e.g., octyl and dodecyl) proving more potent than short alkyl-chain QAs (e.g., methyl and butyl). The functionalization of particles with both QA groups and NO donors resulted in particles with even more favorable antimicrobial activity against *S. aureus* compared to monofunctional QA-functionalized or NO-releasing particles alone. Conversely, the antimicrobial activity of the hybrid particles against *P. aeruginosa* was unchanged relative to the NO-releasing only

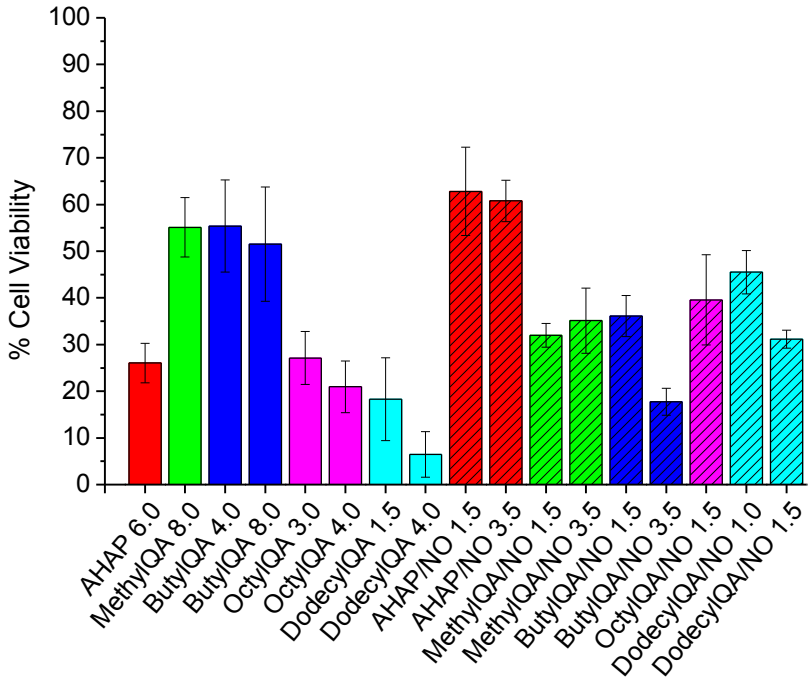

Figure 5.7 Percent viability of L929 mouse fibroblasts cells following 24 h exposure to non-NO-releasing (solid) and NO-releasing (hashed) AHAP (red), methylQA (green), butylQA (blue), octylQA (magenta), and dodecylQA (cyan) particles compared to control (untreated) cells with the numbers corresponding to the MBC_{24h} against *S*. *aureus* and *P*. *aeruginosa* (in mg/mL dose).

particles. Overall, *S*. *aureus* was more sensitive to QA particle treatment, while the inverse was true for *P*. *aeruginosa* (greater sensitivity to NO). In addition, hybrid NO release/QA-functionalized particles proved to be more effective at microbial killing than mixtures of NO-releasing and QA-functionalized particles. The design of scaffolds expressing multiple antimicrobial mechanisms of action may represent an important strategy for lowering the concentration of therapy required and reducing the risk of potential resistance.

References

1. Coates, A.; Hu, Y. M.; Bax, R.; Page, C. "The future challenges facing the development of new antimicrobial drugs." *Nat*. *Rev*. *Drug Discov*. **2002**, *1*, 895-910.

2. Fischbach, M. A. "Combination therapies for combating antimicrobial resistance." *Curr*. *Opin*. *Microbiol*. **2011**, *14*, 519-523.

3. Allahverdiyev, A. M.; Kon, K. V.; Abamor, E. S.; Bagirova, M.; Rafailovich, M. "Coping with antibiotic resistance: Combining nanoparticles with antibiotics and other antimicrobial agents." *Exp*. *Rev*. *Anti*. *Infect*. *Ther*. **2011**, *9*, 1035-1052.

4. Mintzer, M. A.; Dane, E. L.; O'Toole, G. A.; Grinstaff, M. W. "Exploiting dendrimer multivalency to combat emerging and re-emerging infectious diseases." *Mol*. *Pharmaceut*. **2012**, *9*, 342-354.

5. Huh, A. J.; Kwon, Y. J. ""Nanoantibiotics": A new paradigm for treating infectious diseases using nanomaterials in the antibiotics resistant era." *J*. *Control*. *Release* **2011**, *156*, 128-145.

6. Tashiro, T. "Antibacterial and bacterium adsorbing macromolecules." *Macromol*. *Mater*. *Eng*. **2001**, *286*, 63-87.

7. Li, Z.; Lee, D.; Sheng, X.; Cohen, R. E.; Rubner, M. F. "Two-level antibacterial coating with both release-killing and contact-killing capabilities." *Langmuir* **2006**, *22*, 9820-9823.

8. Dong, H.; Huang, J.; Koepsel, R. R.; Ye, P.; Russell, A. J.; Matyjaszewski, K. "Recyclable antibacterial magnetic nanoparticles grafted with quaternized poly(2-(dimethylamino)ethyl methacrylate) brushes." *Biomacromolecules* **2011**, *12*, 1305-1311.

9. Jiang, S.; Wang, L.; Yu, H.; Chen, Y. "Preparation of crosslinked polystryenes with quaternary ammonium and their antibacterial behavior." *React*. *Funct*. *Polym*. **2005**, *62*, 209-213.

10. Yao, C.; Li, X.; Neoh, K. G.; Shi, Z.; Kang, E. T. "Surface modification and antibacterial activity of electrospun polyurethane fibrous membranes with quaternary ammonium moieties." *J*. *Membr*. *Sci*. **2008**, *320*, 259-267.

11. Huang, J.; Koepsel, R. R.; Murata, H.; Wu, W.; Lee, S. B.; Kowalewski, T.; Russell, A. J.; Matyjaszweski, K. "Nonleaching antibacterial glass surface via "Grafting onto": The effect of the number of quaternary ammonium groups on biocidal activity." *Langmuir* **2008**, *24*, 6785-6795.

12. Oosterhof, J. J. H.; Buijssen, K. J. D. A.; Busscher, H. J.; van der Laan, B. F. A. M.; van der Mei, J. C. "Effects of quaternary ammonium silane coatings on mixed fungal and bacterial biofilms on tracheoesophageal shunt prostheses." *Appl*. *Environ*. *Microbiol*. **2006**, *72*, 3673-3677.

13. Majumdar, P.; Crowley, E.; Htet, M.; Stafslien, S. J.; Daniels, J.; VanderWal, L.; Chisholm, B. J. "Combinatorial materials research applied to the development of new surface coatings XV: An investigation of polysiloxane anti-fouling/fouling-release coatings containing tethered quaternary ammonium salt groups." *ACS Comb. Sci* **2011**, *13*, 298-309.

14. Chen, C. Z.; Beck-Tan, N. C.; Dhurjati, P.; van Dyk, T. K.; LaRossa, R. A.; Cooper, S. L. "Quaternary ammonium functionalized poly(propylene imine) dendrimers as effective antimicrobials: Structure-activity studies." *Biomacromolecules* **2000**, *1*, 473-480.

15. Song, J.; Kong, H.; Jang, J. "Bacterial adhesion inhibition of the quaternary ammonium functionalized silica nanoparticles." *Colloids Surf. B* **2011**, *82*, 651-656.

16. Beyth, N.; Yudovin-Farber, I.; Perez-Davidi, M.; Domb, A. J.; Weiss, E. I. "Polyethyleneimine nanoparticles incorporated into resin composite cause cell death and trigger biofilm stress in vivo." *Proc. Natl. Acad. Sci. U.S.A.* **2010**, *107*, 22038-22043.

17. Song, J.; Kang, H.; Lee, C.; Hwang, S. H.; Jang, J. "Aqueous synthesis of silver nanoparticle embedded cationic polymer nanofibers and their antibacterial activity." *ACS Appl. Mater. Interfaces* **2012**, *4*, 460-465.

18. Wong, S. Y.; Moskowitz, J. S.; Veselinovic, J.; Rosario, R. A.; Timachova, K.; Blaisse, M. R.; Fuller, R. C.; Klibanov, A. M.; Hammond, P. T. "Dual functional polyelectrolyte multilayer coatings for implants: Permanent microbicidal base with controlled release of therapeutic agents." *J. Am. Chem. Soc.* **2010**, *132*, 17840-17848.

19. Lee, J. E.; Lee, N.; Kim, T.; Kim, J.; Hyeon, T. "Multifunctional mesoporous silica nanocomposite nanoparticles for theranostic applications." *Acc. Chem. Res.* **2011**, *44*, 893-902.

20. Hetrick, E. M.; Shin, J. H.; Stasko, N. A.; Johnson, C. B.; Wespe, D. A.; Holmuhamedov, E.; Schoenfisch, M. H. "Bactericidal efficacy of nitric oxide-releasing silica nanoparticles." *ACS Nano* **2008**, *2*, 235-246.

21. Hetrick, E. M.; Shin, J. H.; Paul, H. S.; Schoenfisch, M. H. "Anti-biofilm efficacy of nitric oxide-releasing silica nanoparticles." *Biomaterials* **2009**, *30*, 2782-2789.

22. Carpenter, A. W.; Slomberg, D. L.; Rao, K. S.; Schoenfisch, M. H. "Influence of scaffold size on bactericidal activity of nitric oxide-releasing silica nanoparticles." *ACS Nano* **2011**, *5*, 7235-7244.

23. Jones, M. L.; Ganopolsky, J. G.; Labbe, A.; Wahl, C.; Prakash, S. "Antimicrobial properties of nitric oxide and its application in antimicrobial formulations and medical devices." *Appl. Microbiol. Biotechnol.* **2010**, *88*, 401-407.

24. Ghaffari, A.; Miller, C. C.; McMullin, B.; Ghahary, A. "Potential application of gaseous nitric oxide as a topical antimicrobial agent." *Nitric Oxide* **2006**, *14*, 21-29.

25. Privett, B. J.; Broadnax, A. D.; Bauman, S. J.; Riccio, D. A.; Schoenfisch, M. H. "Examination of bacterial resistance to exogenous nitric oxide." *Nitric Oxide-Biol. Chem.* **2012**, *26*, 169-173.

26. Riccio, D. A.; Schoenfisch, M. H. "Nitric oxide release: Part I. Macromolecular scaffolds." *Chem. Soc. Rev.* **2012**.

27. Carpenter, A. W.; Schoenfisch, M. H. "Nitric oxide release: Part II. Therapeutic applications." *Chem. Soc. Rev.* **2012**, *41*, 3742-3752.

28. Shin, J. H.; Metzger, S. K.; Schoenfisch, M. H. "Synthesis of nitric oxide-releasing silica nanoparticles." *J. Am. Chem. Soc.* **2007**, *129*, 4612-4619.

29. Koh, A.; Riccio, D. A.; Sun, B.; Carpenter, A. W.; Nichols, S. P.; Schoenfisch, M. H. "Fabrication of nitric oxide-releasing polyurethane glucose sensor membranes." *Biosens. Bioelectron.* **2011**, *28*, 17-24.

30. DeRosa, F.; Keefer, L. K.; Hrabie, J. A. "Nitric oxide reacts with methoxide." *J. Org. Chem.* **2008**, *73*, 1139-1142.

31. Reynolds, M. M.; Saavedra, J. E.; Showalter, B. M.; Valdez, C. A.; Shanklin, A. P.; Oh, B. K.; Keefer, L. K.; Meyerhoff, M. E. "Tailored synthesis of nitric oxide-releasing polyurethanes using O^2-protected diazeniumdiolate chain extenders." *J. Mater. Chem.* **2010**, *20*, 3107-3114.

32. Riccio, D. A.; Nugent, J. L.; Schoenfisch, M. H. "Stober synthesis of nitric oxide-releasing *S*-nitrosothiol-modified silica particles." *Chem. Mater.* **2010**, *23*, 1727-1735.

33. Coneski, P. N.; Schoenfisch, M. H. "Nitric oxide release: Part II. Measurement and reporting." *Chem. Soc. Rev.* **2012**.

34. Clogston, J. D., Ncl method pcc-2: Measuring zeta potential of nanoparticles. Nanotechnology Characterization Laboratory, N. C. I., Ed. Frederick, MD, 2009.

35. Shin, J. H.; Schoenfisch, M. H. "Inorganic/organic hybrid silica nanoparticles as a nitric oxide delivery scaffold." *Chem. Mater.* **2008**, *20*, 239-249.

36. Majumdar, P.; Lee, E.; Gubbins, N.; Christianson, D. A.; Stafslien, S. J.; Daniels, J.; VanderWal, L.; Bahr, J.; Chisholm, B. J. "Combinatorial materials research applied to the development of new surface coatings XIII: An investigation of polysiloxane antimicrobial coatings containing tethered quaternary ammonium salt groups." *J. Combin. Chem.* **2009**, *11*, 1115-1127.

37. Thorsteinsson, T.; Masson, M.; Kristinsson, K. G.; Hjalmarsdottir, M. A.; Hilmarsson, H.; Loftsson, T. "Soft antimicrobial agents: Synthesis and activity of labile environmentally friendly long chain quaternary ammonium compounds." *J. Med. Chem.* **2003**, *46*, 4173-4181.

38. Beyth, N.; Houri-Haddad, Y.; Baraness-Hadar, L.; Yudovin-Farber, I.; Domb, A. J.;

Weiss, E. I. "Surface antimicrobial activity and biocompatibility of incorporated polyethylenimine nanoparticles." *Biomaterials* **2008**, *29*, 4157-4163.

39. Shi, Z.; Neoh, K. G.; Kang, E. T.; Wang, W. "Antibacterial and mechanical properties of bone cement impregnated with chitosan nanoparticles." *Biomaterials* **2006**, *27*, 2440-2449.

40. Malvern *Zetasizer nano series user manual*. Malvern Instruments, Ltd.: Worcestershire, 2007.

41. Coneski, P. N.; Schoenfisch, M. H. "Competitive formation of *N*-diazeniumdiolates and *N*-nitrosamines via anaerobic reactions of polyamines with nitric oxide." *Org*. *Lett*. **2009**, *11*, 5462-5465.

42. Bjarnsholt, T.; Kirketerp-Møller, K.; Jensen, P. Ø.; Madsen, K. G.; Phipps, R.; Krogfelt, K.; Høiby, N.; Givskov, M. "Why chronic wounds will not heal: A novel hypothesis." *Wound Repair Regen*. **2008**, *16*, 2-10.

43. Privett, B. J.; Deupree, S. M.; Backlund, C. J.; Rao, K. S.; Johnson, C. B.; Coneski, P. N.; Schoenfisch, M. H. "Synergy of nitric oxide and silver sulfadiazine against gram-negative, gram-positive, and antibiotic-resistant pathogens." *Mol*. *Pharmaceut*. **2010**, *7*, 2289-2296.

44. Simoncic, B.; Tomsic, B. "Structures of novel antimicrobial agents for textiles - a review." *Text*. *Res*. *J*. **2010**, *80*, 1721-1737.

45. Silver, S. "Bacterial silver resistance: Molecular biology and uses and misuses of silver compounds." *FEMS Microbiol*. *Rev*. **2003**, *27*, 341-353.

46. Mohamed, A. F.; Nielsen, E. I.; Cars, O.; Friberg, L. E. "Pharmacokinetic-pharmacodynamic model for gentamicin and its adaptive resistance with predictions of dosing schedules in newborn infants." *Antimicrob*. *Agents Chemother*. **2012**, *56*, 179-188.

47. Wang, J.; Byrne, J. D.; Napier, M. E.; DeSimone, J. M. "More effective nanomedicines through particle design." *Small* **2011**, *7*, 1919-1931.

48. Lv, H.; Zhang, S. W.; Wang, B.; Cui, S.; Yan, J. "Toxicity of cationic lipids and cationic polymers in gene delivery." *J*. *Control*. *Release* **2006**, *114*, 100-109.

49. Lineaweaver, W.; McMorris, S.; Soucy, D.; Howard, R. "Cellular and bacterial toxicities of topical antimicrobials." *Plast*. *Reconstr*. *Surg*. **1985**, *75*, 394-396.

50. Thelestam, M.; Mollby, R. "Cultured human-fibroblasts as a model for evaluation of potential in vivo toxicity of membrane damaging antibiotics." *Chem*. *Biol*. *Interact*. **1980**, *29*, 315-325.

51. Stasko, N. A.; Johnson, C. B.; Schoenfisch, M. H.; Johnson, T. A.; Holmuhamedov, E. L. "Cytotoxicity of polypropylenimine dendrimer conjugates on cultured endothelial cells." *Biomacromolecules* **2007**, *8*, 3853-3859.

Chapter 6:

Summary and Future Directions

6.1 Summary

The synthesis of NO-releasing silica nanoparticles of various physical and chemical properties was thoroughly evaluated and found to impact both NO release properties and therapeutic potential. Chapter 1 reviewed reported methods for designing and synthesizing functionalized silica nanoparticles for biomedical applications, with a focus on their use as nitric oxide delivery scaffolds. The introduction served to instruct on the importance of specific particle properties on therapeutic outcome and to provide methods for varying physical and chemical characteristics of nanoparticles. In Chapter 2, physical properties (e.g., size) of NO-releasing silica nanoparticles was found to greatly influence their bactericidal efficacy. A reverse microemulsion technique was used to achieve particles of specific sizes (diameter= 50, 100 and 200 nm) and monodisperse populations (PDI<0.2), while maintaining constant chemical composition (i.e., amine content and NO donors). The role of scaffold size on bactericidal efficacy against *P. aeruginosa* could thus be evaluated by delivering equal NO release payloads. Minimum bactericidal concentrations improved with decreasing particle size, while cytotoxicity of both control and NO-releasing particles against L929 mouse fibroblasts was not influenced. Using fluorescently tagged particles, scaffold-dependent particle-bacterium interactions were observed via confocal microscopy. Particles with smaller diameters associated with bacteria at a faster rate and to a greater

extent than particles of larger diameters

In Chapter 3, methods for achieving tunable NO release kinetics from silica particles were described. The incorporation of hydrophobic groups onto the particle surface resulted in prolonged NO release rates due to the slowed diffusion of water into the scaffold. The surface-modified particles exhibited NO release half-lives ranging from 0.3–2.7 h. Increasing the particles' surface hydrophobicity also improved their utility as dopants in electrospun polyurethane fibers for NO-releasing porous membranes. Fibers doped with ethyl- and isobutyl-modified particles were characterized by 15 and 11% particle leaching, compared to the 40% particle leaching observed from fibers doped with unmodified particles.

Chapter 4 described an alternative method for achieving NO-releasing silica particles with significantly extended NO release kinetics by directly modifying the *N*-diazeniumdiolate NO donor structure. An O^2-protected NONOate-based silane was synthesized by coupling iodopropyltrimethoxysilane with O^2-methoxymethyl 1-(piperazin-1-yl)diazen-1-ium-1,2-diolate (MOM-Pip/NO). The MOM-Pip/NO silane was then surface grafted onto mesoporous silica particles to yield macromolecular NO release scaffolds with a total NO payload of 2.5 μmol NO/mg and an NO release half-life of 23 d. These particles represent the longest NO-releasing silica particles to date. Nitric oxide-releasing dental composites were prepared by doping MOM-Pip/NO particles into polymer resin composites. The MOM-Pip/NO-doped composites resulted in a 3-log reduction in viability of adhered *Streptococcus mutans* compared to composites doped with faster NO-releasing AHAP/NO particles and undoped controls following 24 h exposure in nutrient conditions.

In Chapter 5, a dually functional antimicrobial silica nanoparticle was described with both NO release capabilities and quaternary ammonium functionalities. Quaternary

ammoniums were tethered to the surface of AHAP particles through a ring opening reaction between synthesized QA-epoxides and primary amines present on the particle surface. The alkyl chain of the QA group was varied to evaluate structure-dependent bactericidal efficacy. Butyl-, octyl-, and dodecylQA-functionalized particles induced a 3-log reduction in *S. aureus* at 4.0, 3.0 and 1.5 mg/mL, respectively. For *P. aeruginosa*, octyl- and dodecylQA-functionalized particles caused a 3-log reduction in viability at 4.0 mg/mL, while butylQA-functionalized required 8 mg/mL. Imparting NO release from the QA-functionalized particles resulted in a decrease in the MBC against *S. aureus* compared to NO-releasing or QA-functionalized particles alone. The combination of NO and QA on a single particle did not result in improved killing against *P. aeruginosa*. Confocal microscopy with fluorescent markers for intracellular NO (DAF-2) and compromised membranes (propidium iodide) indicated the increased efficacy of QA-functionalized NO-releasing particles against *S. aureus* was due to their ability to cause membrane damage followed by delivery of intracellular NO.

6.2 Future Directions

The first report of *N*-diazeniumdiolate-modified silica nanoparticles was established only 9 years ago.[1] Since then, much work has proven the efficacy of these materials as cardiovascular, antimicrobial, anticancer, and wound-healing therapies.[1-6] Yet, further optimization remains to achieve ideal NO-releasing characteristics as different applications require specific NO release totals and kinetics. Our laboratory and others have advanced the synthesis of hybrid silica particles to achieve control over both NO release and particle characteristics (i.e., size, shape, composition and surface chemistries). Translation of the

silica scaffolds from research laboratories to the clinic will require the efforts of many, including those that specialize in the NO chemistry and nanoparticle synthesis and those that specialize in the NO biology of particle-cell interactions. The results described herein still represent the beginning steps toward developing fully optimized NO-releasing macromolecules for biomedical applications.

6.2.1 Studies to further investigate the role of nanoparticle size

In Chapter 1, smaller particles were shown to be more effective against bacteria. The next logical step is to further decrease particle size below 50 nm to determine the optimal scaffold size using constant NO loading and release kinetics. Since prokaryotic cells do not express an endocytotic mechanism, the extent of association of the particles to the bacterial surface will govern their efficacy and therefore must be understood. Nanoparticle-bacterium interactions could be quantified using flow cytometry or ICP-OES where the amount of silica adhered to the cell is determined and translated to the number of associated particles.[7] In order to use these methods, careful experimental design will be required to ensure non-adhered particles are washed from the cells prior to analysis. Atomic force microscopy may also be useful to observe nanoparticle-cell interactions, although quantitative analysis would be difficult. Particle size not only governs the rate of an interaction (i.e., diffusion), but also the number of particles that can adhere to a particular microbe and the relative percentage of those particles' surfaces that are directly in contact with the bacterium. Unfortunately, the synthesis of monodisperse nanoparticles with diameters less than 50 nm and large organic content (i.e., NO loading) is difficult. As an alternative approach, a surface grafting method may be used to incorporate aminosilanes onto commercially available 14 nm TEOS particles

(Nissan Chemical Industries, Ltd, Tokyo, Japan). The exponential relationship between nanoparticle surface area and volume suggests that surface-grafted particles of small sizes may be capable of releasing NO payloads similar to an equivalent mass of larger particles.

To achieve NO release scaffolds of smaller sizes, future work should focus on NO-releasing dendrimers, which are extremely monodisperse and have diameters as low as 2 nm. Sun et al. has recently observed that the MBCs of NO-releasing dendrimers are significantly lower than that of NO-releasing particles, albeit with increased toxicity toward mammalian cells.[8] Confocal microscopy with DAF/PI fluorescent probes indicate that the dendrimers result in greater intracellular NO at a faster rate and to a greater extent than the 50 nm AHAP/TEOS particles presented in Chapter 2. In addition to planktonic cultures, the role of particle size and shape in the ability of NO-releasing particles to penetrate into biofilms is an equally appealing future direction. Microbial biofilms are difficult to treat due to their protective exopolysaccharide matrix.[9] The extent to which NO-releasing scaffolds (silica or dendrimers) may penetrate the dense network and deliver NO within the biofilm interior should be determined to fully understand their antimicrobial efficacy in more clinically relevant environments.

6.2.2 Tuning NO release properties

For many applications, the short NO release kinetics typically exhibited by NONOate-based silica particles is insufficient. Methods such as those discussed in Chapters 3 and 4 are thus desirable for increasing the duration of NO release. While modifying the surface of particles with groups of varied hydrophobicity allowed for tunable release kinetics, the decreased conversion efficiency of amines to NONOates resulted in low NO payloads.

Conversely, greater NO payloads were achieved using MOM-protected NONOates, but the release kinetics were not tunable. While surface modifying particles pre-loaded with NONOates may result in formulations with tunable release kinetics and sufficient NO payloads, the labile nature of the NONOate groups limits the opportunities for chemical modifications on NO-loaded scaffolds. Other O^2-protecting groups have been designed that are stable in acidic conditions and labile in basic conditions.[10, 11] Thus, particles could be loaded with base-labile O^2-protected-NONOates, surface modified with hydrophobic functionalities, and then deprotected under basic conditions. This approach would allow for greater NO payloads and tunability of NO release kinetics.

Lastly, bimodal NO release may be advantageous for wound healing applications where high initial doses are necessary to inhibit microbial colonization, while low NO concentrations over extended durations are necessary to facilitate proper wound healing (i.e., collagen deposition, reepithelialization, etc.).[12] To this end, particles modified with NONOate stabilized by different methods (i.e., cation and O^2-protected) should be investigated. The use of cation-stabilized (i.e., unprotected) NONOates would provide high initial NO fluxes, while the inclusion of protected NONOates would deliver low NO fluxes for long durations. As discussed in Section 1.4.1, MSN are excellent candidates for these efforts as they contain two separate functionalizable surfaces. The outer surface can be modified prior to surfactant removal, then the inner surfaces can be modified following removal of the surfactant from the pores. Moreover, the silica network comprising the MSN may be formed by co-condensing an organosilane with a tetraalkosilane as a means to add a third type of NONOate.

6.2.3 Combination therapies

Combination strategies are particularly effective for antimicrobial applications as exposure to two agents that act via different mechanisms drastically decreases the probability for resistance and often results in synergistic activity.[13, 14] In Chapter 5, NO release was combined with QAs on the same particle scaffold. While QA-functionalization increased the bactericidal efficacy of the silica scaffolds, it also resulted in an increase in toxicity towards mammalian cells. The cytotoxicity of long chain QAs is well reported, thus most current applications for QA-based materials are topical or non-biomedical (e.g., anti-biofouling surfaces for ship hulls). To decrease the cytotoxic effects, QA-functionalized particles may be doped into polymers or resins to impart antimicrobial properties to biomedically relevant matrices. For example, Beyth et al. prepared resins doped with 1 wt% quaternized poly(ethylene imine) nanoparticles and found that their use as dental composites significantly decreased the viability of bacteria within biofilm communities with no observed impact on biocompatibility in vivo.[15] Polymers or resins doped with NO-releasing QA-functionalized particles would likely still exhibit beneficial antimicrobial properties superior to polymers doped with NO-releasing particles alone. Nitric oxide release from the surface would decrease bacterial adhesion, and the presence of QA functionalities may ensure decreased viability of those bacteria that did manage to adhere. As illustrated in Chapter 3, leaching of noncovalently incorporated particles may be decreased due to van der Waals interactions between the alkyl chains and hydrophobic polymers.

Future work should also investigate the design of macromolecular scaffolds that combine NO release with other releasable therapies. Our laboratory previously reported the synergistic effects of co-administering ionic silver (Ag^+) with a LMW NO donor,

PROLI/NO.[16] This work suggests that hybrid NO-releasing nanoparticles containing Ag^+ or silver nanoparticles embedded within the NO-releasing silica nanoparticle may also exhibit synergy. Other metallic nanoparticles with proven antimicrobial activity should also be investigated, including copper,[17-19] zinc oxide,[20-24] and titanium dioxide.[20, 25, 26] The bactericidal properties of metallic nanoparticles arise from the release of metal ions from the particle surface, thus their entrapment within a silica network may decrease their efficacy. If this proves to be true, the metallic particles should be tethered to the surface of the silica particle.[27] In aerobic conditions, NO reacts with O_2 to form NOx species that may react with the metallic nanoparticles. X-ray photoelectron spectroscopy could be used to investigate the oxidation states present in the metallic nanoparticles initially and after exposure to relevant concentrations of NO. Additionally, the use of combination therapies has been shown to increase the sensitivity of microbes to antibiotics to which they had previously developed a resistance toward.[14] Future work should investigate the efficacy of nanoparticles that release both NO and vancomycin against vancomycin-resistant *S. aureus*, or nanoparticles that release NO and methicillin against methicillin-resistant *S. aureus*.

6.2.4 Improving the anticancer potential of NO-releasing nanoparticles

Nitric oxide has an intricate role in cancer biology, serving as a tumor regressor at high concentrations and a tumor progressor at low concentrations.[28] As discussed in Chapter 1, nanoparticle-derived NO was observed to inhibit the growth of ovarian cancer cells while exhibiting low toxicity to normal (i.e., non-tumor) cells.[4] While these results are promising, the ultimate utility of NO-releasing particles for cancer therapy remains hindered by uncontrolled NO release and the undesirable effects that result from the low levels of NO

release (i.e., angiogenesis and tumor growth). For NONOate-based particles, release of the NO payload begins immediately upon introduction into aqueous media, limiting the amount of NO that can be delivered directly to the cell. Methods to target the delivery of the NO-releasing scaffold would significantly increase the percentage of the NO payload delivered directly to the tumor site, and in turn improve their efficacy. Future work in this area should involve designing strategies for targeted delivery and triggered NO release.

The use of magnetic nanoparticles, such as iron oxide, to actively target nanoparticle-based therapies was discussed in Section 1.1.4. This technique could be used to target the delivery of NO-releasing silica nanoparticles to specific locations in vivo. Preliminary experiments were conducted to prepare magnetic NO-releasing silica nanoparticles by forming a hybrid (i.e., aminosilane and tetraalkoxysilane) silica shell around an iron oxide core particle. Iron oxide nanoparticles were synthesized by a thermal degradation method according to a previously reported procedure.[29] Briefly, iron pentacarbonyl (1.52 mmol) was mixed with dioctyl ether (10 mL) and oleic acid (4.56 mmol). The translucent yellow reaction was heated to reflux, and the formation of the iron-oleate complex as indicated by a black color change and confirmed by an absorption maximum at 330 nm. After formation of the iron-oleate complex, the reaction was cooled to room temperature, and 4.56 mmol of dehydrated trimethylamine *N*-oxide was added to control oxidation. The temperature was increased to 240 °C to induce nucleation and further increased to 320 °C to promote nanoparticle growth. The resulting magnetic particles were monodisperse and characterized by a diameter of 7 nm particles (Figure 6.1). X-ray photoelectron spectroscopy (XPS) analysis confirmed that the particles were composed of maghemite (Fe_2O_3) as indicated by binding energies of 710.9 eV and 724.7 eV for the Fe $2p_{3/2}$ and $2p_{1/2}$ electrons, respectively.[30]

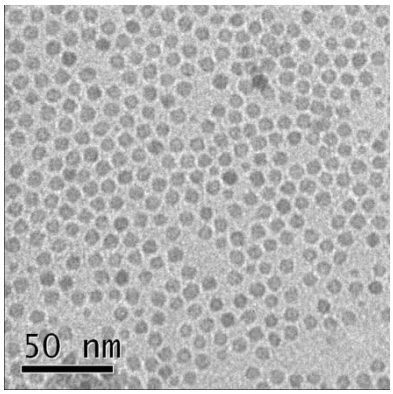

Figure 6.1 Transmission electron micrograph of Fe_2O_3 nanocrystals (diameter = 7 nm) synthesized via the thermal degradation of iron pentacarbonyl in dioctyl ether and oleic acid.

The presence of a small satellite peak at 719 eV and the absence of a shoulder on the $2p_{1/2}$ peak further supported the identification.

As synthesized, the iron oxide nanocrystals are capped with hydrophobic oleate groups. However, encapsulation of the Fe_2O_3 nanoparticles in silica required their dispersion in aqueous solution (i.e., interior of micelles or Stöber conditions). Thus, the surface of the nanocrystals was noncovalently modified with a long-chain alkylsilane, as shown in Figure 6.2. The non-polar alkyl chains of the silane associate with the oleate chains on Fe_2O_3 through van der Waals interactions, leaving the hydrolyzable methoxy groups oriented outward. The resulting n-octyltrimethoxysilane-capped Fe_2O_3 nanoparticles were then suspended in water and added to a reverse microemulsion composed of pentane (organic phase), Triton X-100 (surfactant), hexanol (cosurfactant), and water (aqueous phase). Subsequent addition of TEOS and 3-butylaminopropyltrimethoxysilane (BAP) to the reverse microemulsion resulted in the formation of ~60 nm amine-containing silica particles with Fe_2O_3 cores (Figure 6.3). Of note, use of other water-miscible aminosilanes, such as MAP and AHAP, resulted in a disruption of the emulsion likely because the silanes diffused too quickly into the water droplet.

The amines on the BAP/TEOS-coated Fe_2O_3 nanoparticles were converted to *N*-diazeniumdiolates as described by Shin et al.[31] The total NO released was 3.81 nmol/mg, indicating that only a low amount of BAP was incorporated into the silica particle. Greater amine incorporation may be achieved with increased aminosilane concentrations or the sequential silane addition that was discussed in Chapter 2. Alternatively, the Stöber method could be used to form a silica shell around the Fe_2O_3 nanocrystals. By suspending the n-octyltrimethoxysilane-capped Fe_2O_3 nanocrystals in a basic aqueous solution under dilute

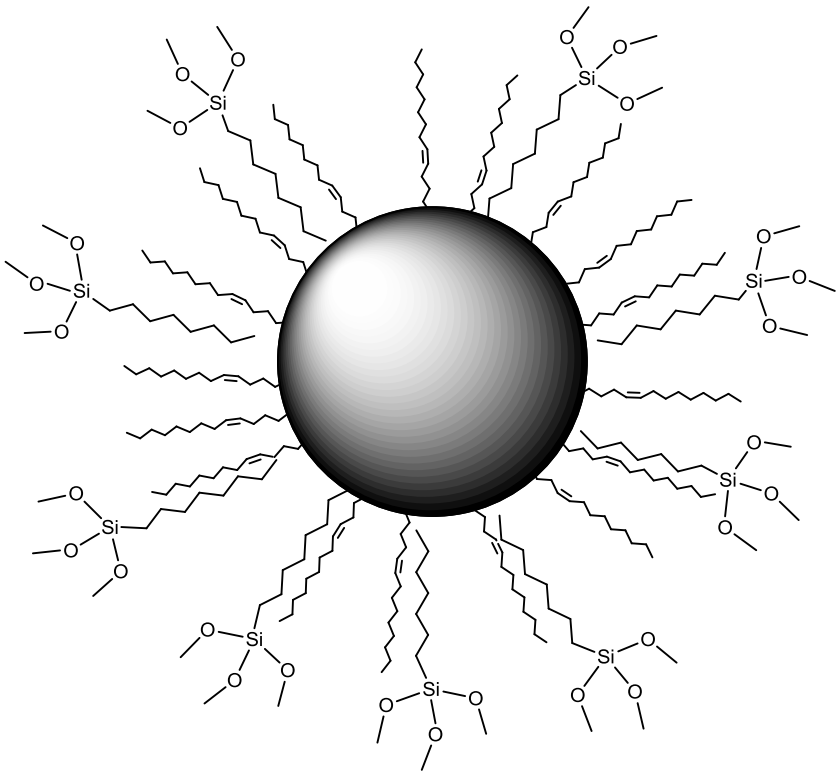

Figure 6.2 The addition of n-octyltrimethoxysilane to the surface of oleic acid-capped Fe_2O_3 nanocrystals via van der Waals interactions allows for their stability in aqueous media and promotes the formation of a silica shell.

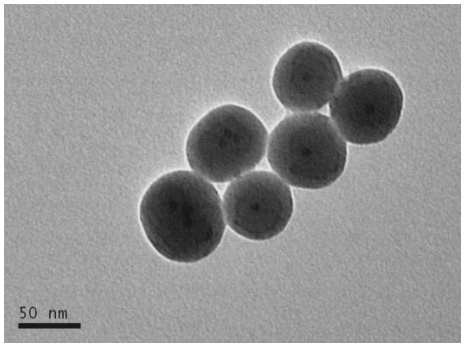

Figure 6.3 Transmission electron micrograph of magnetic NO-releasing silica particles composed of Fe_2O_3 core and a BAP/TEOS shell (diameter = 67 nm).

conditions, a silica shell can be added by sequential addition of small amounts of silane precursors. These dilute reaction conditions are required to inhibit nucleation sites that would result in the growth of silica particles without an Fe_2O_3 core.

While the inclusion of a magnetic particle addresses the need for targeted delivery, methods to delay NO release prior to the particle arriving at the tumor site are also necessary. One possible method for achieving delayed NO release would be to encapsulate the NONOate-based particle within a liposome. The lipophilic region of the lipid bilayers would inhibit diffusion of water to the particle, limiting the decomposition of the NONOate. Once taken up within the cell, the liposome would be ruptured, and the NO would be released to the cellular interior. Modifications to the NO donor moiety may also be studied to prevent premature NO release. Protected O^2-NONOates are excellent candidates, especially those with protecting groups that are labile in the acidic and/or reducing environments common to intracellular compartments. For example, the MOM protecting group described in Chapter 3 is labile at low pH. Other O^2-protecting groups are cleaved selectively by intracellular species. For example, O^2-[2,4-dinitro-5-[4-(*N*-methylamino)-benzoyloxy]phenyl]-1-(*N*,*N*-dimethylamino)diazen-1-ium-1,2-diolate (PABA/NO) is a LMW NO donor that features a protecting group cleaved upon nucleophilic aromatic substitution by glutathione, allowing for intracellular NO release.[32] Alternatively, nanoparticles containing tertiary nitrosothiols or metal nitrosyls may be promising for antitumor applications as their NO payload would only be released upon irradiation with light.[33, 34] Triggerable NO release is most ideal to avoid extended periods where low levels of NO are released, which might enable in cell proliferation and tumor growth.

6.2.5 Next generation NO-releasing macromolecular scaffolds

The two primary NO-releasing scaffolds discussed in this dissertation are silica nanoparticles and dendrimers. The main advantage of silica nanoparticles is their relatively low toxicity to mammalian cells.[35] When normalized by mass however, the NO release from silica particles is restricted by the large relative concentration of Si and O that account for most of the particle mass. Larger particle doses (per mg) are thus required to achieve NO levels necessary for the intended therapeutic response compared to LMW donors. Undesirable cytotoxicity often arises as a result of these large particle doses, negating the motivation for employing silica nanoparticles. Alternative macromolecular scaffolds, such as dendrimers, provide greater NO loading per unit mass, but their ultimate success is hindered by toxicity to mammalian cells.[36]

Next generation NO-releasing scaffolds should incorporate dendrimers within a mesoporous silica particle to take advantage of each scaffold's positive properties (i.e., high NO loading of dendrimers and low toxicity of silica) while minimizing the negative properties. As such, dendrimer-loaded MSNs may be characterized by larger localized NO delivery than silica alone and lower toxicity than dendrimers alone.

Covalently binding dendrimers to mesoporous silica particles has been reported for the purpose of gene transfection carriers.[37] For these materials, the dendrimers were bound to the outer surface of the MSNs to allow for complexing with plasmid DNA. In future work, the dendrimers should also be loaded within the pores of the MSNs to maximize NO storage and delivery. Binding of dendrimers to the particle surface may result in undesirable cytotoxicity, in which case the surface of the MSNs could be passivated with an inert functionality. The dendrimers should be restricted to the particle interior following

surfactant removal. Primary amine-terminated dendrimers, such as poly(amido amine) (PAMAM) and poly(ethylene imine) (PEI), could be covalently bound to a MSN functionalized with glycidylpropyltrimethoxysilane through ring opening reactions similar to those used in Chapter 5. Lower generation dendrimers would provide greater NO release per unit mass and may prove easier to load into the mesopores due to their smaller diameter.

6.3 Conclusions

The work presented here illustrates the versatility available when employing silica nanoparticles for the delivery of nitric oxide for therapeutic applications. The preceding chapters have described methods for tuning both physical and chemical properties of NO-releasing silica particles. Although most of the materials described herein were evaluated for their antimicrobial efficacy, the broad therapeutic utility of NO suggests NO-releasing silica nanoparticles hold potential in other areas including cardiovascular dysfunctions, cancer treatment, and wound healing. Moreover, NO-releasing silica particles may be doped in polymer matrices to prepare biocompatible coatings that improve the fate of biomedical implants. The true success of NO-releasing silica particles for any one of these applications will require tuning of specific particle and NO release properties. Thus, the synthetic techniques described herein will greatly impact future developments of NO-releasing silica nanoparticles.

Appendix A:

Supplemental Information of Chapter 4

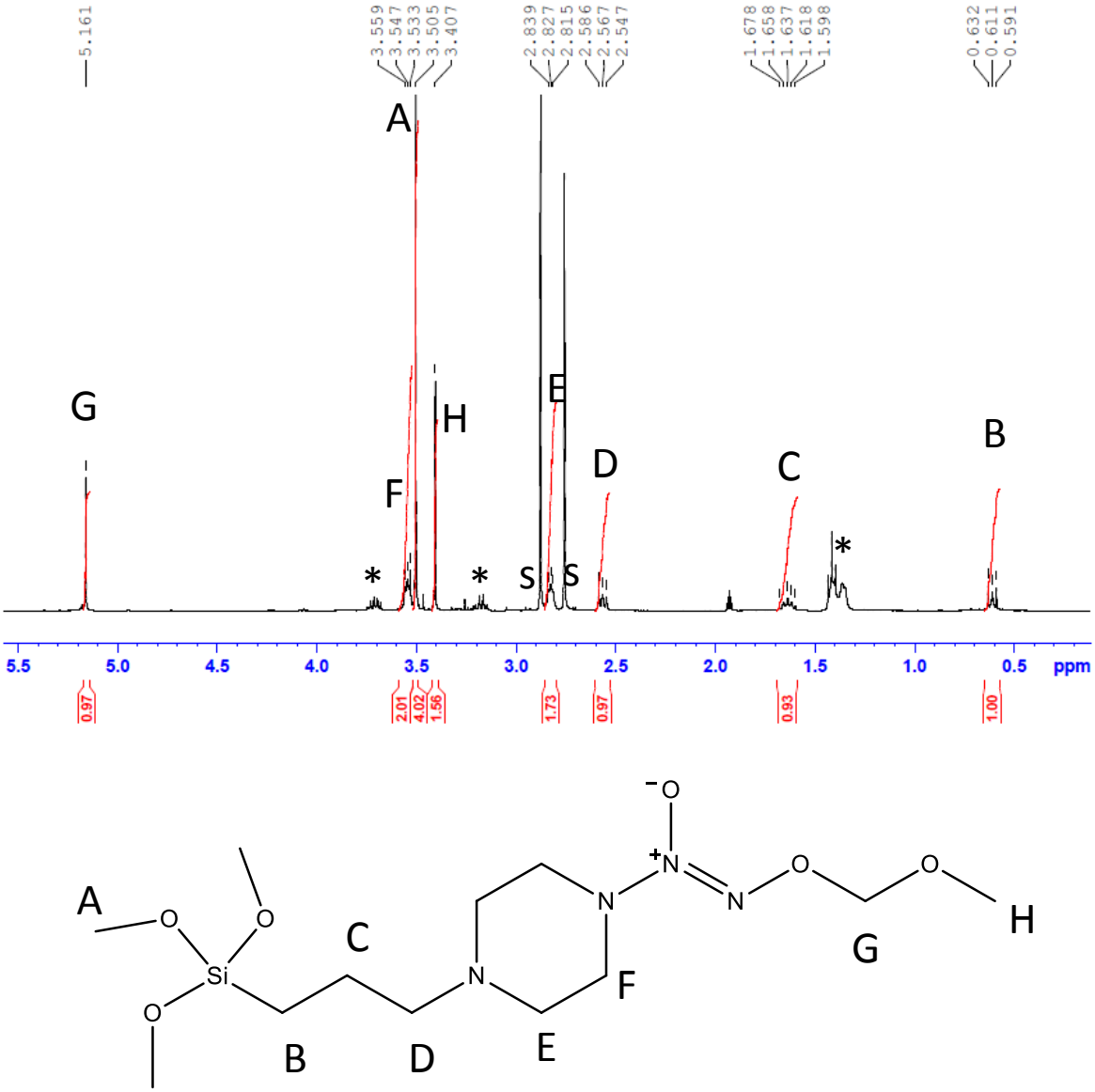

* = Hunig's base, s = solvent (DMF)

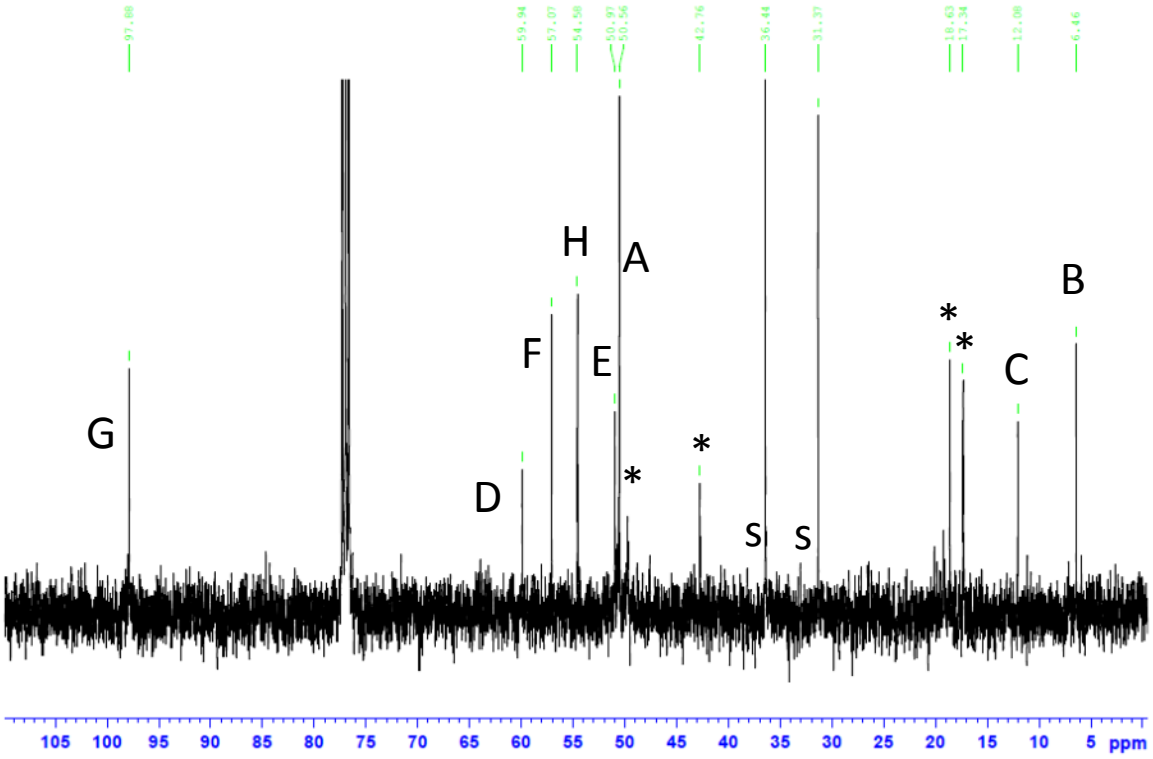

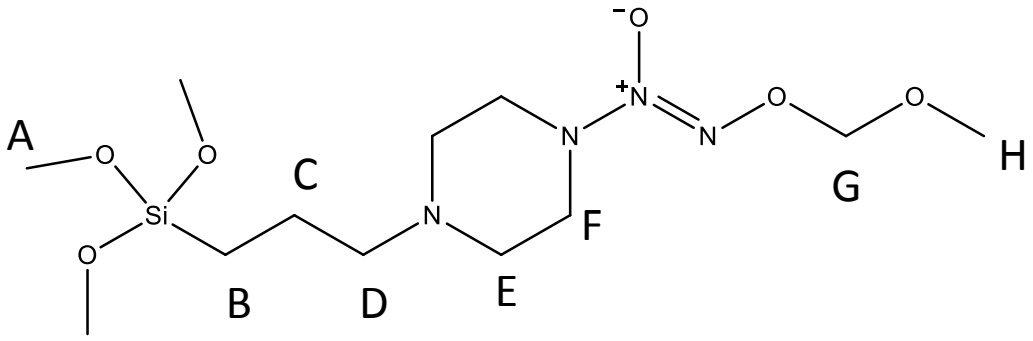

* = Hunig's base, s = solvent (DMF)

Appendix B:

Supplemental Information of Chapter 5

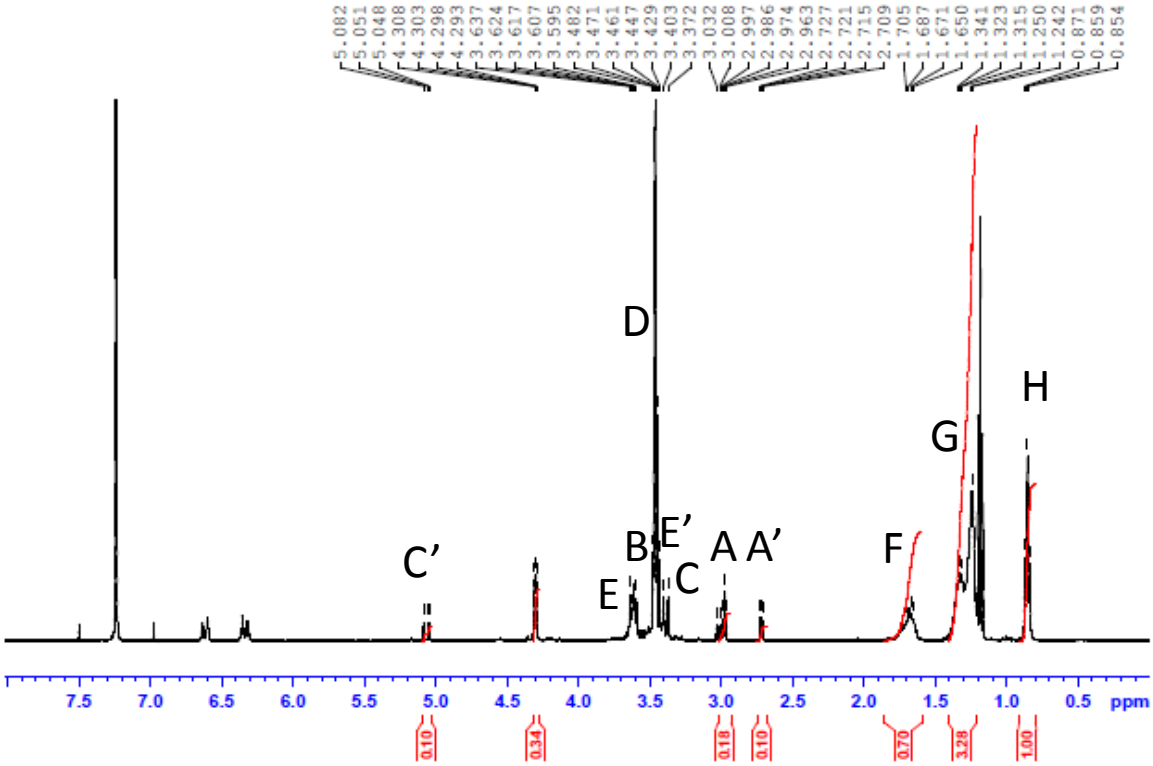

^{1}H NMR of glycidyldimethylbutylammonium chloride.

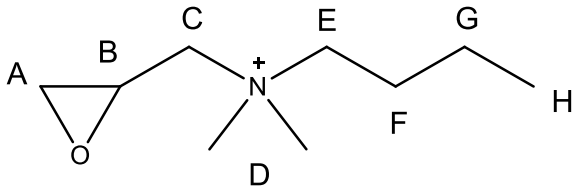

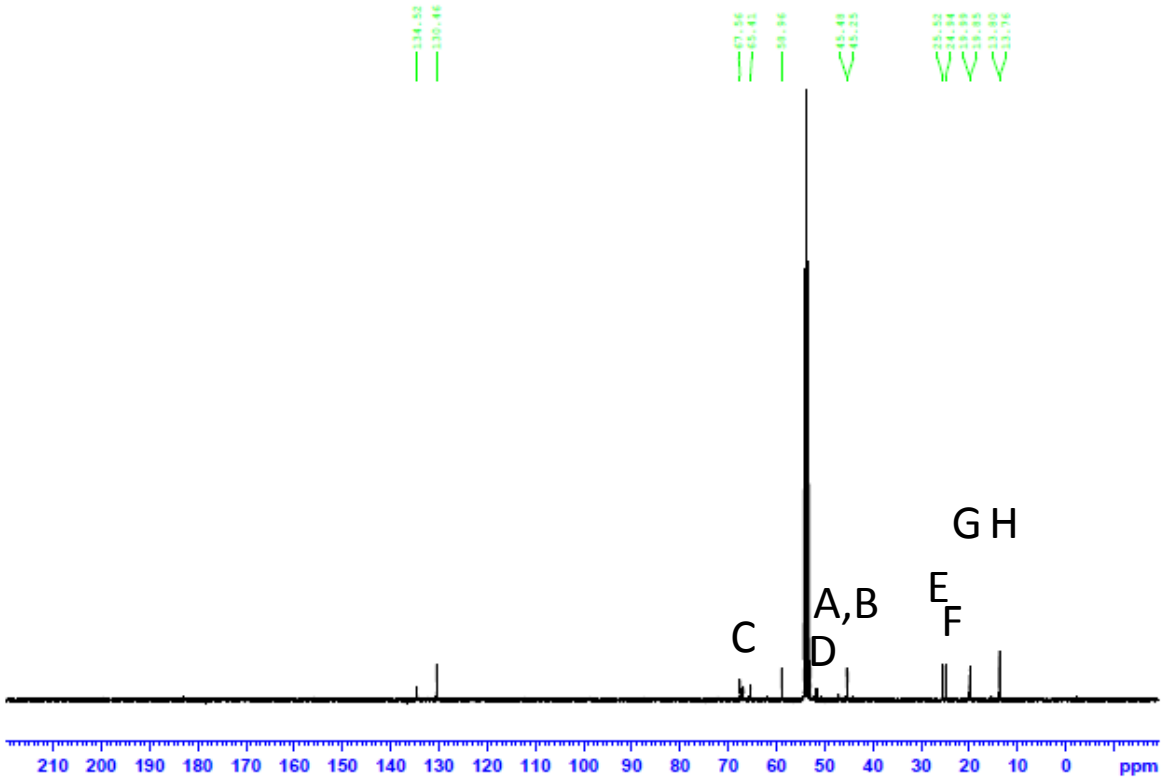

^{13}C NMR of glycidyldimethylbutylammonium chloride

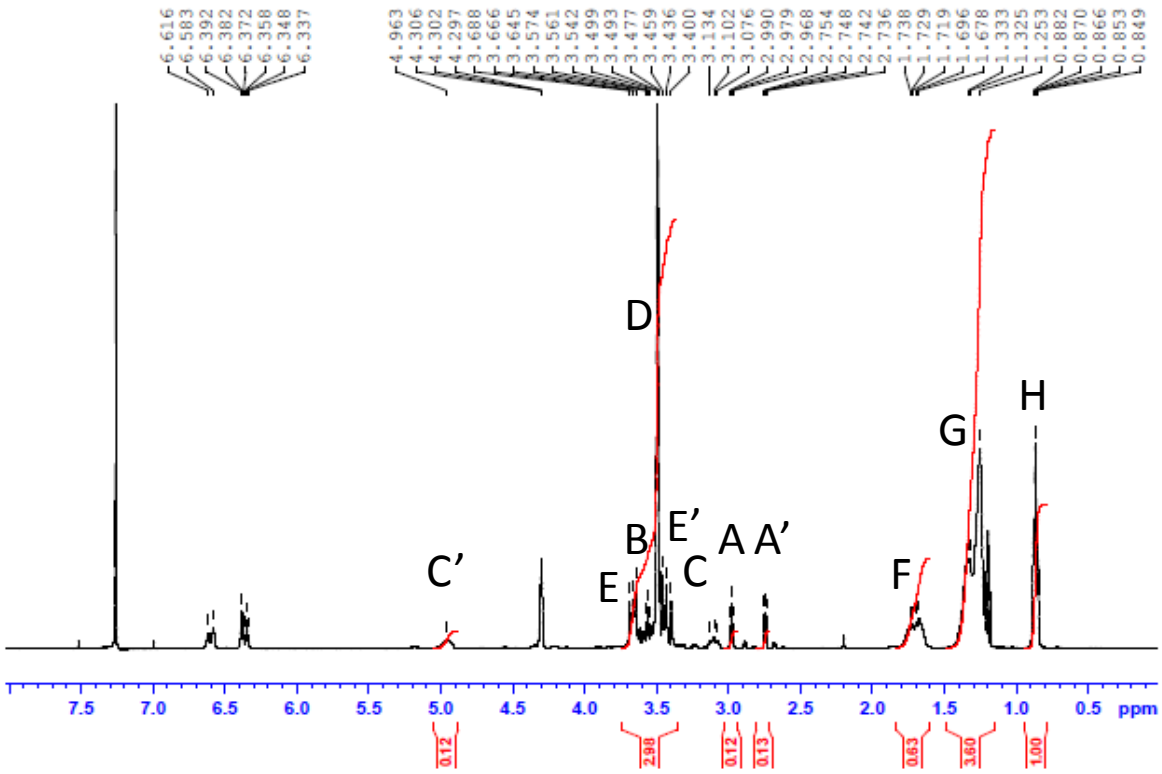

[1]H NMR of glycidyldimethyloctylammonium chloride

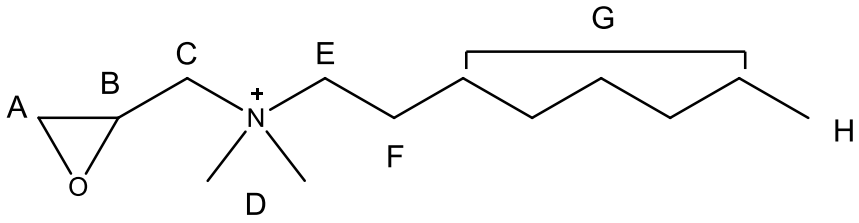

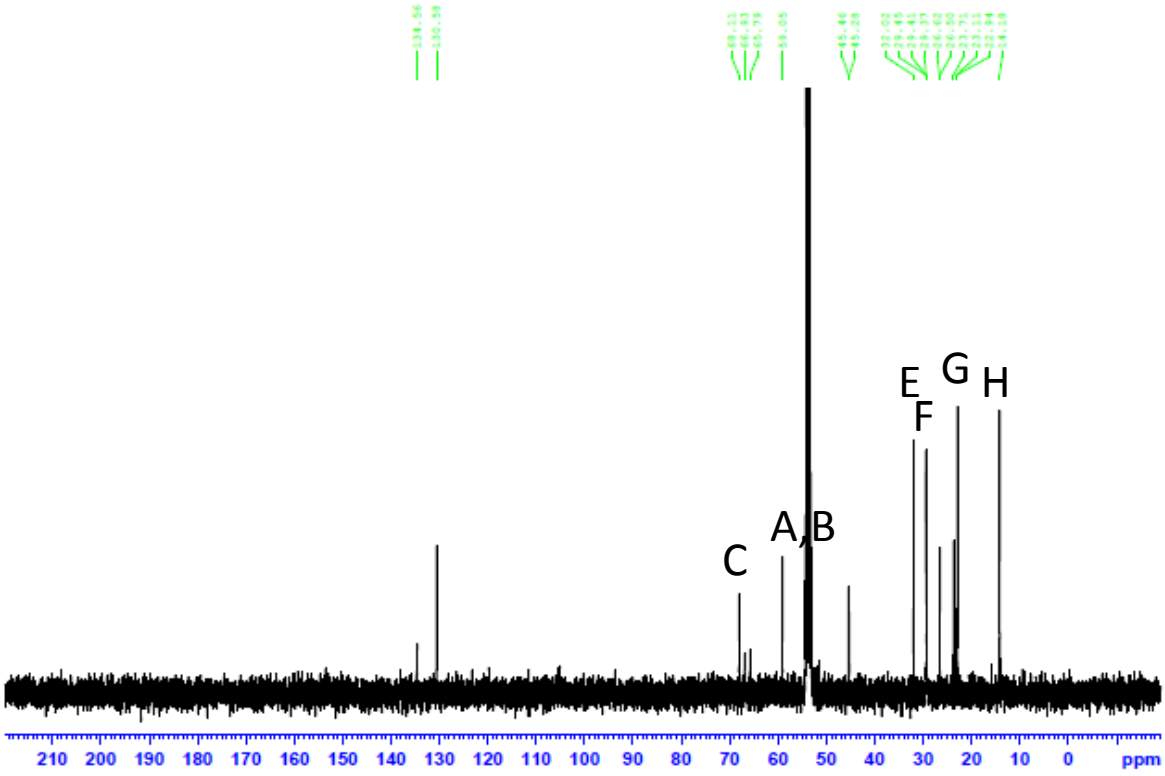

^{13}C NMR of glycidyldimethyloctylammonium chloride

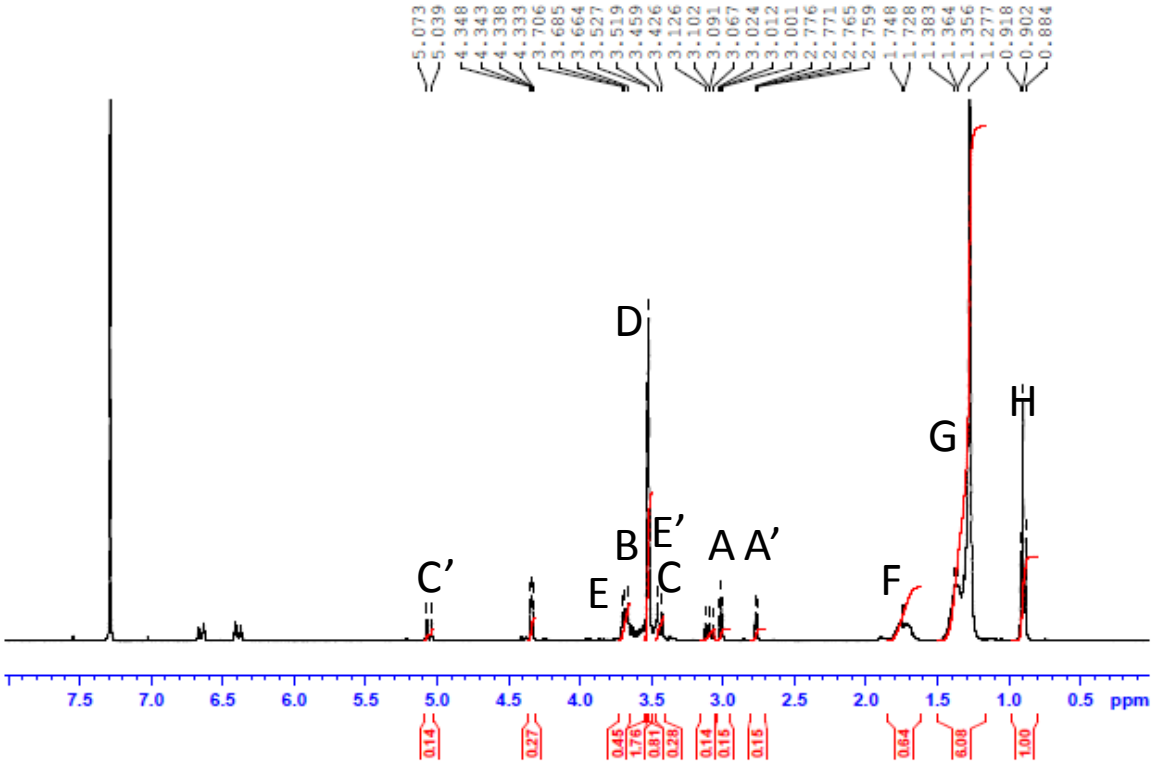

^{1}H NMR of glycidyldimethyldodecylammonium chloride

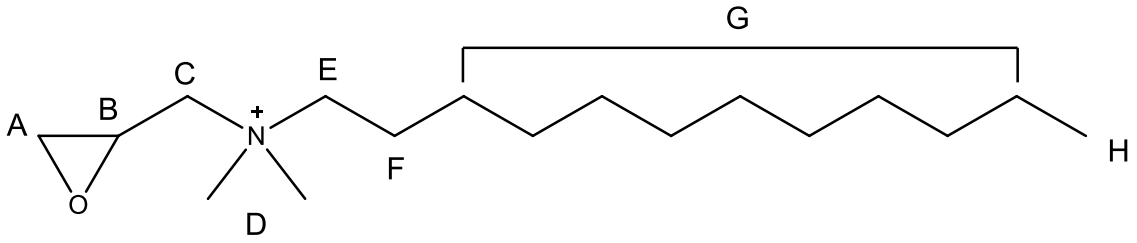

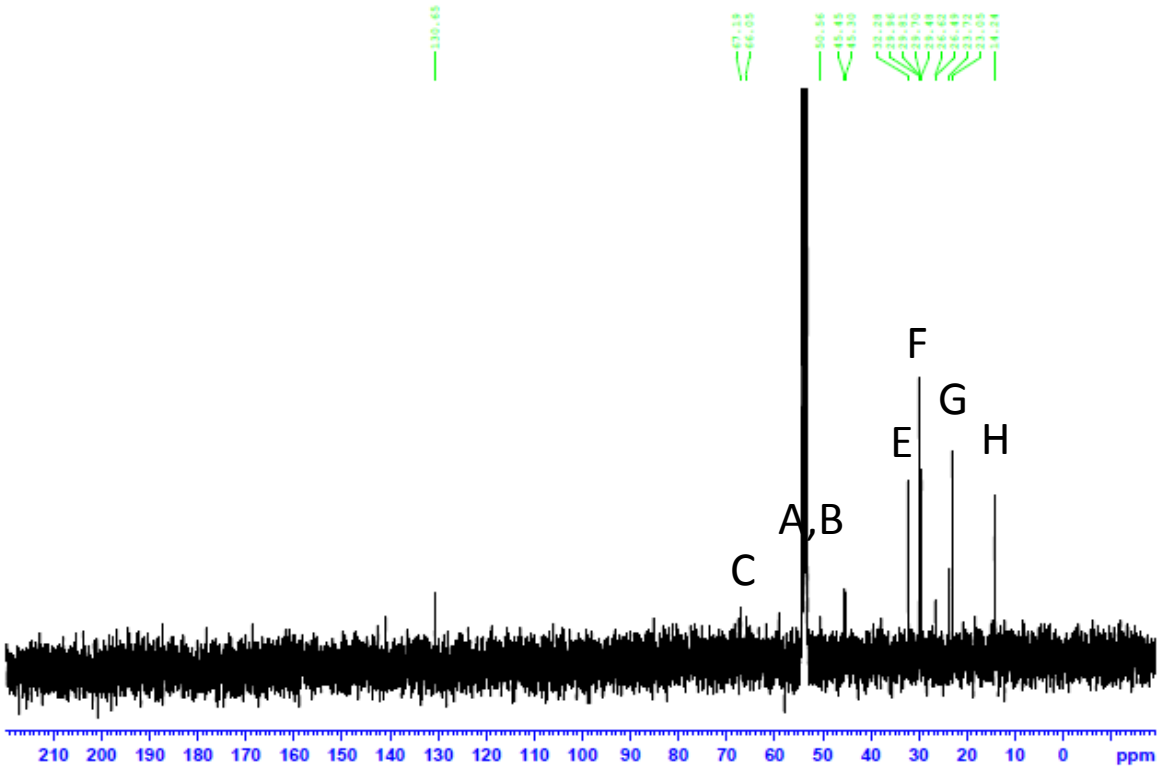

^{13}C NMR of glycidyldimethyldodecylammonium chloride

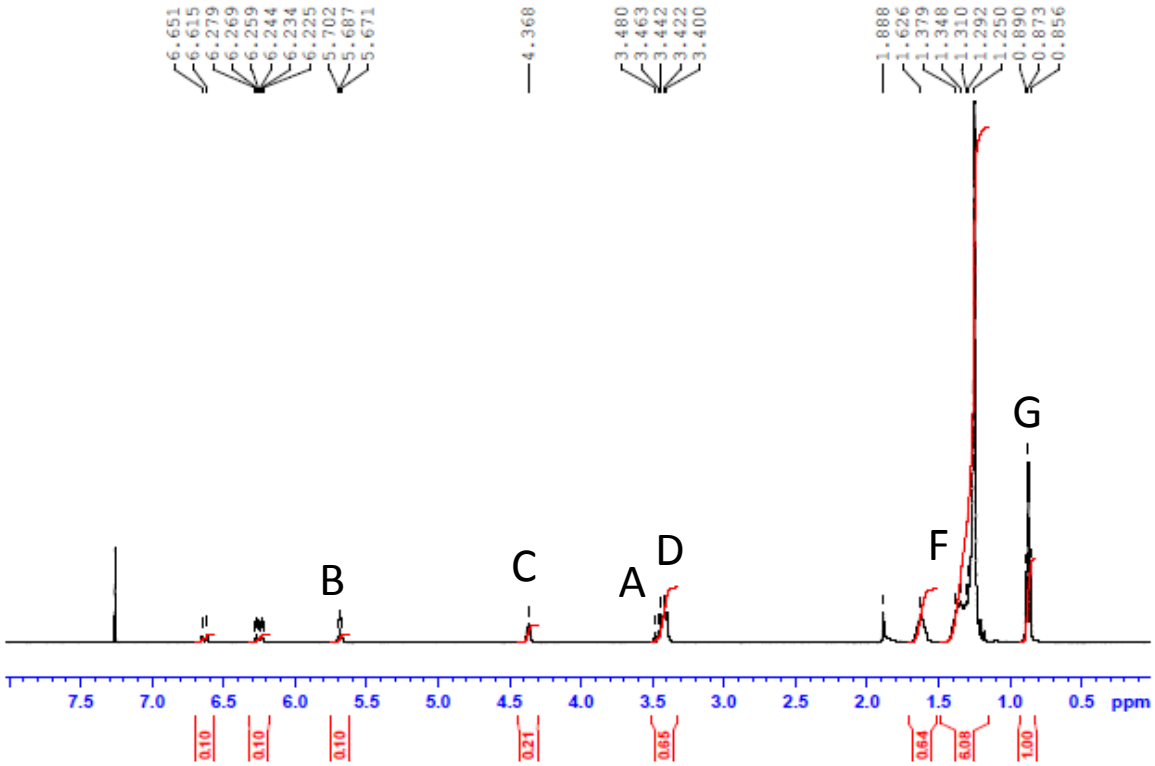

^{1}H NMR of glycidyltridodecylammonium chloride

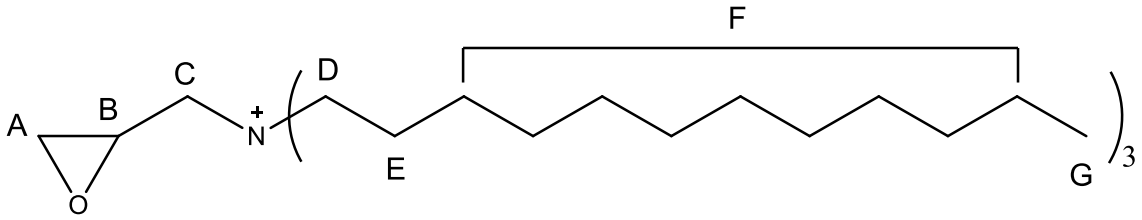

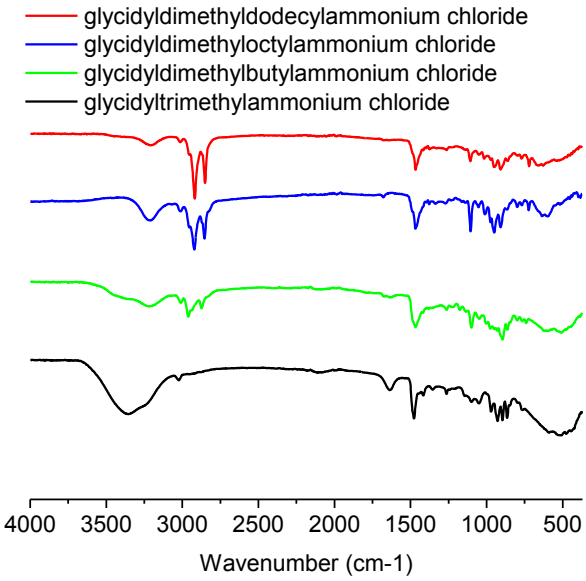

FT-IR spectra of QA-epoxides.

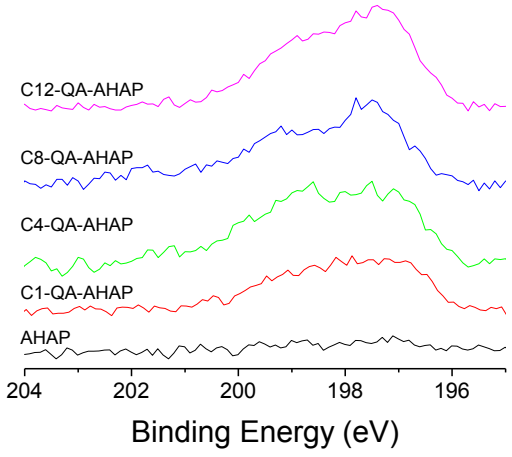

Xray photoelectron spectrum of Cl 2p peak for the five particle systems indicating the presence of the chloride counter ion in the QA-modified particles.

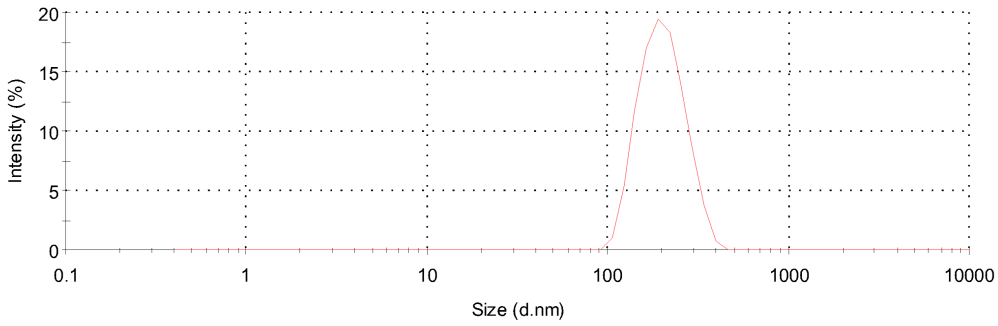

Dynamic light scattering size distribution spectrum for AHAP silica nanoparticles.

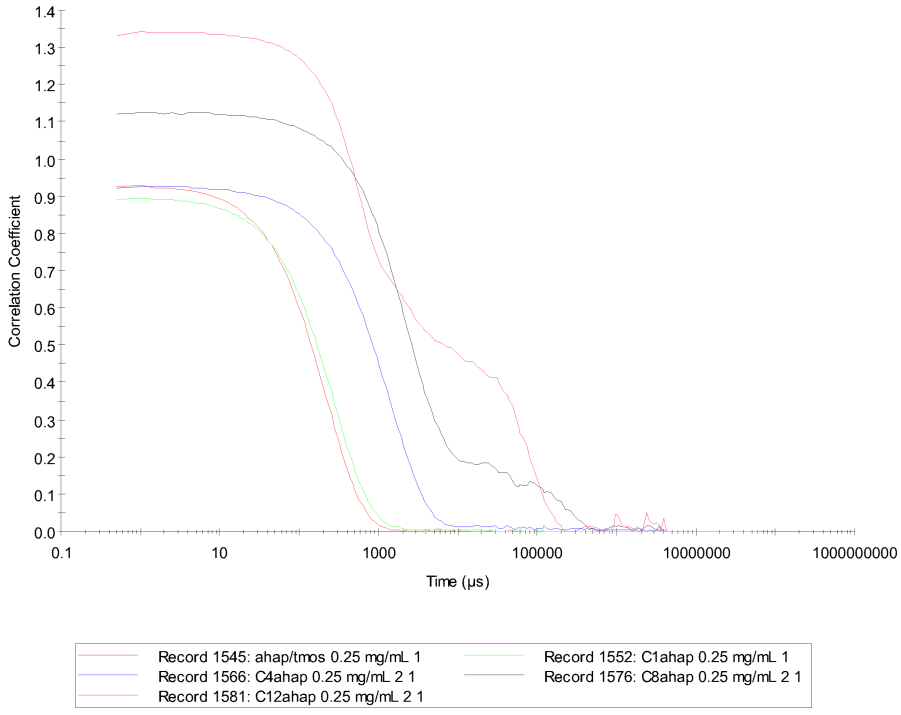

Raw correlation data spectra for dynamic light analysis of AHAP (red), methylQA (green), butylQA(blue), octylQA (black), dodecylQA (pink) silica nanoparticles at 0.5 mg/mL in phosphate buffered saline.

A

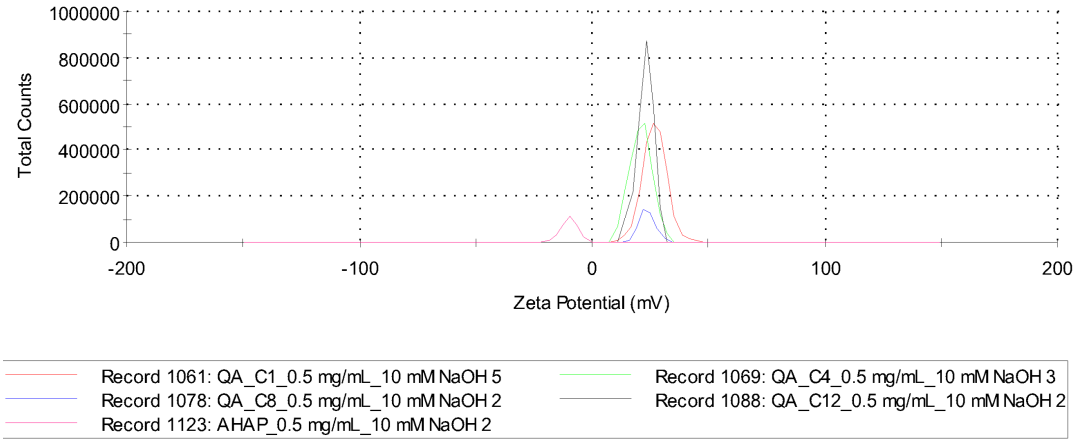

B

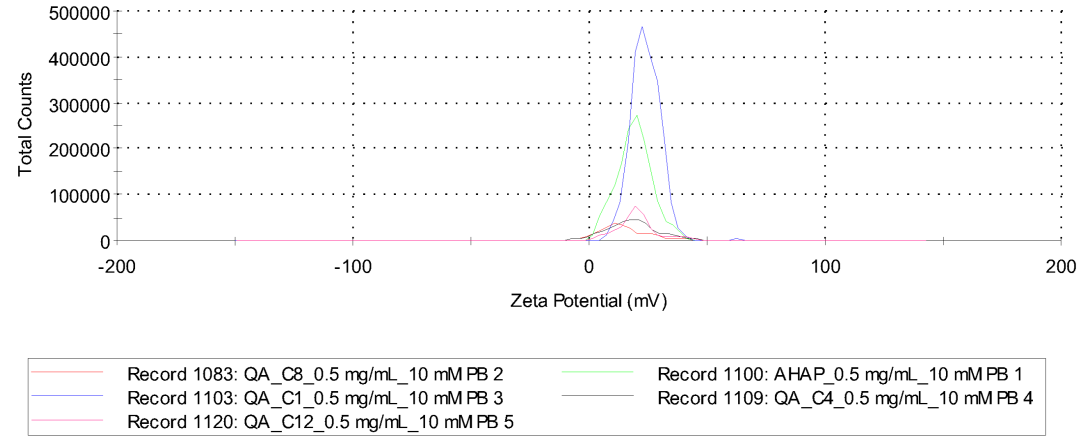

Zeta potential distribution spectra of AHAP (pink), methylQA (red), butylQA (green), octylQA (blue) and dodecylQA (black) in (A) 10 mM NaOH and (B) 10 mM phosphate buffer at 0.5 mg/mL.

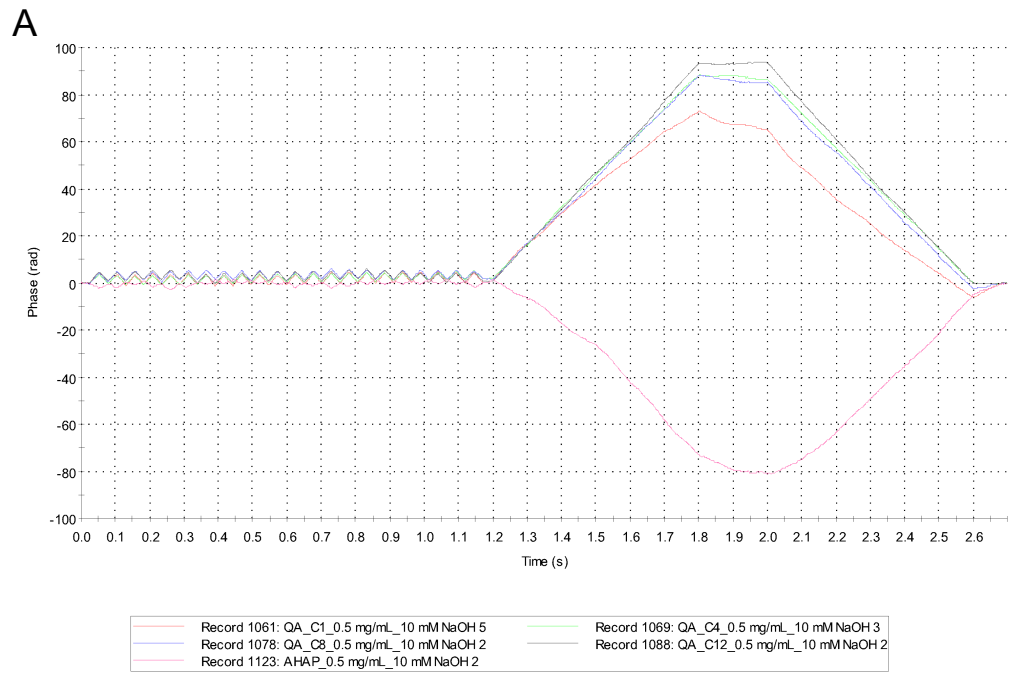

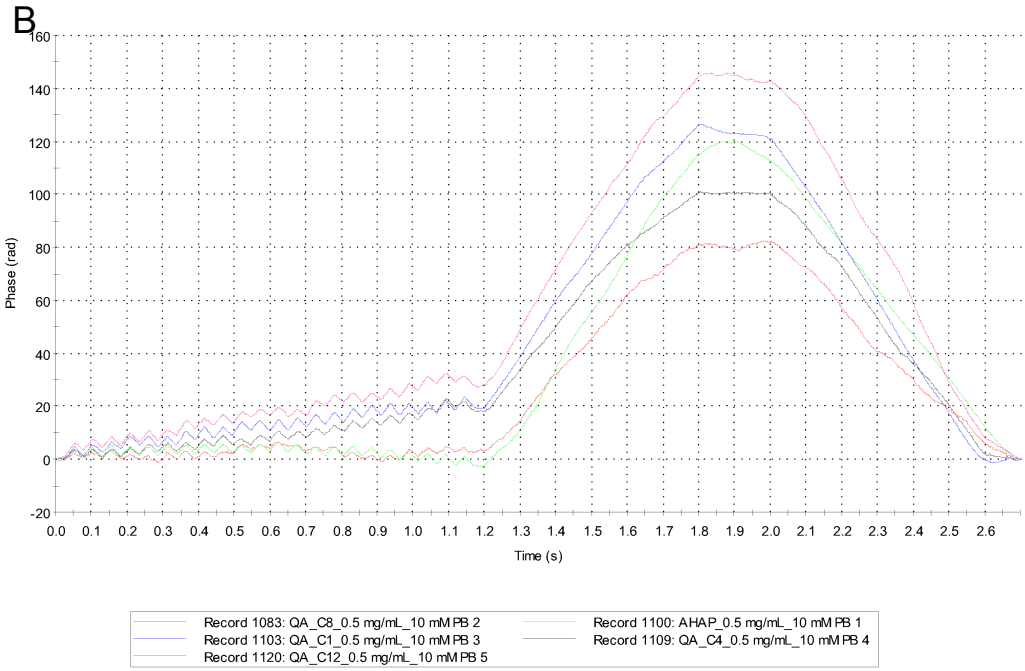

Phase plots from zeta potential analysis of AHAP (pink), methylQA (red), butylQA (green), octylQA (blue) and dodecylQA (black) in (A) 10 mM NaOH and (B) 10 mM phosphate buffer at 0.5 mg/mL.

References

1. Zhang, H.; Annich, G. M.; Miskulin, J.; Stankiewicz, K.; Osterholzer, K.; Merz, S. I.; Bartlett, R. H.; Meyerhoff, M. E. "Nitric oxide-releasing fumed silica particles: Synthesis, characterization, and biomedical application." *J. Am. Chem. Soc.* **2003**, *125*, 5015-5024.

2. Hetrick, E. M.; Shin, J. H.; Stasko, N. A.; Johnson, C. B.; Wespe, D. A.; Holmuhamedov, E.; Schoenfisch, M. H. "Bactericidal efficacy of nitric oxide-releasing silica nanoparticles." *ACS Nano* **2008**, *2*, 235-246.

3. Hetrick, E. M.; Shin, J. H.; Paul, H. S.; Schoenfisch, M. H. "Anti-biofilm efficacy of nitric oxide-releasing silica nanoparticles." *Biomaterials* **2009**, *30*, 2782-2789.

4. Stevens, E. V.; Carpenter, A. W.; Shin, J. H.; Liu, J.; Der, C. J.; Schoenfisch, M. H. "Nitric oxide-releasing silica nanoparticle inhibition of ovarian cancer cell growth." *Mol. Pharmaceut.* **2010**, *7*, 775-785.

5. Carpenter, A. W.; Slomberg, D. L.; Rao, K. S.; Schoenfisch, M. H. "Influence of scaffold size on bactericidal activity of nitric oxide-releasing silica nanoparticles." *ACS Nano* **2011**, *5*, 7235-7244.

6. Koh, A.; Riccio, D. A.; Sun, B.; Carpenter, A. W.; Nichols, S. P.; Schoenfisch, M. H. "Fabrication of nitric oxide-releasing polyurethane glucose sensor membranes." *Biosens. Bioelectron.* **2011**, *28*, 17-24.

7. Weir, E.; Lawlor, A.; Whean, A.; Regan, F. "The use of nanoparticles in anti-microbial materials and their characterization." *Analyst* **2008**, *133*, 835-845.

8. Sun, B.; Slomberg, D.; Lu, Y.; Schoenfisch, M. H. "Bactericidal efficacy of nitric oxide-releasing dendrimers." *Biomacromolecules* **2012**, *submitted*.

9. Costerton, J. W.; Stewart, P. S.; Greenberg, E. P. "Bacterial biofilms: A common cause of persistent infections." *Science* **1999**, *284*, 1318-1322.

10. Wu, X.; Tang, X.; Xian, M.; Wang, P. G. "Glycosylated diazeniumdiolates: A novel class of enzyme-activated nitric oxide donors." *Tetrahedron Lett.* **2001**, *42*, 3779-3782.

11. Showalter, B. M.; Reynolds, M. M.; Valdez, C. A.; Saavedra, J. E.; Davies, K. M.; Klose, J. R.; Chmurny, G. N.; Citro, M. L.; Barchi, J. J., Jr.; Merz, S. I.; Meyerhoff, M. E.; Keefer, L. K. "Diazeniumdiolate ions as leaving groups in anomeric displacement reactions: A protection-deprotection strategy for ionic diazeniumdiolates." *J. Am. Chem. Soc.* **2005**, *127*, 14188-14189.

12. Carpenter, A. W.; Schoenfisch, M. H. "Nitric oxide release: Part II. Therapeutic applications." *Chem. Soc. Rev.* **2012**, *41*, 3742-3752.

13. Fischbach, M. A. "Combination therapies for combating antimicrobial resistance." *Curr. Opin. Microbiol.* **2011**, *14*, 519-523.

14. Allahverdiyev, A. M.; Kon, K. V.; Abamor, E. S.; Bagirova, M.; Rafailovich, M. "Coping with antibiotic resistance: Combining nanoparticles with antibiotics and other antimicrobial agents." *Exp. Rev. Anti. Infect. Ther.* **2011**, *9*, 1035-1052.

15. Beyth, N.; Yudovin-Farber, I.; Perez-Davidi, M.; Domb, A. J.; Weiss, E. I. "Polyethyleneimine nanoparticles incorporated into resin composite cause cell death and trigger biofilm stress in vivo." *Proc. Natl. Acad. Sci. U.S.A.* **2010**, *107*, 22038-22043.

16. Privett, B. J.; Deupree, S. M.; Backlund, C. J.; Rao, K. S.; Johnson, C. B.; Coneski, P. N.; Schoenfisch, M. H. "Synergy of nitric oxide and silver sulfadiazine against gram-negative, gram-positive, and antibiotic-resistant pathogens." *Mol. Pharmaceut.* **2010**, *7*, 2289-2296.

17. Anyaogu, K. C.; Fedorov, A. V.; Neckers, D. C. "Synthesis, characterization, and antifouling potential of functionalized copper nanoparticles." *Langmuir* **2008**, *24*, 4340-4346.

18. Esteban-Cubillo, A.; Pecharroman, C.; Aguilar, E.; Santaren, J.; Moya, J. S. "Antibacterial activity of copper monodispersed nanoparticles into sepiolite." *J. Mater. Sci.* **2006**, *41*, 5208-5212.

19. Mary, G.; Bajpai, S. K.; Chand, N. "Copper (II) ions and copper nanoparticles-loaded chemically modified cotton cellulose fibers with fair antibacterial properties." *J. Appl. Polym. Sci.* **2009**, *113*, 757-766.

20. Adams, L. K.; Lyon, D. Y.; Alvarez, P. J. J. "Comparative eco-toxicity of nanoscale TiO_2, SiO_2, and ZnO water suspensions." *Water Res.* **2006**, *40*, 3527-3532.

21. Liu, Y.; He, L.; Mustapha, A.; Li, H.; Hu, Z. Q.; Lin, M. "Antibacterial activities of zinc oxide nanoparticles against *Escherichia coli* O157:H7." *J. Appl. Microbiol.* **2009**, *107*, 1193-1201.

22. Rekha, K.; Nirmala, M.; Nair, M. G.; Anukaliani, A. "Structural, optical, photocatalytic and antibacterial activity of zinc oxide and manganese doped zinc oxide nanoparticles." *Physica B* **2010**, *405*, 3180-3185.

23. Zhang, L. L.; Jiang, Y. H.; Ding, Y. L.; Povey, M.; York, D. "Investigation into the antibacterial behaviour of suspensions of ZnO nanoparticles (ZnO nanofluids)." *J. Nanopart. Res.* **2007**, *9*, 479-489.

24. Nair, S.; Sasidharan, A.; Rani, V. V. D.; Menon, D.; Nair, S.; Manzoor, K.; Raina, S. "Role of size scale of ZnO nanoparticles and microparticles on toxicity toward bacteria and osteoblast cancer cells." *J. Mater. Sci.: Mater. Med.* **2008**, *20*, 235-241.

25. Armelao, L.; Barreca, D.; Bottaro, G.; Gasparotto, A.; Maccato, C.; Maragno, C.; Tondello, E.; Stangar, U. L.; Bergant, M.; Mahne, D. "Photocatalytic and antibacterial activity of TiO_2 and Au/TiO_2 nanosystems." *Nanotechnology* **2007**, *18*, 375709-375716.

26. Brunet, L.; Lyon, D. Y.; Hotze, E. M.; Alvarez, P. J. J.; Wiesner, M. R. "Comparative photoactivity and antibacterial properties of Cc-60 fullerenes and titanium dioxide nanoparticles." *Environ. Sci. Technol.* **2009**, *43*, 4355-4360.

27. Lee, J. E.; Lee, N.; Kim, T.; Kim, J.; Hyeon, T. "Multifunctional mesoporous silica nanocomposite nanoparticles for theranostic applications." *Acc. Chem. Res.* **2011**, *44*, 893-902.

28. Mocellein, S.; Bronte, V.; Nitti, D. "Nitric oxide, a double edged sword in cancer biology: Searching for therapeutic opportunities." *Med. Res. Rev.* **2007**, *27*, 317-352.

29. Hyeon, T.; Lee, S. S.; Park, J.; Chung, Y.; Na, H. B. "Synthesis of highly crystalline and monodisperse maghemite nanocrystallies without a size-selection process." *J. Am. Chem. Soc.* **2001**, *123*, 12798-12801.

30. Yamashita, T.; Hayes, P. "Analysis of xps spectra of Fe^{2+} and Fe^{3+} ion in oxide materials." *Appl. Surf. Sci.* **2008**, *254*, 2441-2449.

31. Shin, J. H.; Metzger, S. K.; Schoenfisch, M. H. "Synthesis of nitric oxide-releasing silica nanoparticles." *J. Am. Chem. Soc.* **2007**, *129*, 4612-4619.

32. Findlay, V. J.; Townsend, D. M.; Saavedra, J. E.; Buzard, G. S.; Citro, M. L.; Keefer, L. K.; Ji, X. H.; Tew, K. D. "Tumor cell responses to a novel glutathione *S*-transferase-activated nitric oxide-releasing prodrug." *Mol. Pharmacol.* **2004**, *65*, 1070-1079.

33. Frost, M. C.; Meyerhoff, M., E. "Synthesis, characterization, and controlled nitric oxide release from *S*-nitrosothiol-derivatized fumed silica polymer filler particles." *J. Biomed. Mater. Res.* **2005**, *72*, 409-419.

34. Barone, M.; Sciortino, M. T.; Zaccaria, D.; Mazzaglia, A.; Sortino, S. "Nitric oxide photocaging platinum nanoparticles with anticancer potential." *J. Mater. Chem.* **2008**, *18*, 5531-5536.

35. Barbe, C.; Bartlett, J.; Linggen, K.; Finnie, K.; Qiang, L. H.; Larkin, M.; Calleja, S.; Bush, A.; Calleja, G. "Silica particles: A novel drug-delivery system." *Adv. Mat.* **2004**, *16*, 1959-1966.

36. Boas, U.; Heegaard, M. H. "Dendrimers in drug research." *Chem. Soc. Rev.* **2004**, *33*, 43-63.

37. Radu, D. R.; Lai, C.-Y.; Jeftinija, K.; Rowe, E. W.; Jeftinija, S.; Lin, V. S. Y. "A polyamidoamine dendrimer-capped mesoporous silica nanosphere-based gene transfection reagent." *J. Am. Chem. Soc.* **2004**, *126*, 13216-13217.